Characteristics of Distributed Cracking for Analysis and Design of Strain Hardening Cement Based Composites

by

Yiming Yao

A Dissertation Presented in Partial Fulfillment
of the Requirements for the Degree
Doctor of Philosophy

Approved July 2016 by the
Graduate Supervisory Committee:

Barzin Mobasher, Chair
Benjamin Underwood
Narayanan Neithalath
Subramaniam Rajan
Yongming Liu

ARIZONA STATE UNIVERSITY

August 2016

ABSTRACT

As the demand of sustainable construction materials increases, use of fibers and textiles as partial or full reinforcement in concrete members present a tremendous opportunity. Proper characterization techniques and design guides for hybrid materials are therefore needed. This dissertation presents a comprehensive study on serviceability-based design of strain softening and strain hardening materials. Multiple experimental procedures are developed to document the nature of single crack localization and multiple cracking mechanisms in various fiber and fabric reinforced cement-based composites. In addition, strain rate effects on the mechanical properties are examined using a high speed servo-hydraulic tension test equipment.

Significant hardening and degradation parameters such as stiffness, crack spacing, crack width, localized zone size are obtained from tensile tests using digital image correlation (DIC) technique. A tension stiffening model is used to simulate the tensile response that addresses the cracking and localization mechanisms. The model is also modified to simulate the sequential cracking in joint-free slabs on grade reinforced by steel fibers, where the lateral stiffness of slab and grade interface and stress-crack width response are the most important model parameters.

Parametric tensile and compressive material models are used to formulate generalized analytical solutions for flexural behaviors of hybrid reinforced concrete (HRC) that contains both rebars and fibers. Design recommendations on moment capacity, minimum reinforcement ratio etc. are obtained using analytical equations. The role of fiber in reducing the amount of conventional reinforcement is revealed. The approach is extended

to T-sections and used to model Ultra High Performance Concrete (UHPC) beams and girders.

The analytical models are extended to structural members subjected to combined axial and bending actions. Analytical equations to address the P-M diagrams are derived. Closed-form equations that generate the interaction diagram of HRC section are presented which may be used in the design of multiple types of applications.

The theoretical models are verified by independent experimental results from literature. Reliability analysis using Monte Carlo Simulation (MCS) is conducted for few design problems on ultimate state design. The proposed methodologies enable one to simulate the experiments to obtain material parameters and design structural members using generalized formulations.

DEDICATION

I dedicate this to family. Without their love, understanding and support this incredible journey would not have been possible.

ACKNOWLEDGMENTS

I would like to express my sincere gratitude to my advisor and committee chair, Dr. Barzin Mobasher, for his undivided attention, guidance, encouragement and motivation throughout my research. I would like to extend my regards to my committee members: Dr. Subramaniam D. Rajan, Dr. Narayanan Neithalath, Dr. Yongming Liu, and Dr. Shane Underwood for serving in my committee and their guidance in my study. I want to thank Dr. Amir Bonakdar for teaching and supporting in the beginning of my research work. I would also like to acknowledge Dr. Deju Zhu, Dr. Chote Soranakom, Dr. Flavio A. Silva and Dr. Mehdi Bakhshi for their support and successful collaborations. I greatly appreciate the assistance provided by lab support team and engineering technical services comprising of Peter Goguen, Jeff Long, Martin Johnson, Brian Ipema, Dennis Golabiewski, Dallas Kingsbury and Kenneth Witczak for all of their assistance during my active years of research. I would like to acknowledge all my colleagues and friends for their help. I would not be where I am today without all the great support, and love that I have received from my parents and fiancé, Wanlei Quan.

TABLE OF CONTENTS

LIST OF TABLES

Table Page

Table Page

LIST OF FIGURES

Figure Page

Figure Page

Figure Page

Figure Page

1. INTRODUCTION

1.1 Overview

Portland cement industry is among the primary producers of green-house gases generating up to 5% of worldwide man-made CO_2 emissions. The point-source nature of release of green-house gases from cement plants has led to pervasive discussions on the carbon footprint of concrete materials [1,2,3]. Finding alternative construction products is however a daunting task since according to Hammond and Jones [4], cement and concrete contain the lowest embodied energy of all man-made industrial and construction materials. In addition, challenges in practical engineering applications include catastrophic failure due to brittleness of cement materials, impact loads, drying shrinkage, excessive and complicated reinforcement work etc.

As choices of sustainable, economical, and durable infrastructure materials, different types of fiber reinforced concretes (FRC), textile reinforced concrete (TRC), ultra-high performance concrete (UHPC) are among the many new materials developed for the construction industry [5]. Strain-hardening cement-based composites (SHCC) represent a class of fiber reinforced cementitious materials which exhibit improved load bearing capacity and ductility under uniaxial tensile loading [6]. SHCC with tensile strain capacity in excess of 3% under quasi-static uniaxial tensile loading can be attained with only 2% fiber content by volume [7,8]. Several design guides address the contribution of fibers to the post-cracking region by means of a residual strength approach. However, the empirical methods are limited by their inability to be extended to back-calculation approaches or hybrid reinforcement; hence development of an equivalent residual strength method is not possible. This is partially because of failure to incorporate the strain parameter hence the

constitutive model cannot be used for serviceability criteria, deflection calculation, hybrid reinforcement, or shear strength calculations.

The present study is therefore focused on developing methods to better analyze and model concrete structures while pursuing a much more sustainable manner with new materials and design approaches. The core ideology is to model the flexural behavior of strain hardening composites based on the characterization of tensile behavior, by studying the distributed cracking mechanisms. Subsequently, rational and user friendly design approaches for both ultimate and serviceability states for tension, flexural, shear, and combined axil-bending behaviors are addressed. A research path based on the characterization of multiple cracking mechanisms is established and followed throughout the study, as illustrated in Figure 1-1.

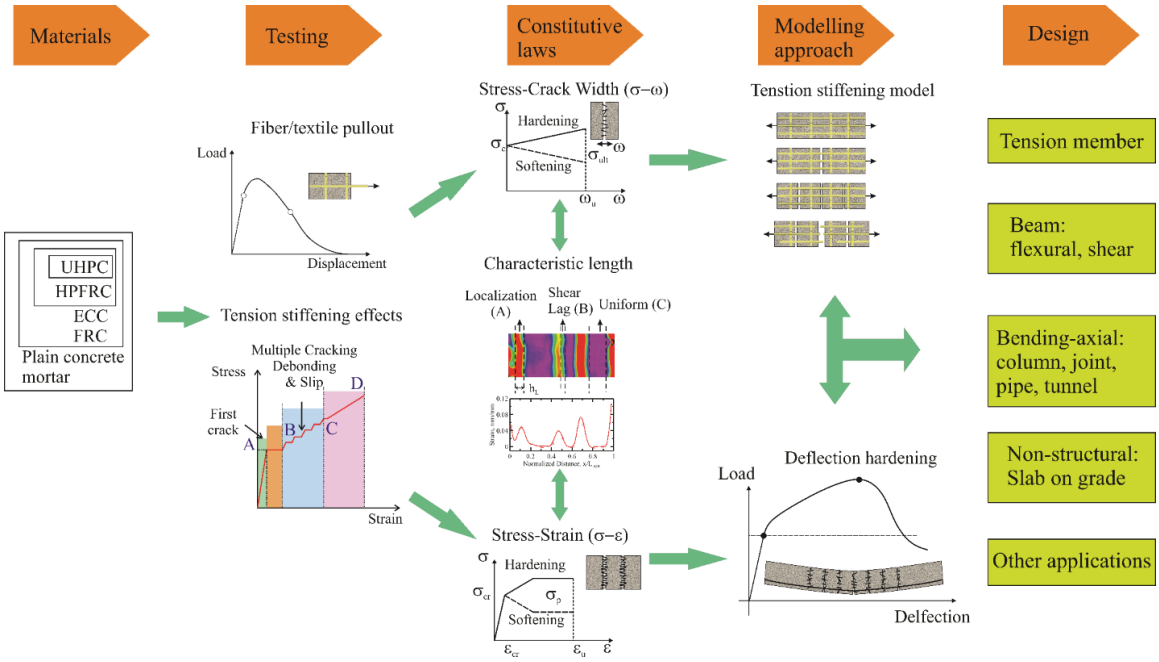

Figure 1-1 Research Path of the Present Study.

The first step is to experimentally investigate the strain hardening behaviors by conducting fiber/textile pullout tests and tensile tests. After the formation of first crack, the tensile

stress keeps increasing at a reduced stiffness. The ability of load carrying in intact concrete matrix is defined as the tension stiffening effect, which is attributed to the interfacial load transfer from fibrous reinforcements to matrix. Pullout load-slip behaviors obtained from experiments are therefore integrated in the modelling approach of tensile behavior. With the conventional data analysis technique and digital image correlation (DIC) method, significant material parameters derived from tension data include tensile strength, ultimate ductility, toughness, stiffness degradation, crack width and crack spacing. These parameters are used to construct and calibrate the tension model.

In the flexural members made of strain hardening cement composites, tension stiffening effects are important in post-cracking behavior where distributed cracking and deflection hardening are observed. The constitutive laws that addresses the strain hardening behavior are then used in the development of flexural models. The contribution of traditional reinforcement and FRC are integrated in a cross sectional analysis. The distributed cracking mechanisms are characterized by the sequential formation of nonlinear hinges denoting the zones subjected to post-cracking damages. Smeared cracking approach is used such that the strain field within each hinge is averaged. Analytical flexural model is developed in this study by addressing the aforementioned aspects which can thus correlate the tension and flexural behaviors. Analytical solutions would keep track of the strain and curvature distribution and enable the measurement of effective deflection and ductility requirements, and therefore enable the development of a serviceability design approach based on deflection, ductility or allowable stress. Design recommendations such as moment capacity, minimum reinforcement ratio are proposed and compared to current design guidelines. Size effects based on serviceability check is investigated.

The proposed analytical model is further improved and extended in the following areas: 1) flexural modelling of concrete beam with T-section; 2) incorporate the role of axial action and model the structural members subjected to combined axial-bending loads; 3) extend to a two dimensional field and determine the shear stress and shear failure in the flexural members. In addition, the two dimensional analysis is compared with finite element (FE) analysis. As a verification and demonstration of the proposed design models, reliability analysis is conducted that takes the randomness in the model parameters into account.

The comprehensive research study makes substantial contributions to the field, which are very useful and may be inspired to the researchers, engineers and designers. The research is summarized with the proposed design guideline for strain hardening cement composite systems that are subjected to varying loading cases. The rational guidelines provide systematic approaches of material characterizations to obtain design parameters and the use of design parameters to determine the ultimate and serviceability limits.

1.2 Background

1.2.1 Common Issues

Cement based materials may be subjected to dynamic loading due to potential projectiles, explosions, earthquakes, wind gusts, or moving objects. Due to the inherent brittleness and low tensile strength of most cement-based elements, dynamic loading may cause severe cracking and damage [9,10]. To properly analyze and design structures, it is necessary to develop, document, and utilize materials with the mechanical properties that are in compliance with the realistic strain and loading rates expected in service. Characterization of dynamic tensile properties in cement composites is challenging as the failure process is affected by the mode and method of testing. Techniques to investigate high-strain rate

material properties include: split Hopkinson pressure bar (SHPB), falling weight devices, flywheel facilities and hydraulic machine [11,12,13,14]. Servo-hydraulic machines are used in medium-strain rate tensile testing of steel [15], plastics [16] and composite materials [17], and cement-based composites [18]. The effect of specimen geometry and size was addressed by the Society of Automotive Engineers (SAE) for the medium strain rates [19], the International Iron and Steel Institute (IISI) [20], as well as ISO standards [21]. Difficulties include inertial effects, non-uniform loading, and reliable measurement of deformations, which are aggravated by the lack of standards and methodology in conducting dynamic tests [16]. Correlation of dynamic properties therefore depends on the loading rate, testing method, and sample geometry [22,23].

The restraint associated with shrinkage is the main causes of cracking. SFRC joint free floors without sawn cuts have been built for more than 30 years for bay sizes up to 3000m^2 [24] and suspended slabs on piles have also been used since 1995 [25]. Despite the benefit from this practical application, design tools for specifying the design parameters are still needed. Although widely used and a number of national floor design standards and recommendations are available, these floors have been adopted primarily by heavy duty users and contractors using the state of the art techniques including low shrinkage concrete and a combination of materials and processes. Thus the overall shrinkage of the slab is limited and cracking is predictable at pre-assigned locations [26]. Shrinkage cracks reduce load carrying capacity and accelerate deterioration, leading to increased maintenance costs and reduced service life [27]. These cracks are the main routes through which aggressive agents such as chloride ions penetrate into and affect the long-term durability of structures [28]. Two common sources are plastic shrinkage and drying shrinkage. Plastic shrinkage

cracking is principally due to a high rate of water evaporation at early age although several driving forces such as differential settlement, thermal dilation, and autogenous deformation are also influential [29]. While drying shrinkage is defined as the contracting of the hardened concrete due to the loss of excessive capillary water [30]. In presence of restraints, the tensile stress builds up and results in cracking once reaching tensile strength of concrete [31,32].

Since standard approaches for treating a combined short fiber-continuous reinforcement system are not available, design of hybrid reinforcement gets further complicated when the shear failure is also considered as a potential failure mechanism. Various empirical models are available for calculating the strength of fiber reinforced concrete beams in shear. Voo and Foster [33, 34] carried out an extensive study on shear strength of steel fiber reinforced concrete by comparing various models for the strength of fiber reinforced concrete beams in shear without stirrups. Model results were compared with data from 220 prestressed and non-prestressed beams reported by 27 researchers with the compressive strengths varied from 20MPa to 170MPa, the shear span to effective depth ratios were in the range of 0.46 to 5.2, the total depths of 100 mm to 800 mm, the volume of steel fibers of 0.2 to 3.0% and the longitudinal steel ratio from 0.8 to 9.6%. On the other hand, large scatters are observed for most of the models, such as Narayanan and Darwish [35], Al-Ta'an and Al-Feel [36] resulting in covariance of 46% and 41 % respectively. Several available empirical models for shear capacity proposed by Nemegeer and Khuntia et al. [37] fail to predict a safe design as the ratios between theoretical and measured values were larger than one for a portion of the data pool. These approaches are not conducive to clear correlations since so many data points for different studies are combined and an empirical curve-fitting equation is the best

outcome of such studies. It is therefore essential to better understand the modes of shear stress distribution and a more rational mechanical approach may provide a general vision.

1.2.2 Fiber and Textile Reinforcements

For more than forty years FRC has been used in many construction applications such as slabs on grade, industrial floors, tunnel linings, precast and presstressed concrete products. Use of discrete fibers significantly improves fracture toughness, ductility, fatigue resistance, as well as tensile and shear strength. Recent advances in performance of FRC have been based on a sufficiently high fiber content ($0.5\% < V_f < 1\%$) to gain significant ductility and strength. A fiber content of 0.75% without stirrups is considered sufficient to achieve the equivalent ultimate resistance of a conventional RC flexural member with stirrups [38]. The use of fiber also enhances the behavior at service life conditions by increasing the stiffness and residual strength in the serviceability loading stage by means of restraining the crack opening and limiting excessive deformations [39]. This has led to development of structures such as elevated SFRC slabs and precast tunnel lining segments that use a hybrid reinforcement approach [40, 41, 42]. Portions of the conventional reinforcement are replaced by steel fibers in most parts to address the flexural capacity. In the case of elevated slabs only a small amount of reinforcement is needed along the column strips to prevent progressive failure, while the amount of rebar in precast segmental sections is substantially reduced.

The use of textiles as reinforcement in cement based systems greatly enhances the strength, strain capacity, and work-to-fracture of the composite by means of multiple cracking mechanism and leads to strain hardening behavior. The outstanding mechanical performance can be utilized for load bearing structural members, structural panels, impact

and blast resistance, repair and retrofit applications [43,44]. The mechanical response and distributed damage zones have been studied under both static and dynamic loads using conventional technique [45,46]. Figure 1-2 shows the use of such Steel-FRC elevated slabs with material properties obtained from flexural tests and designed using a limit analysis approach. The slabs contain no continuous reinforcement, and a progressive collapse mechanism is unlikely due to use of about 1% steel fiber reinforcement, and a set of minimum continuity reinforcing bars discussed earlier [47,48,49].

Figure 1-2 Construction and Applications of SFRC Slabs as the Main Reinforcing Material Used in Multistory Buildings. b) Failure Patterns of Distributed Fan Cracking Patterns in a Round Panel Test Method.

1.2.3 Review of Existing Design Approaches

By integrating the reinforcement within the material design, one can be creative with non-conventional shapes or connections which may otherwise be quite difficult with rebar lay outs. Forming becomes easier and faster and savings in cranes costs and scheduling aspects of the limited resources is obvious since the reinforcement can be pumped along with the concrete. The key advantages of using fiber composite systems include savings in labor and construction time attributed to installation of layers of rebars and stirrups. The FRC

concrete is discharged from the truck mixer or pumped, saving time of the order of days for large to medium projects, eliminating the need to use heavy equipment, or maintain an inventory for rebars. From a design perspective, an elasto-plastic design approach results in reductions in material weight and improves ductility. Moreover, as the requirements for concrete cover are omitted, global cost saving as much as 10-30% vs. plain traditional methods can be achieved by accounting for all cost aspects. Better shrinkage control directly results in a reduced number of surface cracks, narrower crack widths, and extended service life. Used in a hybrid manner to reduce the congestion of rebars in reinforced concrete, fibers in self-consolidated concrete increase the cost-effectiveness, and labor efficiency of structures such as water and wastewater structures with improved durability and minimized need of maintenance and repair operations during lifetime.

The enhancement in the load capacity and ductility depend on the fiber parameters such as type, shape, aspect ratio, bond strength and volume fraction [229]. Tensile characteristics are defined in terms of strain softening and hardening, and within the strain softening category, sub-classes of deflection-softening and -hardening may be defined based on the behavior in bending. Several building codes provide guidelines on design with FRC materials [50,51,52,53]. Combinations of FRC and rebars or welded wire mesh may be used to meet the strength criteria, hence HRC is referred to as a section that combines a continuous reinforcement with randomly distributed chopped fibers. Many available models for FRC [54, 55, 56, 57] require a strain compatibility analysis of the layered beam section in order to obtain moment capacity, which may be impractical for general users. Development of a unified approach for both continuous and discrete reinforcements is therefore needed.

Several design guides address the contribution of fibers to the post-cracking region by means of a residual strength approach. The flexural data obtained from beam tests include three-point bending (3PB) by RILEM, EN 14651, or four-point bending (4PB) test used by JCI and ASTM C1609 are used in back-calculation of tensile properties. In the RILEM TC 162-TDF [57] test, the tensile σ–ε relation is obtained from the load capacity at certain deflections based on closed loop controlled bending tests on notched beams, and calibrated using finite element method. Residual tensile strength is also obtained from simplifications proposed by RILEM, or fib Model Code 2010 [58,59]. For example, the residual tensile strength is taken as f_{res}=0.37$f_{t,eq}$, where $f_{t,eq}$ is the average equivalent bending strength recorded between 0.5 and 2.5mm deflection. Factor 0.37 expresses the ratio between the tensile stress in the uncracked section and the equivalent tensile stress in the cracked section assuming the validity of plane sections remaining plane, and further assuming a depth of the compressive zone in the cracked stage as 10% of the original depth [60].

Development of a serviceability design approach based on deflection, ductility or allowable stress would require the computation of load capacity of a cracked section based on a given curvature or crack width. Such solutions would keep track of the strain and curvature distribution and enable the measurement of effective deflection and ductility requirements. Soranakom and Mobasher used a parametric material tensile and compression constitutive model and derived analytical flexural load-deflection behavior from closed form moment-curvature expressions [61,62]. Constitutive properties are then obtained by inverse analysis of load-deflection response. This approach was used by Van Zijl and Mbewe [63] for an analytical flexural model for hybrid SFRC, however they employed a single mode of failure which limits the applicability to strain softening, deflection hardening SFRC. Taheri

et. al. used a similar approach to develop a design model for hybrid SFRC with steel and FRP bars using the constitutive model of Soranakom and Mobasher and investigated post-cracking strength, and reinforcement ratio [54].

This study addresses a potential direction for a serviceability based design and promises to deliver a much more robust design methodology that integrates serviceability with the ultimate strength approach. Analytical solutions for serviceability based nonlinear design address a variety of structural HRC systems. For example, sustainability, serviceability, and durability perspectives for design of elevated slabs, structural vaults, retaining walls, and pump and lift stations for environmental structures are proposed by limiting the curvature, and crack width. Strain based serviceability limit states can be specified using short and long-term deformations, cracking, shrinkage, and verified to address ultimate limit states requirements [64, 65]. Moreover, analytical equations can be used for selection of variables using a design automation procedure; hence gradient-based optimization algorithms can be conducted much faster. The moment-curvature relationship can also be directly implemented in a structural analysis codes, limit analysis, and implemented in structural analysis software.

1.3 Thesis Structure

Chapter 2 presents the mechanical characterization of tensile behavior for both reinforcing materials (fiber/textile) and fibrous reinforced cement composites. The tensile testing is performed both at static and high strain rates. Multiple cracking mechanisms and non-uniform deformation fields are captured analyzed by DIC method. Based on DIC observations and modelling assumptions, three different zones localization, shear lag and uniform are documented. The strain rate effects in tensile properties are investigated on

both reinforcements and cement composites. In addition, the effects of temperature on the stiffening behaviors are also evaluated from low to high temperatures.

Chapter 3 introduces a tension stiffening model that addresses the cracking mechanisms by using four basic aspects: cement cracking criterion, fiber/textile stress-strain model, interface bond-slip model and mechanical anchorage provided by transverse yarns (specifically for TRC). The applications of the tension model in this chapter include the simulation of direct tension tests, and the sequential cracking behaviors in slab on grade due to drying shrinkage. Even though the driving forces of these two types of applications are different, the fundamental cracking and tension stiffening mechanisms are similar, and the cause of cracking is essentially the built up of tensile stress.

Chapter 4 describes the development of the analytical model for the flexural members. Multi-linear stress-strain models are used to represent the compressive and tensile responses of FRC, as well as the tensile behavior of rebars. Using the parametrized material models, analytical solutions for moment-curvature responses are derived through cross sectional analysis. Subsequently, load-deflection solutions are also obtained. Design recommendations on RC members with addition of steel fiber in a hybrid manner are proposed in this chapter. In addition, size effects on the serviceability limits are studied.

Chapter 5 extends the analytical model to the structural members subjected to combined axial-bending loads by considering the axial action. Using the same material models, and similar section analysis method, analytical solutions to construct interaction diagram are derived. The application of this model may include the design of short column, beam-column joint, and tunnel lining segments.

Chapter 6 addresses the shear behavior in flexural members by performing two dimensional stress analysis throughout the entire beam model. The full field distributions of normal strain and stress are first obtained based on the moment-curvature distribution and material models. Then classical stress analysis approach is employed to calculate the shear stress, principal stress and principal directions. The analysis indicates that the principal stresses at the tip of flexural cracks are along the diagonal direction which may explain the propagation of flexural cracks into diagonal crack. FE analysis on the shear behavior of strain hardening composites are also presented in this chapter.

Chapter 7 presents the reliability analysis as a demonstration and verification of the proposed design methods. The procedure is illustrated by a beam example. The random parameters are identified and reliability indices are determined using Monte Carlo Simulation (MCS).

Chapter 8 summarizes the content of the dissertation and gives the recommendation for the future work into these topics.

2. MECHANICAL CHARACTERIZATION OF DISTRIBUTED CRACKING

2.1 Reinforcing Materials

High performance fabrics are known for their high strength/modulus to weight ratio, fatigue and corrosion resistance, lower manufacturing costs and the ability to tailor composites compared to conventional metals [66]. This class of materials have been extensively studied and used in the fields of structural and aerospace engineering, such as aircraft construction [67], fabrics reinforced concrete structures [68], strengthening and retrofit of RC beams and masonry walls [69,70]. High strength fabrics in the engineering fields of structural, military, aerospace, and sports disciplines might be subjected to dynamic loadings, such as wind loads, earthquake loads, fast moving traffic, explosions, etc. The common strain rates observed in static and high speed experiments range from 10^{-6} to 10^{3} s^{-1} which demonstrates orders of magnitude difference. Mechanical properties such as strength, modulus, toughness, ductility at high strain rate can significantly differ from those obtained under quasi-static loading. The material characterization under high speed loading conditions is therefore of great importance. However, the experimental techniques to generate tensile stress–strain data at the medium strain rates in the range of 1–100 s^{-1} are not well established.

Research on tensile strength of fiber bundles and woven fabrics under quasi-static and dynamic loadings has been reported by different authors. Wang and Xia [71] found that the strength and ultimate strain (strain corresponding to the maximum tensile stress) of E-glass fiber bundles were increased when the strain rate increased from 90 to 1100 s^{-1}. Zhou et al. [72] reported that the tensile strength and ultimate strain of T700 carbon fiber bundles were insensitive to the strain rate ranging from quasi-static (0.001 s^{-1}) to high speed (100,

300 and 1300 s^{-1}). Hou et al. [73] tested 3-D angle-interlock woven carbon fabrics (3DAWF) on a SHPB under high strain rates from 1080 to 2040 s^{-1} and conducted finite element analyses (FEA) using a microstructure geometrical model. The fracture morphologies in different layers and stress wave propagation along the weft and warp fiber tows were revealed by the FEA, which may explain the strain rate sensitivity of the material. Sanborn and Weerasooriya [74] tested single Kevlar KM2 fiber at three strain rates: 0.001, 1, and 1200 s^{-1} using a load frame system (Electroforce) and SHPB. The average tensile strength increased from 4.3 GPa to 5.1 GPa from quasi-static to high rate. Wang and Xia [75] observed that failure stress, ultimate strain, and Young's modulus of Kevlar® 49 were directly proportional with the strain rate ranging from 10^{-4} to 1350 s^{-1}. Nevertheless, other researchers have presented different observations. Wagner et al. [76] reported that Kevlar® 29, Kevlar® 49, and Kevlar® 149 fibers were insensitive to the strain rate in the range of $3x10^{-4}$ to 0.024 s^{-1}. Cheng et al. [77] tested Kevlar® KM2 fibers in the range of 0.00127 - 2451 s^{-1}. The results were insensitive to the loading rates and fibrillation was the major cause of failure at both quasi-static and dynamic loading rates. According to Farsi et al. [78], the failure strengths of Kevlar® 129, Kevlar® KM2 and Kevlar® LT yarns showed limited dependence on strain rate. Lim et al. [79] investigated the tensile properties of single fibers of Kevlar, Kevlar 129 and Twaron using a miniature tension Kolsky bar at strain rates from 0.001 to 1500 s^{-1}. It was found that the tensile strengths of these single fibers did not exhibit significant strain rate sensitivity.

Basalt is a low cost material that brings interesting opportunities to the construction industry because of high modulus, strength and strain to failure, as well as good thermal and chemical resistance. Basalt fiber is made from melting basalt rock which is non-toxic

and non-combustible. The manufacturing process is similar to that of glass fiber, but with less energy consumed and no additives, which makes it superior to glass or carbon fibers in terms of cost [80,81,82,83,84]. With the help of these mechanical properties, basalt fiber and its composite can be widely applied in the field of engineering like glass or carbon reinforcements [85]. Deak and Czigany [86] compared the mechanical properties of continuous basalt fibers with E-glass fibers by means of static tensile tests. The tensile strength of several different types of basalt fibers ranged from 1811 to 2016 MPa, while the strength of glass fiber was 1472 MPa. In addition, the measured ductility and elastic modulus of basalt fibers were competitive with those of E-glass. However, study on the tensile behavior of basalt fibers or in fabric form under dynamic loading is very limited. Zhu et al. [87,88] conducted quasi-static (0.001 s^{-1}) and high strain rates (up to 3000 s^{-1}) tensile tests on basalt filament tows and observed increases in tensile strength, stiffness and toughness as the strain rate increased, while the ultimate strain decreased. A single Weibull constitutive model was proposed to describe the stress-strain relationship of the fiber bundles under different strain rates. Both the scale and shape parameters increased with the strain rate. However, the tensile behaviors at intermediate strain rates were not characterized in the study.

In the present work, dynamic tensile tests using high-rate servo-hydraulic system were conducted on basalt, carbon, glass and aramid fabrics at strain rates ranging from 25 to 100 s^{-1} [89]. Quasi-static tensile tests were also performed as a comparison. The deformation and failure behaviors of the specimens were captured using a Phantom v7.3 high speed digital camera. Materials parameters including the Young's modulus, tensile strength, ultimate strain, maximum strain, and toughness were investigated and compared at these

strain rates. Statistical study by means of ANOVA was conducted to verify the significance of strain rate effect on different material properties. In addition, probabilistic distributions of fabrics strength at varying strain rates were obtained using Weibull analysis in order to account for the random imperfections in fabrics.

2.1.1 Experimental Methodology

Glass, carbon and basalt unidirectional fabrics were manufactured with woven densities of 5.3 glass yarns (12K), 3.75 carbon yarns (12K) and 2.7 basalt yarns (12K) per cm in the warp direction, respectively. Aramid (Kevlar® 29) fabric had a plain-woven structure of 6.5×6.5 yarns (1K) per cm. The fabrics were manufactured by local companies in China (Yixing Hengtong Carbon Fibers Co., Ltd. and Nanjing Hitech Composites Co., Ltd). The details of the typical properties are shown in Table 2-1. The total cross-sectional area for each ply was calculated using the values of the linear density and bulk density of the material. The cross-sectional area of the specimen was defined as the cross-sectional area per yarn multiplied by the number of the yarns of the specimen. Glass, carbon, basalt and aramid fabrics were cut to the width of 22 mm using an electric scissor allowing 8, 8, 8 and 12 yarns in the section of 25 mm gage length. In order to reduce the stress concentration and improve load transfer in grips, thin aluminum sheets, 40 mm long, 22 mm wide and 0.3 mm thick, were glued on the two ends of each specimen using two-component epoxy resin. Prepared specimens are shown in Figure 2-1.

Table 2-1 Basic Material Property of Fabrics [89]

Material	Yarn Count (yarn/cm)	Bulk Density (g/cm^3)	Linear Density (g/cm)	c/s Area per Yarn (cm^2)
Glass	5.3	2.54	$12.0(10^{-3})$	$4.73(10^{-3})$
Carbon	3.75	1.8	$8.11(10^{-3})$	$4.51(10^{-3})$
Basalt	2.7	2.8	$7.98(10^{-3})$	$2.85(10^{-3})$
Aramid	6.5	1.44	$1.64(10^{-3})$	$1.14(10^{-3})$

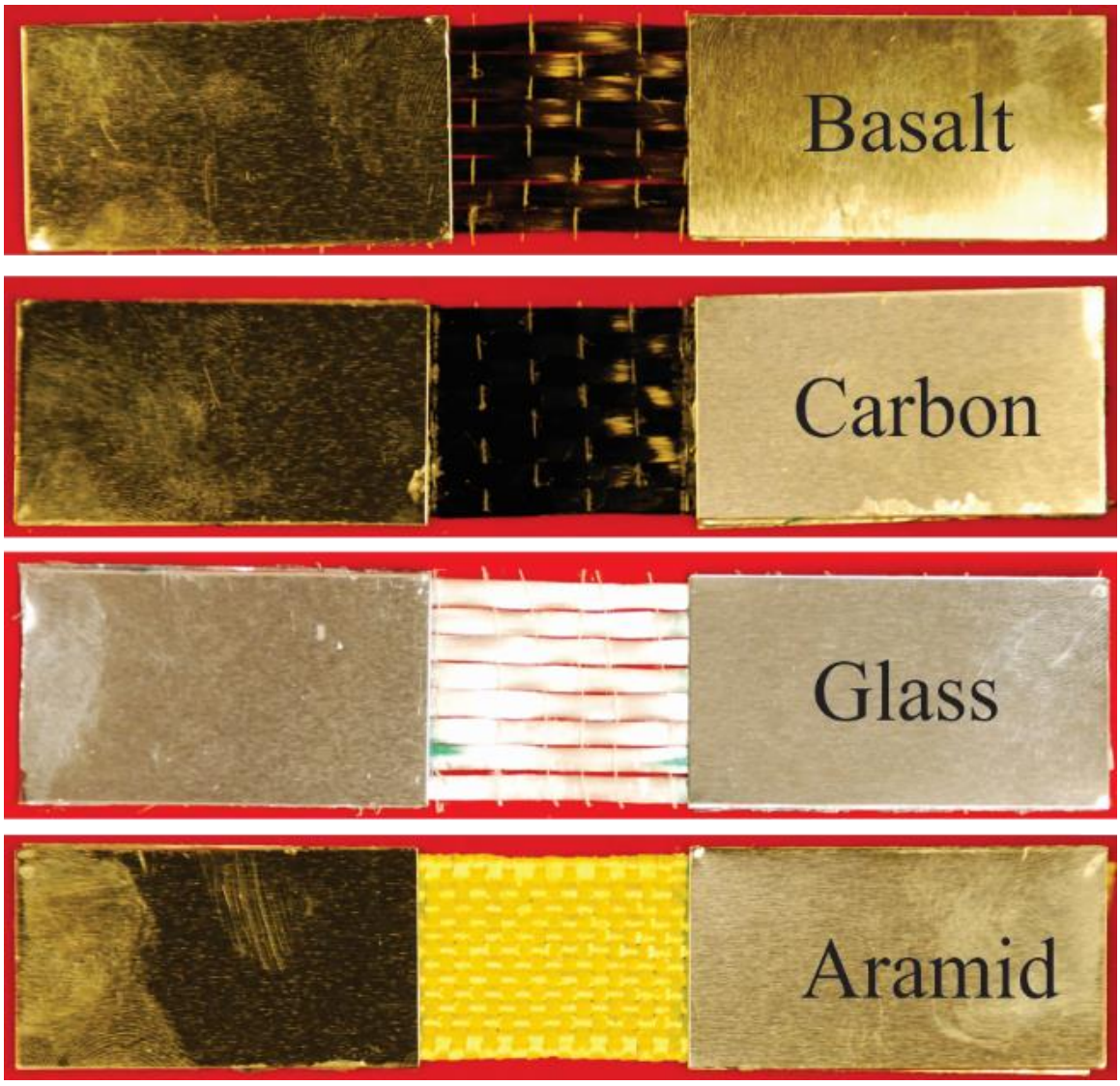

Figure 2-1 Prepared Typical Specimens for Dynamic Tests Including Glass, Carbon, Basalt and Aramid [89].

Quasi-static testing was performed on a MTS load frame (C43.304) at Hunan University.

A load cell with 1 kN capacity was used for force measurement with a sampling rate of 20

Hz, and the cross head velocity was set to be 2.5 mm/min. The nominal strain rate thus equals to the velocity divided by the gage length, which is 1/600 s^{-1}. Additionally, an extensometer was attached to measure the strain within gage area.

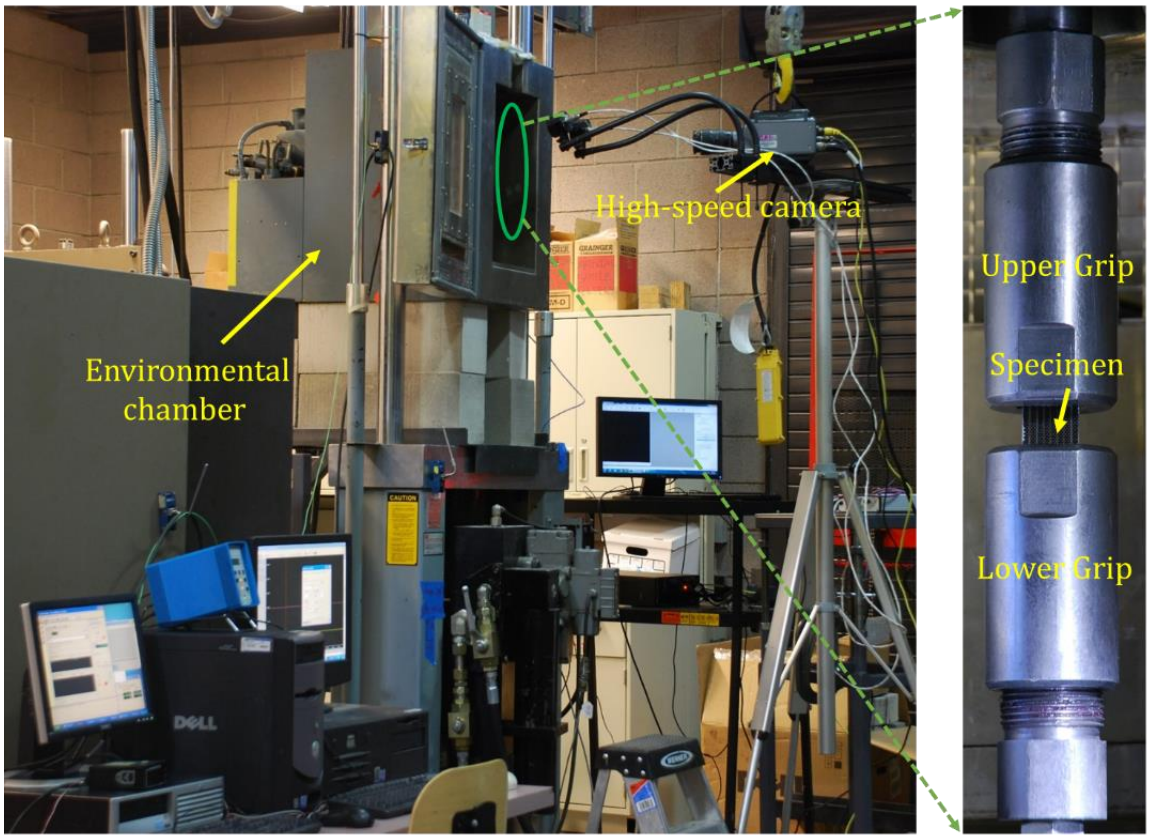

Figure 2-2 High Speed Test Setup [89].

The dynamic tensile tests were conducted using a MTS high-rate servo-hydraulic testing machine at Arizona State University. The speed of the stroke is controlled by the opening and closing of the servo-valve of hydraulic supply. By manually turning the servo-valve, the flow rate of hydraulic fluid can be controlled, resulting in different stroke speeds. The initial strain rate applied to the test specimen is defined by the stroke speed divided by the gage length of specimen. And the stroke speed can be obtained as the slope of the stroke displacement versus loading time curve. Figure 2-2 shows the high strain rate testing system. In addition to the loading frame, the system includes MTS Flex SE control panels

and a high speed data acquisition card with a maximum sampling rate of 5 MHz. More discussion of the testing equipment, development of high speed test procedure can be found elsewhere [106]. A state-of-the-art Phantom v7.3 high speed digital camera was used to record the failure behavior of the specimens at a sampling rate of 20,000 frame per second (fps) with resolution of 256 x 256 pixels and exposure time of 48 μs. Two heat-free LED lamps were used to offer bright and flicker free light in order to capture high quality images. Specimens of 25 mm gage length were tested at three initial strain rates of 25, 50 and 100 s^{-1}. Six replicates were tested under quasi-static loads for each material. Since larger scatter in the data obtained from dynamic tensile tests was expected, eight replicates were tested for each fabric at each strain rate. Therefore, the total number of specimen tested in the present study is 120. The actual strain rate of individual test might be slightly different from the strain rates listed above.

The signals from the load washer and stroke were recorded at a sampling rate of 500 kHz. These signals contained high frequency noises which were eliminated using a low pass filter with cut-off frequency of 3 kHz during the data processing. Figure 2-3(a) shows the stress-strain response of an aramid specimen obtained from a typical test. Figure 2-3(b) schematically illustrates the four distinct regions observed in the tensile stress-strain behavior during loading: crimp region, elastic region, nonlinear failure region, and post-peak region. The initial curvature of the weaving pattern is referred to as the crimp in woven fabrics, and in this portion, the load essentially straightens the yarns and removes the crimp. Therefore, the stress-strain graph shows a relative large increase in strain at low stress level during crimp region. Once the straightened yarns start to take more loads, the slope of the curve increases and this zone is referred to as the elastic region. Young's

modulus of the fabric is measured as the slope of the curve in elastic region. The stress-strain response exhibits nonlinearity (nonlinear failure region) before reaching the tensile strength which can be traced back to the initiation and propagation of random fracture in the individual filament within yarn bundle prior to its localized failure. The final stage of response is characterized by a rapid decrease in the stress beyond the tensile strength that correlates with progressive yarn failure (post-peak region). Typical tensile stress-strain responses of the other three fabrics investigated in this study are similar except that there is no crimp region in the unidirectional fabrics. The stress-strain curves were analyzed to measure the Young's modulus, tensile strength, ultimate strain (strain at peak stress), maximum strain and toughness for all the specimens. The toughness is evaluated using the area under the stress-strain curve.

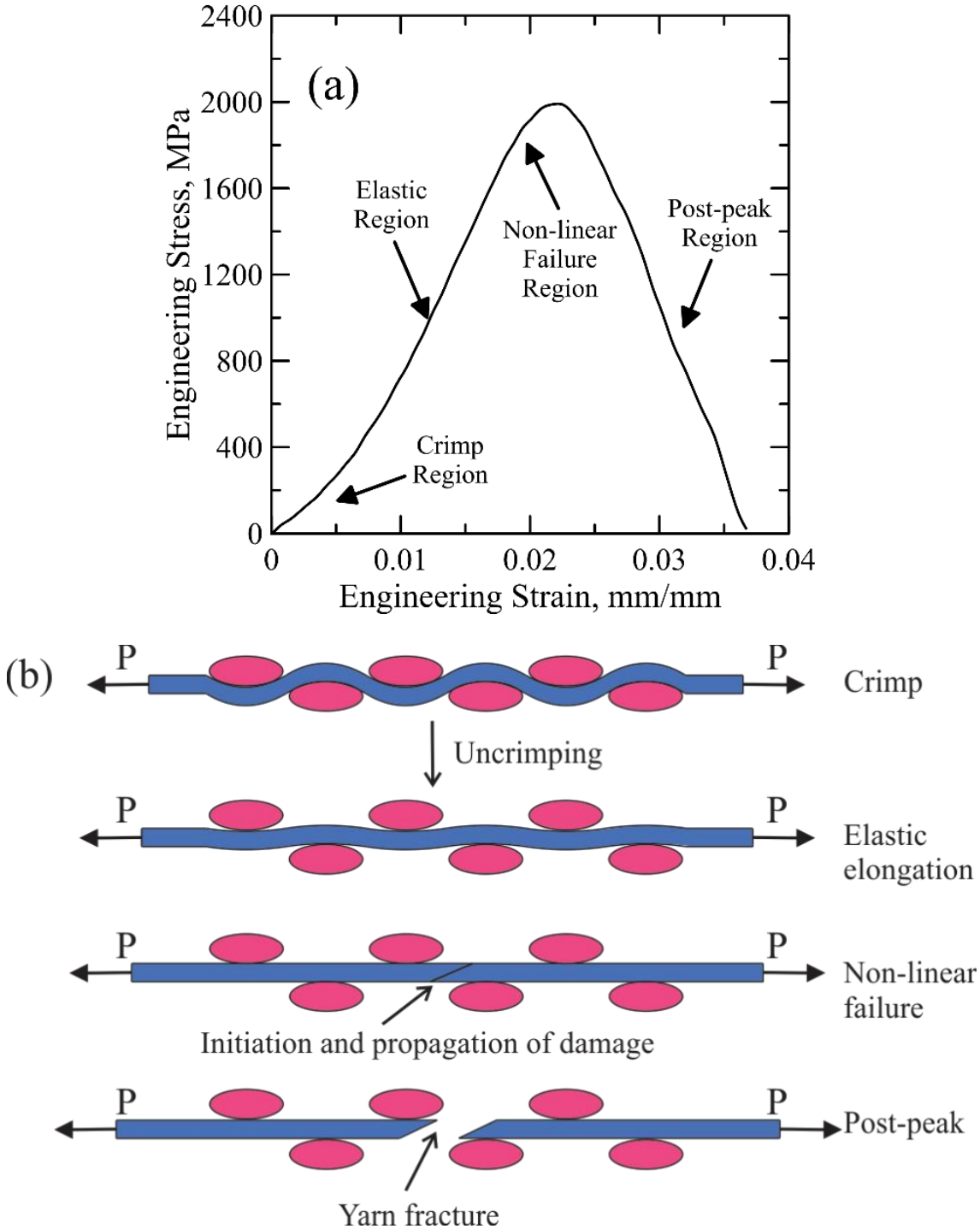

Figure 2-3 (a) Four Regions in a Typical Stress-Strain Curve of a Test Specimen Subjected to Dynamic Tensile Loading, (b) Schematic Diagram of the Tensile Behavior of Aramid Fabric [89].

2.1.2 Results and Discussions

Table 2-2 summarizes the averaged experimental results of different fabrics where the values in parenthesis indicate their respective standard deviations. Figure 2-4 shows the experimental stress-strain responses of all aramid replicates tested at various initial strain rates where the four regions including crimp, elastic, nonlinear failure and post-peak can be identified. Increases in tensile strength with increasing strain rate can be evidently observed and the shape of the curves is also affected. Slight vibrations are observed in the stress-strain curves at 25 s^{-1}, but disappear at higher strain rates, which are attributed to the system ringing as previously studied by Zhu et al. [44]. Figure 2-5(a)-(d) compare the representative stress-strain curves of the four types of fabrics at three different initial strain rates, i.e. 25, 50, and 100 s^{-1}. While uniform stress-strain behaviors at different strain rates are observed for each material, different Young's modulus, tensile strength, ultimate strain, maximum strain, and toughness are obtained which reveal the strain rate effects. The average tensile strength of basalt fabrics increases from 1095 MPa to 1743 MPa and the average toughness increases from 31.2 mJ/mm^3 to 45.3 mJ/mm^3 when the strain rate increases from 25 to 100 s^{-1}. Average ultimate strain and maximum strain as measurements of ductility increase from 0.0236 mm/mm to 0.0324 mm/mm, and 0.0475 mm/mm to 0.0515 mm/mm, respectively, which contributes to the increased capability of energy absorption at higher strain rates.

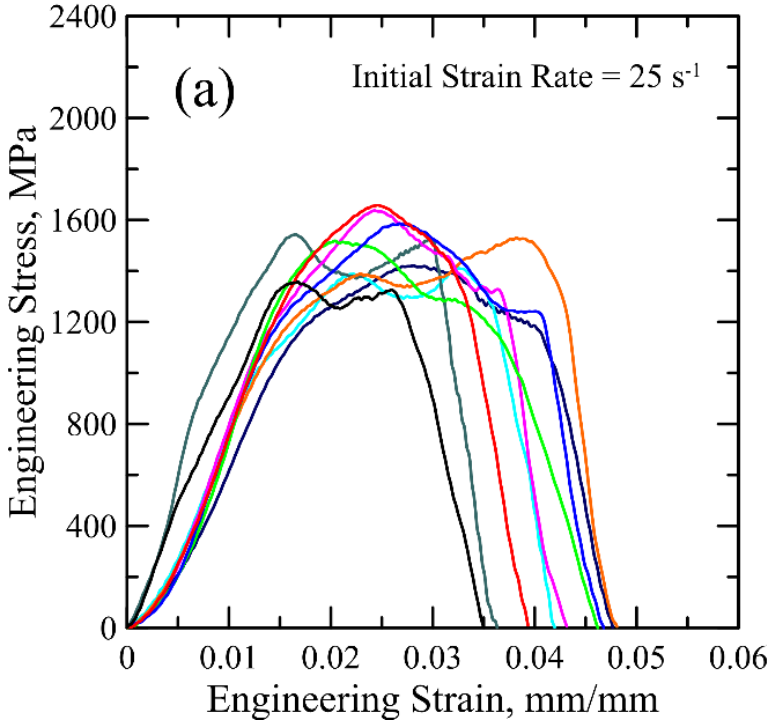
(a)
Initial Strain Rate = 25 s-1
Engineering Stress, MPa
Engineering Strain, mm/mm
0
400
800
1200
1600
2000
2400
0
0.01
0.02
0.03
0.04
0.05
0.06

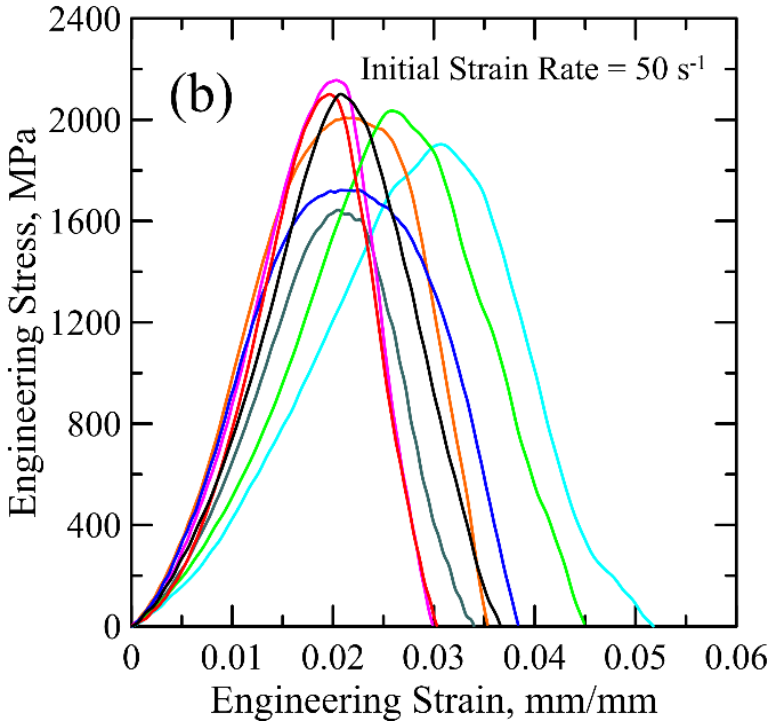
(b)
Initial Strain Rate = 50 s-1
Engineering Stress, MPa
Engineering Strain, mm/mm
0
400
800
1200
1600
2000
2400
0
0.01
0.02
0.03
0.04
0.05
0.06

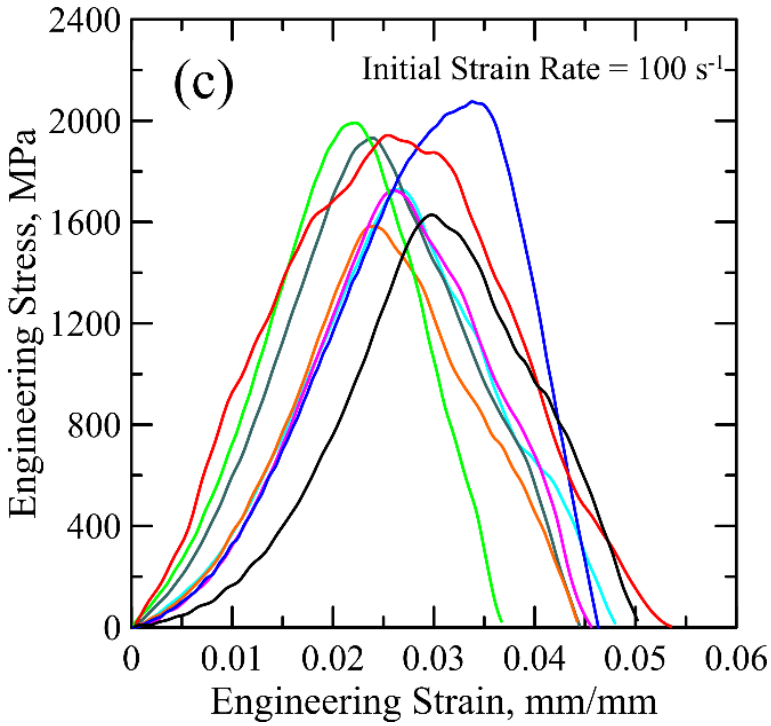

Figure 2-4 Experimental Stress-Strain Curves of Aramid Replicates Tested at Initial Strain Rate of (a) 25 s^{-1}, (b) 50 s^{-1} and (c) 100 s^{-1} [89].

For carbon fabrics, when the initial strain rate increases from 25 to 100 s^{-1}, the average tensile strength increases by as much as 30% from 1516 MPa to 1974 MPa, while the average maximum strain increases from 0.0392 mm/mm to 0.0511 mm/mm. As a result of increasing strength and ductility, the average toughness is raised from 35.0 mJ/mm^3 to 51.3 mJ/mm^3. The same trends are also observed in the average tensile properties of glass fabrics as the strain rates increases from 25 to 100 s^{-1}: tensile strength increases from 1072 MPa to 1462 MPa, toughness increases from 29.3 mJ/mm^3 to 42.1 mJ/mm^3, the ultimate strain and maximum strain consistently increases from 0.0328 mm/mm to 0.0430 mm/mm, and 0.0446 mm/mm to 0.0626 mm/mm, respectively. The average tensile strength of aramid increases from 1530 MPa to 1920 MPa from 25 to 50 s^{-1}, but remains nearly the same (1897 MPa) at 100 s^{-1}. Toughness, ultimate and maximum strains all increase with the strain rate.

However, the values of Young's modulus for different fabrics are not monotonically increasing or decreasing with changing strain rate.

Table 2-2 Summary of Testing Results [89]

Material	Strain Rate (s^{-1})	Tensile Strength (MPa)	Toughness (mJ/mm^3)	Ultimate Strain (mm/mm)	Maximum Strain (mm/mm)
Basalt	1/600	1427 (85)	37.2 (5.7)	0.0338 (0.0044)	0.0420 (0.0039)
	25	1095 (65)	31.2 (5.2)	0.0236 (0.0025)	0.0475 (0.0040)
	50	1545 (187)	43.5 (11.1)	0.0295 (0.0111)	0.0447 (0.0095)
	100	1743 (131)	45.3 (9.6)	0.0324 (0.0043)	0.0515 (0.0098)
Carbon	1/600	2302 (171)	46.2 (4.2)	0.0168 (0.0035)	0.0278 (0.0053)
	25	1516 (169)	35.0 (8.1)	0.0237 (0.0037)	0.0392 (0.0041)
	50	1623 (228)	38.8 (11.9)	0.0229 (0.0075)	0.0419 (0.0079)
	100	1974 (199)	51.3 (14.5)	0.0333 (0.0101)	0.0511 (0.0091)
Glass	1/600	1048 (66)	20.6 (2.5)	0.0207 (0.0016)	0.0304 (0.0036)
	25	1072 (66)	29.3 (3.4)	0.0328 (0.0043)	0.0446 (0.0036)
	50	1220 (80)	38.5 (5.7)	0.0346 (0.0091)	0.0528 (0.0061)
	100	1462 (117)	42.1 (10.3)	0.0430 (0.0096)	0.0626 (0.0139)
Aramid	1/600	2273 (124)	92.4 (12.9)	0.0596 (0.0085)	0.0655 (0.0051)
	25	1530 (97)	41.4 (4.8)	0.0248 (0.0067)	0.0418 (0.0042)
	50	1920 (174)	40.0 (7.4)	0.0252 (0.0065)	0.0398 (0.0070)
	100	1897 (109)	46.4 (7.2)	0.0301 (0.0058)	0.0511 (0.0084)

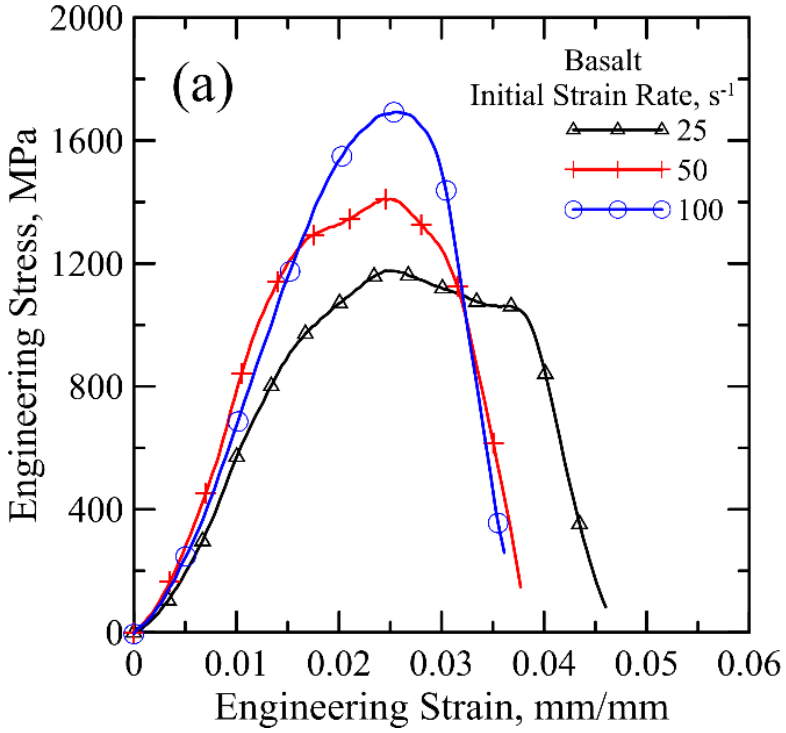
(a)
Basalt
Initial Strain Rate, s-1
25
50
100
Engineering Stress, MPa
Engineering Strain, mm/mm
0
400
800
1200
1600
2000
0
0.01
0.02
0.03
0.04
0.05
0.06

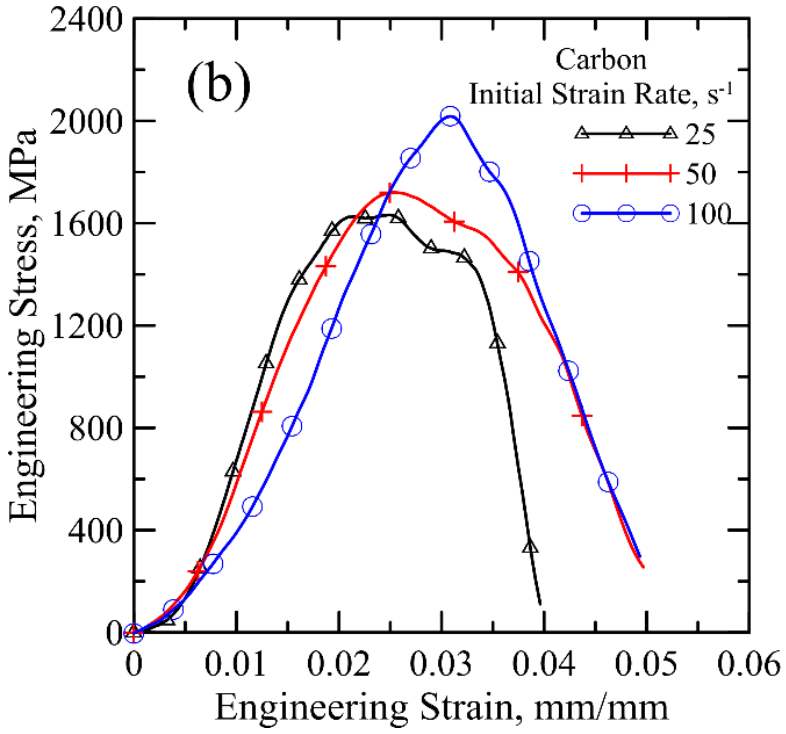
(b)
Carbon
Initial Strain Rate, s-1
25
50
100
Engineering Stress, MPa
Engineering Strain, mm/mm
0
400
800
1200
1600
2000
2400
0
0.01
0.02
0.03
0.04
0.05
0.06

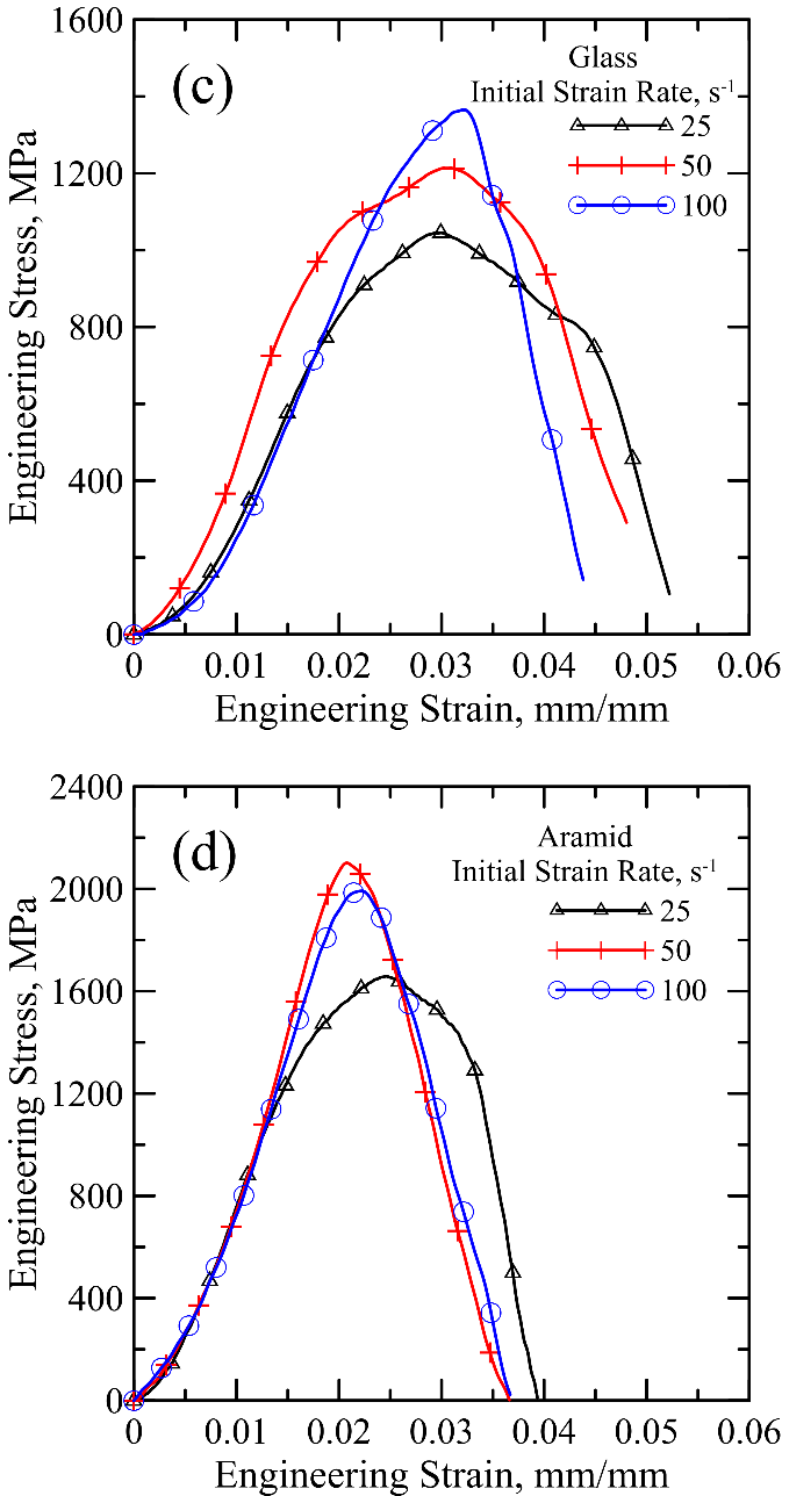

Figure 2-5 Representative Engineering Stress-Strain Responses of (a) Basalt, (b) Carbon, (c) Glass and (d) Aramid Fabrics Tested at Varying Initial Strain Rates [89].

Figure 2-6 compares the material properties for various fabrics at different strain rates, which are characterized by the average and standard deviations. As shown in Figure 2-6(a), the tensile strength of carbon and aramid fabrics from quasi-static tests are higher than that of high speed tests, which may be explained by the different failure patterns. The fracture of warp yarns tends to occur simultaneously under quasi-static loading, while the failure initiates from one yarn or some yarns at high strain rates as captured by the high speed camera, which leads to load (and stress) redistribution within unbroken yarns and results in a lower actual strength compared to an average strength value. The phenomenon may be attributed to the different test configurations as well as the interactions between random flaws/imperfections in the fiber structure and dynamic loads which need further study. When the number of yarn bundles is reduced to one, there are less amount of flaws in samples with less yarns, which results in a more uniform distribution of strength. For example, preliminary results of the single yarn tensile tests performed by authors show that as the strain rate increases from quasi-static (1/600 s^{-1}) to high strain rates (40, 80, 120 and 160 s^{-1}), tensile strength of aramid (Kevlar® 29) single yarn increases monotonically from 2026 to 2247, 2439, 2465 and 2691 MPa, respectively. Similar trends are also observed in carbon, basalt and glass single yarns. In addition, when the epoxy resin is used as matrix binder in glass reinforced polymer (GFRP), the tensile strengths of GFRP with one yarn in the width under the same dynamic loadings (high strain rates) are also found to be higher than the quasi-static result, as shown in the work done by Ou and Zhu [90]. Use of matrix binder enables the redistribution of the tensile stress through interfacial load transfer mechanism between fibers and matrix, as discussed by Yao et al. [115]. When it comes to ductility, aramid and basalt fabrics exhibit larger ultimate and maximum strains at quasi-

static loading compared to high speed loads while the other two materials show increasing trends from low to high strain rate. As a result of high tensile strength and ductility, aramid fabric demonstrates highest toughness under quasi-static loading condition compared to other strain rates. Except the carbon fabric, higher Young's moduli are obtained under dynamic tensile loads for the other three materials as compared to quasi-static results.

From a perspective of materials comparison, tensile strengths and Young's modulus of carbon and aramid specimens are generally higher than those of basalt and glass under all strain rates investigated. The glass fabrics exhibit larger ultimate and maximum strains under dynamic tensile loads while carbon and aramid are less ductile. Intermediate level of material properties is observed in basalt fabrics demonstrating that its strength, stiffness and ductility are competitive with other materials tested.

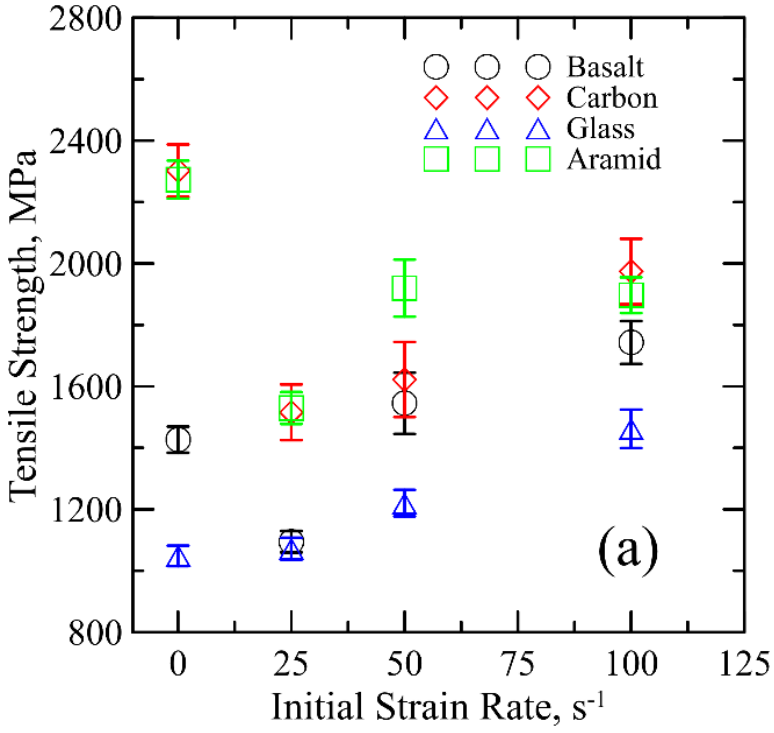
Tensile Strength, MPa
2800
2400
2000
1600
1200
800
0
25
50
75
100
125
Initial Strain Rate, s-1
Basalt
Carbon
Glass
Aramid
(a)

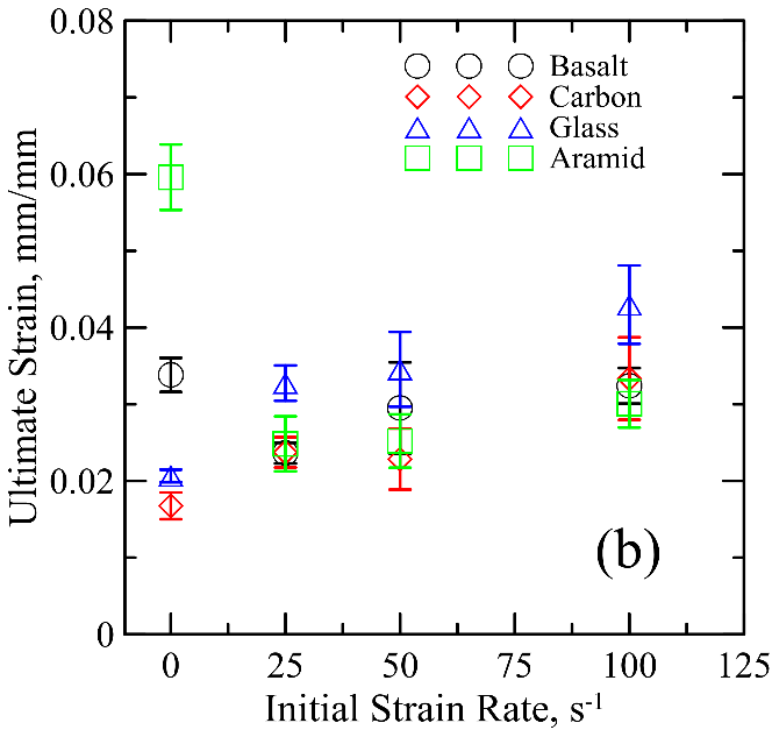
Ultimate Strain, mm/mm
0.08
0.06
0.04
0.02
0
0
25
50
75
100
125
Initial Strain Rate, s-1
Basalt
Carbon
Glass
Aramid
(b)

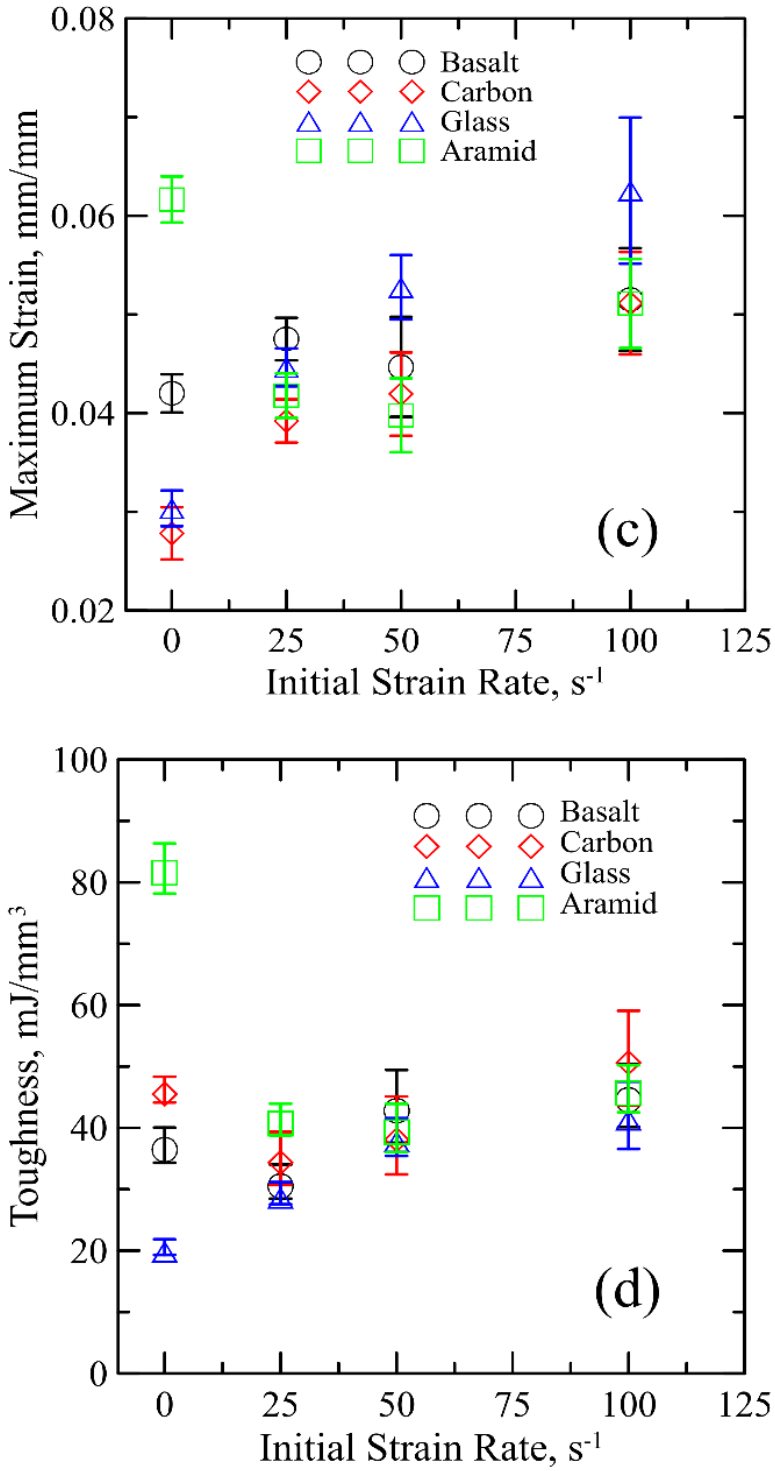

Figure 2-6 Mechanical Properties of the Tested Fabrics at Different Strain Rates: (a) Tensile Strength, (b) Toughness, (c) Maximum Strain, (d) Ultimate Strain [89].

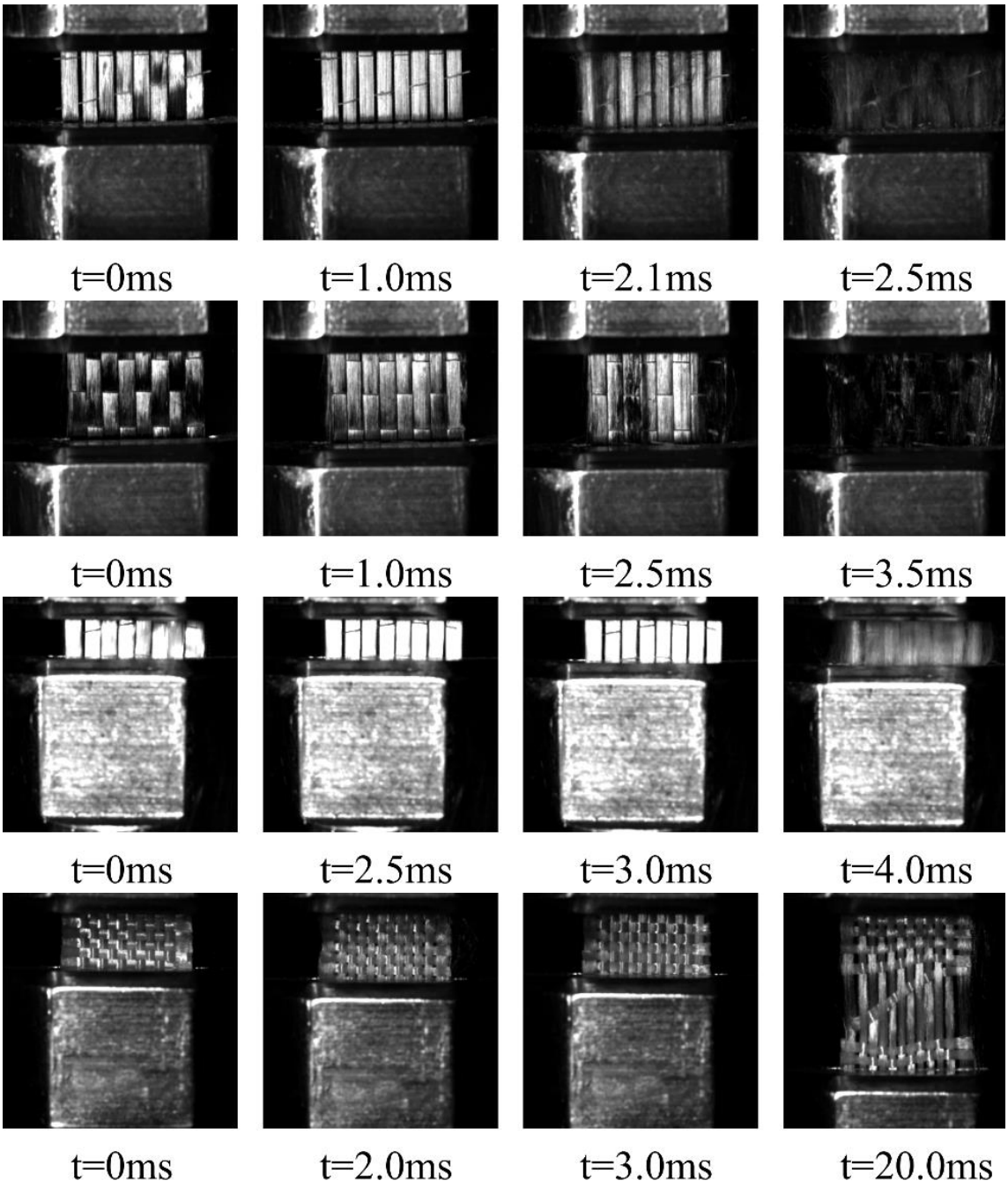

Figure 2-7 Failure Process of Various Fabrics (a) Basalt, (b) Carbon, (c) Glass, (d) Aramid Tested at 25 s^{-1} [89].

Figure 2-7 shows the images of the different fabrics tested at the strain rate of 25 s^{-1}, representing the stages of deformation during loading. The first sub-images show the sample before tests start and the second sets demonstrate the uniform stretching as the load

increases. However, partial failure is observed in the third sub-images of carbon and basalt fabrics as previously discussed while the phenomenon is less pronounced in glass fabrics. Unlike other three materials, the failure of aramid specimen occurs around 3 ms but the pull-out process of warp yarns from the woven structure extends to about 20 ms or even longer. Partial failure is also exhibited by aramid fabrics but not as distinguishable in the time lapsed images as unidirectional fabrics since the warp and weft yarns are interlaced with each other. The damage morphologies of various samples tested at 25 s^{-1} are compared in Figure 2-8. The fracture of carbon and aramid specimens tends to localize and all the yarn bundles fail at approximately the same location. The distributions of longitudinal yarns and stitches/weft yarns at far fields are not evidently altered by the fiber failure. Nevertheless, the damage morphologies of basalt and glass fabrics are quite different where the energy spreads throughout the entire gage length leading to the damage of the whole structure. According to the experimental results summarized in Table 2-2, glass and basalt specimens exhibit higher ultimate and maximum strains than carbon and aramid. Therefore, the two types of failure may be attributed to the differences in the ductility of various materials. Glass and basalt fibers are more ductile compared to other two materials such that pronounced plastic deformations are found in the longitudinal yarns before failure. The failure modes of all fabrics turn out to be independent of the strain rate while the images of the specimens tested at other strain rates are not presented here.

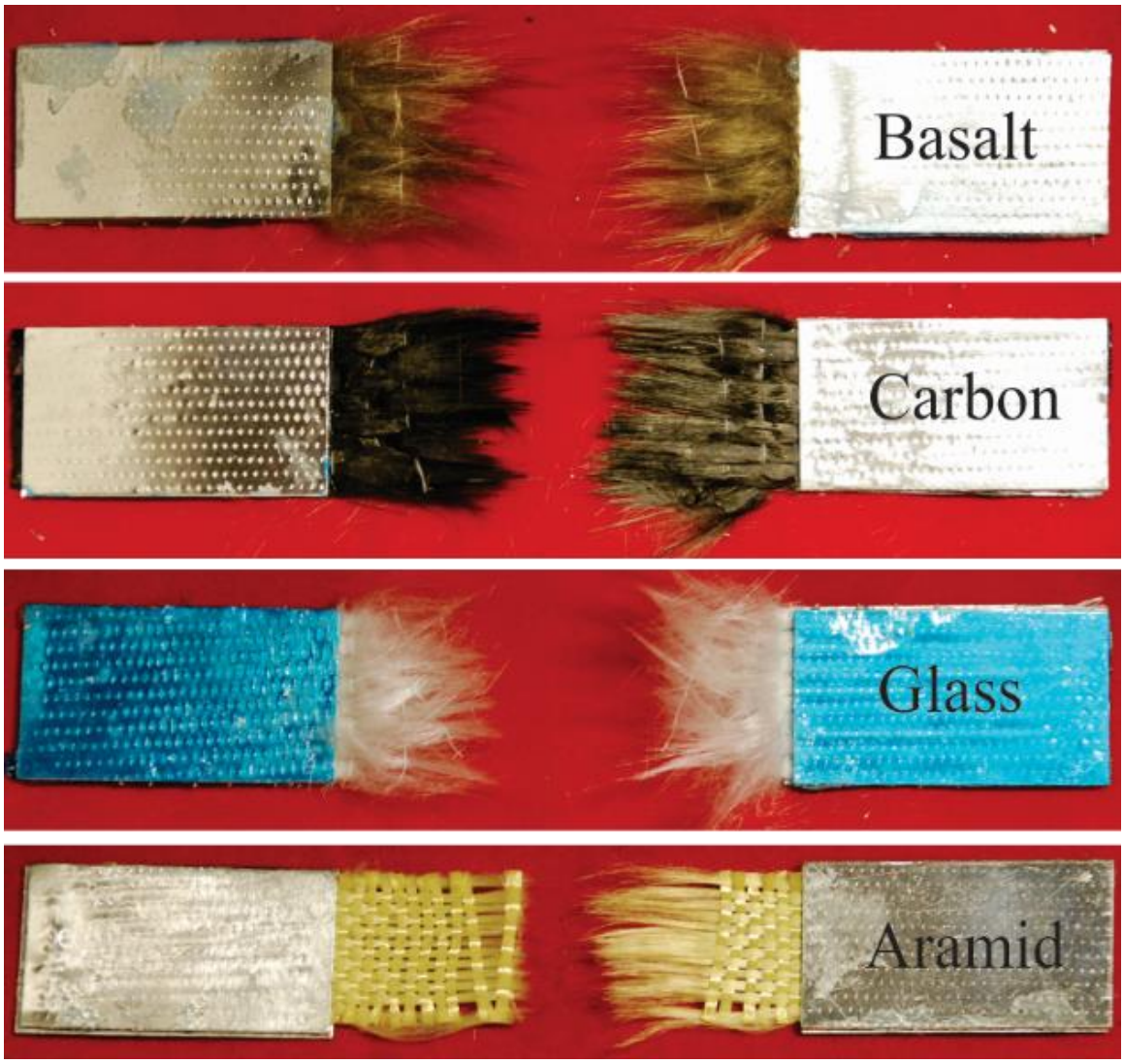

Figure 2-8 Damage Morphologies of Various Fabrics Tested at the Strain Rate of 25 s^{-1} [89].

2.1.3 One-Way Analysis of Variance (ANOVA)

Tabulated data in Table 2-2 is not sufficiently accurate to determine the significance of strain rate effect as a result of the variation of raw data to the mean values. In order to investigate the statistically significant relationship between the material parameters and strain rate under high speed loads, One-way Analysis of Variance (ANOVA) was performed which has been widely adopted for decades [91,92,93]. The statistical results

are more valuable especially in the industry field for manufactures to decide the suitable material in their production and design [94]. ANOVA uses *F*-distribution to test the equality of three or more population means.

Table 2-3 summarizes the ANOVA results of tensile strength, toughness, maximum strain, ultimate strain and Young's modulus of basalt fabrics as an example. The term "sum of squares" is the sum of the squared deviation of certain parameter as a measure of variability in the data; "degrees of freedom" represents the number of factor levels and observations; "mean square" is the sum of square divided by degree of freedom; "F_0" is the ratio of two means square, which is used to test if the null hypothesis can be rejected. In the present study, a significance level of 5% (α=0.05) is adopted and the critical value of F is $F_{0.05,2,21}$ = 3.24 according to the *F*-distribution table. Thus the null hypothesis H_0 ($\mu_1 = \mu_2 = \mu_3$ i.e., strain rate has no effect) can be rejected if F_0>3.24 or *P*-value is smaller than 0.05. The results of the ANOVA reported in Table 2-3 shows that for tensile strength, toughness and Young's modulus, there is a significant difference among the three strain rates since the *P*-Values are smaller than 0.05. In the case of maximum strain, the *P*-value is recorded 0.3134 > 0.05, indicating that there is no evidence against the null hypothesis that mean values of maximum strain under all strain rates are equal. Thus the effect of strain rate on the maximum strain of basalt fabrics is insignificant.

ANOVA was applied to the rest of the fabrics tested at varying strain rates, and the results are summarized in Table 2-4. It is found that strain rate has significant effects on tensile strength, toughness, maximum strain and Young's modulus for most of the tested materials. A smaller *P*-value indicates stronger evidence against H_0. It can be seen that the strain rate effects are significant on all of the mechanical properties of carbon fabrics, while the

parameters of aramid fabrics including toughness, ultimate strain and Young's modulus turn out to be more stable with varying strain rates. The strain rate effect on the ultimate strain is found to be generally insignificant.

Table 2-3 ANOVA of Basalt Tensile Strength [89]

Properties	Source of Variation	Sum of Squares	Degrees of Freedom	Mean Square	F_0	P-Value
Tensile Strength	Model	1766089	2	883045	41.144	<0.0001*
	Error	450710	21	21462		
	Total	2216799	23			
Toughness	Model	935.9	2	468.0	5.057	0.0381*
	Error	1943.5	21	92.5		
	Total	2879.4	23			
Max. Strain	Model	$(1.88)10^{-4}$	2	$(0.94)10^{-4}$	1.227	0.3134
	Error	$(16.11)10^{-4}$	21	$(0.77)10^{-4}$		
	Total	$(18.00)10^{-4}$	23			
Ultimate Strain	Model	$(3.20)10^{-4}$	2	$(1.60)10^{-4}$	2.812	0.0828
	Error	$(11.94)10^{-4}$	21	$(0.57)10^{-4}$		
	Total	$(15.14)10^{-4}$	23			
Young's modulus	Model	4472.1	2	2236.1	11.356	0.0005*
	Error	4135.1	21	196.9		
	Total	8607.2	23			

*P-value indicates that the effect of strain rate is statistically significant based on a 5% significance level, i.e. α=0.05.

Table 2-4 Summary of ANOVA for Various Fabrics [89]

Material	Property	F_0	P-Value
Basalt	Tensile Strength	41.144	<0.0001*
	Toughness	5.057	0.0161*
	Max. Strain	1.227	0.3134
	Ultimate Strain	2.812	0.0828
Carbon	Tensile Strength	10.013	0.0009*
	Toughness	3.694	0.0422*
	Max. Strain	4.731	0.0201*
	Ultimate Strain	4.174	0.0298*
Glass	Tensile Strength	33.107	<0.0001*
	Toughness	6.028	0.0085*
	Max. Strain	6.969	0.0048*
	Ultimate Strain	3.253	0.0588
Aramid	Tensile Strength	19.580	<0.0001*
	Toughness	1.842	0.1832
	Max. Strain	5.565	0.0115*
	Ultimate Strain	1.482	0.2500

*P-value indicates that the effect of strain rate is statistically significant based on a 5% significance level, i.e. α=0.05.

2.1.4 Weibull Analysis

To address the variability in the tensile strength of different fabrics as a result of randomly distributed imperfections and possible eccentric load, Weibull analysis was conducted using a two-parameter model:

$$P(\sigma) = 1 - \exp[-(\frac{\sigma}{\sigma_0})^m] \qquad \text{Equation 2-1}$$

where σ is the tensile strength and σ_0 is the reference or scaling value related to the mean and m is the Weibull modulus or shape parameter. The cumulative probability density, P is estimated as

$$P = \frac{i}{N+1} \qquad \text{Equation 2-2}$$

where N is the total number of tests and i is the current test number.

Fitted cumulative distribution functions (CDF) of the different fabrics at varying strain rates are compared in Figure 2-9. The Weibull parameters identified from dynamic testing are presented in Table 2-5. For the dynamic experimental data, as the strain rate increases, σ_0 of all the materials increases and the cumulative probability plot shifts towards higher stress values, which clearly indicates the positive effect of strain rate on the tensile strength. The other parameter m is a measure of the amount of scatter in the responses as the smaller m value corresponds to larger variability. Weibull analysis shows that the strain rate effect on the variability of glass fabrics is not pronounced indicating its uniform behavior at all strain rates selected. However, the m values changed with varying strain rates for the other three materials and the smallest values were obtained at 50 s^{-1}. On the other hand, the largest data scatters were found in carbon fabric specimens at all strain rates.

Tensile responses of fabrics are affected by the intrinsic material properties of single fiber, stress distribution in different bundles and its propagation. The probability of the existence of flaws differs from one yarn to another which leads to various tensile strengths along the cross section of the specimen. On the other hand, the initial waviness and slack along the length of the filaments leads to unequal stress distribution [95]. As a result, a simultaneous state of fracture in different bundles is difficult to be achieved and this irregularity in fracture process is responsible for the variability in the experimental response.

Table 2-5 Weibull Parameters for the Tensile Strength of Dynamic Data [89]

Strain Rate (s^{-1})	Material	Basalt	Carbon	Glass	Kevlar
25	σ_0 (MPa)	1126	1590	1105	1574
	m	18.7	11.7	15.5	19.4
50	σ_0 (MPa)	1624	1726	1258	1998
	m	10.3	7.1	16.3	13.3
100	σ_0 (MPa)	1804	2065	1513	1948
	m	14.8	10.8	15.6	19.5

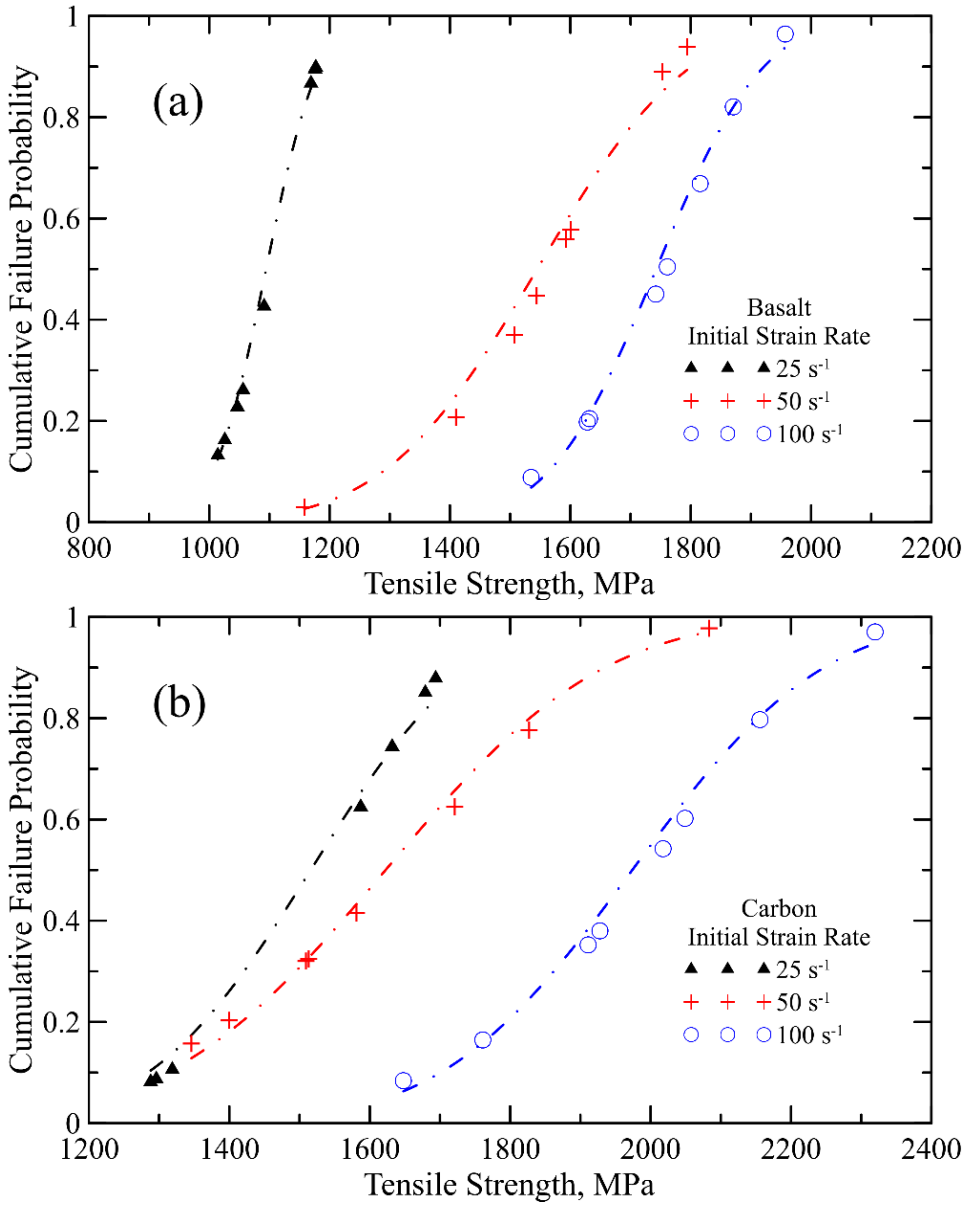

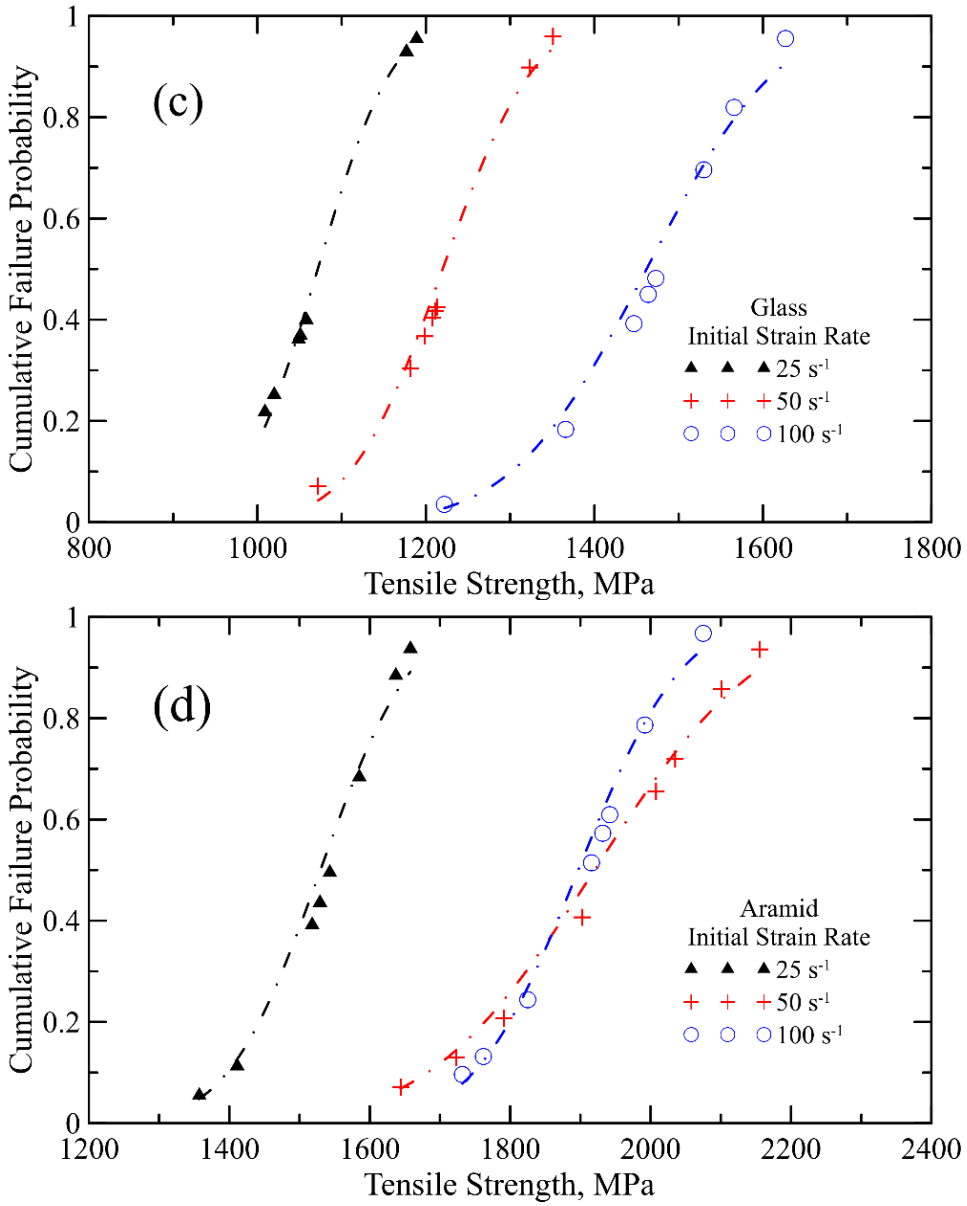

Figure 2-9 CDF of Weibull Analysis on the Tensile Strength at Different Initial Strain Rate of Various Fabrics: (a) Basalt, (b) Carbon, (c) Glass and (d) Aramid [89].

Four types of high performance fabrics of carbon, glass, basalt and aramid were tested at strain rates ranging from 1/600 to 100 s^{-1}. The material properties including Young's modulus, tensile strength, ultimate strain, maximum strain, and toughness were investigated. ANOVA was conducted to test the statistical significance of strain rate effects on the material properties. The following conclusions can be drawn:

Larger tensile strength, Young's modulus and toughness were observed in carbon and aramid fabrics while higher ductility was exhibited by glass fabrics. Material properties of basalt fabrics were at intermediate level and competitive with other materials at the strain rates investigated.

When the initial strain rate increased from 25 to 100 s^{-1}, average tensile strength, maximum strain and toughness of different fabrics were found to increase. While the trend of Young's modulus obtained at different strain rates was not clear. Tensile strengths of carbon and aramid fabrics obtained from quasi-static tests were higher than those under dynamic loads, which may be due to the non-simultaneous failure of individual yarns observed at high strain rates.

ANOVA with a 5% significance level was applied to the test results to examine the statistical significance of the strain rate effects on various material properties. It was found that strain rate had significant effects on tensile strength, toughness, maximum strain and Young's modulus for most of the tested materials except on the maximum strain of basalt (*P*-Value of 0.3134), as well as toughness (*P*-Value of 0.1832) and Young's modulus (*P*-Value of 0.0662) of aramid.

Weibull analysis was performed on the tensile strength of various fabrics and the model parameter σ_0 was found to increase with increasing strain rate, which confirmed the positive effect of strain rate from a probabilistic point of view. Additionally, uniform behavior at all strain rates was obtained in glass fabrics while largest data scatters were found in carbon fabrics.

2.2 Characterization of Localized Damage

SHCC with tensile strain capacity in excess of 3% under quasi-static uniaxial tensile loading can be attained with only 2% fiber content by volume [7,8]. The increase in load-bearing capacity and hardening behavior are attributed to the formation of multiple fine cracks, which gives rise to high energy absorption both under quasi-static and dynamic loading conditions [96,97]. The superior mechanical properties of SHCC enable many possible applications in structures subjected to static and dynamic loads, as primary materials for structural elements, reinforcing layers, or strengthening/repair materials [7,98,99].

The improved ductility, tensile strength and energy absorption of SHCC, results in extensive damage characterized by severe cracking andmake it a suitable material in such applications. The tensile behavior of a typical SHCC, i.e., made with polyvinyl alcohol (PVA) fibers, under low and high strain rates up to 50 s^{-1} was investigated by Mechtcherine et al. [18, 100]. For the tests performed at strain rates of 10^{-1} s^{-1} and below, SHCC showed a moderate increase in tensile strength and a simultaneous decrease in strain capacity with increasing strain rate. The decrease in strain capacity could be traced primarily to a less pronounced multiple cracking in comparison to testing under quasi-static conditions. However, when tested in the high-speed regime at strain rates from 10 to 50 s^{-1}, a considerable increase in tensile strength and strain capacity was measured [18], even though no pronounced multiple cracking was visually observed. Similar phenomena were observed in a highly dynamic spall experiments on SHCC under strain rates between 140 and 180 s^{-1} using the Hopkinson bar [97]. Curosu et al. [101] studied the behavior of high-strength and normal-strength SHCCs reinforced by high-density polyethylene (HDPE)

fibers under quasi-static and impact tensile loading, using the Hopkinson bar at strain rates of 150 s^{-1}. Considerable increase in tensile strength and fracture energy and a clear decrease in strain capacity, as manifested in the number of cracks were observed at the high strain rate.

Soe et al. [102] performed projectile impact tests on a hybrid-fiber cementitious composite panels reinforced with PVA and steel fibers under impact velocities ranging from 300 m/s to 657 m/s. The results demonstrated that the samples with combination of PVA and steel fibers have increased impact resistance and energy absorption capability than the plain concrete. Li et al. [103] investigated the static and impact behavior of extruded sheets reinforced with short PVA and glass fibers. Results indicated that PVA fibers increased the tensile strain capacity and absorbed energy Despite several studies addressing the dynamic behaviors on SHCC, there is still limited information available with respect to the impact resistance of SHCC samples subjected to flexure and tensile properties at the medium strain rate of 1–100 s^{-1}.

The objective of the current section is to study mechanical behavior of SHCC under high-speed tensile loads and address the nature of failure. The strain rates of 25 s^{-1}, 50 s^{-1}, and 100 s^{-1} were employed by tensile testing. In addition, DIC was used to obtain the full-field deformation, quantitative measurement of strain as well as the crack width response of SHCC specimens.

2.2.1 Experimental Program

The mix design of the SHCC composition used is shown in Table 2-6. A combination of Portland cement 42.5 R and fly ash was used as binder. The aggregate was uniformly graded quartz sand with particle sizes ranging from 0.06 mm to 0.20 mm. PVA fibers with

a volume fraction of 2.2%, measuring 12 mm in length and 0.04 mm in diameter (Kuraray Co., Ltd., Kuralon K-II REC15) were used as reinforcement. A super plasticizer on a polycarboxilate-ether basis (SP) and a viscosity agent (VA) were added to the mix in order to adjust its rheological properties. Furthermore, some superabsorbent polymer (SAP) was added to the mixture as a multi-purpose concrete admixture. The effects of SAP on properties of cement-based materials are described, e.g., in [104].

The matrix was blended using a bench-mounted mixer of 20 liters' capacity. The fines and sand were homogenized by dry mixing for 30 s. Water mixed with one half of the super plasticizer was added into the dry mix during 30 s and mixed for an additional 60 s. PVA fibers were added over a period of 30 s and mixed for an additional 180 s. The second half of the super plasticizer was added at this stage for 30 s and mixed for another 180 s. The mix was cast horizontally in steel molds. The molds were stored for 2 days in a room with controlled temperature (T = 25 °C) and humidity (RH = 65%). After demolding the specimens were sealed in plastic foil and stored at room temperature until testing.

2.2.2 Discussion and Analysis

Figure 2-10(a) shows representative stress-strain curves for SHCC specimens obtained at various strain rates (25 s^{-1}, 50 s^{-1}, and 100 s^{-1}). Figs. 2-10(b)-(d) compare the average values and standard deviations of the tensile strength, strain capacity and toughness measured at different strain rates. The material parameters derived from the measured data are given in Table 2-7. Specifically, Figure 2-10(b) compares the direct tensile strength and nominal flexural strength at varying strain rates ranging from 2.5 s^{-1} to 100 s^{-1}. As the strain rate increases, nominal flexural strength increases from 12.4 MPa to 13.5 MPa while tensile strength increases from 8.1 MPa to 9.9 MPa. Note that the flexural strengths calculated

using eqn. (3) are higher than the direct tensile strengths for the same material, even though the strain rate is much lower. This is attributed to differences in the stress distribution profiles of the two test methods. In the tension test, the entire volume of the specimen is a potential zone for crack initiation. Comparatively, in the flexural test, only a small fraction of the tension region is subjected to an equivalent ultimate tensile stress. On the other hand, strain capacity (strain at peak) and failure strain (5% of maximum load in post-peak) increase from 0.86% to 1.82% and 1.67% to 5.21%, respectively. As a result, absorbed energy also shows an improvement with the increasing strain rate, from 0.5 J to 1.4 J up to peak and 1.1 J to 4.1 J up to failure. The observed trends agree with the studies conducted by Mechtcherine et al. [97] on the tensile behavior of dumbbell-shaped SHCC specimens at strain rates ranging from 10 to 50 s^{-1}.

Static tensile tests of SHCC specimens under quasi-static strain rates were previously performed by the authors [97], which are presented for comparison with the failure behaviors with dynamic results. Figure 2-11 shows the stress-strain curves of the SHCC specimens tested at strain rate ranging from 10^{-5} to 10^{-2} s^{-1}. While the tensile behavior under the very low rate of 10^{-5} s^{-1} was characterized by a relatively pronounced strain-hardening stage accompanied by multiple cracking, measurably less ductile behavior and less multiple cracking were revealed at higher rates (up to 10^{-2} s^{-1}). The development of multiple cracking under tensile loads are affected by multiple factors such as rheological properties, fiber distribution, interface bonding strength, fiber strength and effects of strain rate [100,47]. Within this range of strain rates the increase in strength, decrease in strain capacity and reduced number of cracks are due to an increase in the bond strength between fiber and matrix according to the reported pullout experiments performed at different strain

rates [105]. As a result of the higher bond strength and relatively lower fiber tensile strength, fiber failure becomes more frequent, with a decrease in the frequency of fiber pullout, leading to a more brittle failure of the composites. For strain rates in the dynamic range, multiple cracking of SHCC specimens are not visible and the composite failure tends to localize at the region of macro crack. According to the microscopic observation, fiber pullout with an average length of approximately 2.5mm turns out to be the dominating failure mechanism and pronounced plastic deformation are observed in PVA fibers compared to static loading [97]. Therefore, the high strain capacity and work to fracture under dynamic tensile loads are provided by the increased pullout length and fiber plastic deformations.

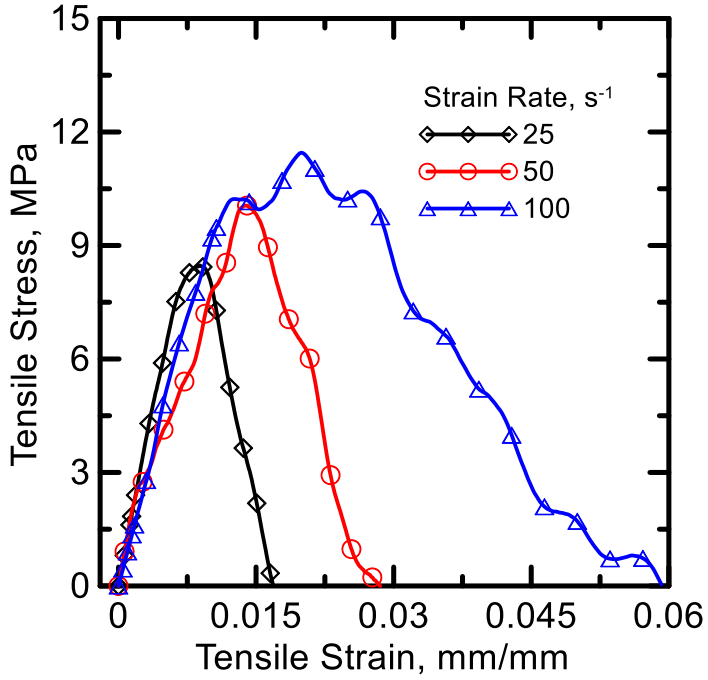
Strain Rate, s-1
25
50
100
Tensile Stress, MPa
Tensile Strain, mm/mm
0
3
6
9
12
15
0
0.015
0.03
0.045
0.06

(a)

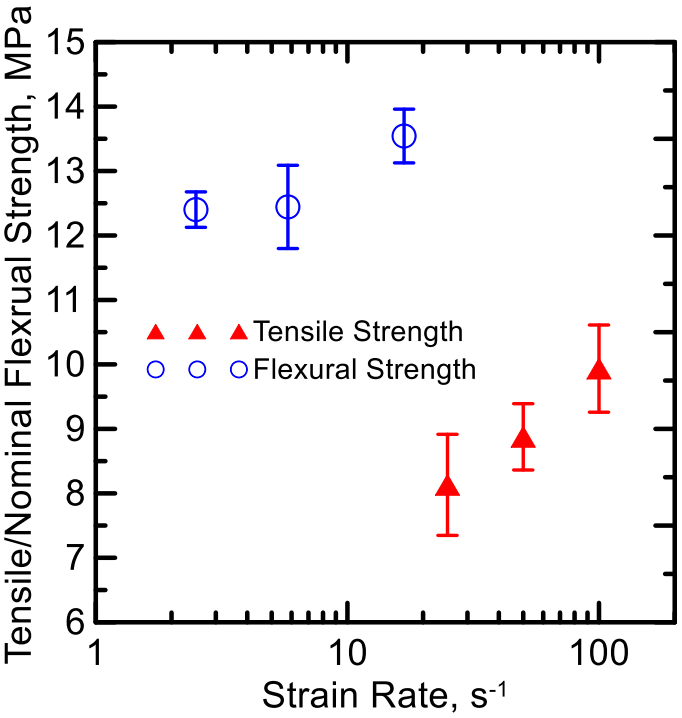
Tensile Strength
Flexural Strength
Tensile/Nominal Flexrual Strength, MPa
Strain Rate, s-1
6
7
8
9
10
11
12
13
14
15
1
10
100

(b)

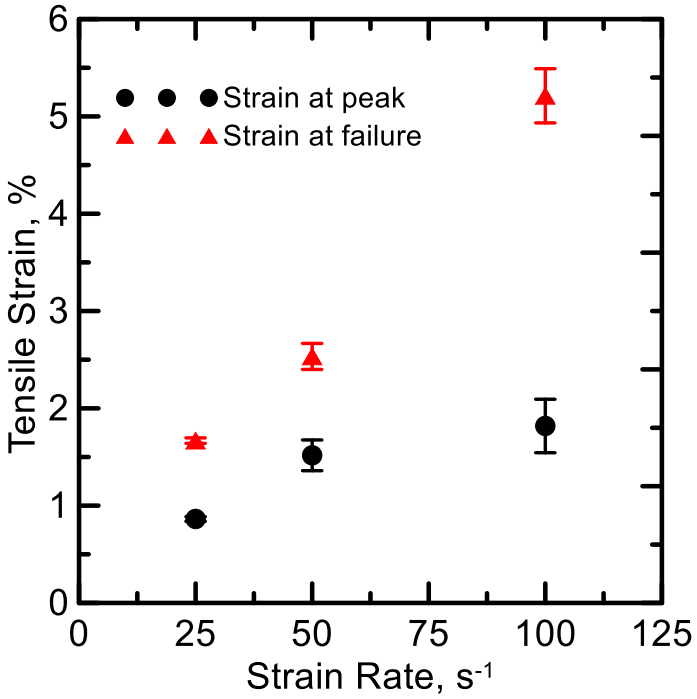

(c)

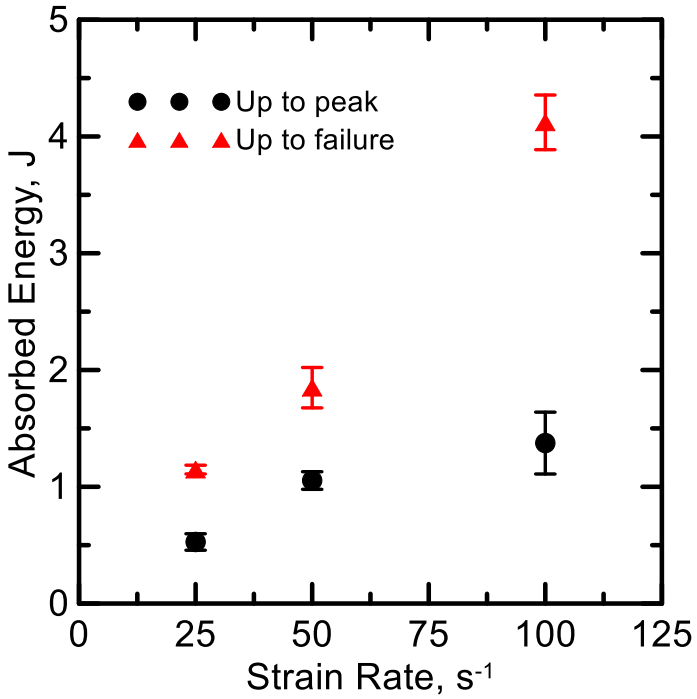

(d)

Figure 2-10 (a) Tensile Stress-Strain Responses of SHCC at Different Strain Rates; Effects of Strain Rate on (b) The Average Tensile Strength, (c) Strain at Peak Load (Strain Capacity) and Strain at Failure (5% of Maximum Load in Post Peak), (d) Work-To-Fracture up to Peak and up to Failure.

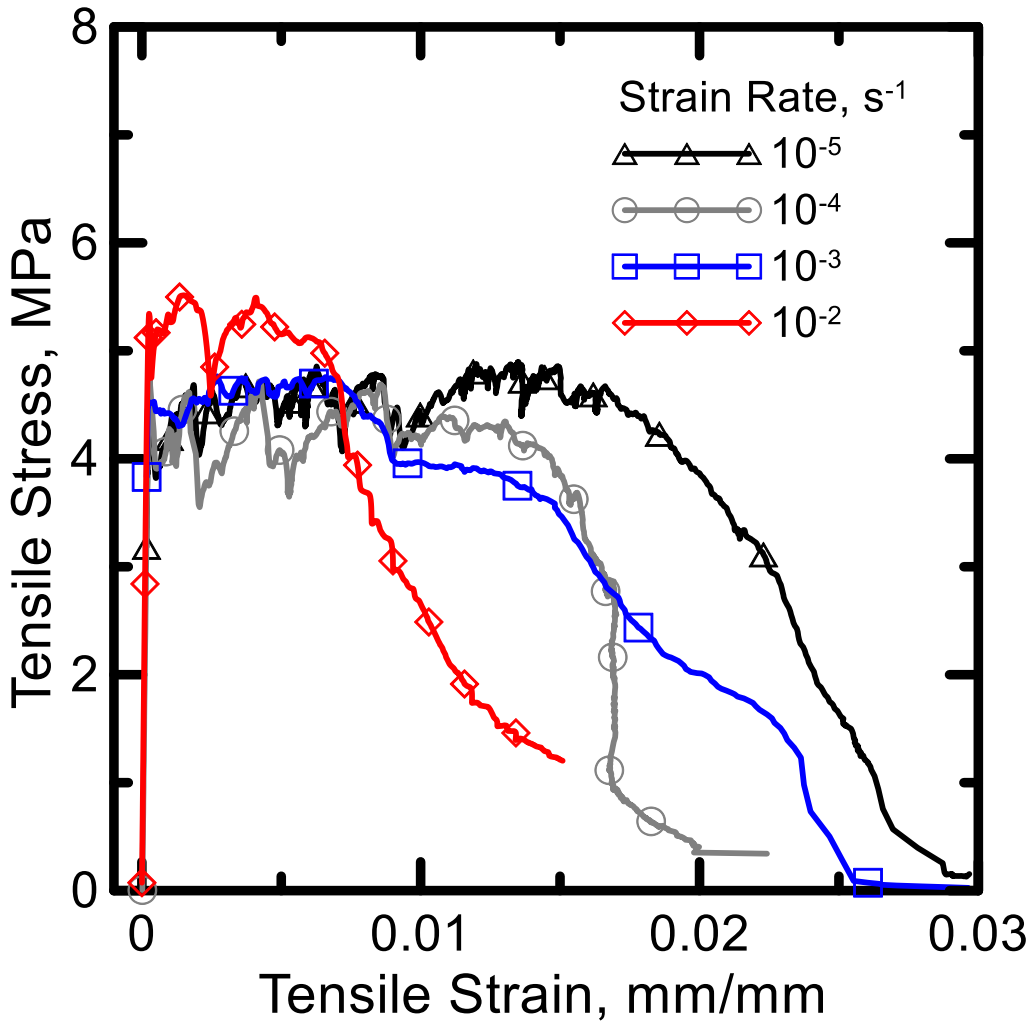

Figure 2-11 Tensile Stress-Strain Responses of SHCC Tested at Quasi-Static Strain Rates Ranging From 10^{-5} to 10^{-2} s^{-1}.

2.2.3 Image Analysis Using Digital Image Correlation (DIC)

Due to the intrinsic vibrations in dynamic testing, conventional data analysis procedures may not sufficiently address the material behavior, hence further study of distributed cracking and damage by means of imaging is warranted. When the tension tests are conducted at high speed, a high sampling rate in the range of 10-1000 kHz [106] is required to acquire sufficient data points within a few milliseconds. Additionally, slipping in the grips and the inertial effect of mass of grips and transducers to the samples during dynamic

testing may affect the test results and limit experimental accuracy. Therefore, the strain measured at an isolated spot or within a gauge length by conventional devices such as LVDT, extensometer and strain gage is insufficient to study the inhomogeneous results. Digital Image Correlation (DIC), is a non-contacting optical full field deformation measurement approach that can better address the complex behavior of this class of materials. DIC technique was developed by Sutton et al. [107] and Bruck et al. [108] and has been widely applied for composites, and reinforced concrete sections [109,110,111] while its application in cement-based composites tested under dynamic loads is limited [46, 112, 113].

In order to perform DIC, an area of interest (AOI) is manually specified and further divided into an evenly spaced virtual grid as shown in Figure 2-12(a). The displacements are computed at each point of the virtual grids to obtain full-field deformation. The imposed red square is the subset (a set of pixels) for tracking the movement of its center point $P(x, y)$ from the reference image (before deformation) to deformed images $P'(x', y')$, see Figure 2-12(b). The tracking of subset is conducted using selected correlation functions such as cross-correlation (CC) or normalized cross-correlation (NCC) [114]. Subsequently, the strain fields can be derived by smoothing and differentiating the displacement fields. A commercial software Vic-2D 2009 developed by Correlated Solutions, Inc. was used to conduct image analysis.

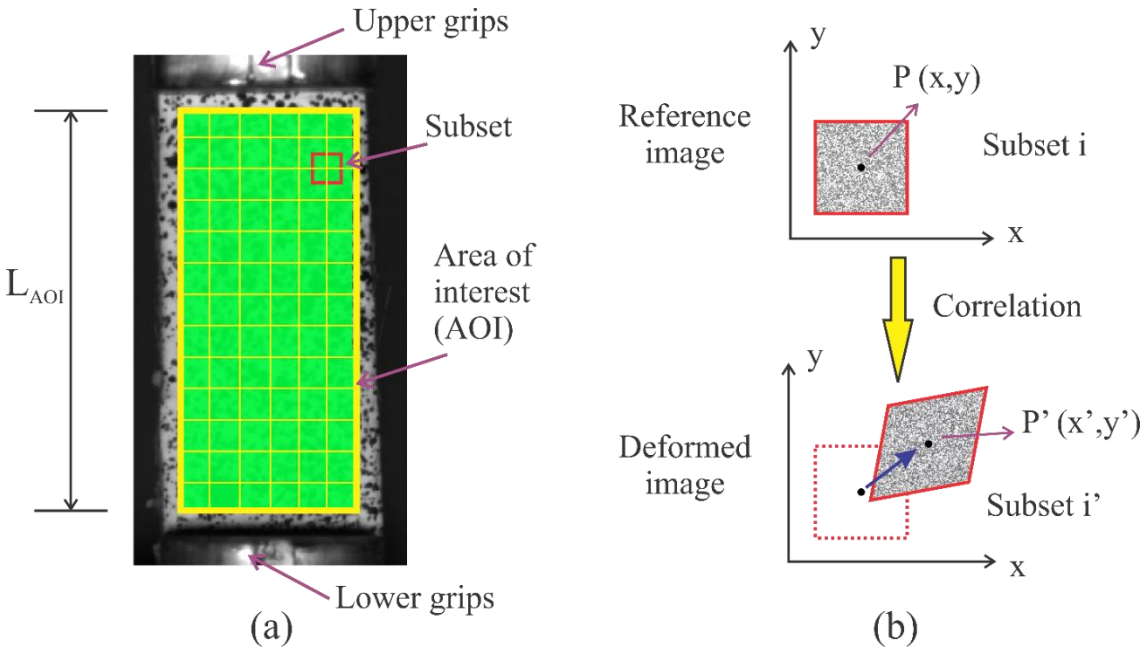

Figure 2-12 (a) Area of Interest (AOI) and Subset in a Reference Image; (b) Schematic Presentation of a Reference Subset Before Deformation and the Corresponding Target Subset After Deformation.

The longitudinal strain (ε_{yy}) fields of a SHCC specimen tested at 25 s^{-1} are shown in Figure 2-13 using a color code with purple representing the lowest strain values and red at 6.0% strain. The time associated with incremental steps of strain distribution is indicated below each sub-image. The correspondence of each strain map to the experimental stress-strain behavior is represented by the numbers 2-4. Damage evolution shows a relatively uniform strain distribution at the beginning of the test, a uniform distribution is observed that corresponds to the elastic-linear range for both matrix and fiber. As the load increases (t = 0.1 ms), tensile strain localize above the center of the area of interest (AOI) shown as the blue region, indicating the formation of the first crack. After the matrix cracks, the load carrying capacity does not vanish as the cracks are bridged by the PVA fibers, leading to ductile behavior and stiffening effects.

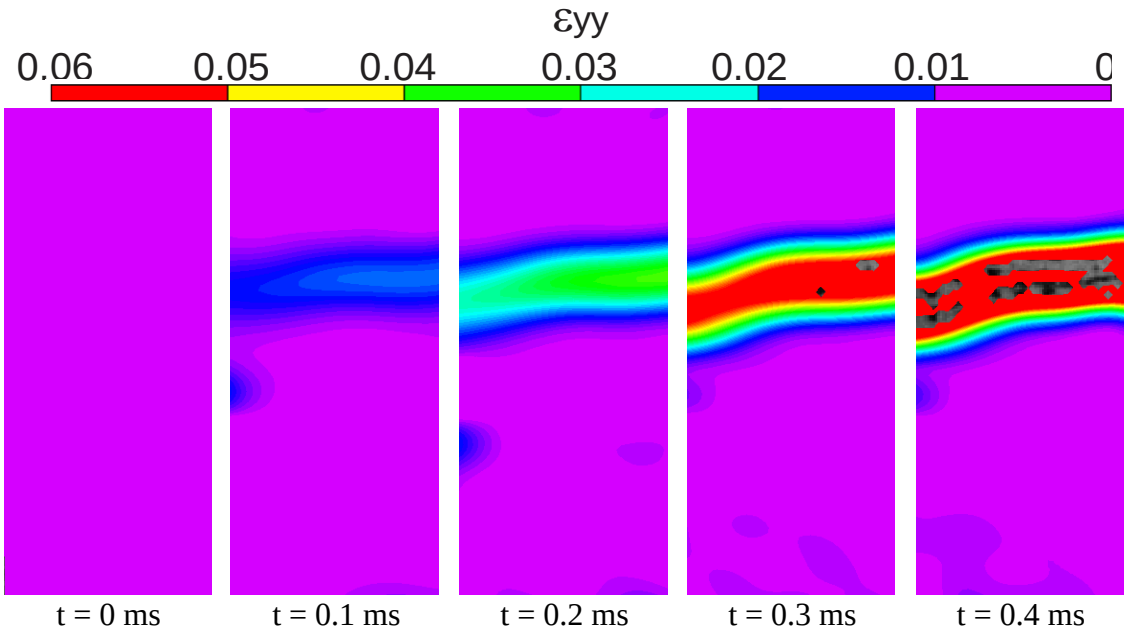

(a)

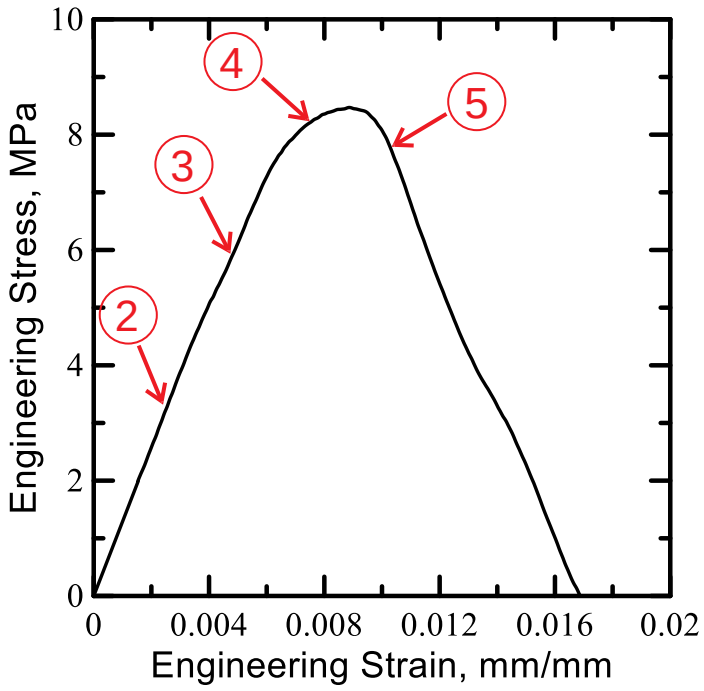

(b)

Figure 2-13 (a) Strain Map of SHCC Specimen Tested at 25 s^{-1}; (b) Corresponding Stress-Strain Response.

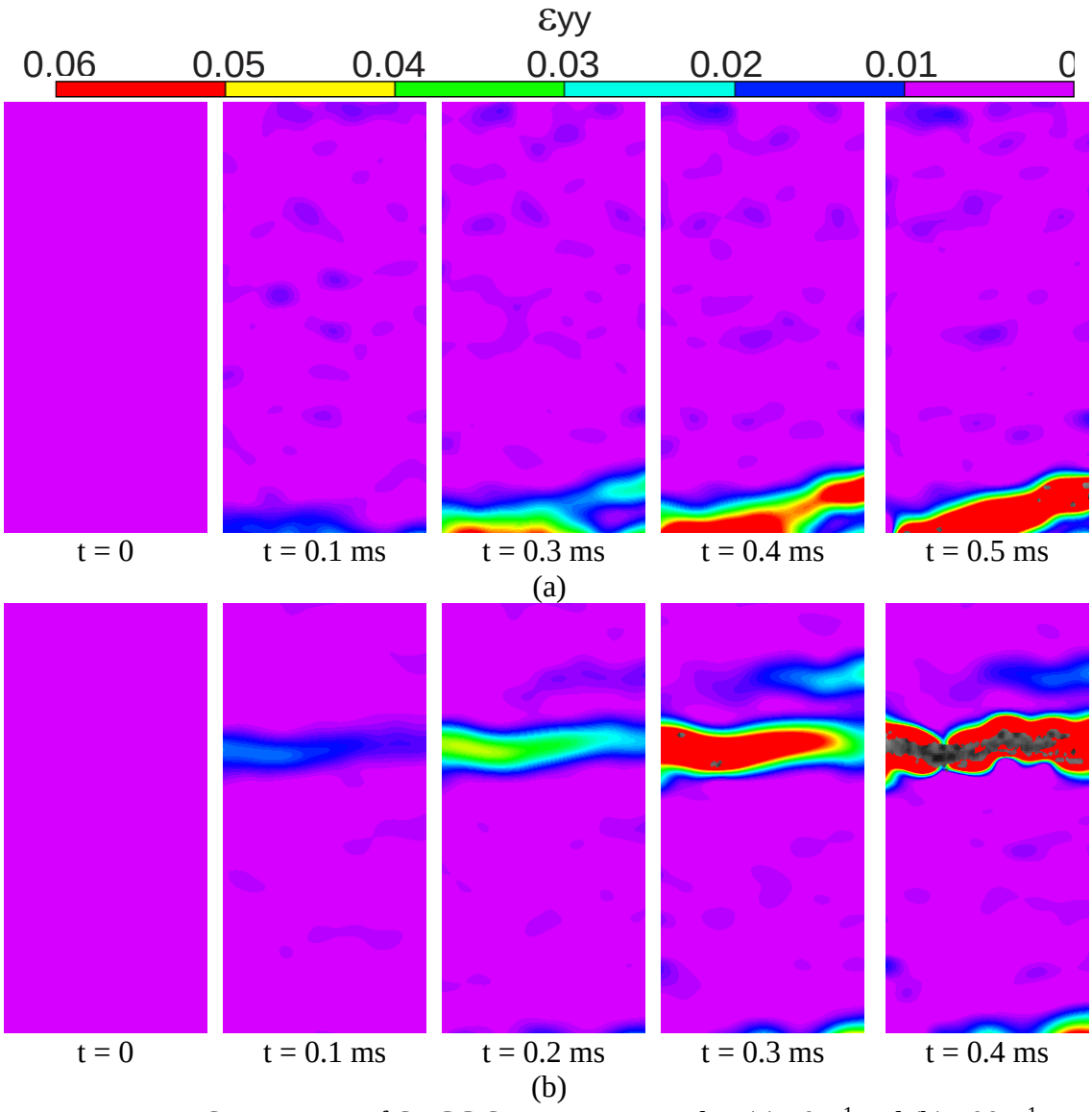

Figure 2-14 Strain Maps of SHCC Specimens Tested at (a) 50 s^{-1} and (b) 100 s^{-1}.

The localized zones grow with increasing load and the color changes from blue to red. Macro- and micro-cracks form and grow within the localization zone until the macro-crack eventually propagate along the transverse direction of the specimen. The sub-image at t = 0.4 ms depicts the strain distribution at the end of the test showing the crack widening stage ultimately leading to failure. Similar pattern of strain map was also observed in the specimens tested at other strain rates (Figure 2-14).

As shown in Figure 2-15, three zones can be identified as: (A) the localization zone in red which contains the transverse crack with the majority of the load carried by the fiber phase; (B) the shear lag zone in green/blue where the slip between fiber and matrix cannot be ignored and the bond stress follows a shear lag pattern; (C) the uniform zone where no crack is formed, the composite is behaving linearly and slip is negligible. Identification of the three zones have also been observed in textile reinforced concrete (TRC) specimens [46]. To quantitatively investigate the strain responses within different zones, regions on the surface of a specimen tested at 25 s^{-1} are selected as shown in Figure 2-16(a). The average strains of these regions are plotted as a function of time in Figure 2-16(b). Significant variations in the strain values are observed among different zones. The strain in zone A is higher than twice of that in B after 0.1 ms, while the uniform strain (<200 με) is much lower compared to other zones. However, the displacement rapidly increased along the loading direction and the strain field becames discontinuous across the cracks due to crack opening and fiber pullout; thus the excessively large strain values towards failure may not be reliable any longer. Sample failure occurred around 0.4 ms when the peak strain values are reached.

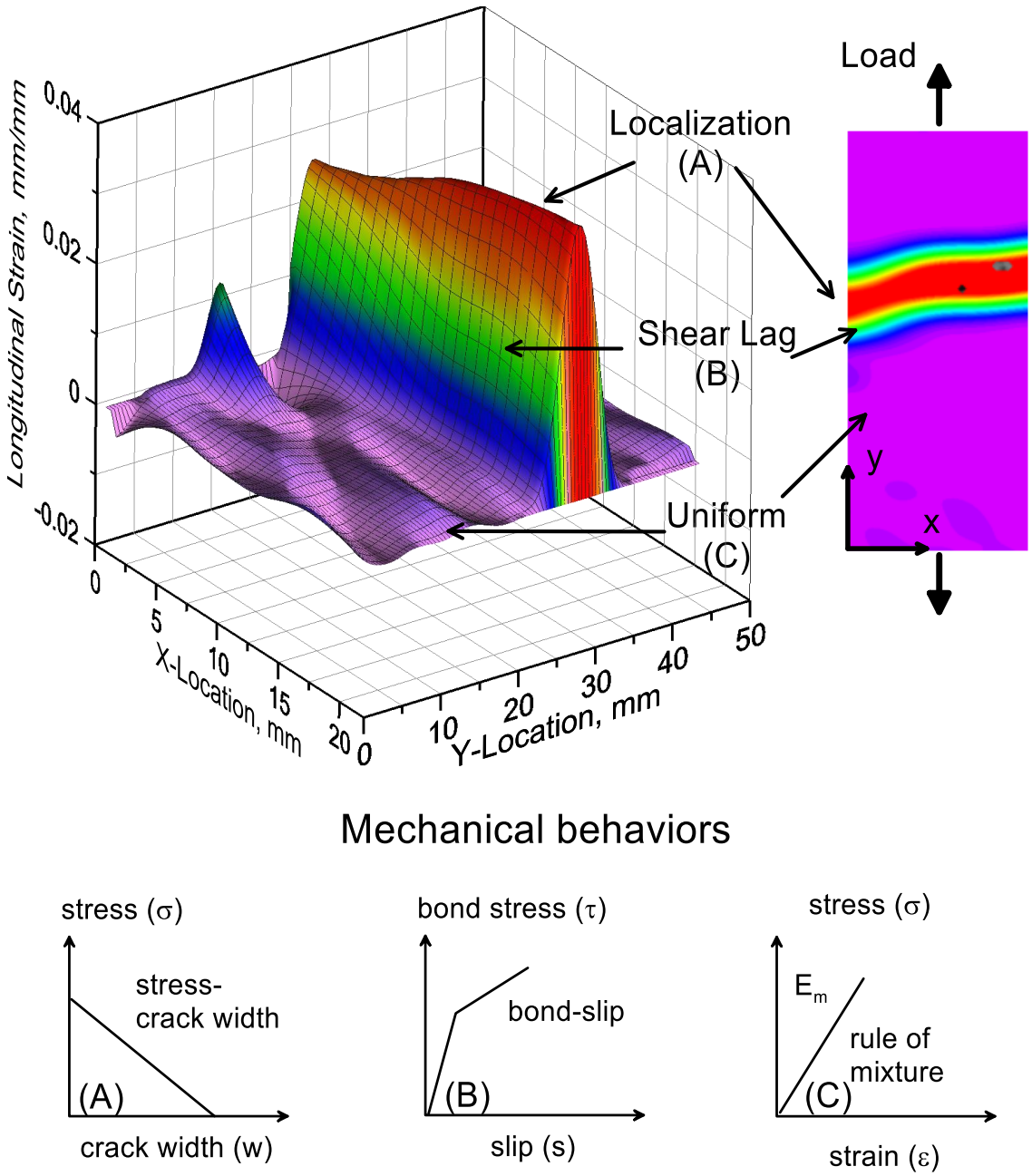

Figure 2-15 Identification of Three Zones: Localization, Shear Lag, and Uniform Strain as Well as Corresponding Mechanical Behaviors.

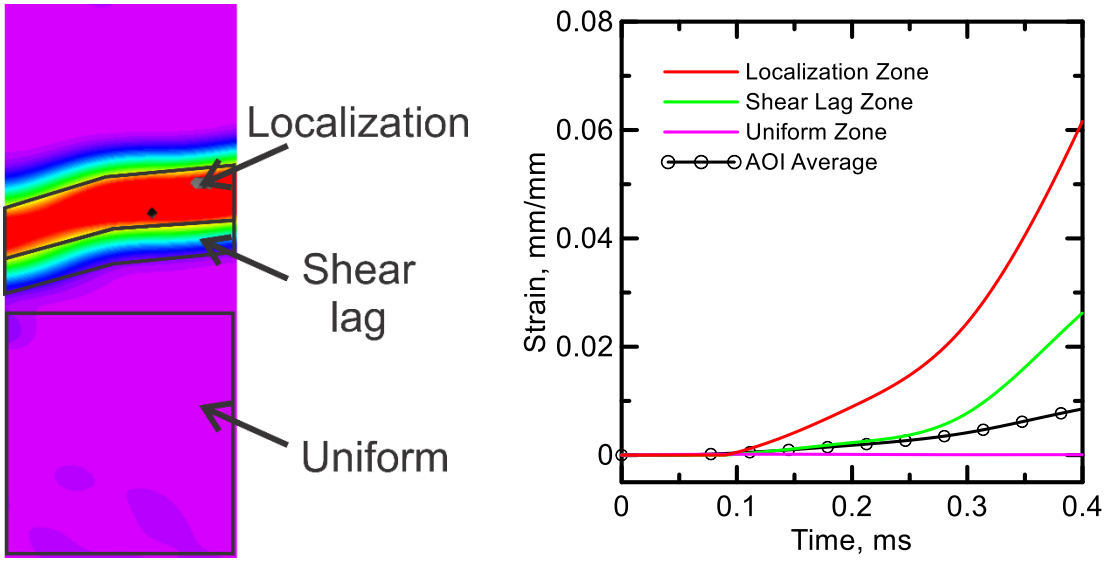

Figure 2-16 (a) Stress-Strain Responses Based on DIC Method and (b) Comparison Between Regular Analysis and DIC.

Figure 2-17(a) shows the three-dimensional contour of axial displacement of the same SHCC sample at failure with the macro-crack identified as discontinuous displacement. The location and width (w) of a certain crack is represented by the y-coordinate and the vertical amplitude of the discontinuity. The deformation in between two parallel cracks is insignificant compared to w. The distributions of the average displacement field represented as two-dimensional curves are shown in Figure 2-17(b) for various stress levels. It is clear that the w increases with increasing stress. Figure 2-17(c) shows the stress versus time history as well as the evolution of w versus time up to failure. Correlation of crack width obtained by DIC with the stress response and expressed as a stress-crack width response, is shown in Figure 2-17(d). The linear elastic stage is represented by an almost vertical line and extends to the bend over point as the first cracking strength. A pronounced strain hardening effect is observed after cracking as the tensile stresses increase with a reduced stiffness. The post-peak response is dominated by crack widening, fiber pull out, and fracture.

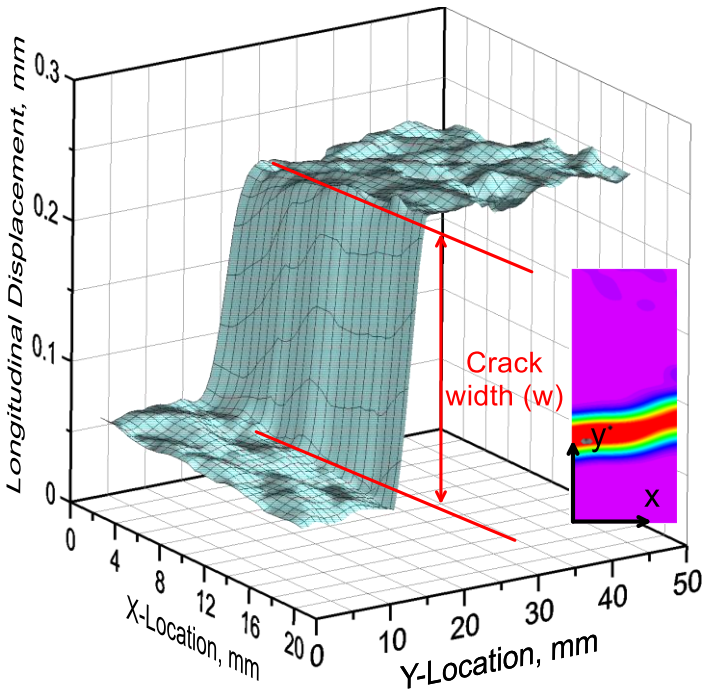
Longitudinal Displacement, mm
0.3
0.2
0.1
0
Crack
width (w)
y
x
0
4
8
12
16
20
X-Location, mm
0
10
20
30
40
50
Y-Location, mm

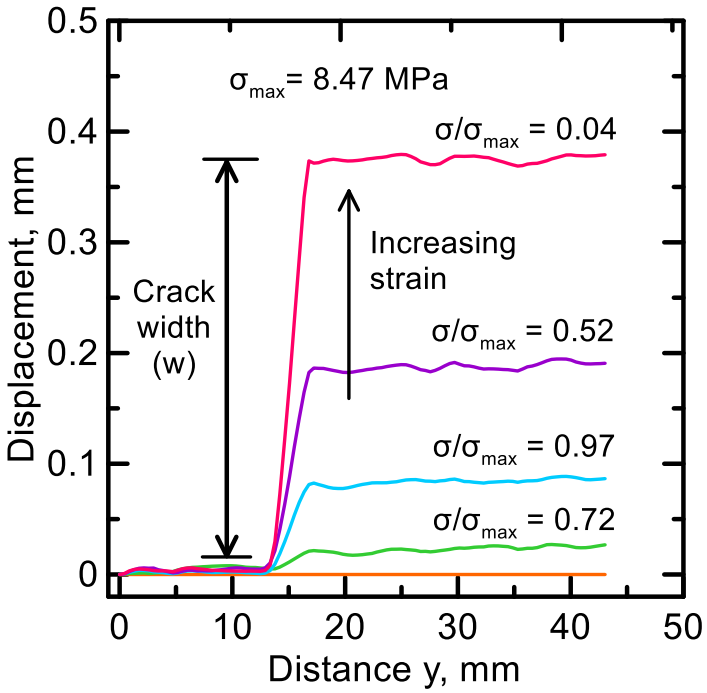
0.5
0.4
0.3
0.2
0.1
0
Displacement, mm
σmax= 8.47 MPa
σ/σmax = 0.04
Increasing
strain
σ/σmax = 0.52
Crack
width
(w)
σ/σmax = 0.97
σ/σmax = 0.72
0
10
20
30
40
50
Distance y, mm

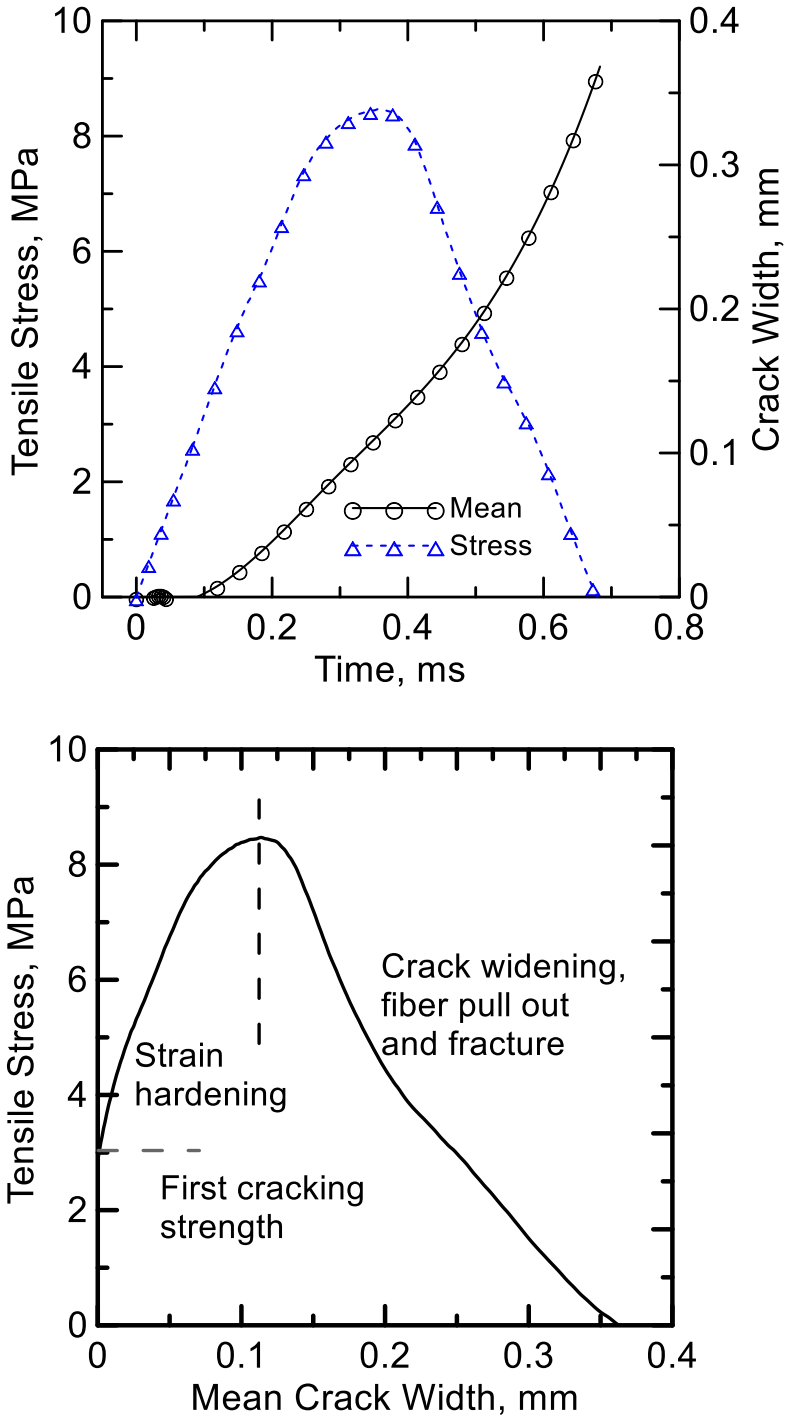

Figure 2-17 (a) Longitudinal Displacement Contour of a SHCC Specimen Tested at 25 s^{-1}, (b) Distribution of Displacement at Four Stress Levels, (c) Crack Width and Tensile Stress Versus Time Histories, (d) Stress-Crack Width Response.

2.3 Characterization of Distributed Damage

2.3.1 Multiple Cracking Mechanism

Tension test is a fundamental and important approach to characterize the nonlinear behavior of fiber reinforced concrete. The critical material parameters that can be extracted from tensile data include elastic modulus, cracking stress, post-peak stiffness, ultimate tensile strength, residual strength, crack width and spacing etc. These parameters are required for the analytical and numerical modeling of the flexural behavior of concrete beams and slabs. With the help of novel technique applied in the field such as digital image correlation, indirect measurement of softening zone size is also available [115].

Figure 2-18 illustrates the schematic tensile stress-strain behavior of TRC represented by initiation cracking that leads to multiple cracking mechanism. Four distinct stages of the stress-strain curve are identified. Stage 1 corresponds to the linear-elastic range where both matrix and the fiber behave linearly and the rule of mixture is applicable. The linear elastic stage is terminated by the initiation of first crack at point A, when the matrix cracking strength $\sigma_{m,cr}$, which is generally referred to as the bend over point (BOP) is reached. Stage 2 represents the stage between the initiation of the first crack and its propagation across the width of the sample which may cover a sufficiently notable stress range for large fiber contents. The stiffness gradually degrades in stage 3 by the formation of distributed cracks at regular intervals. The load carrying capacity of uncracked matrix segments does not vanish, as referred to tension stiffening. After the completion of cracking phase and initiation of debonding, progressive damage takes place in Stage 4 by means of crack widening due to fiber pull out and fracture.

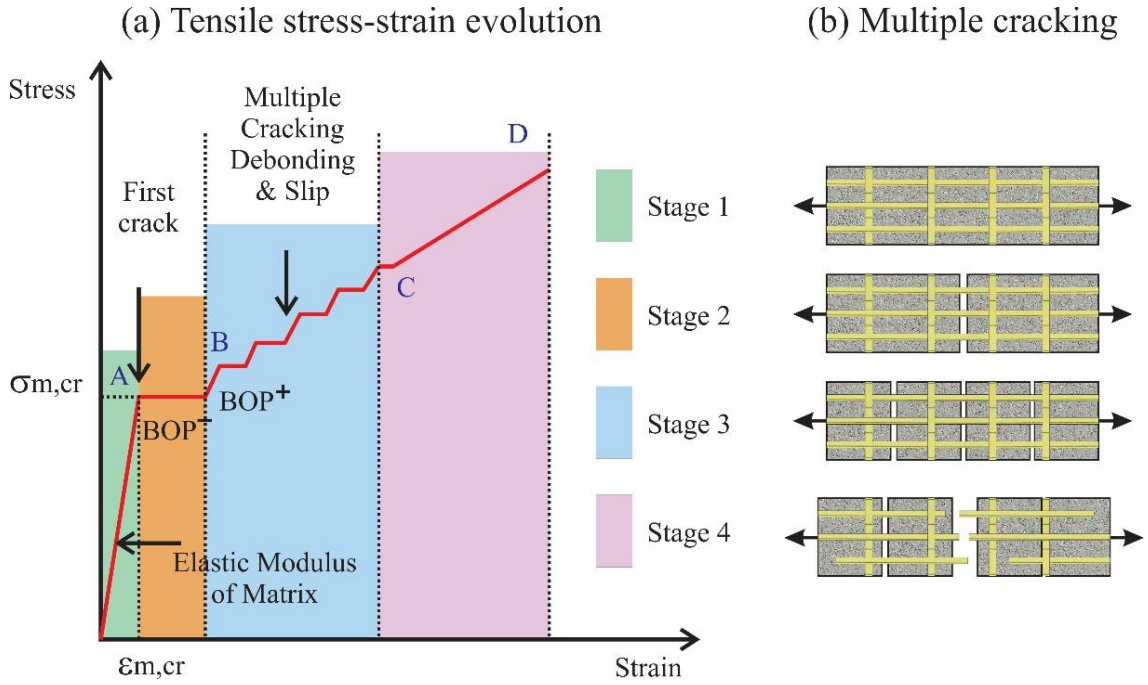

Figure 2-18 Schematic Presentation of the Tensile Behavior of TRC Including (a) Tensile Stress-Strain Evolution, (b) Multiple Cracking Mechanism [115].

The parameters measured from static and high speed tensile tests with the strain rate ranging from 10^{-5} up to 100 s^{-1} have been addressed for a variety of TRC materials with glass, polypropylene, polyethylene, carbon, and natural fibers in the following studies [44,116]. Results indicate that the strain rate, when used as a variable, is affected by the textile type, bonding mechanism, monofilament vs. roving bundle, number of layers, volume fraction, sample length and stiffness [117,118]. For example, the average tensile strength of TRC reinforced by glass textile varied from 15.4 MPa [119] to 20.1 MPa [120] as the number of layers increased from 6 to 8. Silva et. al [45] reported that both tensile strength and work-to-fracture of glass TRC exhibited pronounced improvements as the strain rate increased from 10^{-4} to 50 s^{-1}.

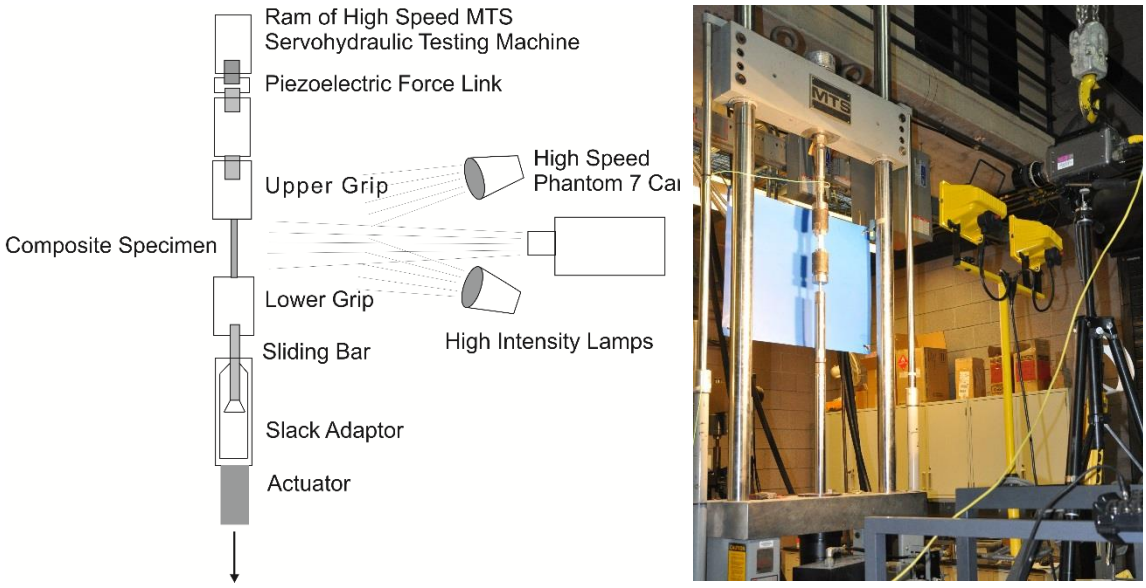

(a) (b)

Figure 2-19 (a) Sechematic Drawing and (b) Setup of the Testing System With High Speed Camera [115].

2.3.2 Strain Rate Effects

A finely grained matrix was used in making the mortar and TRC samples with the mix design summarized in Table 2-6. The average slump flow value measured with a small cone (bottom diameter 100mm, top diameter 60mm, height 70mm) was 200mm. Polymer-coated biaxial fabric made of AR-glass was used in 3 layers as reinforcement. The degree of reinforcement was calculated for one layer of fabric in volume as 66.33 mm^2/m in both longitudinal and transverse directions. The fineness and the mean spacing of the weft and warp threads were 2*640 tex and 7.2 mm, respectively. Dispersed ARG with an average diameter of 14μm and length of 6 mm were used in a total volume fraction of 0.5%. The ARG has a density of 2.68 g/cm^3, tensile strength of 1700 MPa and Young's modulus of 72 GPa and disperse in water and distributed in the mixture as single mono-filaments.

Slender rectangular plates, with 50 mm gauge length, 25 mm wide and 10 mm thick, were produced using a lamination technique to ensure the identical spacing between fabric layers

and symmetry by calculating and weighing the exact matrix content per layer in advance. The plates were demolded at the age of two days and stored in water until the age of 7 days and then transferred to a climate-controlled room at 20 °C and 65% RH until the age of 28 days.

Table 2-6 Matrix Composition (kg/m³) [115].

Water-to-binder ratio	0.37
CEM III B 32.5 NW-HS-NA	632
Fly ash	265
Micro silica suspension*	101
Fine sand 0/1	947
Water	234
Superplasticizer	11

* solid:water = 50:50

The dynamic tensile tests were conducted using a MTS high-speed servo-hydraulic testing machine with a load capacity of 25 kN operating under open-loop at a maximum speed of 14 m/s. The tensile test apparatus with set up of a Phantom v7 high speed camera are presented in Figure 2-19 [121]. The load was measured by a Kistler 9041A piezoelectric force link (load washer) with a capacity of 90 kN, rigidity of 7.5 kN/μm and frequency response of 33 kHz. A high speed digitizer (up to 10 MHz) collected the force and the stroke LVDT (0.025 mm resolution) signals. The speed of the actuator was controlled by the servo-valve and the nominal strain-rate was measured from the stroke rate and sample gauge length. The full size length pictures recording cracking and failure of different samples were captured at a sampling rate of 10,000 fps.

Four different types of specimens including plain mortar, mortar with addition of ARG, TRC, and TRC with addition of ARG defined as Mortar, TRC, Mortar-ARG and TRC-ARG specimens to designate that short fibers are used respectively. Samples were tested at nominal strain rates of 25 s^{-1}, 50 s^{-1}, and 100 s^{-1} and parameters addressing stress-strain

curves, tensile strength (peak stress), strain capacity (strain at peak stress), maximum strain, and work-to-fracture were collected. The work-to-fracture was evaluated using the total area under load vs. displacement curve as a measure of energy absorption capability.

Representative stress-strain curves of all the systems studied are shown in Figure 2-20 with the accompanying results tabulated in Table 2-7. Since the actuator displacement records both the sample deformation and the slippage in grips, thus the term "apparent strain" is used. Brittle failure was observed for Mortar and Mortar-ARG specimens, and their tensile strengths can be related to the first cracking strengths of TRC specimens. Oscillations in the response of specimens tested at 25 s^{-1} and 50 s^{-1} are traced back to the effects of system ringing which can result in a stress amplitude ranging from 2 to 7 MPa [44]. The test duration of 100 s^{-1} was only about 0.8 ms with the stress reaching peak value at about 0.5 ms while for the other two strain rates the durations ranged from about 3-6 ms. Modal analysis [122] conducted previously on the testing system has shown that ringing effects are present in the responses at 25 and 50 s^{-1} with a more pronounced stress amplitude at 50 s^{-1}, however these effects diminish at 100 s^{-1}. Therefore, the stress oscillation in Figure 2-20(a) and (b) is the coupled result of specimen failure and system ringing. The crack spacing calculated based on the recorded images was correlated with the applied strains and plotted in Figure 2-20(c) and (d). The measurements and macrocrack patterns do not seem to be affected by the strain rate under the dynamic loading regime: the saturated mean crack spacing is approximately 10 mm and not a function of strain rate. However, the addition of ARG reduced the final mean crack spacing as discussed in the next session.

The average tensile strength and work-to-fracture of all samples are compared in Figure 2-21(a) and (b). Compared to the Mortar and Mortar-ARG specimens, significant

improvements in tensile strength and work-to-fracture can be observed in TRC and TRC-ARG samples. The enhanced energy absorption capability is attributed to multiple mechanisms that include elastic energy of longitudinal yarns, interfacial debonding and pull out, as well as energy due to failure at the mechanical anchorage. Yarn anchorage is a main benefit of textile over conventional fibers and is offered by the crimped geometry of the longitudinal yarns and the restraint from transverse yarns at the junctions [123]. The estimated elastic energy of longitudinal yarns using equation $ALE\varepsilon_{ult}^2/2$ (A = composite cross sectional area, L = gauge length, E = Young's Modulus of fiber, ε_{ult} = ultimate tensile strain) is about 4% out of the total energy absorbed with E = 70 GPa and ε_{ult} = 1%. Therefore, the major component of the work-to-fracture is attributed to the nonlinear dissipative mechanisms. As summarized in Table 2-7, the tensile strength of TRC increased from 26.5 to 31.2 MPa as strain rate increased from 25 to 50 s^{-1}, but slightly decreased to 30.0 MPa at 100 s^{-1}. On the other hand, the work-to-fracture dropped from 18.2 to 17.4 and 15.0 as strain rate increased. Since the variation of strain rates (25 to 100 s^{-1}) in the present study is not sufficiently large, its effect may not be very pronounced. Direct tensile tests of Mortar and Mortar-ARG specimens may be affected by high stress concentrations at the grip and unstable fracture due to the low matrix strain capacity which results in a high scatter in the data. No clear trend of the strain rate effect can be observed from Mortar and Mortar-ARG samples at the dosage rates studied.

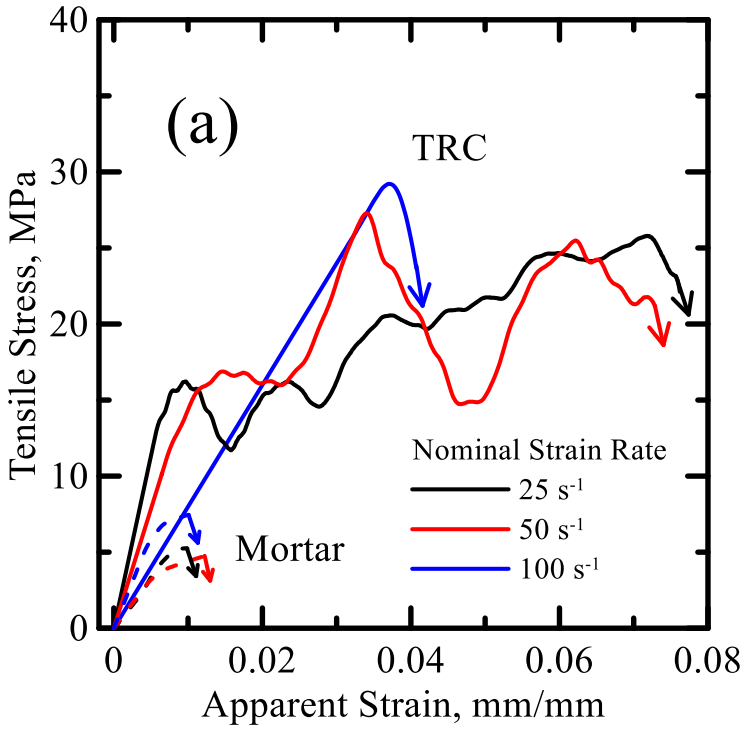
(a)
TRC
Mortar
Nominal Strain Rate
25 s-1
50 s-1
100 s-1
Tensile Stress, MPa
Apparent Strain, mm/mm
0
10
20
30
40
0
0.02
0.04
0.06
0.08

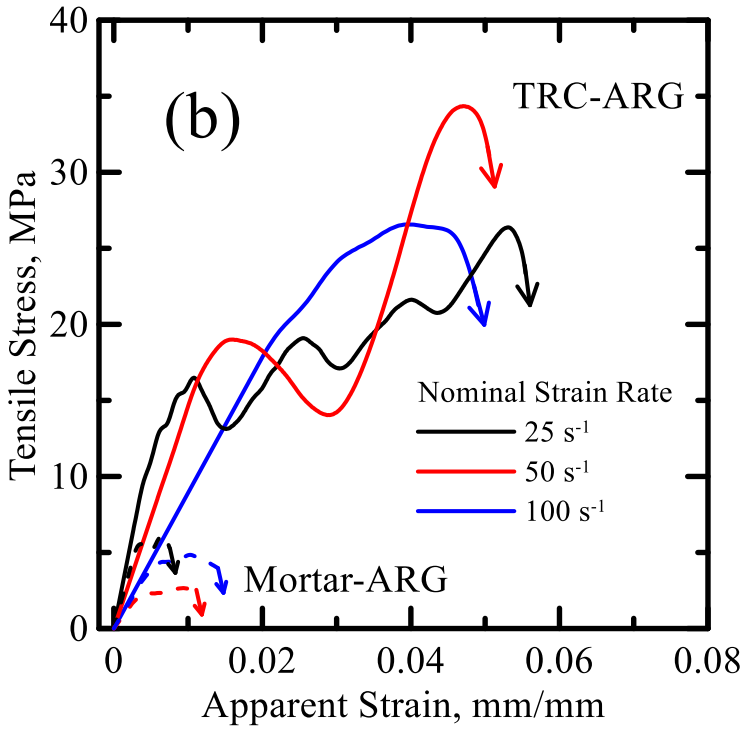
(b)
TRC-ARG
Mortar-ARG
Nominal Strain Rate
25 s-1
50 s-1
100 s-1
Tensile Stress, MPa
Apparent Strain, mm/mm
0
10
20
30
40
0
0.02
0.04
0.06
0.08

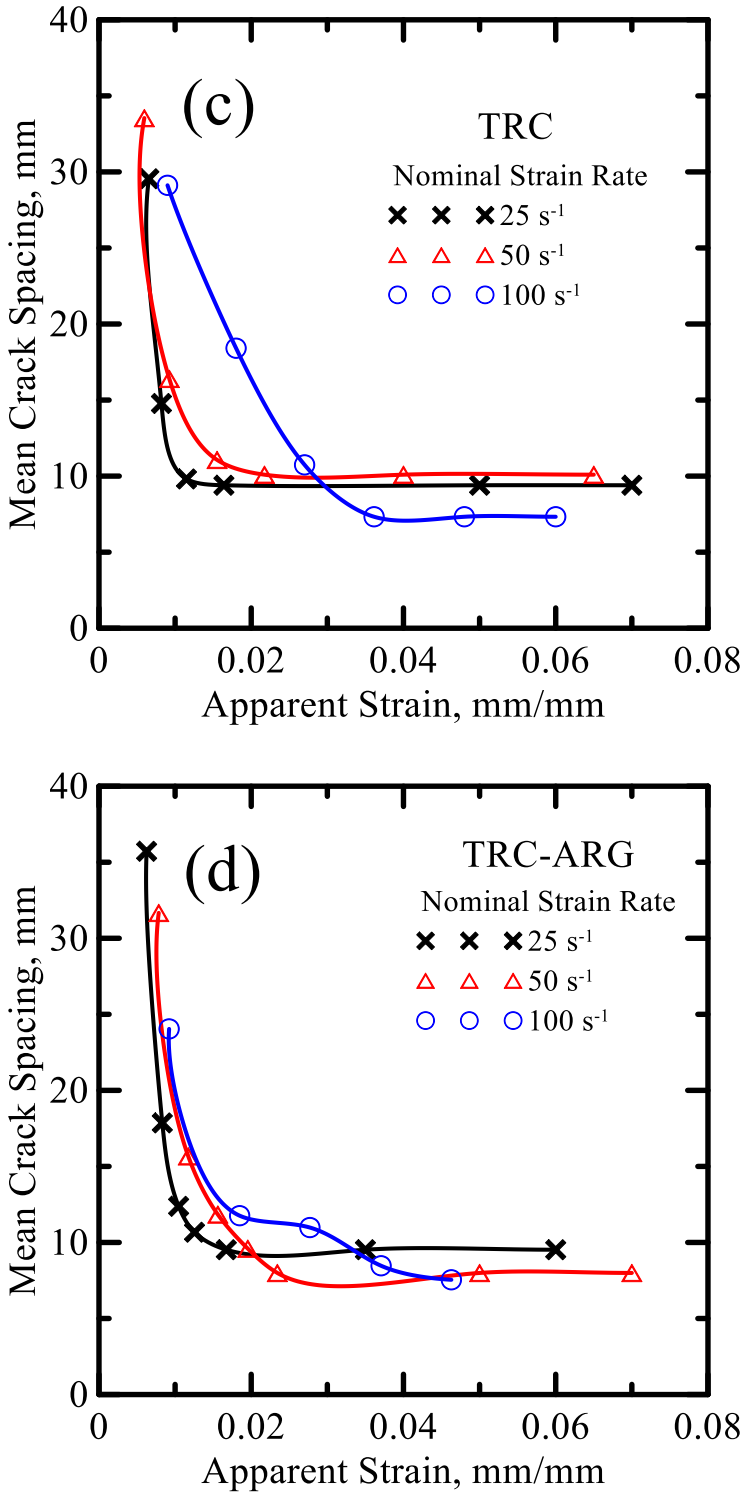

Figure 2-20 Stress-Strain Responses of (a) TRC and Plain Mortar, (B) TRC-ARG and Mortar-ARG Specimens, Mean Crack Spacing-Strain Responses of (c) TRC and (d) TRC-ARG at Varying Strain Rates [115].

When ARG was added to TRC composites, the average tensile strength slightly decreased both at strain rates of 25 s^{-1} (from 26.5 MPa to 25.3 MPa) and 100 s^{-1} (30.0 MPa to 24.4 MPa), while it increased from 31.2 MPa to 35.9 MPa at 50 s^{-1}. The strain capacity, maximum strain, and work-to-fracture decreased as well. Similar trends were also found in Mortar specimens. Earlier studies have shown that addition of discrete short glass fibers usually increases the work-to-fracture but decreases the strain capacity and maximum strain under static tensile tests while the improvement in the tensile strength is moderate [124,125]. There are two opposing mechanisms: short fibers' positive contribution to strength and energy absorption versus the negative effect of increased porosity due to fiber addition to a relatively small specimen size. Decreases in strain capacity and maximum strain were attributed to the mitigation of cracking by short fibers that enables the finer crack pattern and smaller crack width as confirmed in the next section by DIC. Additionally, the enhancement in bond strength leads to a reduction in pull out displacement at maximum load. Therefore, the total deformation measured by the stroke is reduced and subsequently decreases in strain capacity and maximum strain are observed. On the contrary to static tensile test results [124, 125], the decrease in work-to-fracture may be attributed to the interaction among the porosity, strength, and strain rate. Similar behavior was also observed in larger plates containing textiles and short fibers [45]. Further work is needed to address the multi-scale phenomenon and interaction of different mechanisms.

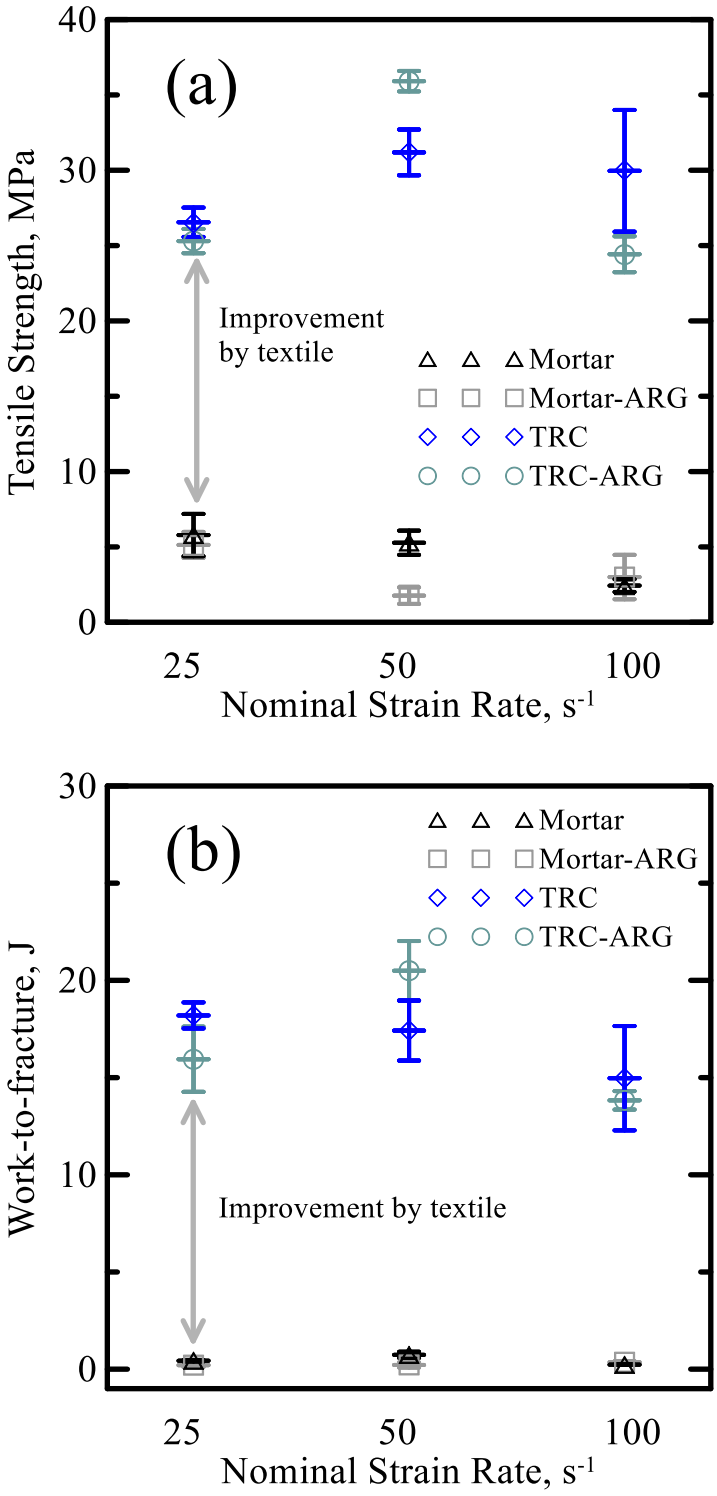

Figure 2-21 Average Tensile Strength (b) Average Work-to-Fracture of All the Materials Tested at Varying Strain Rates [115].

Table 2-7 Experimental Results of All the Specimens Tested at Various Strain Rates [115].

Specimen	Nominal Strain Rate	Tensile Strength	Strain Capacity	Max. Strain	Work-to-fracture
	(s^{-1})	(MPa)	(%)	(%)	(J)
Mortar	25	5.8	1.06	1.67	0.69
		(1.1)	(0.13)	(0.16)	(0.05)
	50	5.3	1.60	3.19	1.41
		(0.7)	(0.42)	(0.45)	(0.2)
	100	2.4	1.36	4.79	0.86
		(0.3)	(0.18)	(0.58)	(0.25)
Mortar-ARG	25	5.1	0.52	1.23	0.46
		(0.7)	(0.09)	(0.12)	(0.05)
	50	1.8	1.27	3.09	0.41
		(0.5)	(0.6)	(0.81)	(0.15)
	100	3.0	1.58	4.17	0.86
		(1.2)	(0.56)	(0.61)	(0.17)
TRC	25	26.5	6.06	7.62	18.20
		(1.7)	(0.96)	(0.65)	(1.16)
	50	31.2	3.64	6.59	17.42
		(2.7)	(0.78)	(1.24)	(2.76)
	100	30.0	5.21	7.31	14.97
		(7)	(1.28)	(1.06)	(4.65)
TRC-ARG	25	25.3	5.98	7.13	15.94
		(1.4)	(0.6)	(0.97)	(2.9)
	50	35.9	5.16	7.78	20.50
		(1.1)	(1.65)	(0.75)	(2.5)
	100	24.43	5.07	6.89	13.8
		(2.06)	(0.77)	(0.69)	(0.8)

When ARG was added to TRC composites, the average tensile strength slightly decreased both at strain rates of 25 s^{-1} (from 26.5 MPa to 25.3 MPa) and 100 s^{-1} (30.0 MPa to 24.4 MPa), while it increased from 31.2 MPa to 35.9 MPa at 50 s^{-1}. The strain capacity, maximum strain, and work-to-fracture decreased as well. Similar trends were also found in Mortar specimens. Earlier studies have shown that addition of discrete short glass fibers usually increases the work-to-fracture but decreases the strain capacity and maximum strain under static tensile tests while the improvement in the tensile strength is moderate [124, 125]. There are two opposing mechanisms: short fibers' positive contribution to strength and energy absorption versus the negative effect of increased porosity due to fiber addition to a relatively small specimen size. Decreases in strain capacity and maximum strain were attributed to the mitigation of cracking by short fibers that enables the finer crack pattern and smaller crack width as confirmed in the next section by DIC. Additionally, the enhancement in bond strength leads to a reduction in pull out displacement at maximum load. Therefore, the total deformation measured by the stroke is reduced and subsequently decreases in strain capacity and maximum strain are observed. On the contrary to static tensile test results [124,125], the decrease in work-to-fracture may be attributed to the interaction among the porosity, strength, and strain rate. Similar behavior was also observed in larger plates containing textiles and short fibers [45]. Further work is needed to address the multi-scale phenomenon and interaction of different mechanisms.

2.3.3 Temperature Effects

Recent work has addressed the effect of temperature on the fiber and matrix interfacial properties and thus the mechanical performance of composite. Bhat et. al [126] studied the effect of temperature on PVA reinforced strain hardening cement composites (SHCC) and

documented the degradation in fiber/matrix interfacial properties at temperatures below or equal to 200 °C. Silva et al. [127] used TRC reinforced with carbon fibers heating up to temperatures of 150 °C and showed that in polymer coated carbon fiber TRC, an interlocking mechanism between filaments and matrix is observed which results in significant increases in the maximum pull-out load. Krüger and Reinhardt [68] conducted fire tests on four different I-shaped mortar beams reinforced with AR-glass and carbon textiles. Due to the softening of the styrene-butadiene rubber (SBR) coating (at about 90 °C) the fiber–matrix interface was impaired, resulting in fiber pull-out and subsequent failure. This session presents the results of high-speed tensile testing in the formation of parallel cracking and strain distribution of TRC with various textiles. Full field displacement mapping techniques to address the strain distribution were applied to multiple TRC samples. Mechanical properties of textiles and TRC samples were obtained at temperatures of -30, 25 and 80 °C. Finally, a tension stiffening model was used to compute the load deformation response as well as the crack spacing evolution.

Figure 2-22 shows the three types of textiles used in the present study: 1) laminated alkali-resistant (AR) glass that is coated with sizing and referred to as SG; 2) warp-knitted AR-glass without sizing and referred to as GL; 3) warp-knitted polypropylene-glass hybrid referred to as PP. Table 2-8 includes the properties and dimensions for the various textiles where weft is in the transverse direction and warp is in the longitudinal direction. The knitted textiles with glass or polypropylene yarns were produced using a commingling setup at Institut für Textiltechnik der RWTH Aachen [128].

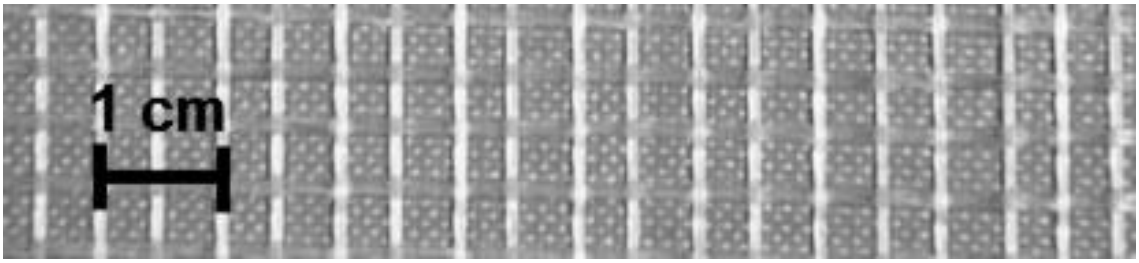

(a)

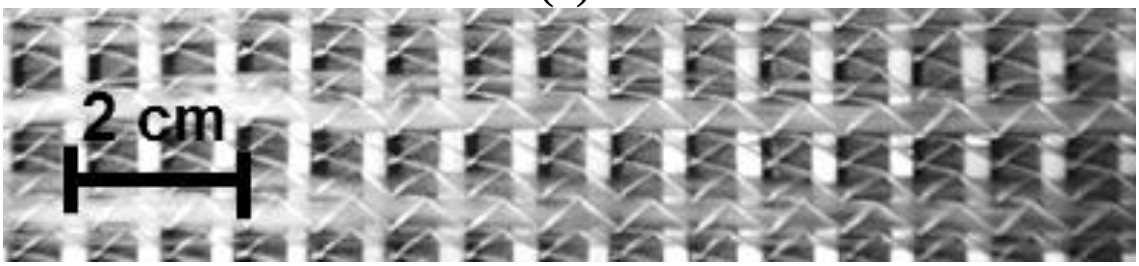

(b)

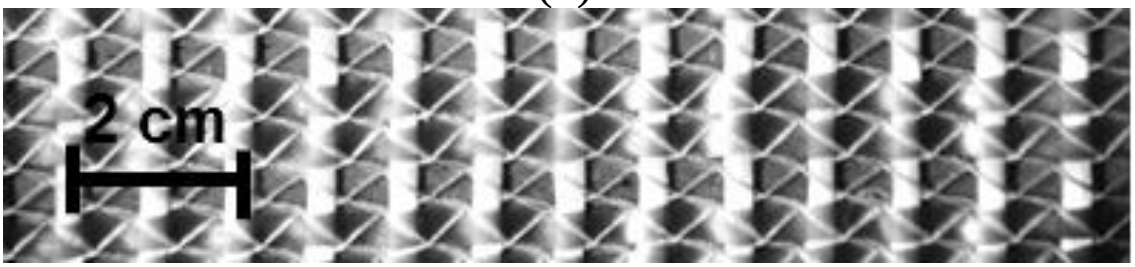

(c)

Figure 2-22 Close-up Pictures of (a) Laminated AR-Glass Textile (SG), (b) Warp-Knitted AR-Glass Textile (GL), and (c) Warp-Knitted Polypropylene Textile (PP). Weft: Horizontal and Warp: Vertical [46].

Table 2-8 Geometrical and Mechanical Characteristics of Textiles [46]

Material	Warp (90°)	Weft (0°)	Knitting Yarn	Yarn Count (Weft or Warp) [tex]	Density [g/cm^3]	Fiber modulus (Gpa)	Fiber ultimate tensile strength (MPa)
Laminated AR-Glass (SG)	SG	SG	-	1200	-	78	1360
AR-Glass (GL)	AR	AR	PES (167 tex)	1200	2.68	78	1360
Polypropylene (PP)	PP	AR	PES (167 tex)	400	0.9	6.9	500

TRC samples were prepared with 4 layers of textiles using the pultrusion process developed by Peled, et al. [129]. The mixture proportions are as follows: 800g cement, 160g fly ash, 290 ml water (water/binder ratio 0.3), 0.5% superplasticizer by mass of cement. The samples were prepared on a plate as layered sheets of 250 × 300 mm in dimension and subjected to a constant pressure of 0.5 MPa. Panels were cured in water at 20±1 °C for 28 days. Specimens of 25 mm x 11 mm in cross section and 150 mm in length were cut from the plates. Aluminum plates were glued onto the gripping edges of the specimen to minimize localized damage. In addition, single-layer plain textile samples with dimensions of 25 mm x150 mm were also tested under same conditions. The gauge length of was 50 mm for both textile and TRC specimens. High speed tensile tests were performed on both plain textile and TRC specimens under three different temperatures: -30 °C, +25 °C, and +80 °C. A stroke rate of 5.08 m/s was chosen to obtain a nominal strain rate of 100 s^{-1}.

Figure 2-23 presents the dynamic tensile stress versus time history of a SG-TRC specimen. From a macroscopic perspective, the bend over point (BOP) corresponds to the formation of matrix cracking. Five distinct stages are identified using roman numerals with two stages prior to and three stages after BOP. Stage I corresponds to the elastic-linear range where both matrix and the fiber behave linearly. Due to relative low fiber content, the stiffness of the composite is dominated by matrix properties. Stage II is associated with formation and propagation of the first crack in the matrix, until it traverses the entire width up to the BOP point.

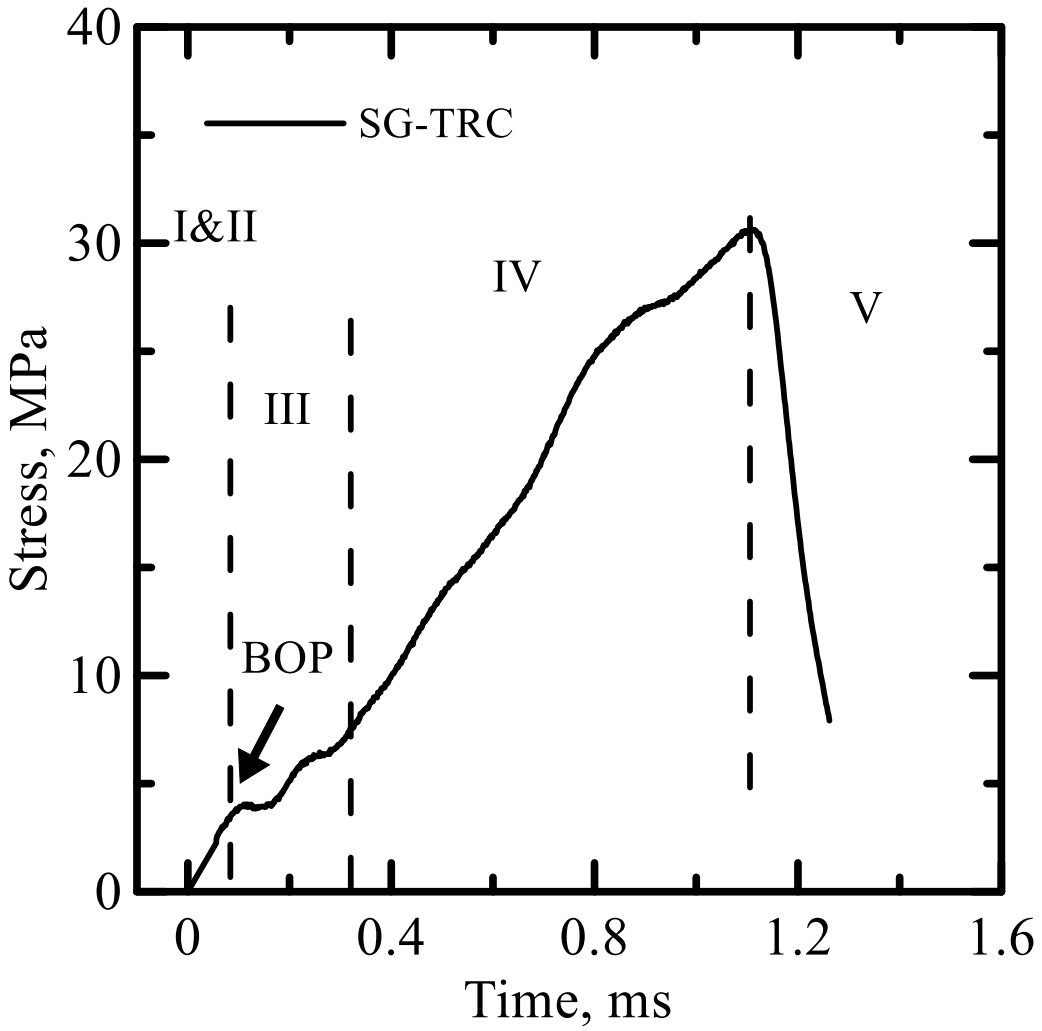

Figure 2-23 Stress Versus Time History of a SG-TRC Specimen Under High Speed Tensile Load [46].

After the formation of the first crack, additional cracks also initiate at approximately regular intervals and begin to propagate across the specimen width. The post-BOP stage III is characterized by distributed cracking and textile bridging mechanisms. The load carrying capacity of intact matrix segments between parallel cracks does not vanish and is referred to as tension stiffening effect. As applied load increases, more cracks form until the characteristic damage state (CDS) where no more cracks can develop due to the inability of the fibers in transferring sufficient load back into the matrix. After completion

of cracking phase and initiation of debonding in Stage IV, progressive damage that includes crack widening, textile delamination and pull-out leads to the ultimate failure during stage V.

Table 2-9 summarizes the average values and standard deviations of test results. The slack in the yarns due to unequal length, twist, and curvature variations requires a modification to the direct use of the nominal cross sectional area of textiles. Thus the total forces applied onto the test specimens were reported in comparing the textiles and TRCs while the determination of tensile stress was only applicable to TRC specimens. Figure 2-24 represents the force versus strain responses of GL-textile and TRC as well as the typical failure pattern of GL-textile specimen.

The range of maximum load and work-to-fracture for GL-textiles were 2561-3367 N and 2.6-4.2 J, respectively. The imperfections in alignment or initial slack of warp yarns may cause the material to fail before a uniform stress in all the fibers is reached. As shown in Figure 2-24(d), the failure initiated from one yarn bundle leads to sample rotation under eccentric load and results in a lower actual strength compared to an average strength value. The effects of imperfections and initial slack were less pronounced in TRCs due to the redistribution of the load by the matrix through interfacial load transfer, as well as the anchorage offered by the fill yarns. As a result, the maximum force almost tripled in GL-TRCs (up to 7615 N) due to the composite action that eliminated such testing effects and improved the tensile properties.

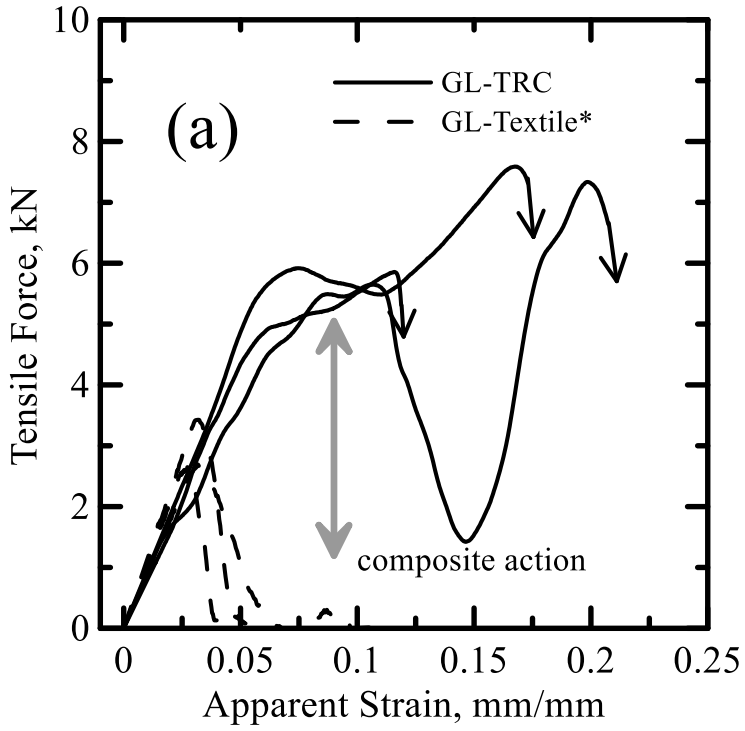
(a)
GL-TRC
GL-Textile*
composite action
Tensile Force, kN
Apparent Strain, mm/mm
0
2
4
6
8
10
0
0.05
0.1
0.15
0.2
0.25

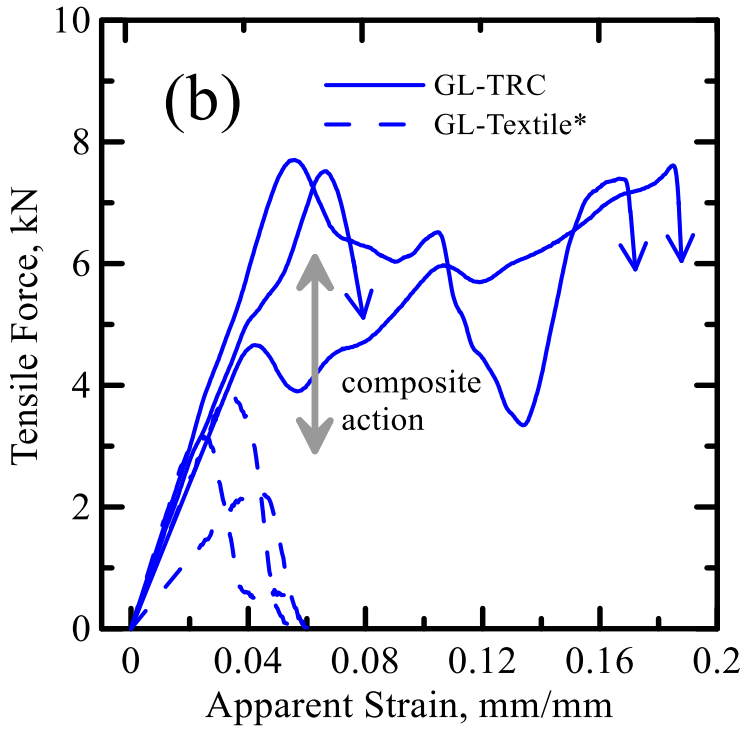
(b)
GL-TRC
GL-Textile*
composite
action
Tensile Force, kN
Apparent Strain, mm/mm
0
2
4
6
8
10
0
0.04
0.08
0.12
0.16
0.2

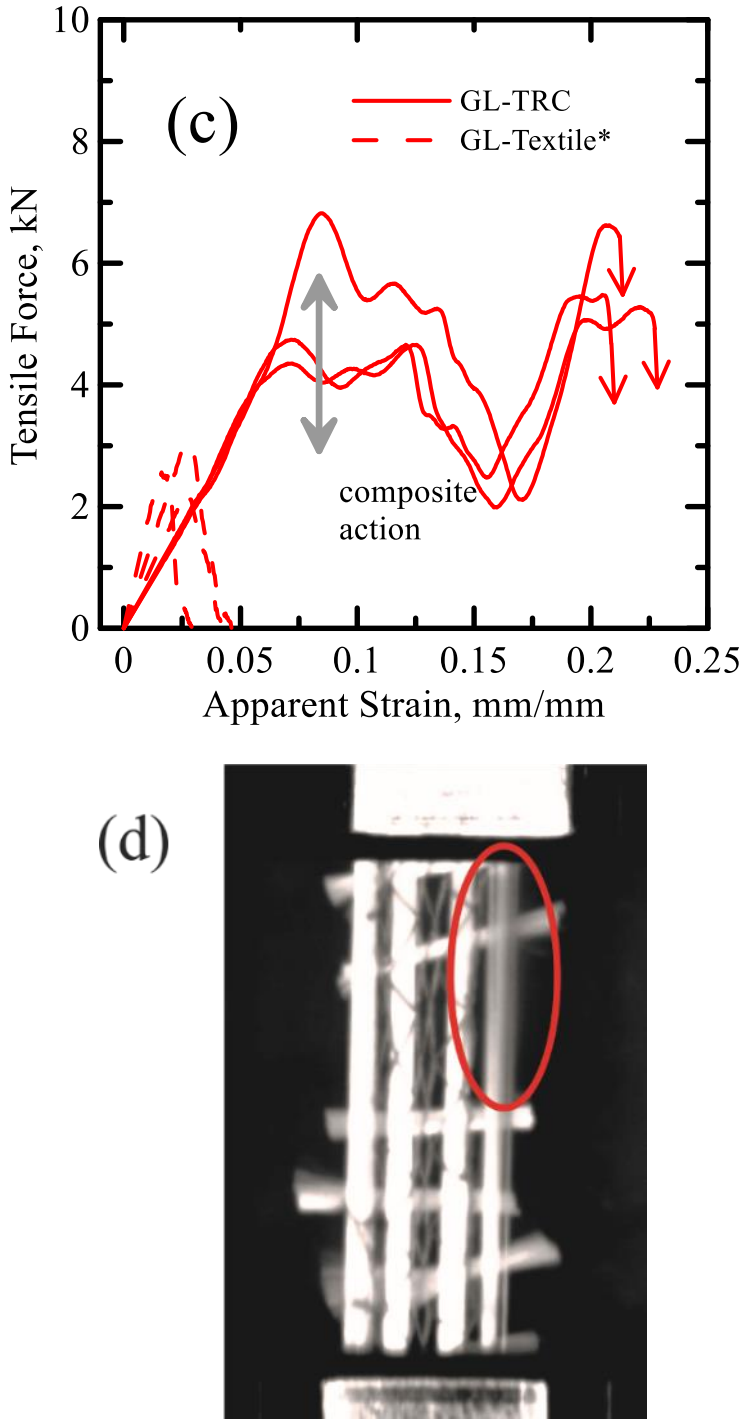

Figure 2-24 Force-Strain Responses for GL-TRC and Textile Replicates at (a) 25 °C (b) -30 °C and (c) 80 °C and (d) Typical Failure Pattern of Textile Specimen [46].

Figure 2-25 compares the force versus strain responses of various TRCs at different temperatures and shows the typical failed samples. Multiple cracking and pronounced

textile pull-out were observed both for GL-TRC and SG-TRC. The work-to-fracture for GL-TRC specimens was in the range of 35.7-46.8 J which was approximately 6 times higher than textiles. The enhanced energy absorption capability is attributed to multiple dissipation mechanisms including formation of crack surfaces, interfacial debonding, pull-out, and failure at the mechanical anchorage points. The maximum load of SG-TRC tested under room temperature was 4329±170 N while the values were 5995±115 N and 4620±156 N under low and high temperatures, respectively. The maximum work-to-fracture was in the range of 12.9-16.1 J which was more than twice of plain textiles. Unlike the GL- and SG-TRCs, failure mode of the PP-TRC was dominated by the fiber fracture due to relatively lower tensile strength of polypropylene. The maximum loads for PP-TRCs were 2151±177 N, 2856±371 N and 2198±271 N under room, low and high temperatures, respectively. The average maximum work-to-fracture was in the range of 10.5-16.8 J. It is noted that the while the work-to-fracture of PP textiles were higher than the two glass textiles, an opposite trend was found in TRC specimens. With a higher ductility of polypropylene compared to glass fibers, the higher energy absorbed by PP textiles was clear, however the energy dissipation mechanisms such as textile pull-out resulted in a substantial increase in the work-to-fracture observed in GL-TRC specimens.

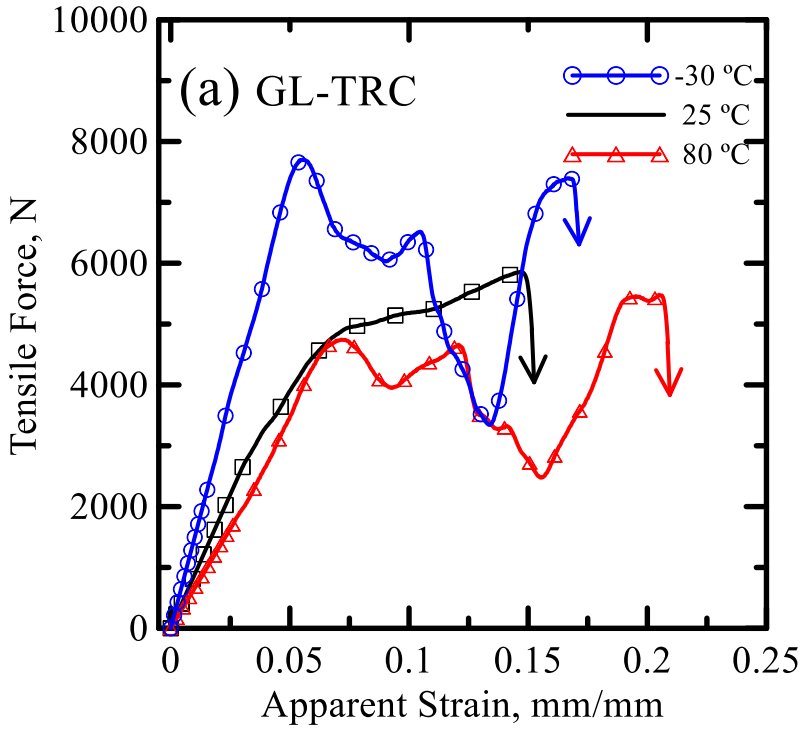
(a) GL-TRC
-30 ºC
25 ºC
80 ºC
Tensile Force, N
Apparent Strain, mm/mm
0
2000
4000
6000
8000
10000
0
0.05
0.1
0.15
0.2
0.25

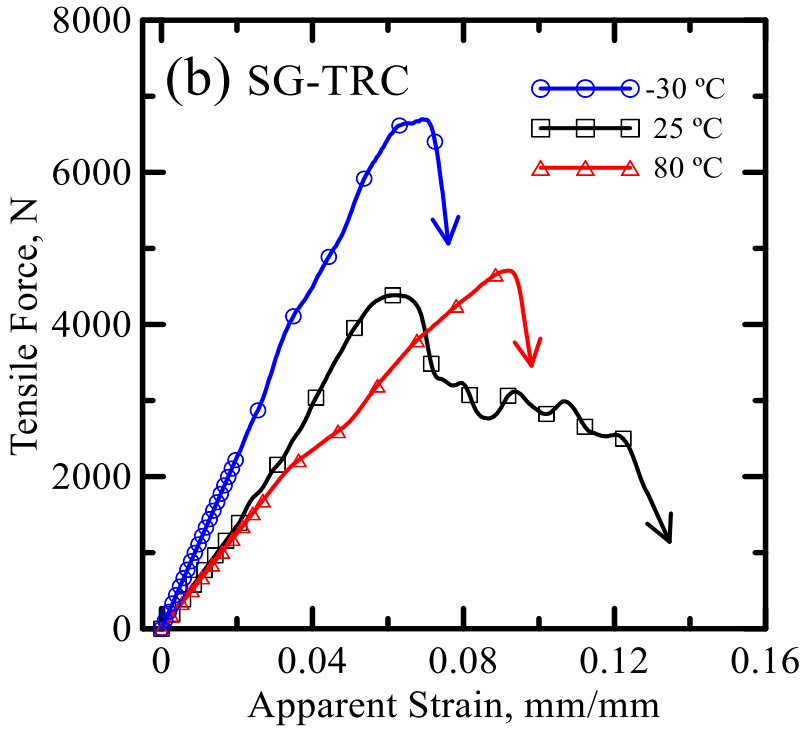
(b) SG-TRC
-30 ºC
25 ºC
80 ºC
Tensile Force, N
Apparent Strain, mm/mm
0
2000
4000
6000
8000
0
0.04
0.08
0.12
0.16

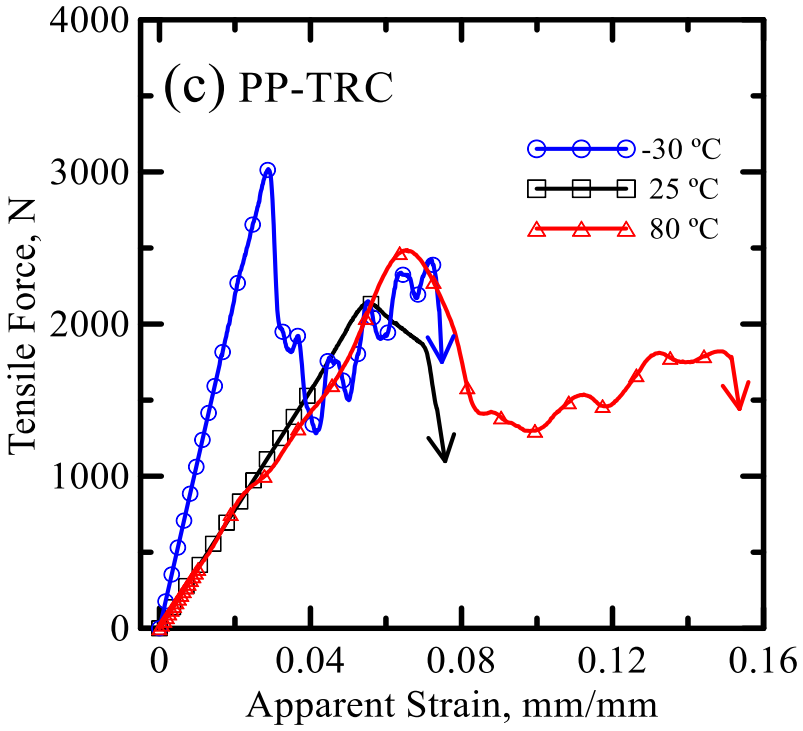

(d)

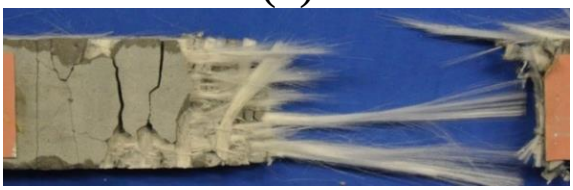

GL

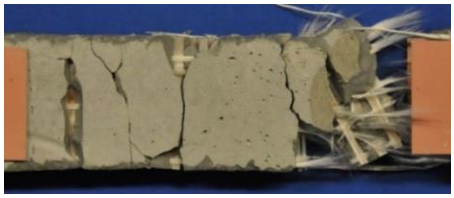

SG

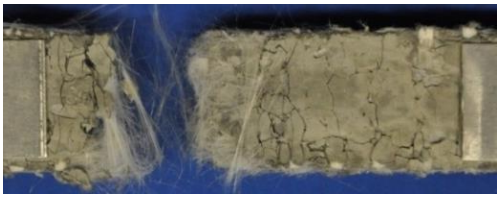

PP

Figure 2-25 Representative Force-Strain Responses at Varying Temperatures for (a) GL-TRC, (b) SG-TRC, (c) PP-TRC and (d) Tested Specimens [46].

Figure 2-26 compares the tensile strength, work-to-fracture and postcrack tensile stiffness of various TRCs at different temperatures. A decreasing trend of tensile strength with increasing temperature was observed for the GL-TRC, from 38.1 MPa at -30 °C to 23.4 MPa at 80 °C. Similarly, the highest tensile strength of 30 MPa and 14.3 MPa for SG- and PP-TRC specimens were obtained at -30 °C, while the effect of elevated temperature was less pronounced. Additionally, decreases in postcrack stiffness with increasing temperature were also found in all TRCs. The postcrack stiffness of GL-TRC was the highest (459.7 MPa) followed by SG (354.5 MPa) and PP (199.2 MPa) at room temperature. Postcrack stiffness of GL- and SG- TRCs compared to PP-TRC at all temperatures was higher due to the relatively higher stiffness of glass textiles. Additionally, the tension stiffening effect and load carrying capacity of the intact matrix between two parallel cracks can also be enhanced by the interfacial bond stiffness. Therefore, the higher postcrack stiffness of GL-TRC compared to SG-TRC at room temperature indicates better bonding characteristics of the warp-kitted glass textile due to the effect of coating. This aspect of study will be further discussed in next section.

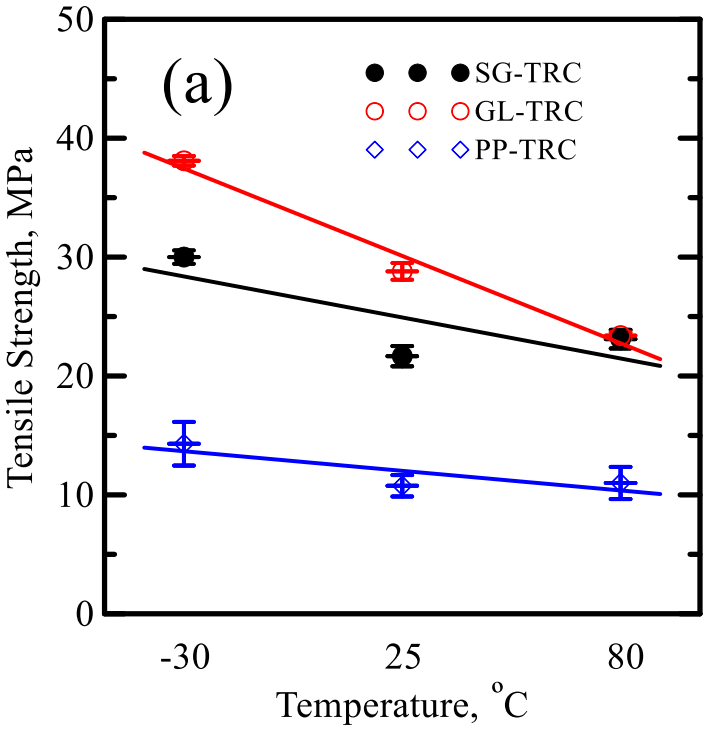
(a)
SG-TRC
GL-TRC
PP-TRC
Tensile Strength, MPa
50
40
30
20
10
0
-30
25
80
Temperature, °C

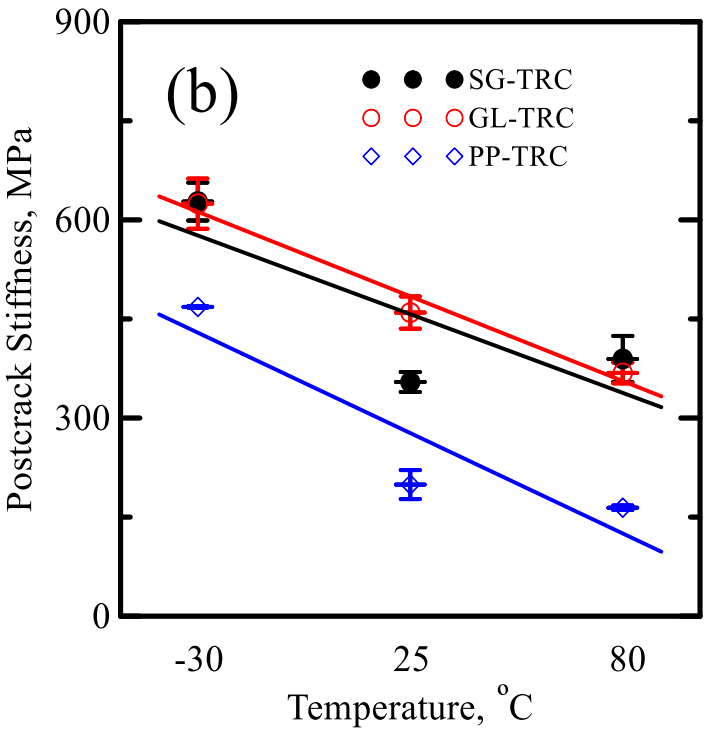
(b)
SG-TRC
GL-TRC
PP-TRC
Postcrack Stiffness, MPa
900
600
300
0
-30
25
80
Temperature, °C

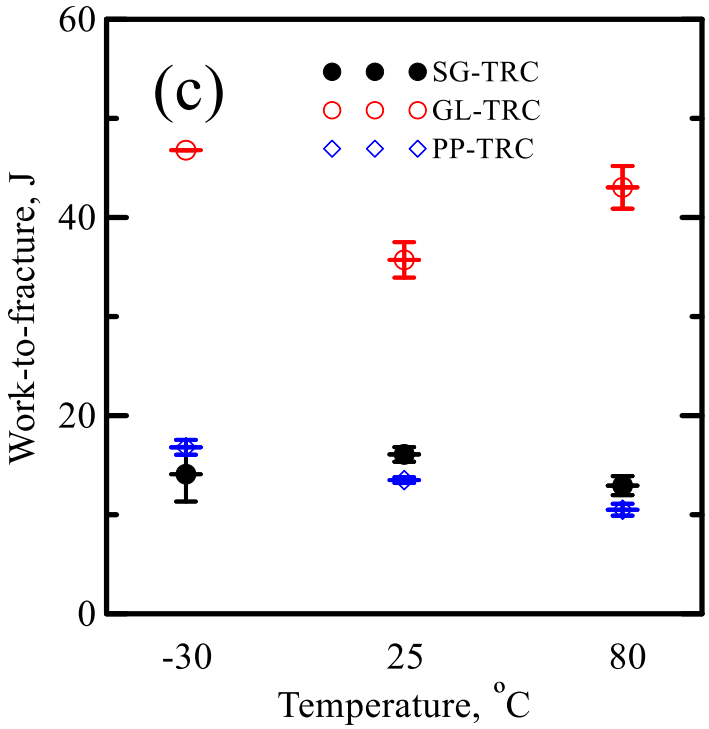

Figure 2-26 (a) Tensile Strength, (b) Postcrack Stiffness, and (c) Work-to-Fracture of Various TRCs at Different Temperatures [46].

Table 2-9 Experimental Parameters for High Strain Rate Test for Various TRCs [46]

Material	Temp. °C	Strain (at Peak) mm/mm	Max. Force N	Tensile Strength MPa	Max. Strain mm/mm	Work-to-fracture J	Postcrack Stiffness MPa
GL	-30	0.055 (0.012)	7615 (80)	38.1 (0.4)	0.14 (0.045)	46.8 (0.01)	624.5 (62.0)
	25	0.084 (0.014)	5761 (141)	28.8 (0.7)	0.177 (0.027)	35.7 (2.53)	459.7 (40.0)
	80	0.074 (0.009)	4679 (52)	23.4 (0.3)	0.159 (0.002)	43.0 (3.5)	368.3 (25.7)
SG	-30	0.075 (0.007)	5995 (115)	30 (0.6)	0.103 (0.006)	14.1 (3.9)	627.7 (46.9)
	25	0.112 (0.017)	4329 (170)	21.6 (0.8)	0.121 (0.098)	16.1 (1.2)	354.5 (24.7)
	80	0.08 (0.01)	4620 (156)	23.1 (0.8)	0.097 (0.012)	12.9 (1.6)	389.4 (56.9)
PP	-30	0.06 (0.024)	2856 (371)	14.3 (1.9)	0.191 (0.005)	16.8 (1.2)	468.2 (1.9)
	25	0.05 (0.008)	2151 (177)	10.8 (0.9)	0.164 (0.075)	13.5 (0.42)	199.2 (35.9)
	80	0.073 (0.007)	2198 (271)	11 (1.4)	0.155 (0.015)	10.5 (1.0)	164.2 (5.6)

Table 2-10 Experimental Parameters for High Strain Rate Test for Various Textiles [46]

Material	Temp. °C	Strain (at Peak) mm/mm	Max. Force* N	Max. Strain mm/mm	Work-to-fracture J
GL	-30	0.031 (0.006)	3044 (828)	0.052 (0.007)	4.2 (1.3)
	25	0.027 (0.007)	3367 (704)	0.049 (0.015)	4.2 (0.4)
	80	0.024 (0.005)	2561 (425)	0.038 (0.008)	2.6 (0.8)
SG	-30	0.062 (0.014)	2767 (213)	0.097 (0.008)	7.5 (1.5)
	25	0.043 (0.007)	1541 (215)	0.125 (0.013)	5.2 (1.1)
	80	0.064 (0.016)	2425 (198)	0.11 (0.033)	7.4 (2.7)
PP	-30	0.047 (0.007)	2360 (203)	0.127 (0.023)	9.3 (1.1)
	25	0.055 (0.016)	2578 (220)	0.117 (0.028)	9.3 (1.7)
	80	0.044 (0.006)	2350 (380)	0.11 (0.014)	7.7 (1.8)

* Force for 4 layers of textiles

2.3.4 Image Analysis Using Digital Image Correlation (DIC)

Figure 2-27(a) shows the contour of longitudinal displacement of a TRC sample tested at 25 s^{-1} with all the cracks formed. The sequential formation of five individual cracks is indicated in the figure. The distribution of the displacement field is shown in Figure 2-27(b) for various stress levels with the cracks identified as the discontinuities in the displacement. The location and width (ω) of a certain crack is represented by the x-coordinate and the vertical amplitude of the discontinuity. The deformation in uncracked segment between two parallel cracks is insignificant compared to ω. Figure 2-27(c) shows the evolution of five cracks and the mean response versus time up to failure. The stress versus time history is also plotted indicating the loading level. The cracks behaved differently as much larger openings were observed for cracks 1 and 3 near the grips compared to those of cracks 4 and 5. And according to high speed images, failure occurred at crack 3.

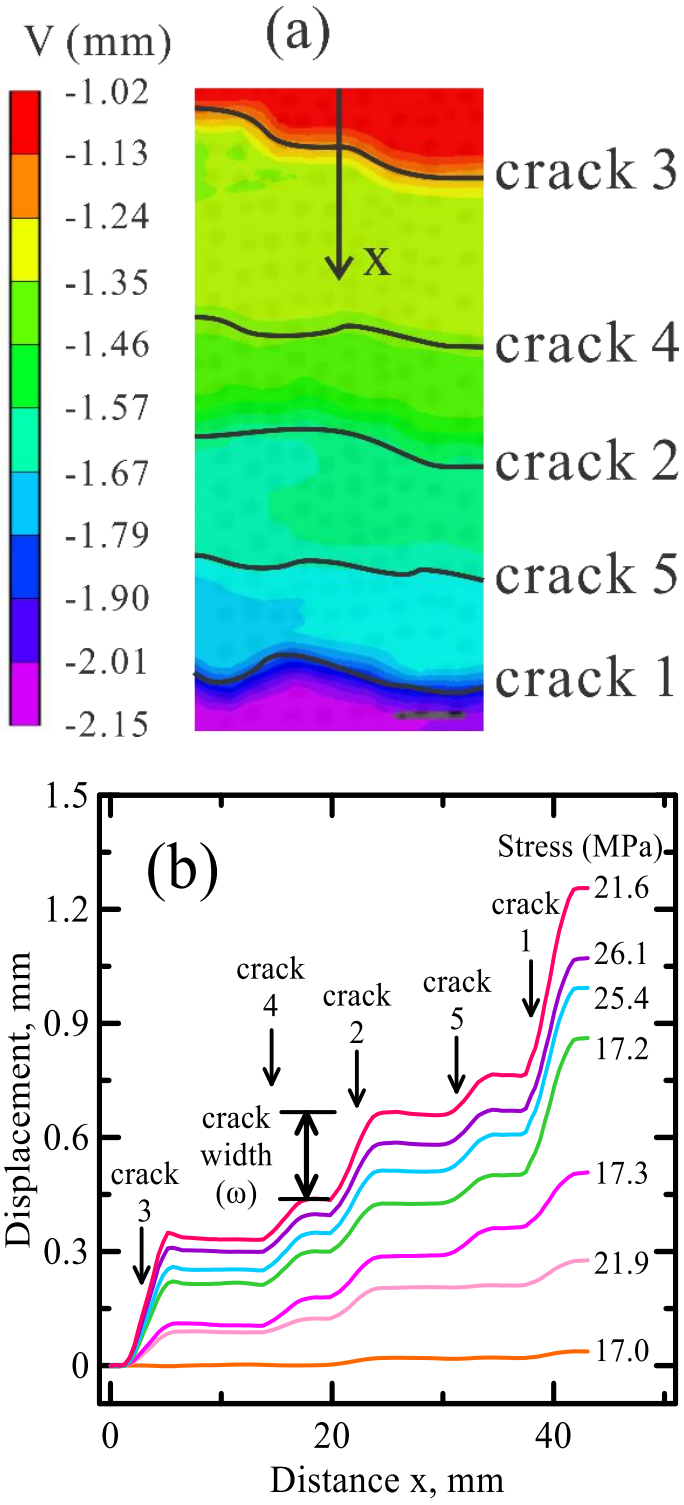
V (mm)
-1.02
-1.13
-1.24
-1.35
-1.46
-1.57
-1.67
-1.79
-1.90
-2.01
-2.15
(a)
x
crack 3
crack 4
crack 2
crack 5
crack 1
(b)
Stress (MPa)
21.6
26.1
25.4
17.2
17.3
21.9
17.0
crack 1
crack 2
crack 3
crack 4
crack 5
crack width (ω)
Displacement, mm
Distance x, mm
0
0.3
0.6
0.9
1.2
1.5
0
20
40

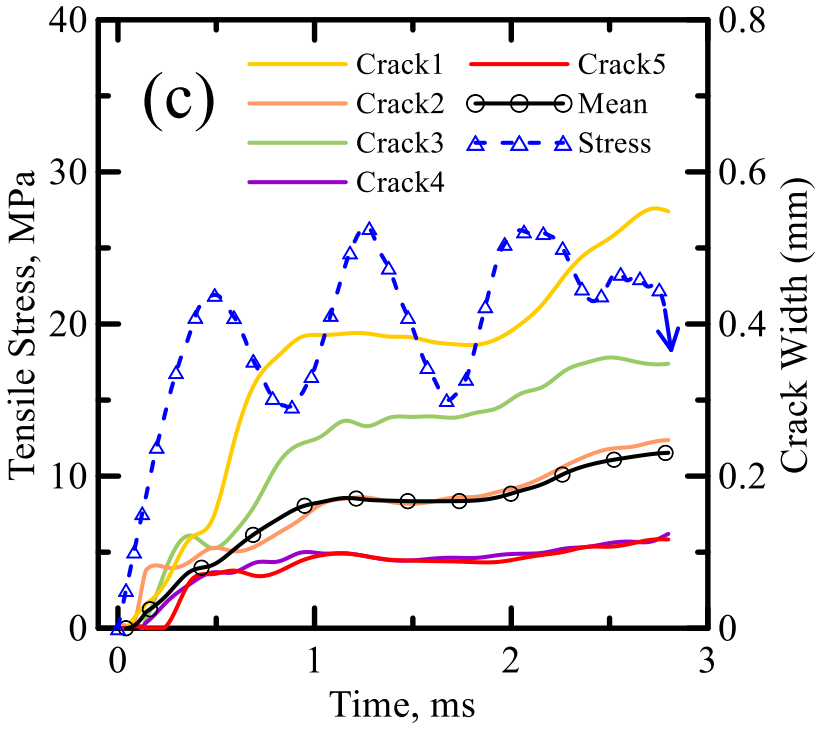

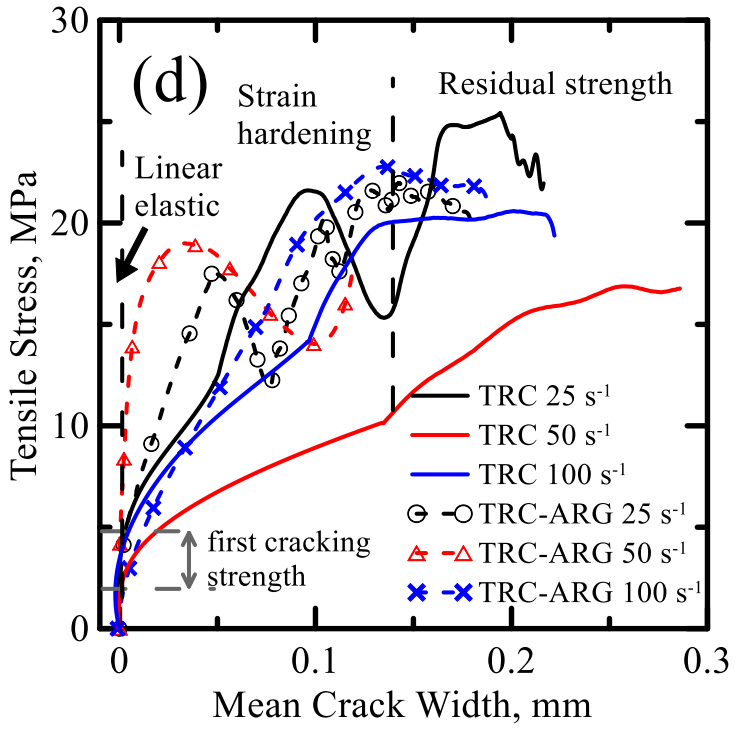

Figure 2-27 (a) Longitudinal Displacement Contour of a TRC Specimen Tested at $25s^{-1}$, (b) Distribution of Displacement at Seven Loading Stages, (c) Crack Width and Tensile

Stress Versus Time Histories, (D) Stress-Crack Width Responses of Representative Specimens [115].

The mean crack widths obtained by DIC were then correlated with the stress responses of representative samples, as shown in. Figure 2-27(d). The linear elastic stage (no crack formed) is represented by an almost vertical line and extends to the bend over point as the first cracking strength, approximately from 2.9 to 4.2 MPa. Pronounced strain hardening effect was observed after cracking as the tensile stresses increased with a reduced stiffness. The experimentally obtained stress-crack width responses are characterized by three parameters: first-cracking strength, post-cracking stiffness and residual strength. The TRC-ARG samples exhibit smaller crack widths and higher post-cracking stiffness at equivalent stress levels.

The longitudinal strain (ε_{yy}) fields of four types of specimens tested at 25 s^{-1} are shown in Figure 2-28 using a color code with purple representing the lowest strain values and red at 5.0% strain. Due to the inherent brittleness of matrix, only one macro crack formed in the Mortar sample and the addition of short fibers at a low volume fraction (0.5%) did not change the failure mode for Mortar-ARG sample, see Figure 2-28(a) and (b). Tensile strain concentrated in the vicinity of the crack while the far-field was uniformly deformed. Previous studies on the tensile behavior of strain-hardening cement-based composites (SHCC) containing 2% of short polyvinyl-alcohol fiber however showed that in such a ductile material only very few cracks formed under high strain-rate loading [18,97]. Figure 2-28(c) and (d) show the strain map of TRC and TRC-ARG samples, respectively. Figure 2-28(d) illustrates the damage evolution such that at the beginning of the test (σ = 3.1 MPa), a relatively uniform strain distribution in accordance with linear-elastic stage (Stage 1) was obtained. As σ increased to 6.1 MPa, two bands in blue were formed indicating matrix

cracking and onset of nonlinear behavior. Increasing tensile stress (σ = 16.7 MPa) resulted in additional transverse cracks into multiple fracture bands. Saturation of transverses cracks was coincident with maximum tensile stress (σ = 19.5 MPa) with three identified zones as: (A) the localization zone in red which contains the transverse crack with the majority of the load carried by the textile phase; (B) the shear lag zone in green/blue where the slip between fiber and matrix cannot be ignored and the bond stress follows a shear lag pattern; (C) the uniform zone where no crack is formed, composite is behaving linearly and slip is negligible. The fiber stress variation along the length reaches a maximum level in the bridge zone (A) and minimum value at the "perfectly bonded" zone (C). Similar pattern of strain map was also observed in the specimens tested at other strain rates.

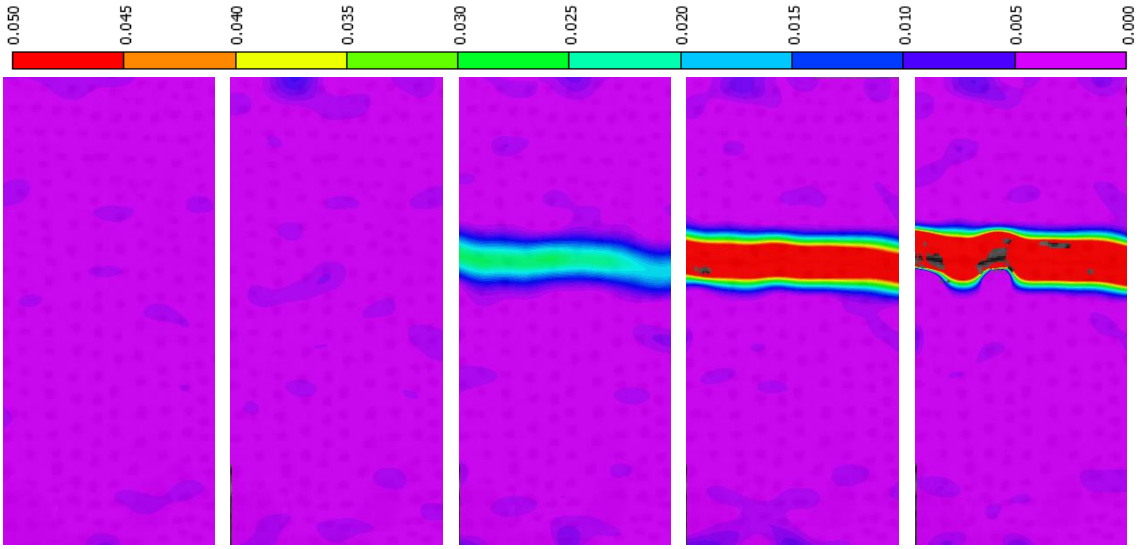

σ = 0.8 MPa σ = 2.9 MPa σ = 4.1 MPa σ = 4.3 MPa σ = 2.6 MPa

(a)

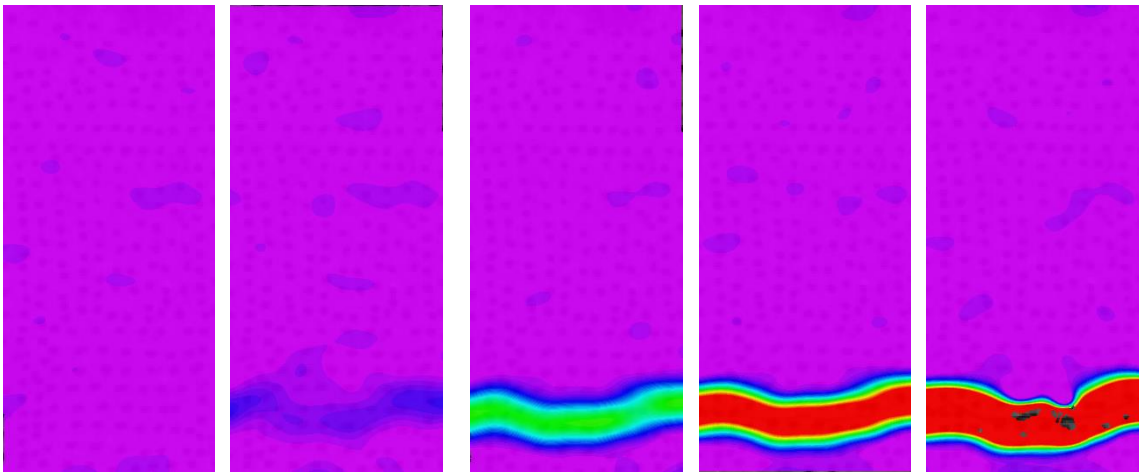

σ = 0.8 MPa σ = 2.0 MPa σ = 4.0 MPa σ = 3.4 MPa σ = 3.0 MPa

(b)

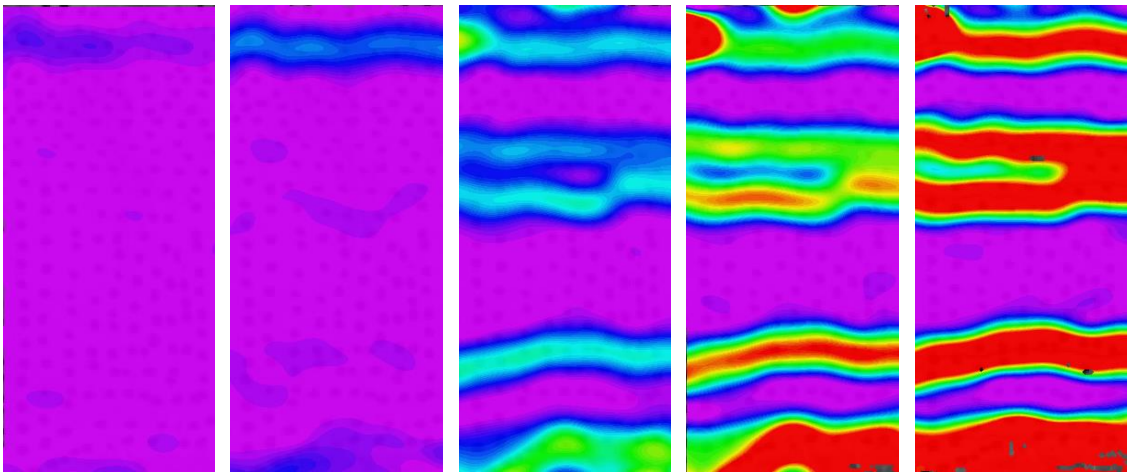

σ = 3.7 MPa σ = 7.4 MPa σ = 16.1 MPa σ = 18.7 MPa σ = 25.8 MPa

(c)

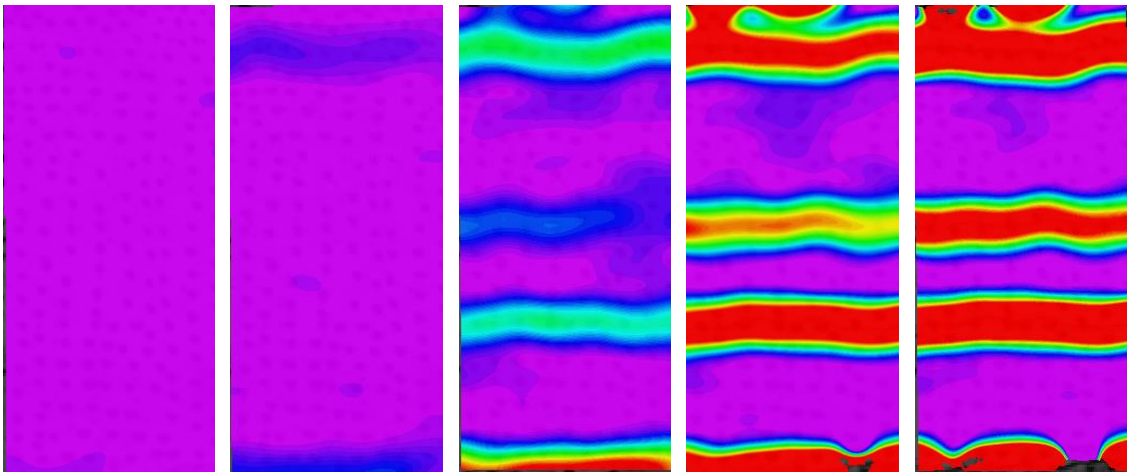

σ = 3.1 MPa σ = 6.1 MPa σ = 16.7 MPa σ = 19.5 MPa σ = 21.6 MPa

(d)

Figure 2-28 Strain Fields (ε_{yy}) Obtained by DIC for Various Specimens Tested at the Strain Rate of 25 s^{-1}: (a) Plain Mortar, (b) Mortar-ARG, (c) TRC and (d) TRC-ARG [115].

The three distinct zones identified by DIC observations are shown in Figure 2-29. The strain map is selected from Figure 2-28(d) at σ = 19.5 MPa and the corresponding distribution of longitudinal strain along the length of specimen is shown in the lower sub-figure of Figure 2-29. The distance is normalized with respect to the length of AOI (in this case L_{AOI} = 44 mm) and different zones are separated by the dashed lines. The behaviors at zones A, B and C, can be modeled as an σ-ω relationship, nonlinear bond stress-slip relationship, and with a linear stress-strain relationship, respectively. These three models are integrated in a finite difference model introduced in next session. Additionally, crack spacing (s) and the width of localization zone (h_L) were measured from the DIC data.

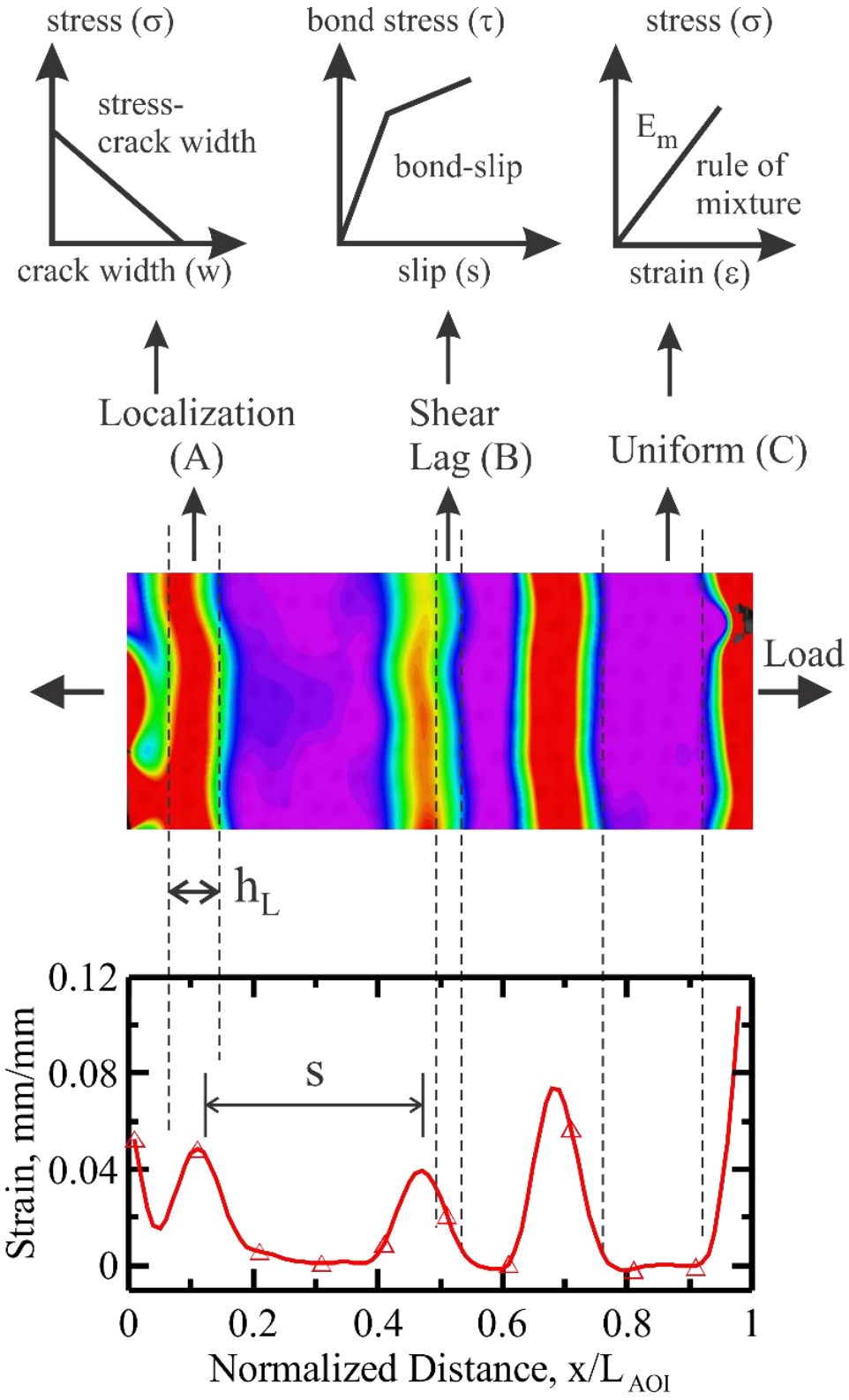

Figure 2-29 Identification of Three Zones: Localization, Shear Lag, Uniform Strain and Corresponding Modelling Approaches [115].

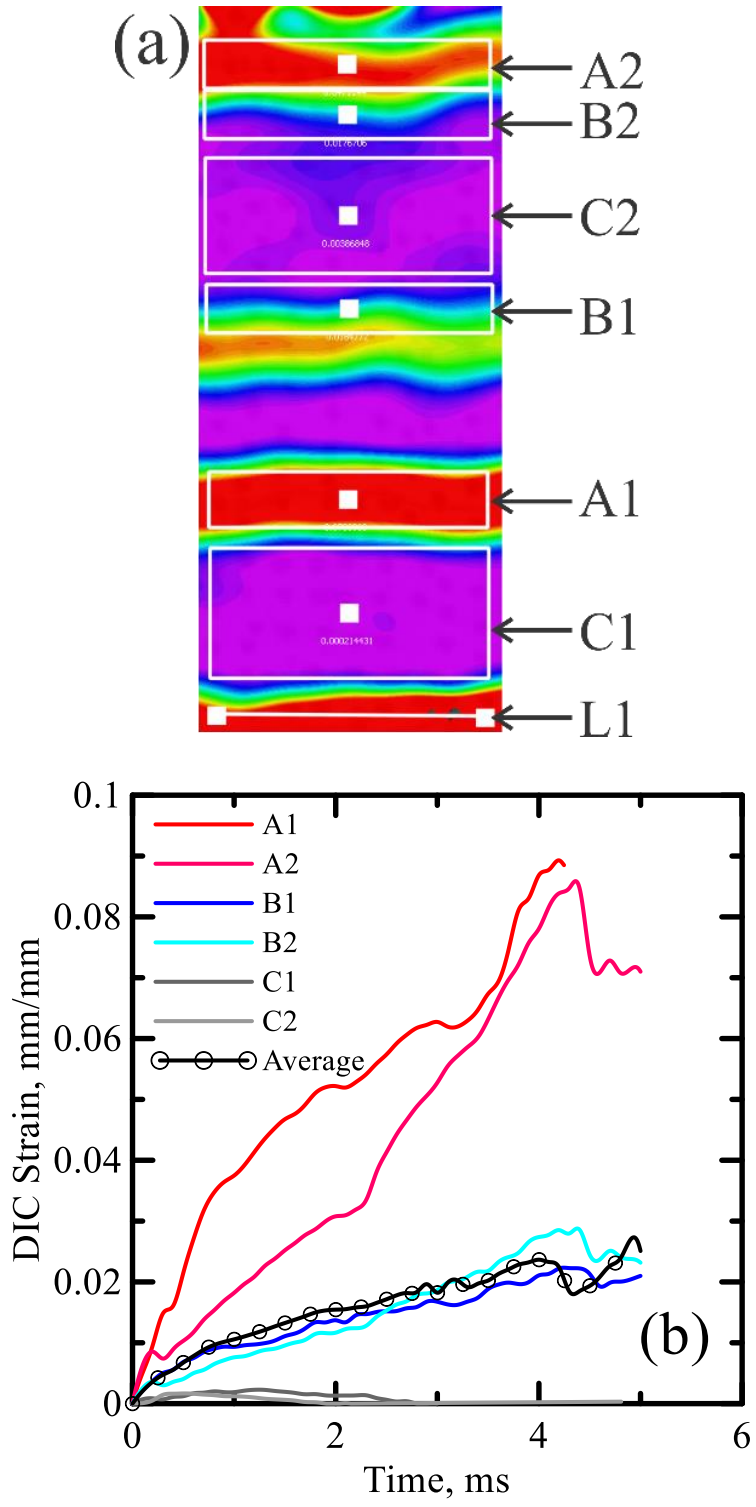
(a)
A2
B2
C2
B1
A1
C1
L1
0.1
0.08
0.06
0.04
0.02
0
DIC Strain, mm/mm
A1
A2
B1
B2
C1
C2
Average
(b)
0
2
4
6
Time, ms

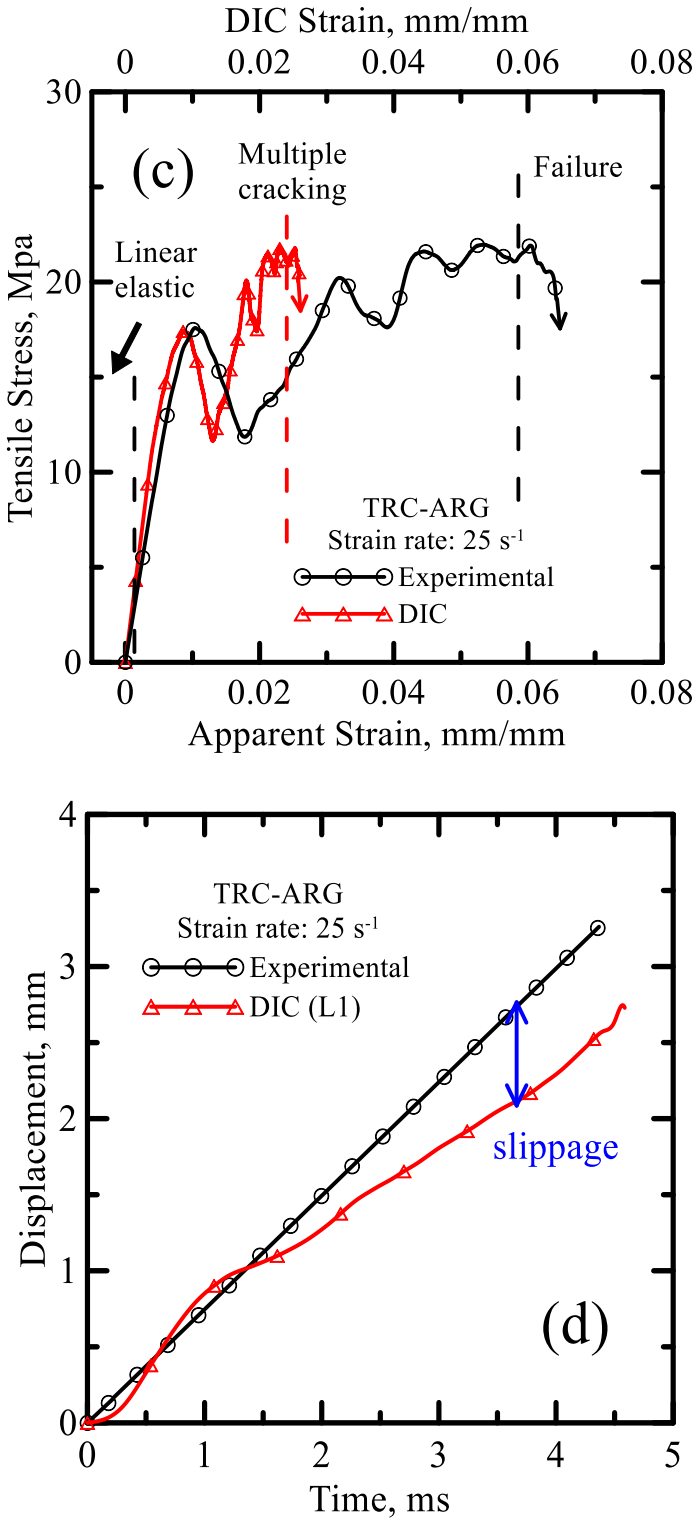

Figure 2-30 (a) Zone Labels, (b) Strain Versus Time Responses in Selected Zones, (c) Comparison of Stress-Strain Responses Between DIC and Experimental Measurements, (d) Time History Responses of DIC and Stroke Displacement [115].

The strain variation as a function of time in different zones and the average response of a TRC-ARG specimen are presented in Figure 2-30. Selection of representative regions in localization (A1 and A2), shear lag (B1 and B2), and uniform (C1 and C2) is shown in Figure 2-30(a). Additionally, a horizontal line (L1) was selected to represent the average displacement along the bottom edge of the specimen. Significant variances in the strain values was observed among different zones of Figure 2-30(b). The maximum strain of 8.9% in zone A is about three times of that in B (2.9%), while the uniform strain (<0.3%) is much lower compared to other zones. As a result of crack opening and fiber pullout, the displacement rapidly increased along the loading direction and the strain field became discontinuous while crossing the cracks; thus the excessively large strain values are no longer reliable. Sample failure occurred around 4.4 ms when peak strain values were reached.

Correlation of the DIC strain with the stress response and conventional stress-strain curve is shown in Figure 2-30(c). The displacement function measured by DIC along line L1 is plotted against the LVDT signal in Figure 2-30(d). The actuator response includes spurious displacement such as grip slippage, sample rotation, and large inhomogeneous crack opening displacements. The apparent strain and experimental displacement were therefore larger than DIC measured properties in the multiple cracking stage although in the linear elastic stage, results were quite comparable.

The width of localization zone *(h_L)* is equivalent to a development length needed for the force transfer from fiber to matrix in order to reach the critical stress necessary for matrix cracking, see Figure 2-31(a). The characteristic damage state (CDS) is a strain level where no more cracks in the matrix can develop due to the inability of the fibers in transferring

sufficient load back into the matrix and correlates with the final crack spacing. The role of bond parameters in formation of additional cracks and slip related multiple cracks are expressed in terms of h_L and s representing the crack spacing. Parameters h_L and s for 15 individual TRC and TRC-ARG specimens were measured using DIC and their probability distribution functions are expressed as a two parameter Weibull distribution [130]:

$$P(\sigma) = 1 - \exp[-(\frac{x}{\lambda})^k] \qquad \text{Equation 2-3}$$

Where x is the measured parameters (h_L or s), λ is the reference or scaling value related to the mean and k is the Weibull modulus or shape parameter. The cumulative distribution function (CDF) of h_L and s as shown in Figure 2-31(b) and (c) indicate that the mean value of h_L decreased from 7.4 to 6.5 mm with addition of short fibers, (Figure 2-31(b)) as well as spacing s reduced from 10.3 to 8.4 mm (Figure 2-31(c)). This measurement confirms the role of short fibers in mitigating and bridging the micro cracks in bond enhancement. At the microstructural level, short fibers improve the bond by means of active load transfer and crosslinking with hydration products thus a greater number of micro-cracks serve as nuclei for macro-crack formation [131]. Addition of short fibers supports stress transfer across cracks as well as crack deflection mechanisms, both of which play a role in toughening. Therefore, stress relaxation of the matrix in the vicinity of cracks is less pronounced and a smaller development length is needed, hence cracks form more closely. As a result of narrower localization zones, finer crack pattern and smaller crack widths were obtained.

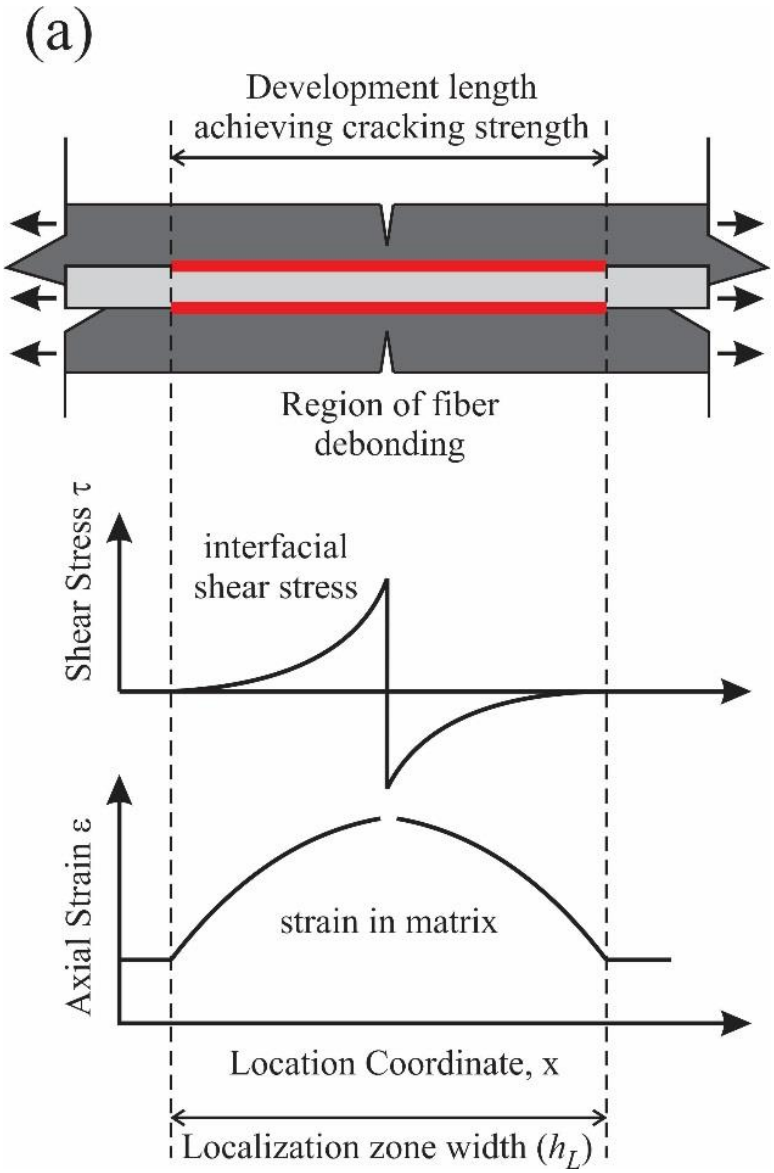
(a)
Development length
achieving cracking strength
Region of fiber
debonding
Shear Stress τ
interfacial
shear stress
Axial Strain ε
strain in matrix
Location Coordinate, x
Localization zone width (h_L)

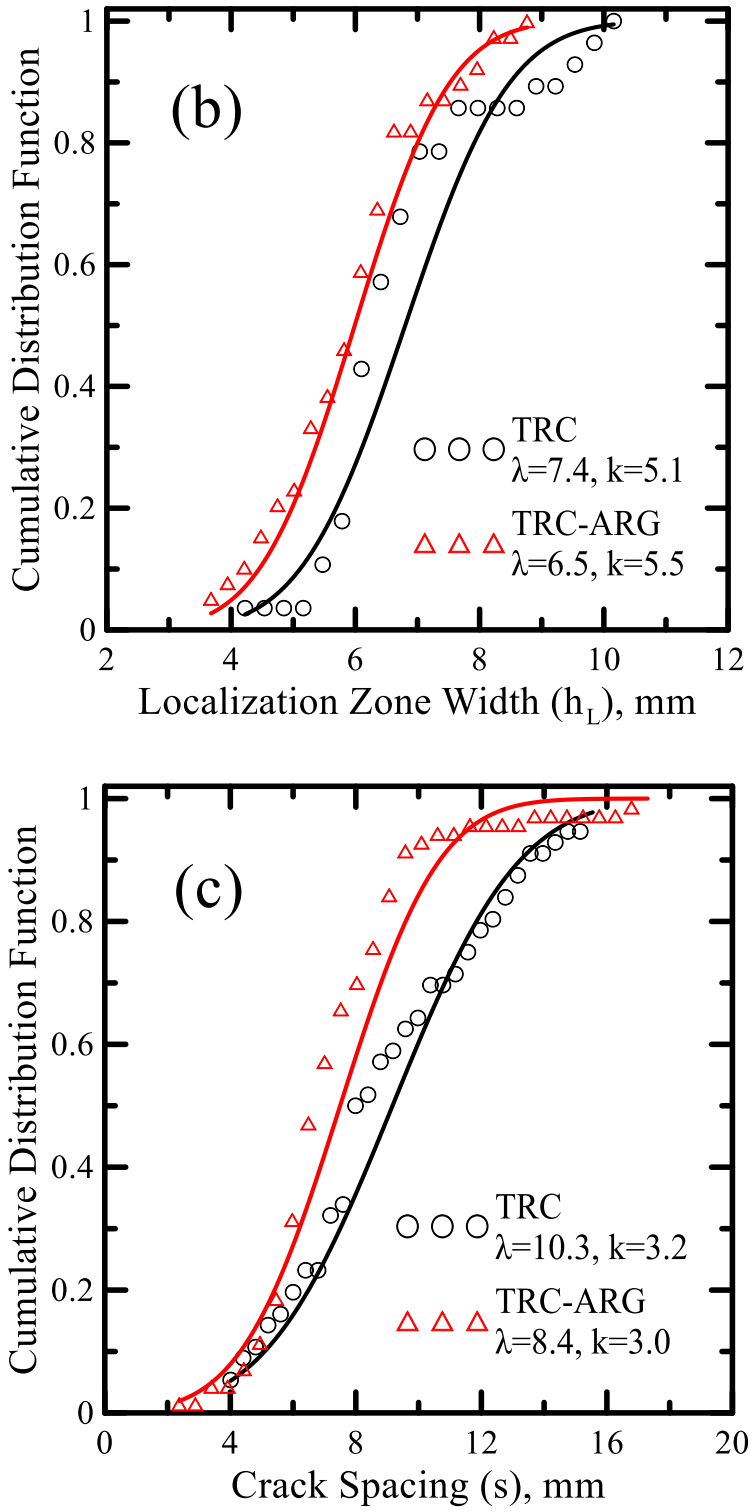

Figure 2-31 (a) Correlation of Localization Zone Width (h_L) With Development Length to Achieve Cracking Strength, and Curve Fitting of Weibull CDF for (b) Localization Zone Width (h_L) and (c) Crack Spacing (s) [115].

Strain fields (ε_{yy}) of various TRCs are shown in Figure 2-32 using color legends with purple representing the lowest strain values and red at 3.0% - 5.0% strain. Figure 2-32(a) shows the time-lapse images of SG-TRC illustrating the longitudinal strain distribution with increasing stress level. At the beginning of test, the strain is uniformly distributed throughout the specimen in accordance with the elastic-linear stage (Stage I) until the tensile stress σ_t reaches 4.1 MPa. Tensile strain localizes in the regions of blue and green implying crack initiation and strain concentration in Stages II and III. After the matrix cracks, its load carrying capacity does not diminish in the uniform zones in purple since the load is still transferred through intact interfaces. Increasing tensile stress results in additional transverse cracks and multiple localized zones accompanied by a rapid increase in tensile strain. The consecutive crack formation is followed by crack widening, extensive debonding, textile pull-out and ultimate failure, as shown in the final sub-image. It is also observed that the far field strains drop back to relatively lower levels which can be traced back to the elastic recovery of textiles and crack closure. Similar strain map and cracking behavior can be observed in the other two systems as shown in Figure 2-32(b) and (c).

The area and length parameters where textile debonding and pull-out occur are crucial parameters that relate interfacial characteristics to the failure pattern and energy dissipation. These parameters are measured at different loading stages using a proposed three-step process which includes: image region cropping, color threshold, determination of outline and measurement, as shown in Figure 2-32(d) [132]. Results show that GL-TRCs demonstrate larger area and length of slip zones prior to failure than PP-TRCs which may be attributed to the spacing between the fill yarns as well as the strength and stiffness of the junction bonds between the warp and fill yarns. The failure modes compared in Figure

2-25(d) show that the textile debonding and pull-out are more pronounced in GL-TRCs compared to PP-TRCs which experienced more fiber fracture. The high ductility observed in these samples demonstrated by distributed cracks as compared to the single crack occurs in plain matrix is associated with the energy dissipation due to debonding and pull-out of textile. The strain relaxation of the matrix in the vicinity of the crack within a region parallel to the crack faces is an indicator of internal debonding since the force is being transferred and carried by the textile in that region. The length slip zone along the longitudinal loading axis is therefore implying the extent of debonding and textile sliding which contribute to frictional energy dissipation. Larger slip zones may be associated with higher energy dissipated during the test which is supported by the experimental results showing higher work-to-fracture values of GL-TRC specimens compared to PP-TRC. Intermediate level of work-to-fracture, slip zone size and mode of failure are observed in the SG-TRC specimen. Different failure modes can be explained by the interaction of fiber tensile strength and interfacial bond strength. Once the shear stress between fiber and matrix reaches the bond strength, fiber debonding takes place and the slip zone is formed. Load transfer between glass fibers and matrix may still be active at higher composite stress levels (e.g. 27.2 MPa as shown in Figure 2-32(b)) while PP-TRC fails at lower stresses (11 MPa in Figure 2-32(c)) and the mechanism terminates. The average lengths of slip zone at the main cracks where failure occurs for SG-, GL- and PP-TRCs are about 7 mm, 9 mm, and 10 mm respectively, as labeled in Figure 2-32(d). It is noteworthy that the distances between weft yarns (cf. Figure 2-22) as 5 mm for SG textile, 10 mm for GL and PP textiles, respectively, correlates with the measured lengths of slip zones. This observation supports

the role of mechanical anchorage provided by the weft yarns in preventing the slip of warp yarns such that the slip zones are limited between two adjacent weft yarns.

During the transverse cracking stage, the load transfer between the matrix and the bridging fibers is an indication of the continuity of total force across the crack, however the stress continuity can only be modeled by means of the shear lag theory. The bond parameters play an important role in the mechanism, ultimately leading to additional cracks associated with parallel cracking. The fiber stress varies along the length of fiber from maximum level in the bridge zone and diminishes in the perfectly bonded zone. Using a simplified assumption, three zones were defined as: (A) localization zone around the transverse crack where the majority of the loads is carried by the fiber phase; (B) shear lag zone associated with an excessively higher strain in the fiber such that the slip between the fiber and matrix cannot be ignored; (C) the uniform zone where the slip is negligible and rule of mixtures is applicable.

The strain variation as a function of time history and position in six selected rectangular regions for a SG-TRC specimen (Figure 2-32(a)) are presented in Figure 2-33. The selection of different regions is shown in Figure 2-33(a) where A1 and A2 represent localization zone, B1 and B2 are in the shear lag zone, C1 and C2 correspond to the uniform zone. Significant variations in the strain values from localization to uniform zones are observed as shown in Figure 2-33(b). The maximum strain of 7.8% prior to sample failure in zone A is more than twice of that in B (3.2%), while the uniform strain (<0.2%) is negligible compared to other zones. As a result of crack opening and textile pull-out, the displacement rapidly increases along the loading direction and the strain field loses its continuity across the cracks. The excessively large strain values up to 13.9% in zone A2

are no longer reliable. Sample failure takes place around 2.2 ms when peak strains in multiple regions are reached. In the post peak range, strains in both zones A and B are found to drop for about 50% of peak values which can be explained by the elastic recovery of textile and closure of cracks.

A comparison of the stress-strain curves measured from DIC method with conventional analysis is shown in Figure 2-33(c). The initial stiffness measured by means of actuator deformation is fairly low due to possible slippage and spurious displacements in the grips, resulting in a lower dynamic friction coefficient. DIC measurements however exclude rigid body motion and a more accurate strain response within the linear elastic stage is obtained. The stress-strain responses of three selected specimens are shown in Figure 2-33(d) where the five distinct stages of damage evolution can be easily distinguished.

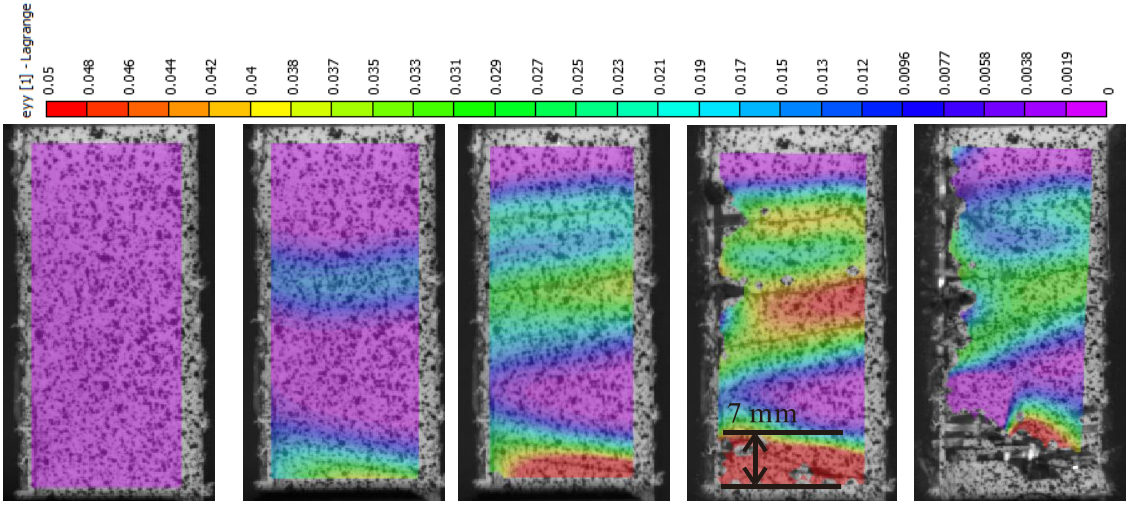

σ_t = 0.0 MPa, A_{slip} = 0%

σ_t = 4.1 MPa, A_{slip} = 2.7%

σ_t = 8.1 MPa, A_{slip} = 21.8%

σ_t = 13.4 MPa, A_{slip} = 50.4%

σ_t = 0.2 MPa, A_{slip} = N/A

(a)

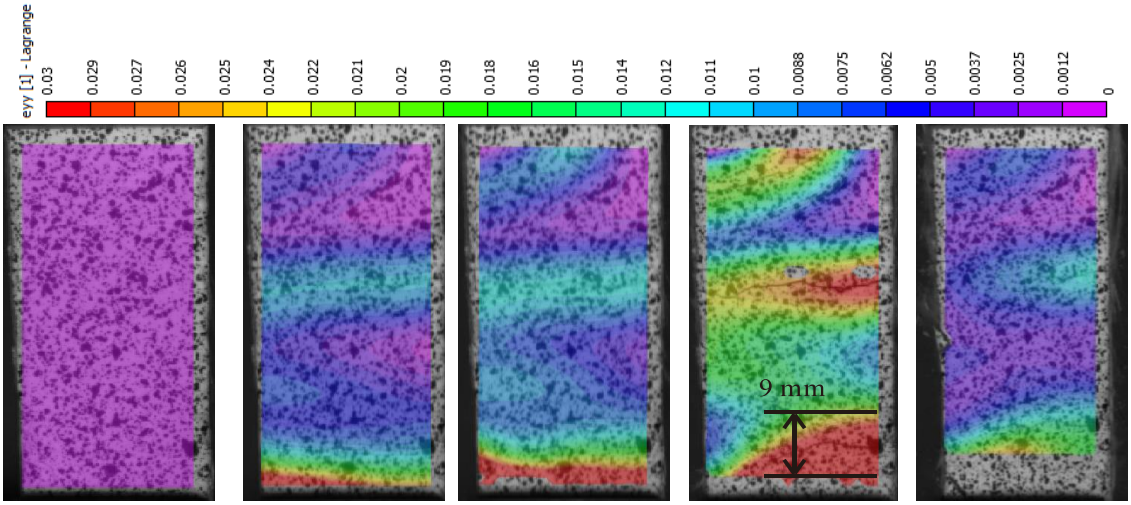

σ_t = 0.0 MPa, A_{slip} = 0%

σ_t = 6.8 MPa, A_{slip} = 5.7%

σ_t = 17.1 MPa, A_{slip} = 9.6%

σ_t = 27.2 MPa, A_{slip} = 50.1%

σ_t = 8.1 MPa, A_{slip} = N/A

(b)

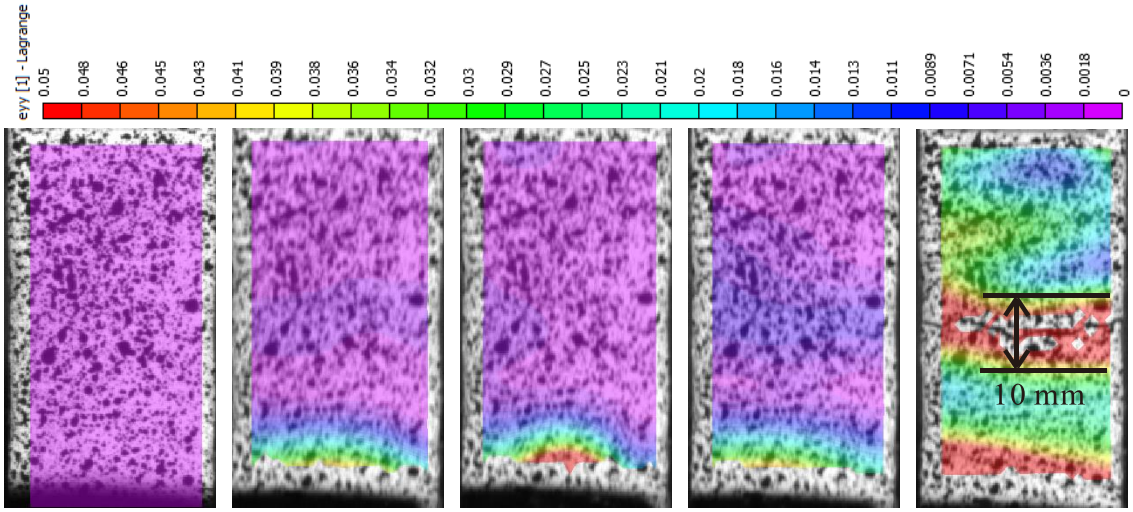

σ_t = 0.0 MPa, A_{slip} = 0%

σ_t = 3.7 MPa, A_{slip} = 2.7%

σ_t = 7.0 MPa, A_{slip} = 3.3%

σ_t = 11.0 MPa, A_{slip} = 3.0%

σ_t = 4.5 MPa, A_{slip} = 43.1%

(c)

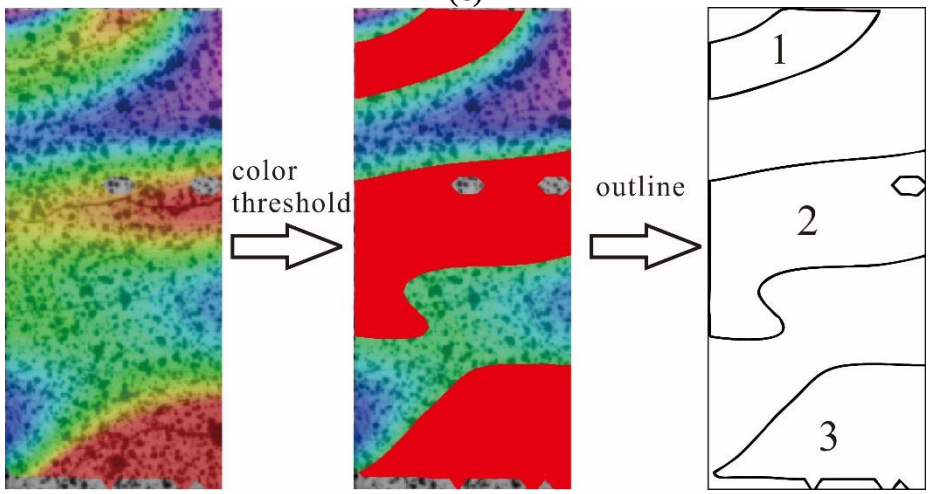

(d)

Figure 2-32 Time Lapsed Images Showing the Development of Strain Field for (a) SG, (b) GL, (c) PP TRCs, and (d) Measurement of Slip Zone Area [46].

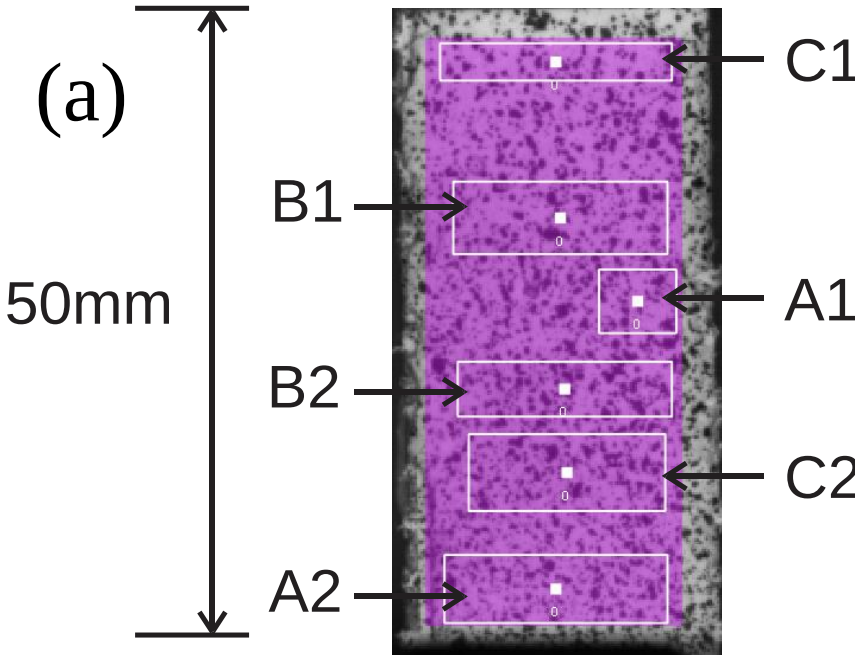
(a)
50mm
B1
B2
A2
C1
A1
C2

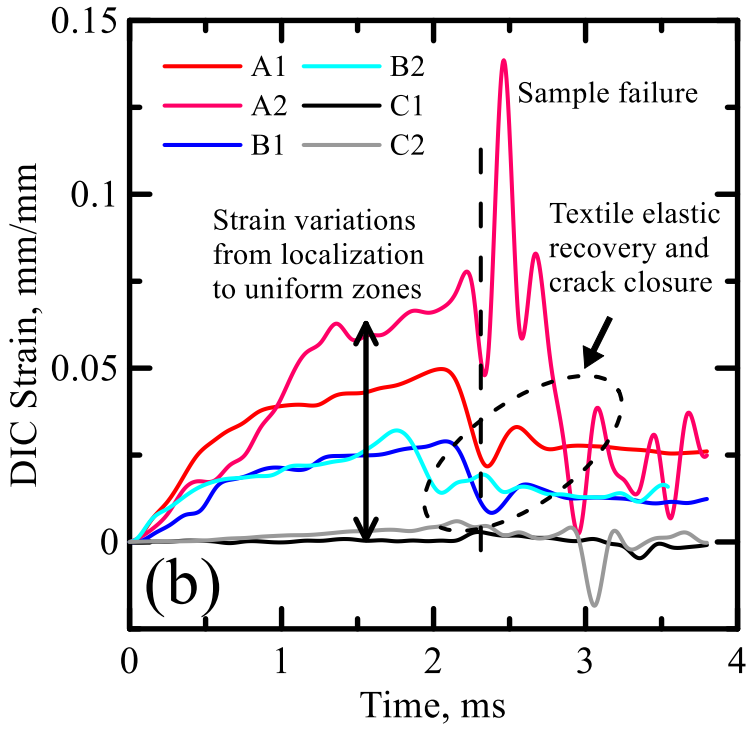
0.15
0.1
0.05
0
DIC Strain, mm/mm
A1
A2
B1
B2
C1
C2
Sample failure
Strain variations
from localization
to uniform zones
Textile elastic
recovery and
crack closure
(b)
0
1
2
3
4
Time, ms

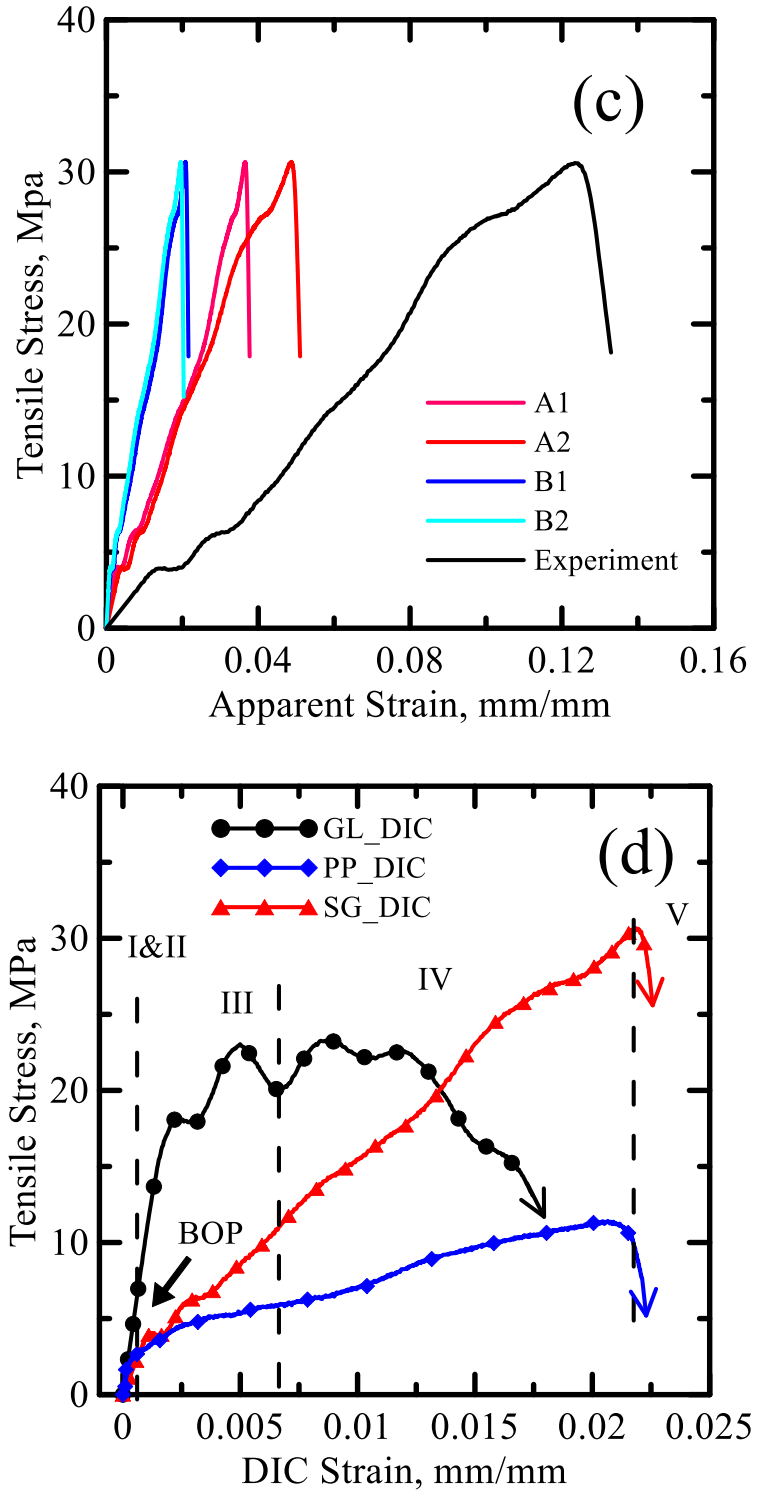

Figure 2-33 (a) Region Selection, (b) Strain Versus Responses of Selected Regions, (c) Comparison Between Image Analysis and Conventional Analysis (d) Representative Stress-Strain Responses of Various Composites Based on DIC Approach [46].

3. TENSION STIFFENING MODEL

3.1 Model Basis

A finite difference method developed by Soranakom and Mobasher [133, 134] was used to simulate the tension hardening behavior in TRC and TRC-ARG specimens. The material model consists of three homogenized phases: matrix, textile, and interface. Since a mean distribution of textile yarns in multiple layers is assumed, the locations of longitudinal yarns were not specified. A tension specimen is idealized as a series of 1-D segments consisting of fiber, matrix, and interface elements with constitutive laws of each phase specified in Figure 3-1(a) including: matrix, longitudinal yarn stress-strain, and interface bond–slip models. The effect of transverse yarns through the mechanical anchorage is represented by a nonlinear spring model. The matrix stress-strain model is linear elastic and specified by its elastic modulus E_m and cracking strength $\sigma_{m,cr}$. Similarly, tension model of textile is characterized by modulus E_f and ultimate tensile strength σ_{ult}. The bond-slip relationship is based on the fiber/textile pull out tests [135, 136] and associated follow up models [137, 138]. The dashed lines indicate the secant modulus k at the slip value s, which is used to compute the force applied at the node. A parameter representing the efficiency of the yarn stiffness ($\eta < 1$) is defined to represent the limitations in bonding which lead to telescopic or sleeve effect [139]. This parameter has been quantified by experiments on sleeve filaments which are partially bonded to matrix and contribute to axial stiffness while the core filaments provide marginal stiffness due to unbonded yarns [140]. Using a uniform strength distribution along the length of specimen and a deterministic sequential crack evolution, the first crack occurs at the center, then at the end grips, followed by 1/4, 1/8 and 1/16 points until crack saturation case is obtained, see Figure 3-1(b).

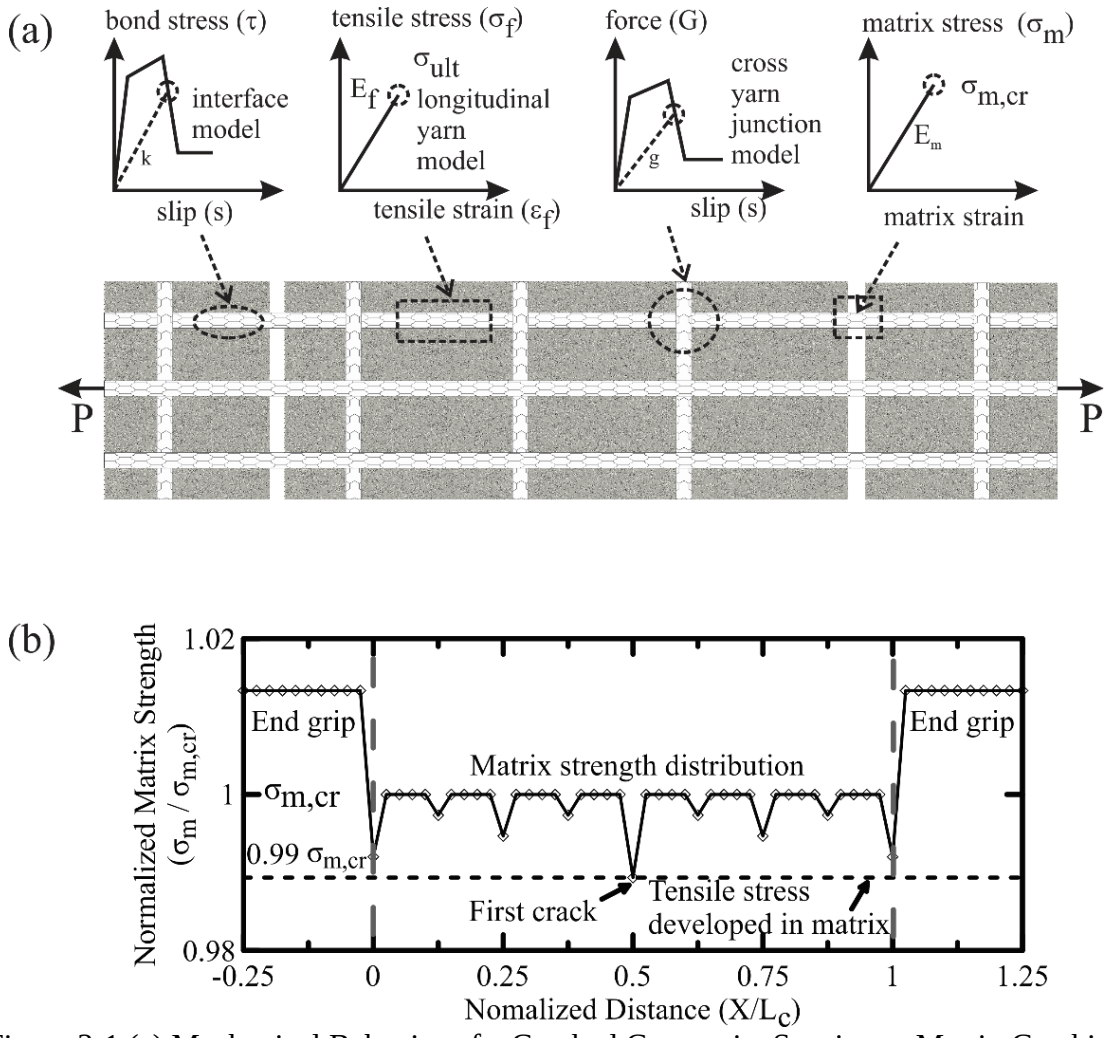

Figure 3-1 (a) Mechanical Behavior of a Cracked Composite Specimen: Matrix Cracking Criterion, Interface Bond–Slip Model, Longitudinal Yarn Tensile Stress–Strain Relationship, Mechanical Anchorage Provided by Cross Yarn Junctions as Nonlinear Spring Model and (b) Deterministic Matrix Strength Distribution and Crack Location [115].

Figure 3-2(a) presents the discretized finite difference model of the cracked specimen with the total embedded length *L* discretized into *N* nodes of equal spacing, *h*. Transverse yarns are simulated by means of springs attached to the nodes at cross yarn junction providing resistance to pullout force. Once cracking takes place, the specimen is divided into smaller segments $L_s^{(1)}$, $L_s^{(2)}$,… $L_s^{(q)}$ with each segment containing $n^{(q)}$ number of local nodes, where

q is the segment index. An additional node is inserted at the crack location such that each cracked segment has its own end nodes and the problem can be solved independently. Free body diagrams of representative nodes are shown in Figure 3-2(b), where s_i = nodal slip, F_i = nodal fiber force, B_i = nodal bond force, G_i = nodal spring force. The equilibrium equations can be derived in terms of the primary unknown variable slip s, defined as the difference between the deformations of the longitudinal yarn with respect to the matrix:

$$s = \int_{x_i}^{x_{i+1}} (\varepsilon_y - \varepsilon_m) dx \qquad \text{Equation 3-1}$$

Where ε_y and ε_m are yarn and matrix strains distributed along the differential length, dx. For typical low fiber volume fraction, the axial stiffness of the yarn $A_f E_f$ is considerably lower than the matrix term $A_m E_m$ and the contribution of matrix elongation to slip is ignored. Thus, the slip s and yarn strain ε_y are simplified to:

$$s = \int_{x_i}^{x_{i+1}} \varepsilon_y dx \quad \text{and} \quad \varepsilon_y = s' = \frac{ds}{dx} \qquad \text{Equation 3-2}$$

Nodal equilibrium equations are constructed and each nodal force is expressed as the product of slip by stiffness. A global system of equations including stiffness matrix [C], nodal slip vector {S}, and force vector {T} was subsequently obtained as follows:

$$[C]_{n,n}\{S\}_n = \{T\}_n \qquad \text{Equation 3-3}$$

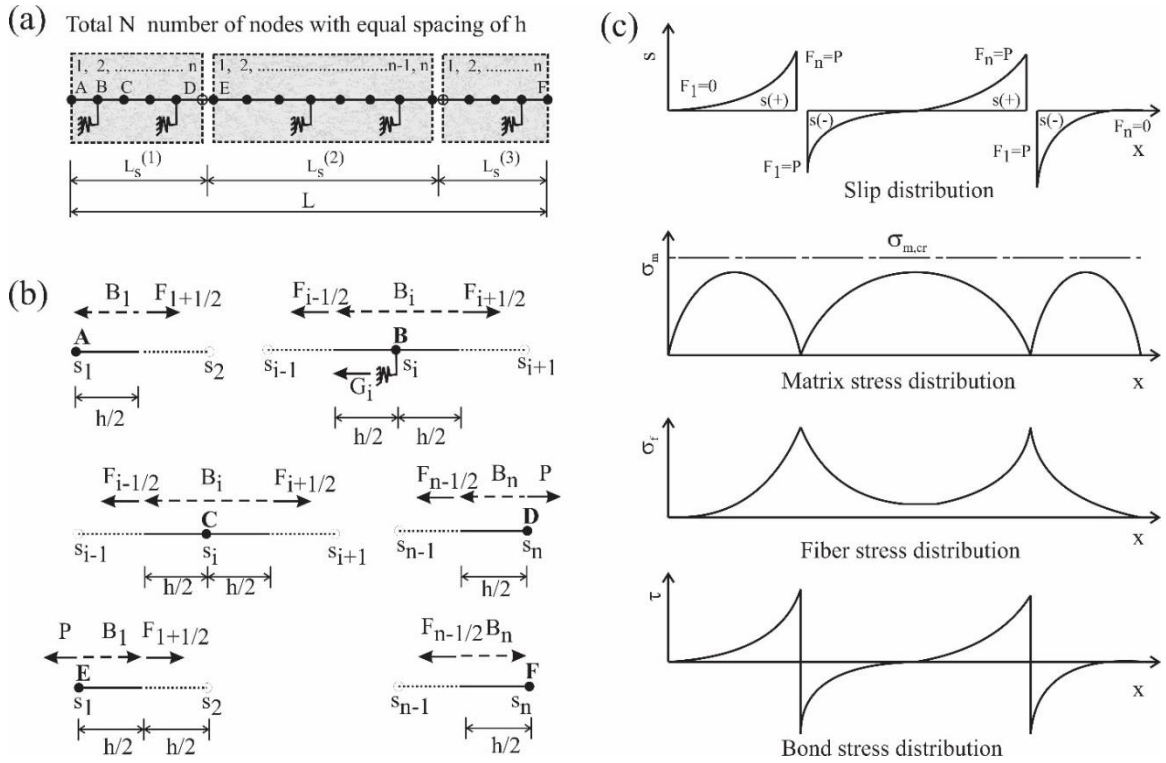

Figure 3-2 Finite Difference Model: (a) Discretized Fabric Pullout Model, (b) Free Body Diagram of Six Representative Nodes Labeled as "A"-"F", (c) Distributions of Slip, Matrix Stress, Fiber Stress and Bond Stress [115].

Once the solution of nodal slip values is obtained, the corresponding stress, strain and crack spacing can be subsequently computed. Set up, assembly, as well as the solution algorithm of equilibrium equations based on several parametric studies were discussed [133,134,141]. Figure 3-2(c) schematically presents the distributions of slip, matrix stress (σ_m), fiber stress (σ_f) and bond stress (τ) in cracked segments. The tension force in both longitudinal yarns and matrix are positive values, while the distribution of the stress in matrix and fiber change in accordance with the placement of cracks. However, the load carrying capacity of matrix in the uncracked segments does not diminish as a sign of tension stiffening effect. The load carried by the fiber is transferred back to matrix and σ_m is maximized at the center line of each cracked segment. As the load increases and σ_m reaches matrix cracking strength $\sigma_{m,cr}$,

new cracks form. Following a shear lag pattern, the bond stress varies from its maximum at the crack to a value of zero at bonded region.

3.2 Application in Tensile Behaviors

3.2.1 Effects of Different Textiles

The model parameters used to simulate the experimental stress-strain and crack spacing responses include: Young's modulus and first cracking strength of matrix E_m = 30 GPa, $\sigma_{m,cr}$ = 4 MPa, Young's modulus and tensile strength for glass fiber $E_{f,GL}$ = 78 GPa, $\sigma f_{u,GL}$ = 1360 MPa and for polypropylene fiber $E_{f,PP}$ = 6.9 GPa, $\sigma f_{u,PP}$ = 500 MPa, efficiency factor η = 0.45. The bond-slip relationship is based on the fiber/textile pull-out tests [135,136] and associated follow up models [138]. A base level bond-slip model shown in Figure 3-3(a) with an initial stiffness of 5.33 MPa/mm and the bond strength of 2.8 MPa was used for parametric study. Figure 3-3(b) shows the varying simulated composite tensile stress-strain and crack spacing-strain responses where increases in the postcrack stiffness and decreases in final crack spacing were observed as the bond strength increased from 1 to 3 times of the base level. Higher bond strength increases the load carrying capacity of intact matrix segments but decreases the interfacial slip. This reduces the composite tensile strain at equivalent loading level and represented as a higher postcrack stiffness. On the other hand, steeper slope and higher bond strength of the bond–slip relationship proportionally increases the force transfer rate (Force/Length) to the matrix. As a result, the development length to achieve the cracking strength is reduced and a finer crack pattern with smaller final crack spacing can be obtained.

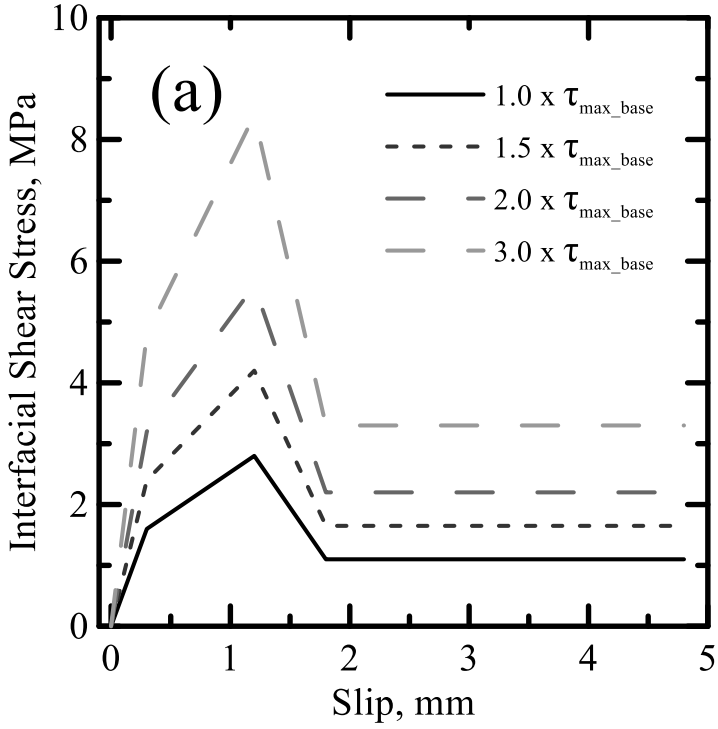
(a)
1.0 x τmax_base
1.5 x τmax_base
2.0 x τmax_base
3.0 x τmax_base
Interfacial Shear Stress, MPa
Slip, mm
0
2
4
6
8
10
0
1
2
3
4
5

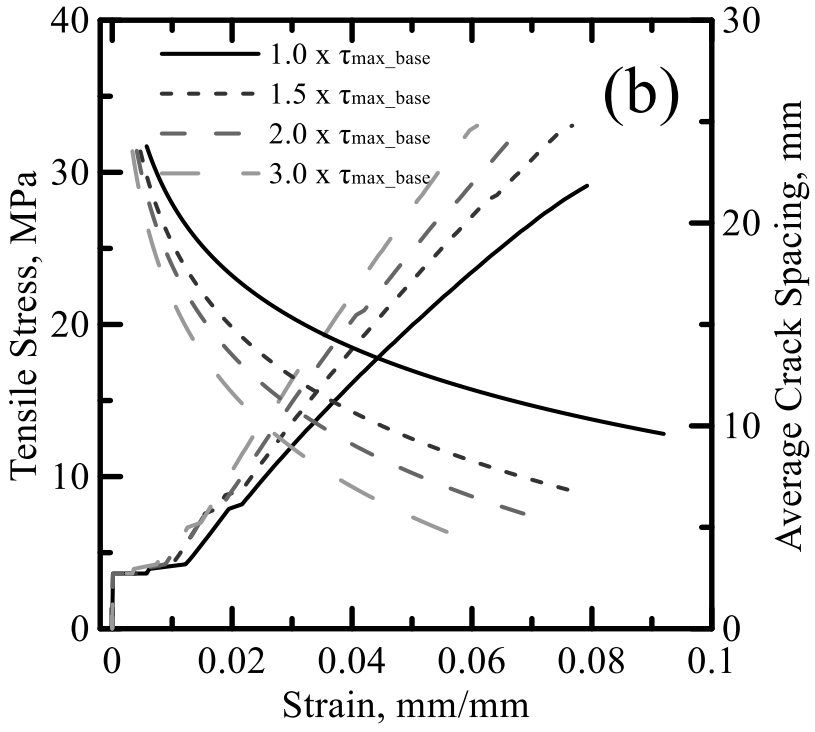
(b)
1.0 x τmax_base
1.5 x τmax_base
2.0 x τmax_base
3.0 x τmax_base
Tensile Stress, MPa
Average Crack Spacing, mm
Strain, mm/mm
0
10
20
30
40
0
10
20
30
0
0.02
0.04
0.06
0.08
0.1

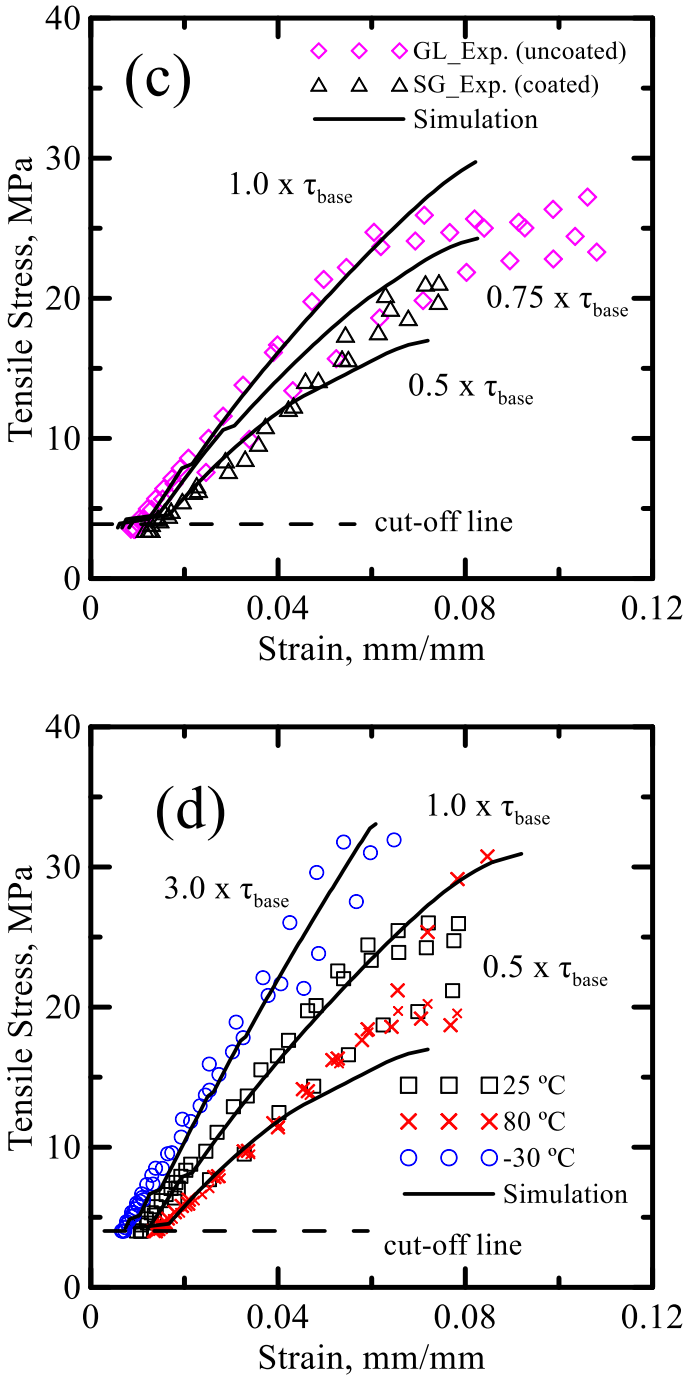

Figure 3-3 (a) Interfacial Bond Model Used in Tension Stiffening, (b) Effect of Bond Strength on Postcrack Tensile Responses and Average Crack Spacing, (c) Experimental and Numerical Tensile Stress-Strain Response of GL and SG-TRCs at Room Temperature, (d) Experimental and Numerical Tensile Stress-Strain Response of GL-TRCs Under Different Temperatures [46].

Figure 3-3(c) shows that as the bond strength increased from 50% to the full base level, simulated stress-strain responses covered the range of experimental data for GL- (high stiffness) and SG-TRCs (low stiffness) at room temperature. As previously discussed, the slope of initial experimental response was fairly low due to the spurious displacement so that only postcrack responses were compared to the simulated responses. This is indicated by a cut-off line, and as predicted by finite difference model, the lower postcrack stiffness of SG-TRC may be caused by the lower bonding strength due coating. This effect was less pronounced at high and low temperatures. It was also observed that the postcrack stiffness reduced as the temperature increased from -30°C to 80°C. Such a temperature dependence of postcrack stiffness was captured by finite difference model as shown in Figure 3-3(d) where bond strength increased from 0.5 to 3 times of base level. Correlation of experiment and simulation indicated higher interfacial bond strength of TRC at low temperature.

Simulations of the experimental responses for all three TRC systems tested at room temperature and the used bond-slip models are presented in Figure 3-4. The finite difference model was able to accurately predict the stress-strain responses of various TRC specimens up to failure as shown in Figure 3-4(b). A lower value of postcrack stiffness of PP-TRC can be traced back to the low tensile stiffness of polypropylene yarns. The crack spacing was measured from the high speed images taken at room temperature. The smallest average crack spacing was observed for PP-TRC, while SG-TRC exhibited the largest crack spacing, see Figure 3-4(c). The crack spacing responses agree with the crack patterns of different TRC samples shown in Figure 2-25(d) and DIC observations. The failure pattern of SG- and GL-TRC specimens was characterized by significant fiber pull-out while PP-TRC was subjected to fiber fracture due to the low tensile strength of

polypropylene. Even though the tensile strength and stiffness of PP-TRC were lower than the other two systems investigated, the strain capacity of polypropylene yarns demonstrated an efficient bond with cement matrix as indicated by the finer crack pattern using the bond-slip models shown in Figure 3-4(a).

High-strain rate tensile tests (100 s^{-1}) were performed for three types of textiles and TRC systems under three different temperatures of -30, 25, and 80 °C. Distributed cracking and tension stiffening effect were observed for all three TRC systems indicating efficient stress transfer mechanism. The following conclusions can be drawn from the present work:

The highest tensile strength of 38.1 MPa and work-to-fracture of 46.6 J were observed in the GL-TRC specimens at -30 °C. Composites with strength ranging from 10.8 to 14.3 MPa under varying temperatures were obtained from PP-TRCs. Tensile strength decreased with increasing temperature for the GL-TRC, from 38.1 MPa at -30 °C to 23.4 MPa at 80 °C. Similarly, the highest tensile strength of 30 MPa and 14.3 MPa for SG- and PP-TRC specimens were obtained at -30 °C, while the effect of elevated temperature was less pronounced. A descending trend in postcrack stiffness for various TRCs with increasing temperature was observed. The postcrack stiffness of GL-TRC was found to be the highest (459.7 MPa) followed by SG (354.5 MPa) and PP (199.2 MPa) at room temperature.

The digital image correlation (DIC) method is a powerful tool to address the complex and nonhomogeneous deformations in TRC systems. Non-uniform distribution of longitudinal strain was observed in contrast with the assumption of conventional data analysis, and three zones of localization, shear lag, and uniform strain were documented based on the shear lag theory. The variations in longitudinal strain values among different zones were captured by quantifying the strain behaviors. Maximum strain in localization zone was more than

twice of that in shear lag zone, while the uniform strain term was insignificant compared to other zones. Measurements of the size and length of the slip zones based on image analysis approach was proposed as an indication of the textile pull-out and sliding region which contributes to frictional energy dissipation. Larger slip zones measured from GL- and SG-TRC specimens were correlated with longer pull-out regions. The DIC method enabled an indirect measurement of the internal load transfer between the textile and matrix. The tension stiffening model accurately simulated the crack spacing and stress-strain behaviors of the TRC under high speed loading conditions. Higher postcrack stiffness of GL-TRC specimens compared to SG-TRC at room temperature was predicted by increasing the bond strength of the bond-slip model. The effect of temperature on the interface properties was simulated by the temperature dependence of the model parameters of bond properties. Additionally, the bond-slip models used to simulate various TRC specimens indicated more efficient bond characteristics of polypropylene yarns to matrix which greed with the observations of finer crack patterns in PP-TRC.

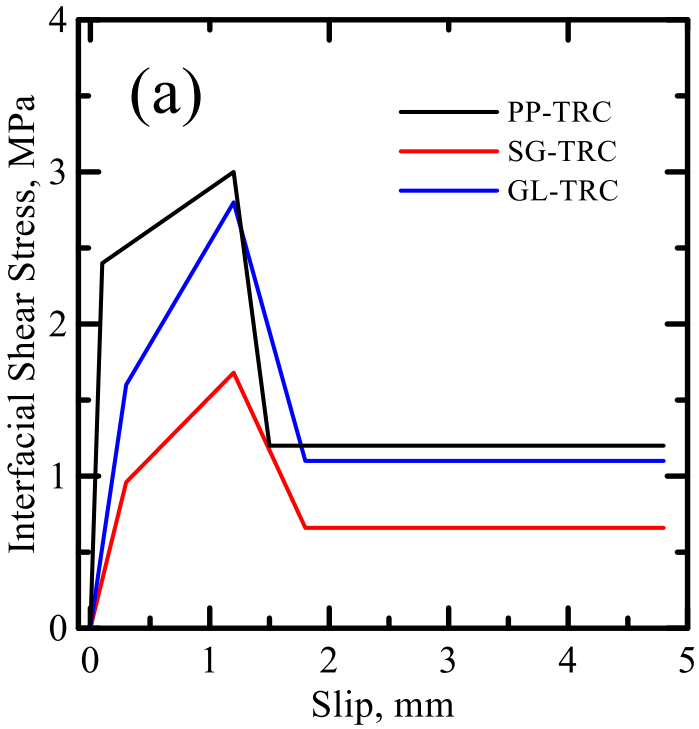
(a)
PP-TRC
SG-TRC
GL-TRC
Interfacial Shear Stress, MPa
Slip, mm
0
1
2
3
4
5

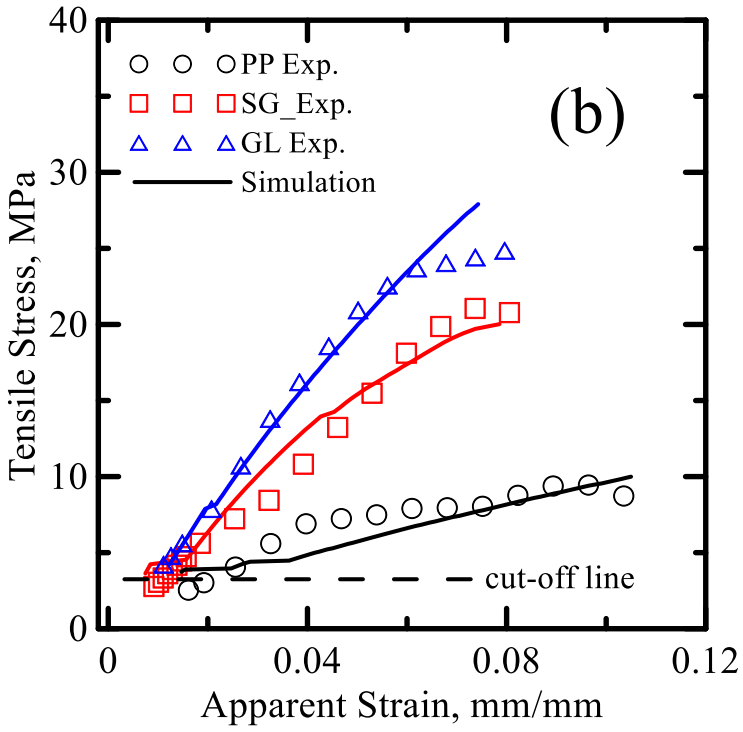
(b)
PP Exp.
SG_Exp.
GL Exp.
Simulation
cut-off line
Tensile Stress, MPa
Apparent Strain, mm/mm
0
10
20
30
40
0.04
0.08
0.12

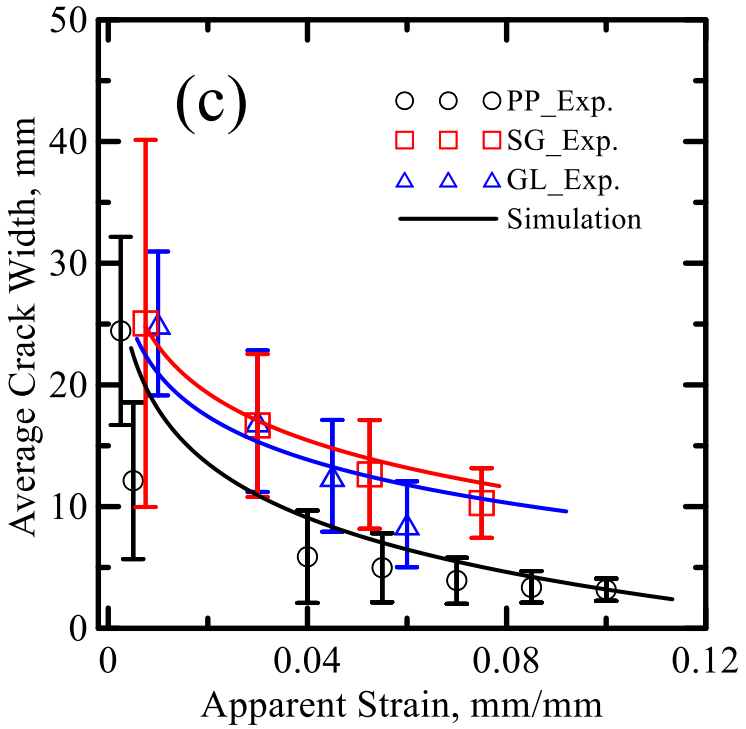

Figure 3-4 (a) Interfacial Bond-Slip Models, Simulations of (b) Tensile Stress-Strain and (c) Average Crack Spacing-Strain Responses for Three TRC Systems [46].

3.2.2 Effects of Short Fibers

The model was used to simulate the experimental stress-strain and crack spacing responses with the following material parameters: E_m = 30 GPa, $\sigma_{m,cr}$ = 3 MPa, E_f = 70 GPa, σ_{ult} = 2000 MPa, η = 0.7. Nonlinear bond and spring models are shown in Figure 3-5. The required maximum bond strength τ_{max} used for simulation of the TRC-ARG specimens is twice as that of TRC. As shown in Figure 3-6(a) and (b), the finite difference model accurately predicted the experimental stress-strain and crack spacing-strain responses of the specimens tested at 100 s^{-1}. The higher simulated post-cracking stiffness and lower final crack spacing are attributed to higher bond strengths. Figure 3-6(c) compares the mean and standard deviations of experimentally measured final crack spacing values of all the samples at different strain rates by means of the error bar, where the effect of short fibers

on the reduction of the final crack spacing at all strain rates is clearly evident. Strain rate effects on crack spacing is evident for the TRC samples, while only a marginal sensitivity is observed for TRC-ARG. This could lead to a simplifying assumption to uncouple and specify a strain rate independent final crack spacing. Parametric studies showed that as τ_{max} increases from 2 to 8 MPa (with all other model parameters held constants), the simulated final crack spacing decreased from 12.5 mm to 6.25 mm, as indicated by horizontal lines. In the finite difference model, higher bond stiffness or a steeper slope of the bond–slip model proportionally increases the force transfer rate to the matrix, thus the development length is reduced and a finer crack pattern is obtained. This agrees well with the previous discussions in this paper on the role of short fibers.

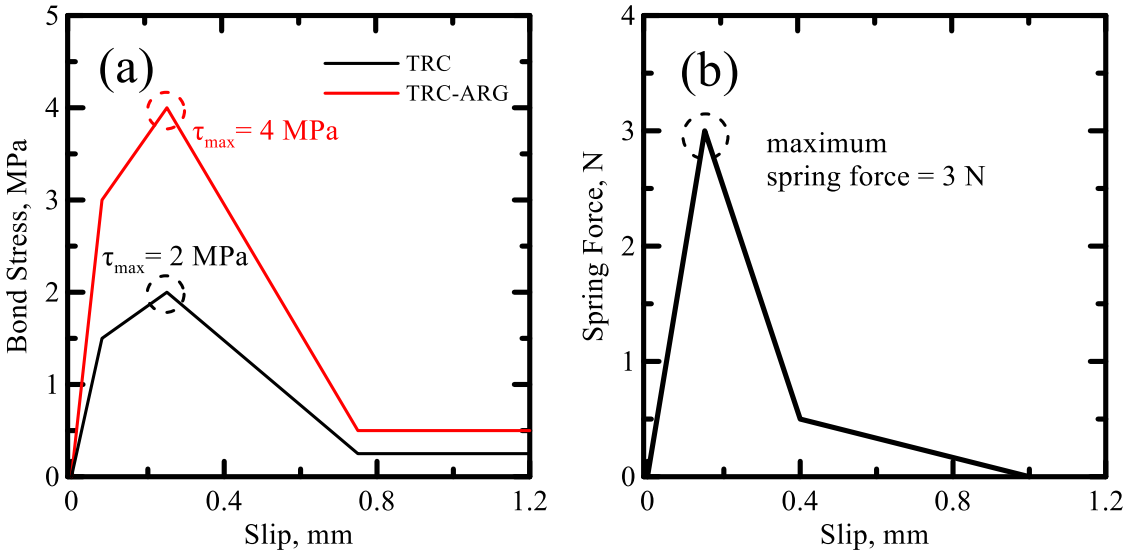

Figure 3-5 Material Models for the Simulation of Experimental Results: (A) Bond-Slip Model, (B) Nonlinear Spring Model (Identical for Both TRC and TRC-ARG Specimens) [115].

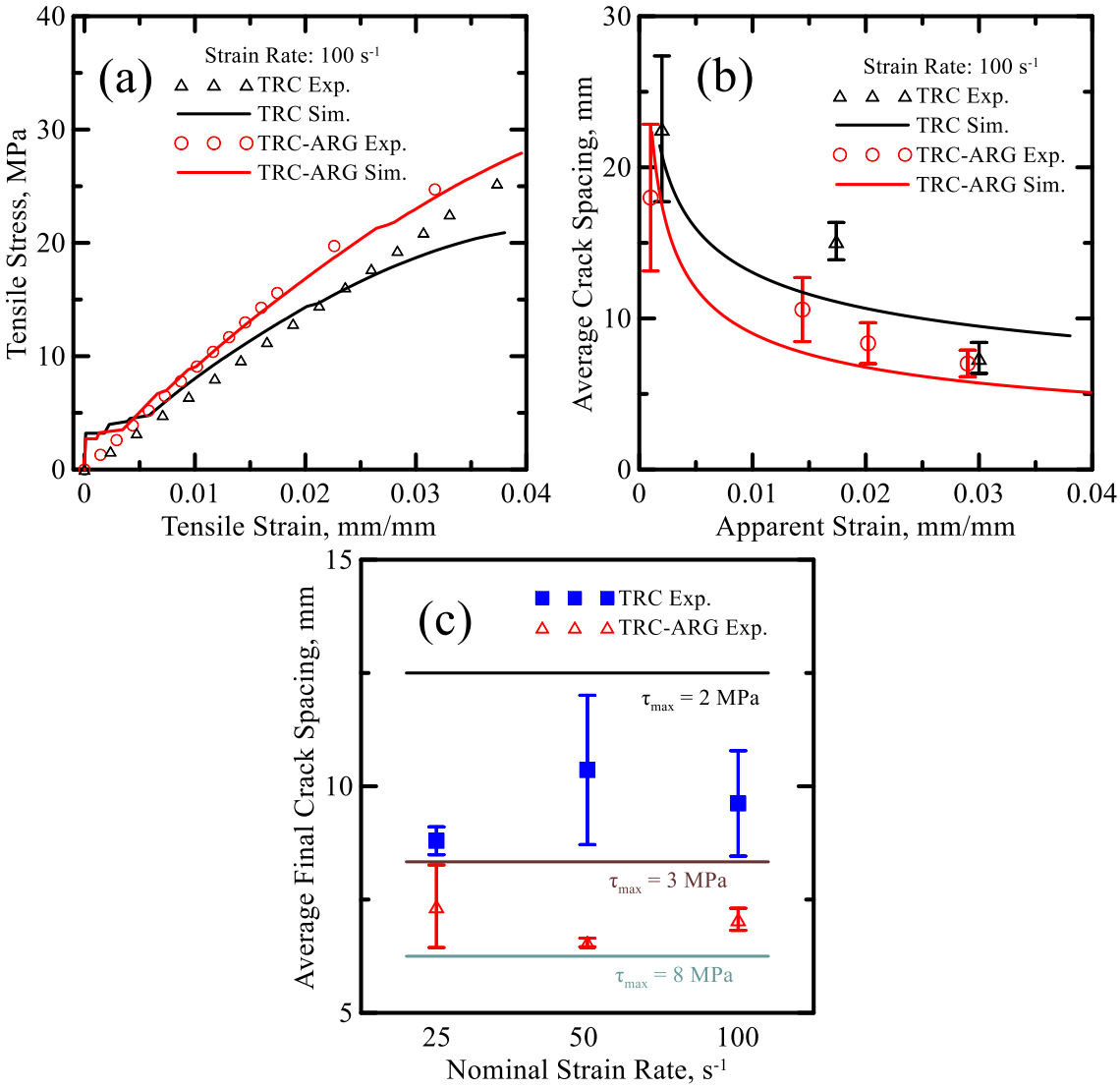

Figure 3-6 Comparison of Experimental and Numerical (A) Tensile Stress-Strain Responses and (b) Crack Spacing for TRC and TRC-ARG Specimens Tested at 100 s^{-1}, (C) Parametric Study on the Influence of Bond Strength on Final Crack Spacing With a Summary of All the Experimental Measurements [115].

High speed tests of four types of TRC specimens at three nominal strain rates of 25 s^{-1}, 50 s^{-1}, and 100 s^{-1} were conducted using a high rate servo-hydraulic testing machine and the crack distribution parameters based on digital image correlation (DIC) method were measured. Results indicate an increase in tensile strength and decrease in work-to-fracture with rising strain rate for the TRC specimens. Finer crack patterns were observed with

addition of short fibers at all strain rates which is attributed to the role of short fibers in bridging the micro-cracks and enhancing load transfer. Crack width evolution measured by DIC method was correlated with experimental stress response and a pronounced strain hardening effect was observed. The addition of short fibers reduced the crack width and improved post-cracking stiffness.

The DIC measurements of the complex strain fields represented a non-uniform distribution of longitudinal strain consisting of three main zones: localization, shear lag and uniform strain. The strain behavior in each zone was addressed by means of three competing models: stress-crack width, bond stress-slip, and composite stress-strain relationships. These models were eventually used as the damage criteria for the finite difference model.

Localization zone width (h_L) and saturated crack spacing (s) as important parameters for modelling of FRC materials were directly measured using DIC method. Both these measures decreased with the addition of short fibers, indicating the improvement in bond characteristics. The finite difference model accurately predicted the crack spacing and stress-strain behaviors by addressing distributed damage in TRC systems. The parametric study showed that the final crack spacing was reduced by increasing the interfacial bonding stresses confirming the role of short fibers which agreed well with experimental and DIC investigations.

3.3 Application in Sequential Cracking Caused by Drying Shrinkage

Steel fibers have been used as the primary reinforcement in concrete slabs on grade for more than four decades. Since the early stage applications, a better control of the opening of the sawn joints with addition of steel fibers have been observed. The horizontal and vertical movements at the shrinkage relieving joints can result in serviceability issues due

to failure at the joint including joint edge chipping, uplift, and corner flexural cracks. Omitting the shrinkage joints to obtain a joint free floor, is then very advantageous and durable. While it is understood that cracking will not be eliminated, crack width can be sufficiently reduced by the fibers such that a non-critical pattern of controlled and distributed cracks is obtained. The parameters influencing these responses are discussed and a predictive model for crack opening calculation is presented [142].

3.3.1 Parameters Affecting the Drying Shrinkage Cracking

The slab geometry, boundary conditions, steps in sequential cracking and uplift due to restrained drying shrinkage are illustrated in Figure 3-7. Evaporation from the surface imposes a non-uniform shrinkage strain which in the presence of restraint, causes tensile stresses and cracking [143]. A deterministic pattern of sequential cracking in Figure 3-7(a) initiates with the first crack in the center of slab, followed by cracks that reduce the slab length into halves, as shown in Figure 3-7(b). The uplift of the slab at the corner joint, also referred to as the curling is modelled as the tip deflection of a cantilever beam, see Figure 3-7(c). The main parameters affecting drying shrinkage are placed into three categories: 1) concrete matrix properties such as the internal porosity, moisture content, potential free shrinkage strain, tensile cracking strength; 2) internal cracking restraint due to the addition of fibers, modelled as a stress-crack width relationship; 3) slab geometry and external boundary conditions in terms of evaporation rate, degree of restraint due to the base friction. Interaction of these aspects are discussed in the following sections.

In addition, ground settlement or swelling also changes the boundary conditions of a slab and contribute to cracking but are not considered here. Construction related issues such as transportation, installation, and finishing of the slab can also adversely affect the drying

shrinkage rate. Excessive concrete temperatures, long duration hauls in transit mixer, addition of water on site, failure to protect the slab from wind may affect the initial stages are also problematic but not addressed directly. A successful joint free floor needs the minimum contraction and restraint along the edges, around columns, or re-entrant corners. The effect of these parameters are discussed under the assumption that sufficient care has been exercised to alleviate the known potential stress concentration areas and the slab is analyzed and built following a simplified 1-D state of stress using the state of the art procedures.

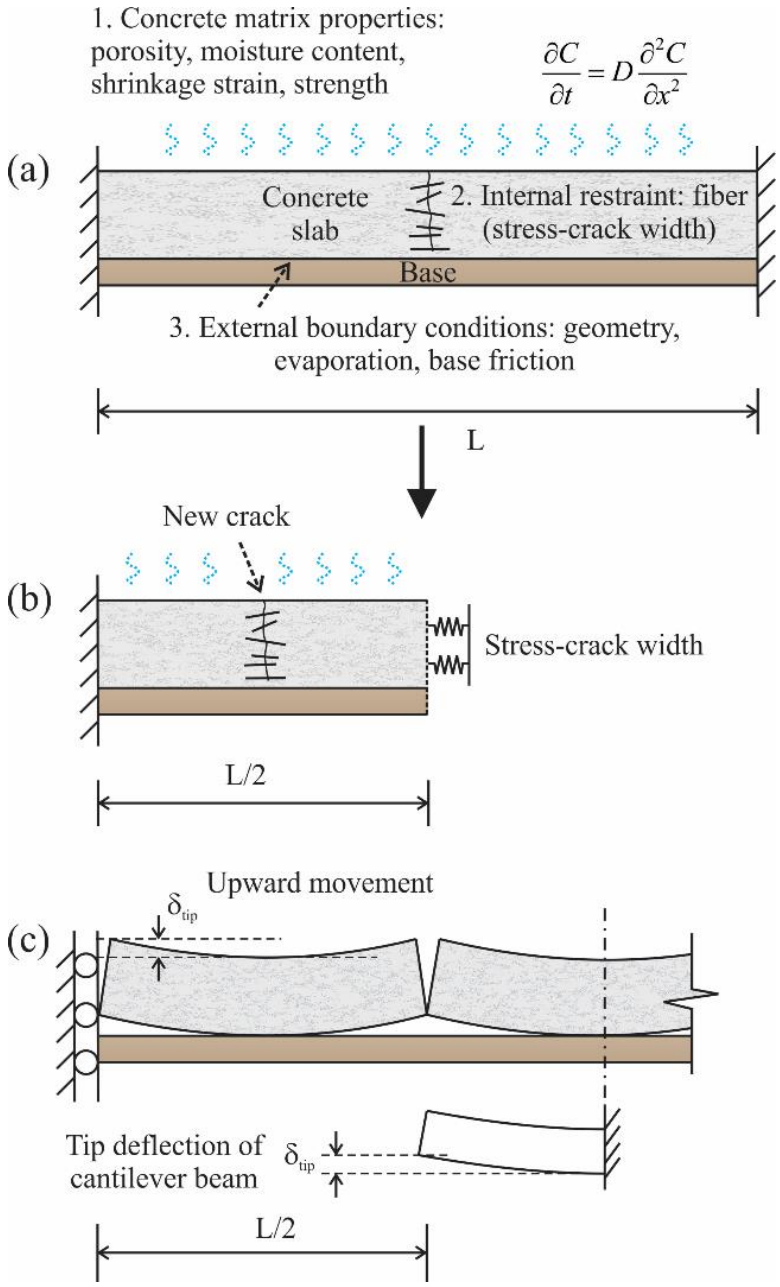

Figure 3-7 Schematic Presentation of Sequential Cracking in the Slab on Grade Due to Drying Shrinkage: (a) Three Main Aspects Affecting Cracking Behavior; (b) Sequential Formation of Cracks and Horizontally Crack Opening; (c) Slab Curling at Joint/Crack [142].

Primary parameters that adversely affect drying shrinkage include: water content, high mortar content, cement with high shrinkage characteristics, and admixtures [144]. Aggregate related issues associated with dirty, or poor shrinkage quality are not addressed. Excessive water content increases the porosity and the rate of moisture loss as the main contributor to shrinkage potential [145]. Addition of high range water reducing admixtures (HRWRA) or superplasticizer may increase the shrinkage especially when the water content is not reduced correspondingly. Low aggregate content, a low coarse/fine ratio, dirty aggregates, may increase the water demand and increase shrinkage. Aggregates with low stiffness also increase the shrinkage. While the effect of aggregates quality and content on the shrinkage is well accepted, in the present study in order to minimize the number of variables, free shrinkage strain is directly used as an input to the model which inherently takes into account the contribution of the aggregate type and content.

It is assumed that the effect of cement type is secondary as the rate of hydration and the particle size affect the pore structure development with time. Hence plastic shrinkage is likely to be more influenced than ultimate shrinkage. The cement content is also not discussed as a primary parameter since it generally ranges between 300 and 350 kg/m^3 of CEM-type I depending on the floor type and installation. The concrete strength is in the range of C25-30 or C30-37 correspondingly. Effect of air content for the interior applications is assumed to be a secondary factor as well.

Mixtures with low *W/C* ratios are not practical for installation, compaction, and finishing for a typical slab in an enclosed building where paving machines are not accessible. The use of HRWRA is necessary to meet the requirement of minimum fluidity and reduce the water content to limit the overall shrinkage. In the empirical model, the combined effect of

water content and HRWRA is introduced as a single factor. The effect of HRWRA when the water content is not reduced is introduced using coefficient λ that ranges from 1.05-1.35 as a function of $0.45 < W/C < 0.65$ and represented as a linear response:

$$\lambda = 1.75\frac{W}{C} + 0.2125 \qquad \text{Equation 3-4}$$

It is well known that fibers reduce the free shrinkage contraction and delay the associated cracking [146]. Randomly distributed-closely spaced fibers significantly extend the micro-cracking stage before a visible surface crack is observed by means of bridging the microcracks and resisting their growth into macrocracks [147,148,149]. Important fiber parameters include the aspect ratio, shape, and the volume fraction [150], which influence the fiber-matrix bond and the stress-crack width relationship. Measurements of maximum crack width show an inverse correlation with the product of fiber concentration and aspect ratio [151]. Bakhshi and Mobasher [152] developed a test method to characterize the evaporation parameters and simulating the sequential cracking in cement paste. Role of fibers in reducing both crack width and area was confirmed by the image analysis technique and analytical model [153].

In order to account for the fiber shape and anchoring, Mangat and Azari [146] defined a parameter for different fiber geometries as μ_m, which is assigned as 0.04 for straight, 0.08 for hooked, and 0.12 for undulated steel fibers. The μ_m influence is integrated in the formulation but the amplitude of variation does not mean that undulated fibers perform as much as three times better than hooked fibers to control the cracking.

The degree of base frictional restraint varies significantly with different slab weight and friction coefficient which represents the interlock mechanism to a significant extent. The

frictions restrict the slab from floating freely so that the slab and its base are considered as two bonded layers resisting the stresses depending on stiffness. The higher is the stiffness of the grade against frictional sliding, the more restraint is provided. It is observed from field trials that the crack opening of a joint free floor tends to be less when the support has a higher stiffness or interlock value.

Table 3-1 Interface Coefficient of Friction Values μ_s [142] (Data Compiled From Chia et. al [154], Lee [155] and Maitra et. al [156])

Base course	Number	Category	μ_s
Stott [157]			
Smooth mortar	1		0.3
Crushed limestone	2		0.4
Friberg [158]			
Sand-loam with paper	3	Fine aggregates	1.5
Chia et. al [154]			
Sand-mix asphalt with single layer of polyethylene sheet	4		0.9
Sand-mix asphalt with double layer of polyethylene sheet	5		0.5
Lee [155]			
Sand and gravel	6	Coarse aggregates	1.1
Graded broken stone	7		1.3
Sparkes [159]			
DLC with polythene sheet	8		1.2
Clinker with waterproof paper	9	Cement/concrete	1.9
Suh et al. [160]			
Clinker	10		3.2
Venkatasubramanian [161]			
WBM with tar paper	11	WBM	2.4
Saturated WBM	12		7.8

Note:
WBM = water bound macadam.
DLC = dry lean concrete.

While the estimation and/or measurement of frictional forces are difficult to attain, the friction coefficient is empirically related to the modulus of subgrade reaction *k* in this paper. The recorded settlement is back-calculated according to both theories of Westergaard elastic base and Boussinesq's *E* modulus. Using the test method *E*, testing disk radius *R*, and the Poisson coefficient υ of the grade, *k* is calculated as [162]:

$$\beta = \frac{\pi R}{2(1-\upsilon_G{}^2)} \qquad k = \frac{E_G}{\beta} \qquad \text{Equation 3-5}$$

The correlation of the slab restraint parameter, μ_s as a function of modulus *k* is proposed as:

$$\mu_s = \alpha + Ln(k) \qquad \text{Equation 3-6}$$

The constant α needs to be calibrated to accommodate varying base conditions. Chia et. al [154] carried out push-off tests to evaluate the friction coefficient between concrete pavement slab and base under multiple conditions. Lee [155] proposed a model to determine the friction of concrete slab on different base materials. Maitra et. al [156] provided a summary of the coefficient values reported by different researchers. Experimentally measured and simulated friction coefficients covering varying slab and base materials as well as interface conditions are summarized in Table 3-1. Equation 3-6 is plotted with varying α of 1.0, 3.0 and 6.0 against these values, as shown in Figure 3-8. It is observed that the computed μ_s values cover most of the experimental results which vary widely from 0.3 to 7.8 for different base courses. After calibrating the empirical model with the finite difference model and field measurements, α = 1.35 is selected in this specific study.

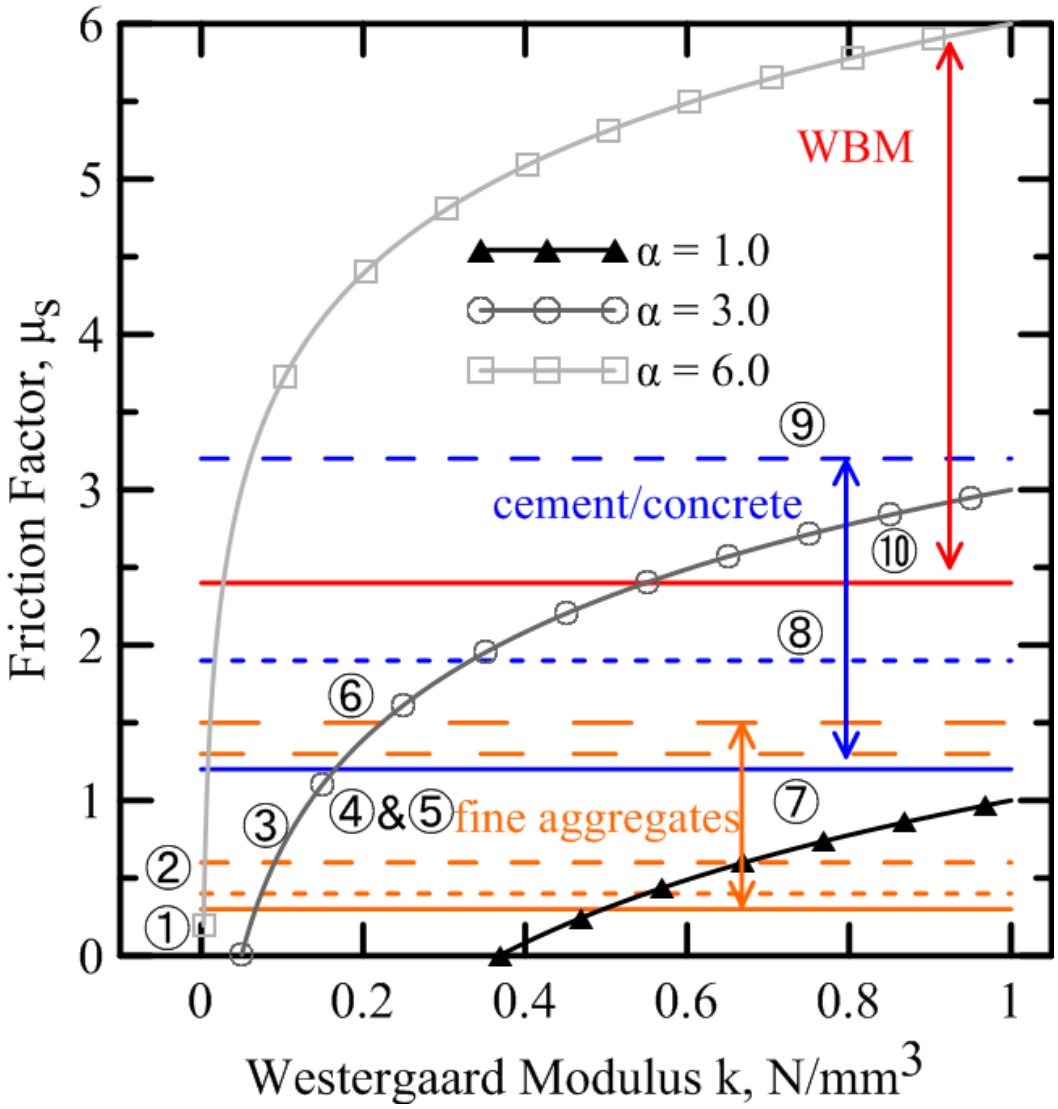

Figure 3-8 Comparison of Coefficient of Friction Values Between the Proposed Equation and Measured Results (Saturated WBM Is Not Shown in This Figure) [142].

3.3.2 Empirical Crack Opening Model

Based on the discussion of different parameters, the following empirical expression is proposed for the prediction of the crack opening ω in mm of a SFRC joint free slab:

$$\omega = \frac{L\lambda\varepsilon_R}{\frac{V_f L_f}{d}\mu_s(1+\mu_m)^{2.5}}$$ Equation 3-7

Where L is the length of the original slab in mm. However as a single crack forms in the slab, in order to simulate the formation of additional cracks, the length between the existing crack and slab end can be considered as a new overall length and the model applied all over again. The parameter ε_R, representing the tensile strain, changes from $2x10^{-4}$ to $5x10^{-4}$ as the W/C ranges from 0.50 to 0.65. High *W/C* indicates an increased amount of free water and capillary porosity as the source of the drying shrinkage. The strain can be expressed in terms of *W/C* as follows:

$$\varepsilon_R = (20\frac{W}{C} - 8)\times 10^{-4}$$ Equation 3-8

The coefficient μ_m varies from 0.04 for straight to 0.08 for hooked and to 0.12 for undulated fibers as discussed earlier. The relationship of fiber volume content V_f and weight fraction is expressed such that a fiber dosage rate W_f of 25-50 kg/m³ corresponds to V_f of 0.32-0.60%:

$$V_f = 0.012786\, W_f$$ Equation 3-9

The parametric study, comparison with finite difference model and simulation of field measurements are performed in the following sections.

3.3.3 Finite Difference Based Tension Stiffening Model

In order to further calibrate and verify the applicability of empirical equation, a numerical model addressing the tension stiffening using finite difference method (F-D model) developed by Soranakom and Mobasher [133] was used. The approach simulated the

sequential formation of multiple cracks and opening responses due to shrinkage. Figure 3-9 presents a schematic drawing of a model slab with the parameters that define three distinct mechanisms governing the cracking behavior: (1) matrix cracking criterion, (2) frictional force at the base, (3) the combination of fiber stiffness and interface bond–slip characteristics, in accordance with the three primary aspects affecting drying shrinkage discussed previously.

The tensile stress-strain model of matrix is governed by the elastic modulus of matrix E_m, and its cracking strength at $\sigma_{m,cr}$, as shown in Figure 3-9(a). The base friction is defined in terms of equivalent distributed nonlinear springs providing the resistance force as a function of slip [138], which can be related to the coefficient of friction μ_s. The modelled fiber and matrix interactions include a linear bond-slip response in crack free stage or segment and a stress-crack width relationship at crack. The stress-crack width relationship essentially correlates with the post peak responses of bond-slip model as the crack width is proportional to the interfacial slip and the bridging stress can be converted to bond stress by means of equilibrium condition [163, 164, 165]. A complete bond-slip model including linear and nonlinear branches is therefore employed to address both situations (Figure 3-9(c)).

A cracked slab under tension is idealized as a series of segments and the slab length L is discretized into N nodes with nonlinear springs attached, see Figure 3-9(e). When the tensile stress in the matrix reaches $\sigma_{m,cr}$, a cracking process starts taking place. The specimen is divided into smaller segments $L_s^{(1)}, L_s^{(2)}, \ldots L_s^{(q)}$ and each contains $n(q)$ number of local nodes, where q is the segment index. An additional node is inserted at the crack

location such that each cracked segment has its own end nodes and the problem can be solved independently.

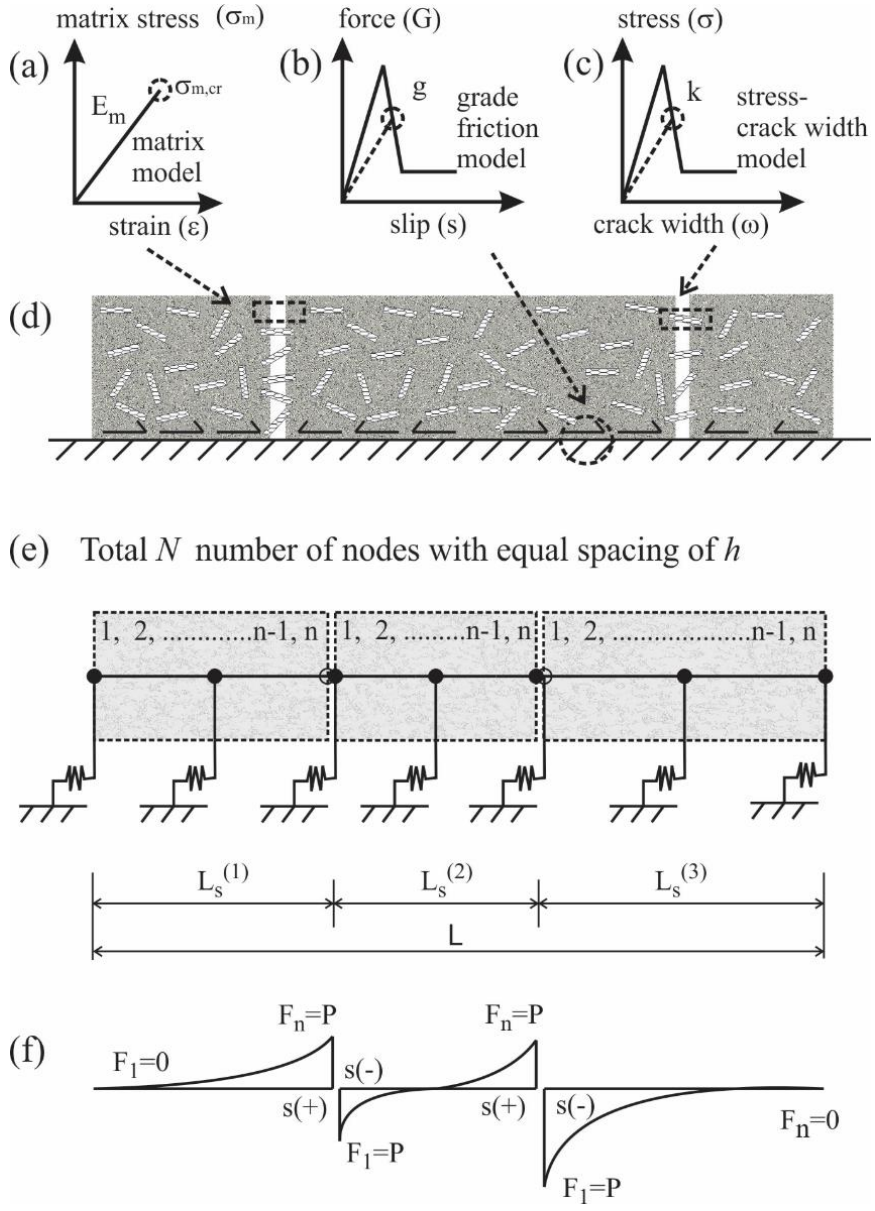

Figure 3-9 Mechanical Behavior and Finite Difference Model of Cracked Fiber Reinforced Cement Composite: (a) Matrix Strength for Cracking Criterion, (b) Nonlinear Spring Model Simulating the Frictional Force, (c) Stress-Crack Width Model, and (d) Cracked Cement Composite, (e) Arrangement of Nodes and Springs, (f) Distribution of the Slip on Cracked Specimens [142].

Figure 3-9(f) shows slip distribution in cracked segments with a positive slip for sliding to the right and negative to the left. The directions of bond stress and spring force follow the sign convention of slip. Further details of construction and assembling of equilibrium equations and solution strategy can be found in the original work [141]. Once the slip distributions are solved, corresponding stress, strain, crack width and crack spacing responses can be subsequently obtained.

Figure 3-10 presents the imposed free shrinkage strain to the model. As the hardened concrete loses its capillary water to the environment, free shrinkage takes place and the humidity profile *h(z)* through the thickness of concrete slab is simplified to follow the Fick's law of diffusion:

$$h(z) = h_s - (h_s - h_i)erf(z) \qquad \text{Equation 3-10}$$

where z is the distance measured from the outside surface inward the specimen, h_s and h_i represent the humidity (fraction) at the outside and inside surface, and *erf(z)* represents the error function [166]. A cubic function is used to relate the free shrinkage strain to the humidity profile [152]:

$$\varepsilon_{sh}(z) = \varepsilon_{sh}(t)(1 - h(z)^3) \qquad \text{Equation 3-11}$$

where $\varepsilon_{sh}(t)$ is the free shrinkage strain as a function of time. To simplify the problem to a 1-D case, the distribution of free shrinkage strain is idealized as uniformly distributed, and in the case of slab curling to a linear distribution across the thickness. The shrinkage strain ranges from about 400 to 900με in various materials and conditions were reported [167, 148, 30,168, 145]. The average strain in the range of 200-500 με was used for F-D model.

$$\overline{\varepsilon_R}(z) = \frac{1}{h}\int \varepsilon_{sh}(z)dz \qquad \text{Equation 3-12}$$

Figure 3-10(b) shows the development of shrinkage imposed stress due to deformation compatibility as follows: Step 1, original slab with both ends fixed; Step 2, free shrinkage leads to a change in length of $\varepsilon_{sh}(t)L$ and a fictitious tensile load P stretching the slab is applied to meet the compatibility condition; Step 3, tensile stress is being built up and once it reaches $\sigma_{m,cr}$, the matrix will crack and the slab is then updated as two uncraked sections and a crack-opening zone. Three mechanisms and the distribution of concrete stress are also schematically presented in accordance with Figure 3-9(a)-(c). Once the stresses in the uncracked segments attain $\sigma_{m,cr}$ again, new cracks will form. Corresponding to the slip distribution shown in Figure 3-9(f), the opening of certain crack is the summation of the slip magnitudes measured at the right and left of crack face:

$$\omega_i = \left|s^+\right| + \left|s^-\right| \qquad \text{Equation 3-13}$$

Subsequently the average crack opening is defined as the total opening divided by number of cracks. And the total crack opening is also equal to the total deformation minus the deformation in concrete matrix and fiber:

$$\begin{aligned} &\omega_{ave} = \sum \omega_i / N_{cracks} \\ &\sum \omega_i = \delta_{TOTAL} - \int \varepsilon_{concrete} dx - \int \varepsilon_{fiber} dx \end{aligned} \qquad \text{Equation 3-14}$$

where the term δ_{TOTAL} equals to zero in this case as enforced by the boundary conditions. An average stress $\sigma_{m,ave}$ can also be obtained as:

$$\sigma_{\mathrm{m,ave}} = \frac{1}{L}\int_0^L \sigma_{\mathrm{m}} dx \qquad \text{Equation 3-15}$$

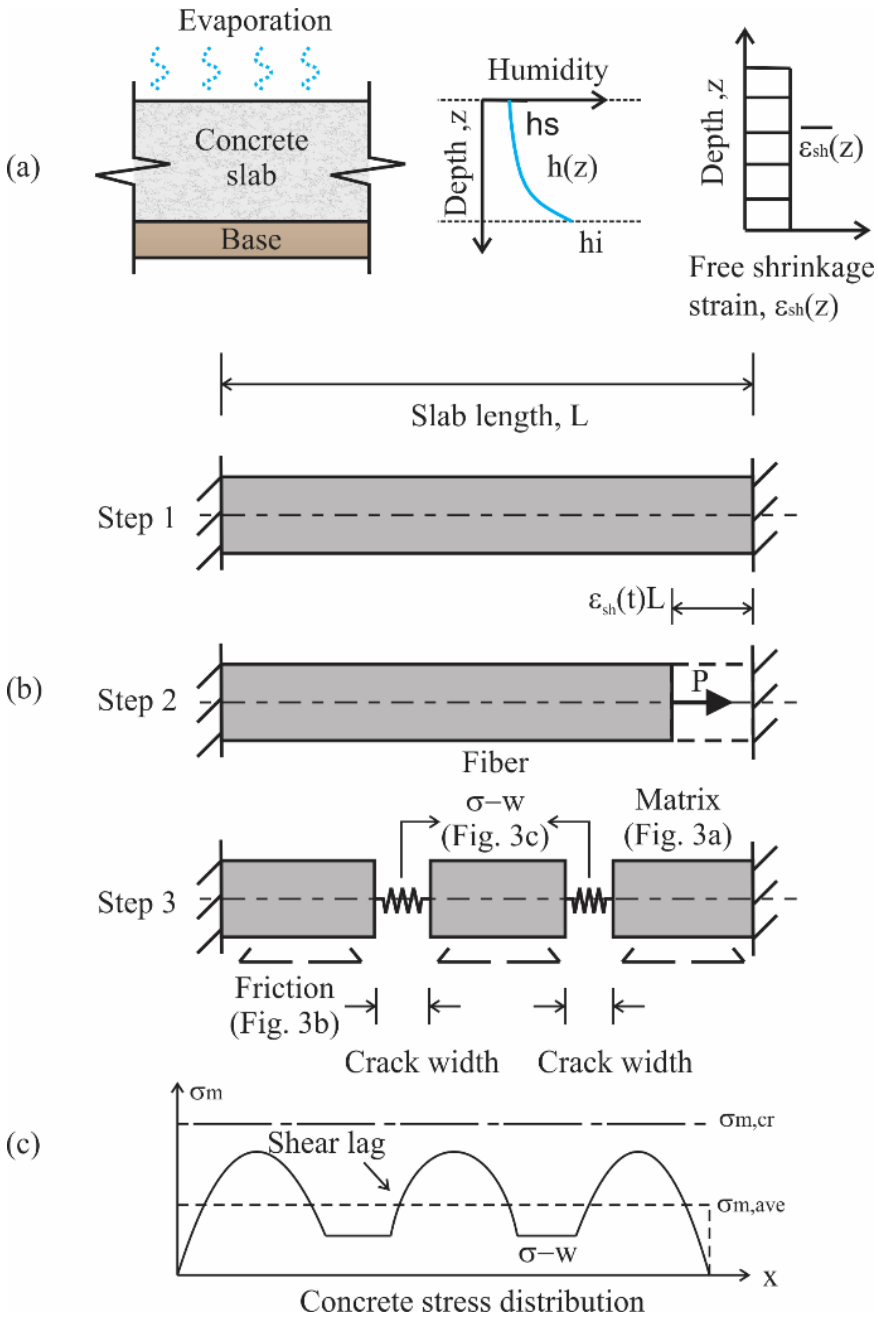

Figure 3-10 (a) Humidity Profile Throughout the Thickness of Concrete Slab Simulated by Fick's Law of Diffusion and Idealized Average Free Shrinkage Strain Applied to the Tension Stiffening Model, (b) Deformation Terms in the Slab, and (c) Conceptual Stress Distribution in Concrete [142].

A numerical model of a 40 m x 40 m slab was simulated to illustrate the process of sequential cracking by F-D model. The 40 m length was discretized into 2431 nodes of

equal spacing. The fiber volume fraction V_f = 0.45% and Young's modulus of the matrix E_m = 30 GPa. Three material models are μ_s = 0.4 for base friction, τ_{max} = 1 MPa for bond, and $\sigma_{m,cr}$ = 3 MPa for matrix.

The simulated evolution of shrinkage induced stress with increasing strain and corresponding state of cracks are presented Figure 3-11(a). Composite stress increased linearly up to $\sigma_{m,cr}$ where the slab cracks. A strain softening response expected due to fiber bridging mechanism is indicated by the dashed line. However, the base friction provided additional resistance and roughly maintained the postcrack stress at $\sigma_{m,cr}$. The matrix stress, slip, and spring force (base friction) distributions in the left half of the model are shown in four different stages of cracking in Figure 3-11(b)–(d). The first subplot at the lower section shows the end point of elastic response while the subsequent subplots present the sequential formation of new cracks.

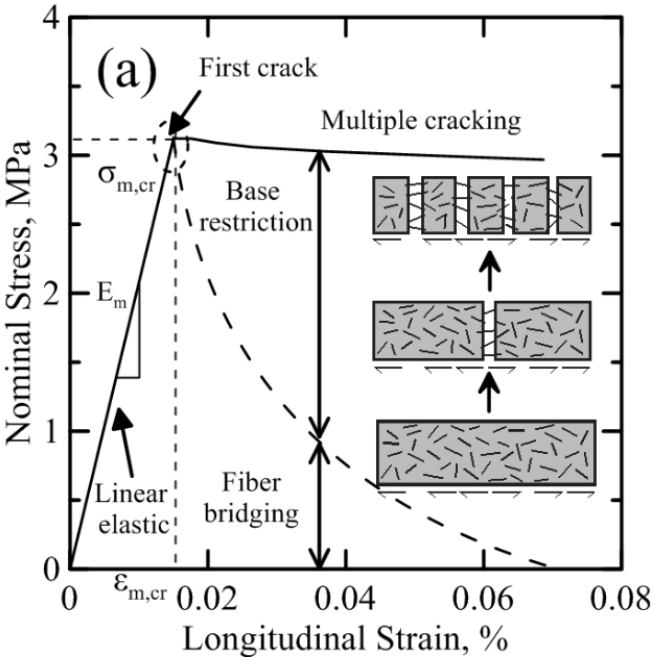
(a)
First crack
Multiple cracking
$\sigma_{m,cr}$
Base restriction
E_m
Linear elastic
Fiber bridging
$\varepsilon_{m,cr}$
Nominal Stress, MPa
Longitudinal Strain, %
0
1
2
3
4
0.02
0.04
0.06
0.08

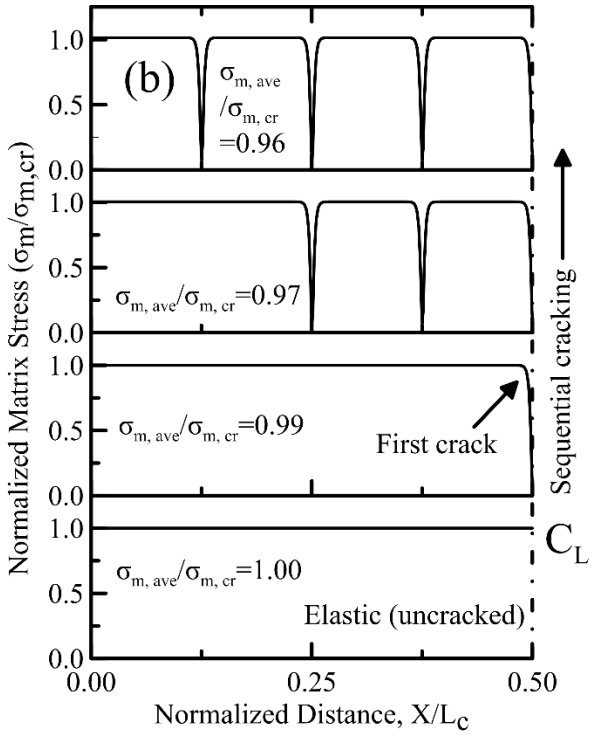
(b)
$\sigma_{m,ave}/\sigma_{m,cr}$ =0.96
$\sigma_{m,ave}/\sigma_{m,cr}$=0.97
$\sigma_{m,ave}/\sigma_{m,cr}$=0.99
First crack
$\sigma_{m,ave}/\sigma_{m,cr}$=1.00
Elastic (uncracked)
Sequential cracking
C_L
Normalized Matrix Stress ($\sigma_m/\sigma_{m,cr}$)
Normalized Distance, X/L_c
0.0
0.5
1.0
0.00
0.25
0.50

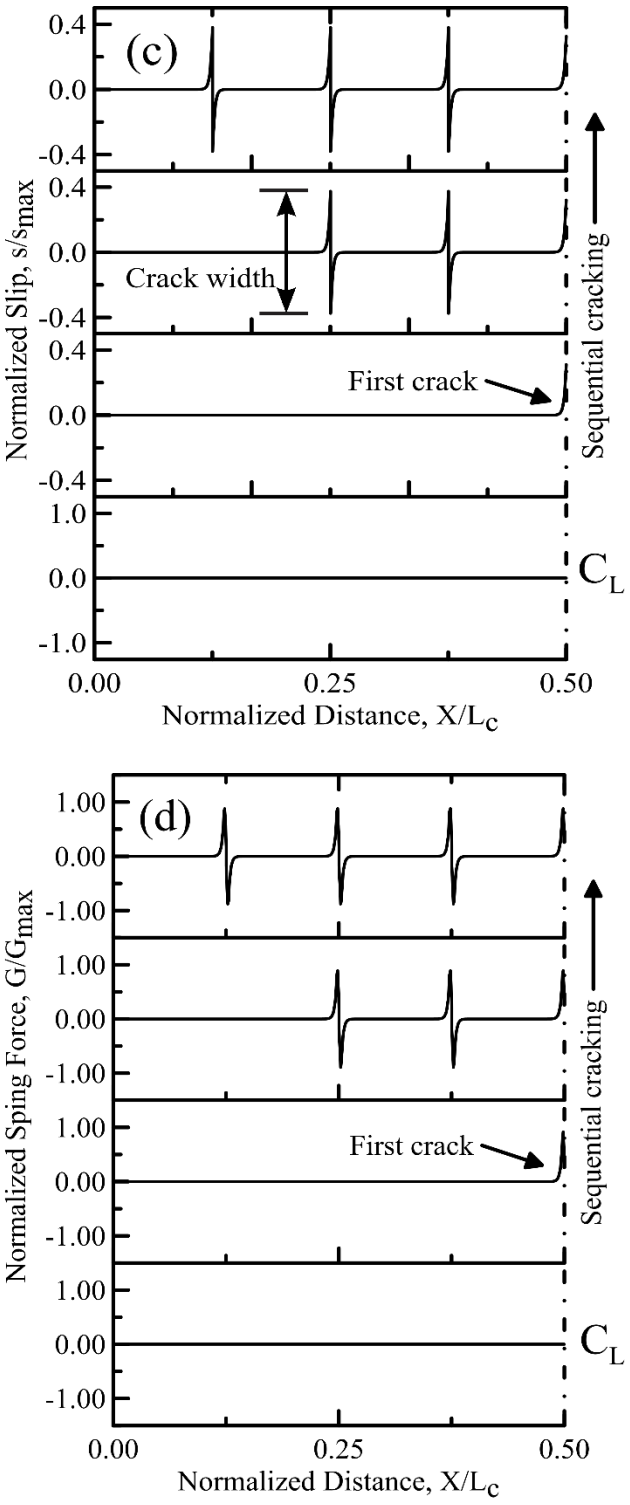

Figure 3-11 (a) Stress-Strain Evolution, and Three Normalized Material Responses of a Numerical Base Model: (b) Matrix Stress Distribution, (c) Slip Distribution, (d) Bond Stress Distribution [142].

The first subplot of Figure 3-11(b) shows uniform matrix stress distribution prior to the first crack. The strain of matrix and fiber are all equal due to strain compatibility. The next stage represents the stress redistribution immediately after the first crack formation at $x=0.5L_c$. The magnitude of stress is limited to $\sigma_{m,cr}$. As the strain increased and the stress redistributed to the matrix strength, new cracks were added to the numerical model. The average stress carried by uncracked concrete segments was found to decrease from 1.0 to 0.96 (normalized with respect to $\sigma_{m,cr}$), which indicates effective load transfer from slab to base and the load carrying capability after cracking. Figure 3-11(c) and (d) illustrate the distributions of slip and spring force developed at the interface of the slab and base. Lower two subplots of Figure 3-11(c) and (d) correspond to the perfect bond state with slip and spring force as zero. The next subplot shows the first crack dividing the specimen into two pieces; the maximum positive slip and spring force, which prevents the movement of slab, appear at the right ($0.5\ X/L_c$) and decrease rapidly toward the left. Subsequent subplots show the slip and spring force distributions at intermediate cracking stages.

In order to compare and calibrate the empirical and finite difference model parameters, parametric study on both methods was conducted to investigate the effects of fiber volume fraction, base friction, bond strength and imposed shrinkage strain. Three numerical models were introduced based on the field case studies: Case Study #1 was a 7000 m^2 slab in Poznan, Poland, constructed for a superstore using jointless bay sizes of 36 m x 36 m in dimension with a 200 mm thickness and a C25-30 mix design. The specified steel fibers were 25 kg/m^3 of 35 mm length by 0.75 mm diameter hooked end. The slab was installed onto a well compacted sand base. Case study #2 addressed another slab where the tenant is Canal Logistics Brussels (CLB). The slab was 26000 m^2 of 40 m x 40 m joint free bay

size, and 150 mm in thickness using a C25-30 mix design with 35 kg/m^3 of 60 mm length by 1.0 mm diameter hooked end steel fibers, installed onto a well compacted sand bottom. The third slab, case study #3 was investigated in Bornem, Belgium. The slab is of 46000 m^2 of 50 m x 50 m joint free bay size, 180 mm thickness using a C30-37 mix design with 40 kg/m^3 of 54 mm long by 1.00 mm diameter steel fiber with conical heads end.

Table 3-2 Parameters and Computed Average Crack Opening (mm) Using Finite Difference Method (E_m = 20 GPa, E_f = 200 GPa) [142]

Parameters	Case Study 1	Case Study 2	Case Study 3
Geometries			
L (m)	36	40	50
t (mm)	200	150	180
L_f (mm)	35	60	54
D (mm)	0.75	1.0	1.0
Fiber volume, V_f (%)			
0.32	0.670	0.914	1.508
0.45	0.484	0.676	1.055
0.51	0.433	0.621	0.763
0.6	0.375	0.532	0.644
Coefficient of friction, μ_s			
0.4	0.670	0.676	0.763
2.0	0.509	0.493	0.437
4.0	0.446	0.432	0.383
Bond Strength (MPa)			
1.0	1.160	1.123	1.281
2.0	0.842	0.850	1.067
3.0	0.738	0.725	0.879
4.0	0.648	0.658	0.788
ε_R ($\mu\varepsilon$)			
2	0.670	0.563	0.763
3	0.770	0.676	0.928
4	0.830	0.731	1.019
5	0.867	0.768	1.070

To perform the parametric study, the parameters for a base empirical model are: k_{base} = 0.45 N/mm^3, $\mu_{m,base}$ = 0.08; and for F-D model: $\mu_{s,base}$ = 0.4, $\tau_{max,base}$ = 1.0 MPa, E_m = 20 Gpa, $\sigma_{m,cr,base}$ = 3MPa. Fiber volume fraction and imposed shrinkage strain are identical for both methods: $V_{f,base}$ = 0.51%, $\varepsilon_{R,base}$ = 200 με. The two approaches are related to each other with respect to multiple mechanisms. For example, geometries, V_f and ε_R have the same physical definitions and input values in both methods. Other aspects are indirectly linked by describing the same mechanical characteristics. The effect of fiber type and anchorage μ_m in empirical equation is related to the bond-slip model, in F-D method. The base friction μ_s computed from the modulus of subgrade reaction k is then in accordance with the spring elements applied at each node.

Figure 3-12 shows the simulated average crack width with varying fiber volume fraction, frictional force, and bond strength. The isolated data points in the figure were computed using the F-D model and listed in Table 3-2 while the fitted curves were obtained from empirical equation as its variables changed continuously. Particularly in Figure 3-12(b) and c, the variables of F-D model are corresponding to the bottom axis, while those of empirical method are indicated by the top axis. As shown in Figure 3-12(a), the predicted average crack widths reduced about 50% while the fiber volume fraction increased from 0.32% to 0.6%. This can be explained by the role of fiber in bridging the crack and transferring the load. The shrinkage induced forces are transferred from the intact concrete segment to the fibers, and then to adjacent uncracked segment.

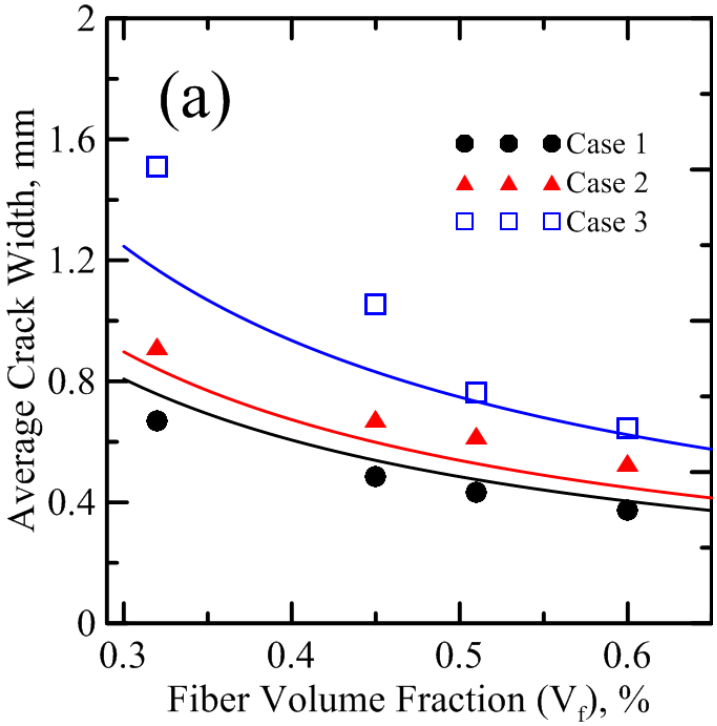
(a)
Case 1
Case 2
Case 3
Average Crack Width, mm
0
0.4
0.8
1.2
1.6
2
0.3
0.4
0.5
0.6
Fiber Volume Fraction (V_f), %

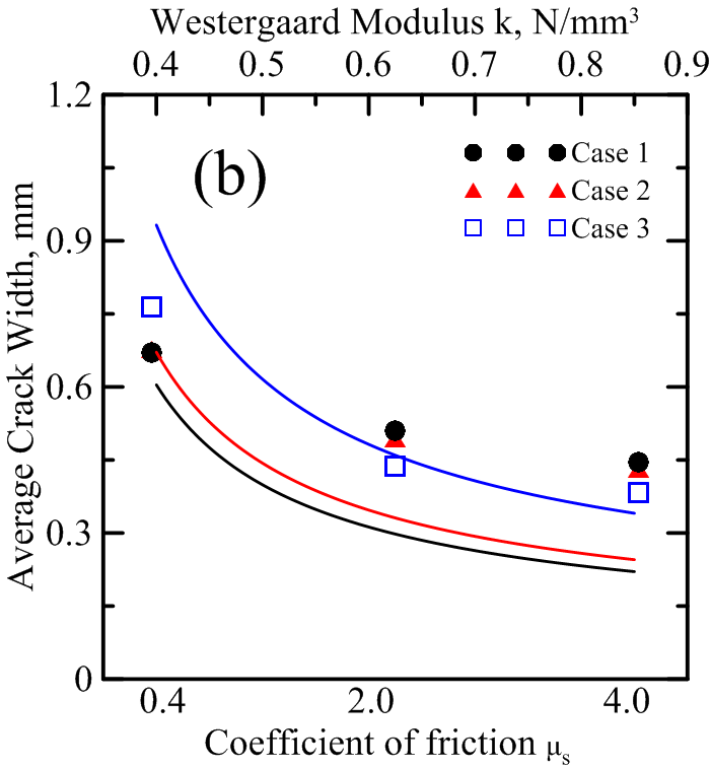
Westergaard Modulus k, N/mm³
0.4
0.5
0.6
0.7
0.8
0.9
(b)
Case 1
Case 2
Case 3
Average Crack Width, mm
0
0.3
0.6
0.9
1.2
0.4
2.0
4.0
Coefficient of friction μ_s

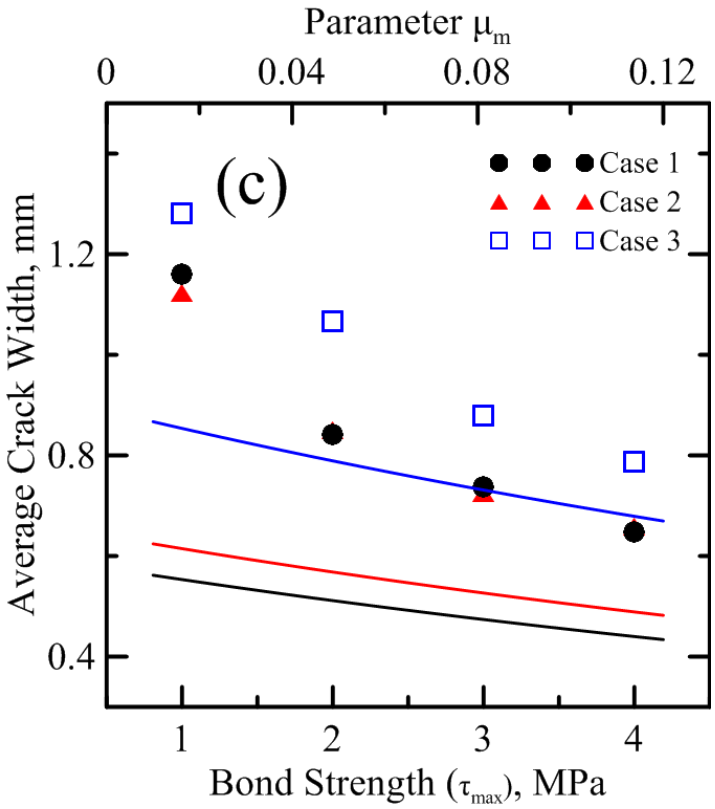
Parameter μ_m
0
0.04
0.08
0.12
(c)
Case 1
Case 2
Case 3
Average Crack Width, mm
1.2
0.8
0.4
1
2
3
4
Bond Strength (τ_{max}), MPa

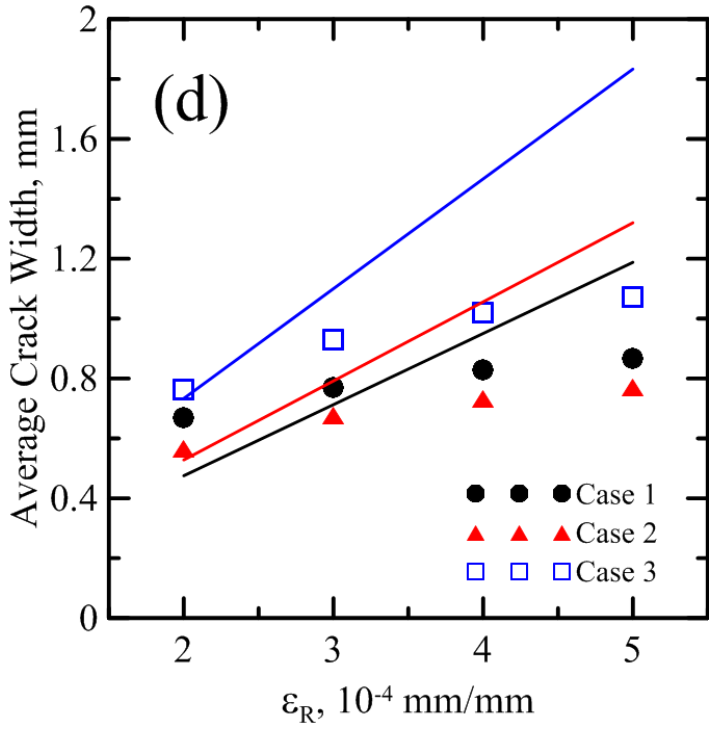
(d)
2
1.6
1.2
0.8
0.4
0
Average Crack Width, mm
Case 1
Case 2
Case 3
2
3
4
5
ε_R, 10^{-4} mm/mm

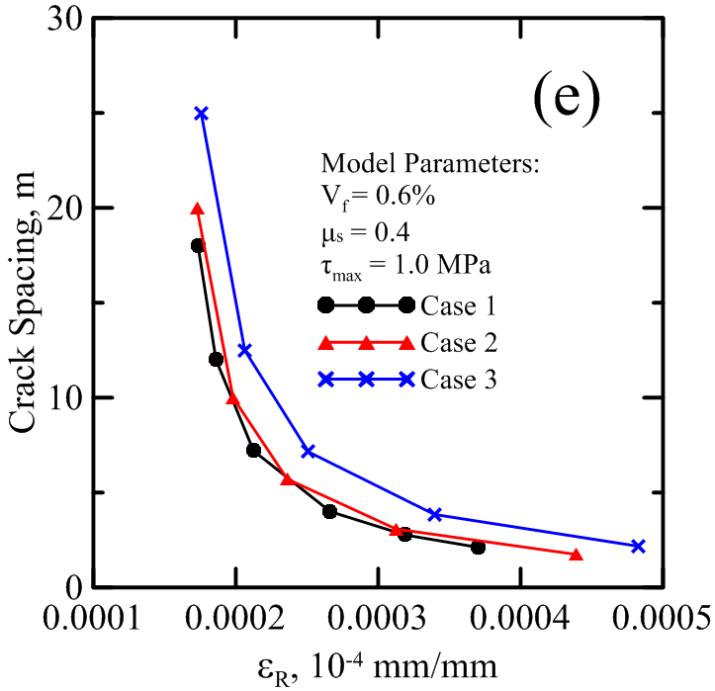

Figure 3-12 Effect of (a) Steel Fiber Content, (b) Coefficient of Friction μ_s, (C) Bond Strength and (d) ε_R on Computed Crack Width, and (e) Crack Spacing Versus Strain Responses [142].

Figure 3-12(b) illustrates the effect of base friction on the crack width. Increasing μ_s by an order of magnitude from 0.4 to 4.0, decreased crack width by 0.2 mm, whereas for the same change predicted by empirical equation, *k* should change from 0.35 to 0.80. The role of the frictional force in crack width control by restricting the deformation of slab before and after cracking is therefore shown.

The effect of stress-crack width model as a constant level of bond strength is used as shown in Figure 3-12(c). The values of crack opening significantly dropped as τ_{max} increased from 1 to 4 MPa. While the parameter μ_m widely ranged from 0.01 to 0.2 to fit the trend. Note that straight, hooked end, and undulated steel fibers, which are corresponding to μ_m values of 0.04, 0.08 and 0.12, correlate with a range of bond strength from 2 to 3 MPa, as specified by F-D model.

The crack opening increased from 0.2 to 0.3 mm for different slabs as ε_R increased from 200 to 500 με, as shown in Figure 3-12(d). This is attributed to higher tensile stress due to larger shrinkage strain in the presence of restraints. The observed trend also agreed with the empirical model. Figure 3-12(e) represents the average crack spacing evolution as a function of composite strain for the three slabs. Constant values of V_f = 0.6%, μ_s = 0.4 and τ_{max} = 1.0 MPa for the three cases are used. It is shown that crack spacing decreased rapidly early on and saturated at the values ranging from 1.6 to 2.2 m at the strain around 400 με.

3.3.4 Comparison of Proposed Methods with Field Measurements

To verify the accuracy of the proposed models, the max crack opening throughout the area of these three slabs were also measured and compared to the numerical results. Selection of model parameters are based on the field information, experimental results, literature and assumption. The compressive strength of concrete used is in the range of 40-45 MPa from cube test, which corresponds to the modulus of elasticity from about 29.7 to 31.5 GPa estimated using ACI equation. Thus a constant modulus E_m = 30 GPa was used in the F-D model. Several papers have been published on the procedures to obtain the back calculated tensile strength and residual tensile capacity of various types of FRC based on flexural tests [61, 169]. For the typical mixture presented in this paper, $\sigma_{m,cr}$ = 4.0 MPa is selected for the three slabs and the residual tensile capacity ranges from 0.3 to 0.7 MPa. Naaman et. al [137, 170] conducted analytical study and experimental verification on the pullout response of steel fibers in concrete matrix. The maximum bond strengths from multiple sets of experiment vary widely from 1.4 MPa to 9.6 MPa. The selected bond strengths for case studies are summarized in Table 3-3 as well as other model parameters.

Table 3-3 Field Measurements and Computed Crack Widths Obtained by Two Models (v_f and ε_R Are Identical for Both Models) [142]

Case	Field Data	Empirical Model					Finite Difference Model			
	ω (mm)	V_f (%)	ε_R (με)	λ	k (N/mm^3)	μ_m	ω (mm)	τ_{max} (MPa)	μ_s	ω (mm)
1	0.5-0.7	0.32	200	1.05	0.5	0.08	0.636	3.0	0.4	0.650
2	0.65	0.45	200	1.35	0.45	0.04	0.658	2.5	0.4	0.676
3	0.8	0.51	200	1.35	0.45	0.04	0.806	1.6	0.4	0.795

The measured and computed crack openings are listed in Table 3-3. The shrinkage crack width of slab 1 was between 0.50 mm and 0.70 mm as measured after the it was in service for 2 years while the following simulations are obtained: ω = 0.636 mm by empirical equation and 0.650 mm by F-D model. For case study 2, the models presented here results in values of 0.658 mm and 0.676 mm, respectively, which conform to the observed 0.65 mm crack opening recorded during the inspection. When it comes to case 3, the measured crack opening was up to 0.80 mm which compares quite well, with the model outputs of 0.806 mm and 0.795 mm. The calculated maximum crack openings are less than 1 mm each and in good agreement with the measured values for all of the three examples, indicating the accuracy of both models in certain cases. However, more studies of various field conditions would help with better calibration of the numerical and empirical models.

3.3.5 Slab Curling

Curling is defined as the upward lift at the slab corner or edge at the joint. Guo et. al [171] reported the curling deflections up to 5 mm and values above 0.5 mm can become critical for top down corner cracking under traffic loading [172]. As schematically shown in Figure 3-13, the curling is caused by the gradient of the strains through the thickness as a result of the varying moisture content or temperature [173,174,175,176]. The strain distribution

results in a net curvature and thus the uplift. In the present study, drying shrinkage induced strain is assumed to be the main effect. The total strain of the slab can be obtained by subtracting the crack opening ω from the free shrinkage strain ε_{sh}:

$$\varepsilon_{TOTAL} = \varepsilon_{sh}(z) - \omega / L_s \qquad \text{Equation 3-16}$$

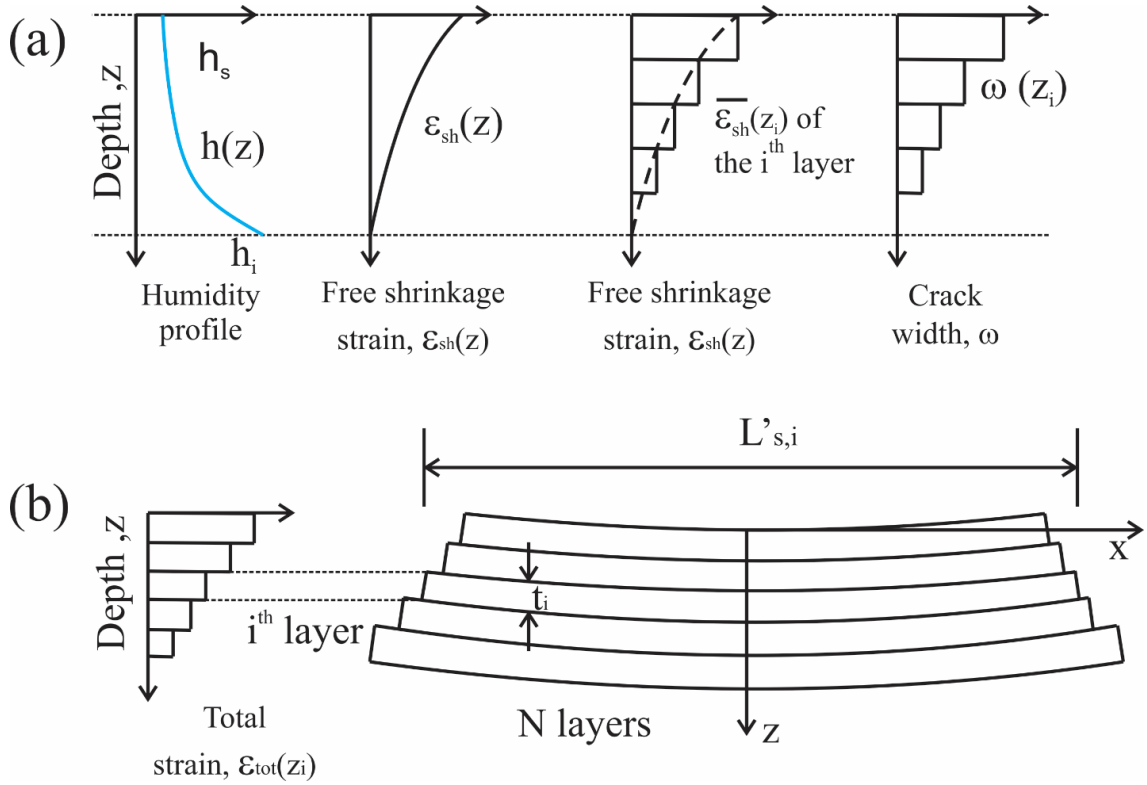

Figure 3-13 Discretization of (a) Strain Distribution and (b) Deformation Through the Slab Thickness as Different Layers [142].

Since the solution addresses the case of ultimate shrinkage, an extended period of time is assumed for the shrinkage to fully take place. But this model can be augmented with an appropriate shrinkage vs. time function to accommodate the temporal effects. As the loss of contact between the slab and the base affects the boundary conditions, flexural stresses and strains generated result in the uplift of the cantilever action. Therefore, the curling behavior of the cracked segment can be modelled as a cantilever beam undergoing flexure and the quantity of upward movement is equivalent to the tip deflection (Figure 3-7(c)).

Using Euler–Bernoulli beam theory, the imposed curvature κ can be obtained from the distribution of total strain throughout the thickness and the deflection δ can be subsequently determined:

$$\kappa = \frac{\varepsilon(h/2) - \varepsilon(-h/2)}{2t}$$
$$\theta(x) = \int_0^L \kappa dx = \kappa x + C_1$$
$$\delta(x) = \int_0^L \theta(x) dx = \frac{1}{2}\kappa x^2 + C_1 x + C_2$$

Equation 3-17

The constants C_1 and C_2 are evaluated by applying boundary conditions at the support ($\theta(0) = 0$ *and* $\delta(0) = 0$) which yields $C_1 = C_2 = 0$. Thus:

$$\delta(x) = \frac{1}{2}\kappa x^2 \quad and \quad \delta_{tip} = \delta(L_s) = \frac{1}{2}\kappa L_s^2$$

Equation 3-18

In order to the use the finite difference model, the slab is discretized into N layers each with a thickness of t/N and a constant free shrinkage $\overline{\varepsilon_{sh}(z_i)}$ is imposed for the ith layer, as shown in Figure 3-13(a) and (b). The numerical simulation is then performed for N times with varying imposed free shrinkage strain and a series of crack openings are calculated. The simplified distribution of total strain is subsequently derived for the calculation of curvature and deflection.

The curling estimation procedure is applicable in cases where the slab at the joint is free from any load transfer mechanism similar to a full depth sawn cut. It is expected that fibers, dowels or longitudinal reinforcement intersecting a shrinkage crack and aggregate interlock mechanism provide both normal and shear resistance [177,178]. But shear stress transferring across the plane is not taken into account in this 1-D model and thus the

computed curling is an upper bound estimate. Even though drying shrinkage is considered as the primary effect, the model is capable of addressing several other factors including temperature change, creep effect and mechanical strains induced by self-weight and service load, by adding the strain terms into Eqn. (13). Note that with a degree of uplift measured, flexural stresses resulted from loading at the edge or corners are additive to the shrinkage induced tensile stresses and may cause flexural cracks. The magnitude of the point load required for corner fracture can be calculated based on the length of separation and amount of slab curl.

A parametric study was conducted for the effect of slab thickness *t*, slab length *L*, and gradient of free shrinkage strain. The slab was discretized into 10 layers while the interaction between the layers was not considered. Figure 3-14(a) shows that as the thickness increased from 0.2m to 0.4m, both the curvature and curling deflection decreased for about 50%. This was expected since the increase in thickness reduces the curvature as it is inversely proportional according to Eqn. (14). The trend agrees with the experiences in the industry which generally consider thinner slabs to be more critical to curling. It is also found that when the slab length *L* was doubled (18 to 36m), the curling deflection increased from 0.82 mm to 3.53 mm as shown in Figure 3-14(b), which is almost quadratic with respect to *L*. Field observations point to the curling of slabs as directly proportional to the length, it is expected that in the case of joint free slabs the curling is reduced by the shear stiffness of the fibers at the cracked sections. The effect of imposed free shrinkage strain gradient is illustrated in Figure 3-14(c). As the range (value from bottom layer to top layer) of imposed strain expanded from 300-550 με to 150-550 με, i.e., the gradient became steeper, the deflection increased from 0.44 to 3.23 mm since the curvature is proportional

to the difference between strains at top and bottom layers. Additionally, the procedure was conducted with varying number of layers (10 to 50) but the results turned out to be insensitive.

Proper modeling and design guides are needed for the development of SFRC joint free slabs in order to address and minimize the potential cracking due to drying shrinkage. Primary parameters affecting the drying shrinkage properties are discussed including water cement ratio, HRWRA, shrinkage induced strain, friction of grade, fiber volume and fiber type. An empirical equation and a numerical model using the finite difference method were proposed to predict the sequential cracking and opening of a restrained slab on grade. Parameters affecting the drying shrinkage cracking were discussed and addressed by both methods. Parametric study showed that the predicted crack opening was reduced with higher level of restraint by increasing fiber volume fraction, base friction, and bond strength. This indicates the role of fiber and base course in controlling the crack opening by restricting the movement of cracked slab segments.

Since the two models address the same mechanical characteristics, they are related to a great extent even though they were developed based on different methodologies. The empirical equation was calibrated and the results demonstrated a good agreement with the F-D model. Case studies were conducted on three slabs in service at different occasions. Crack openings of the selected slabs were measured and compared to the computed values. Both of the models were able to predict the crack openings accurately. A simple method to estimate the curl of slab has been proposed and the effects of slab thickness, length and imposed shrinkage strain have been investigated. The curling deflection was found to be increasing as the slab thickness decreased, slab length increased, and gradient of imposed

strain increased. However, the approach needs to be calibrated against measured data from fields as future study.

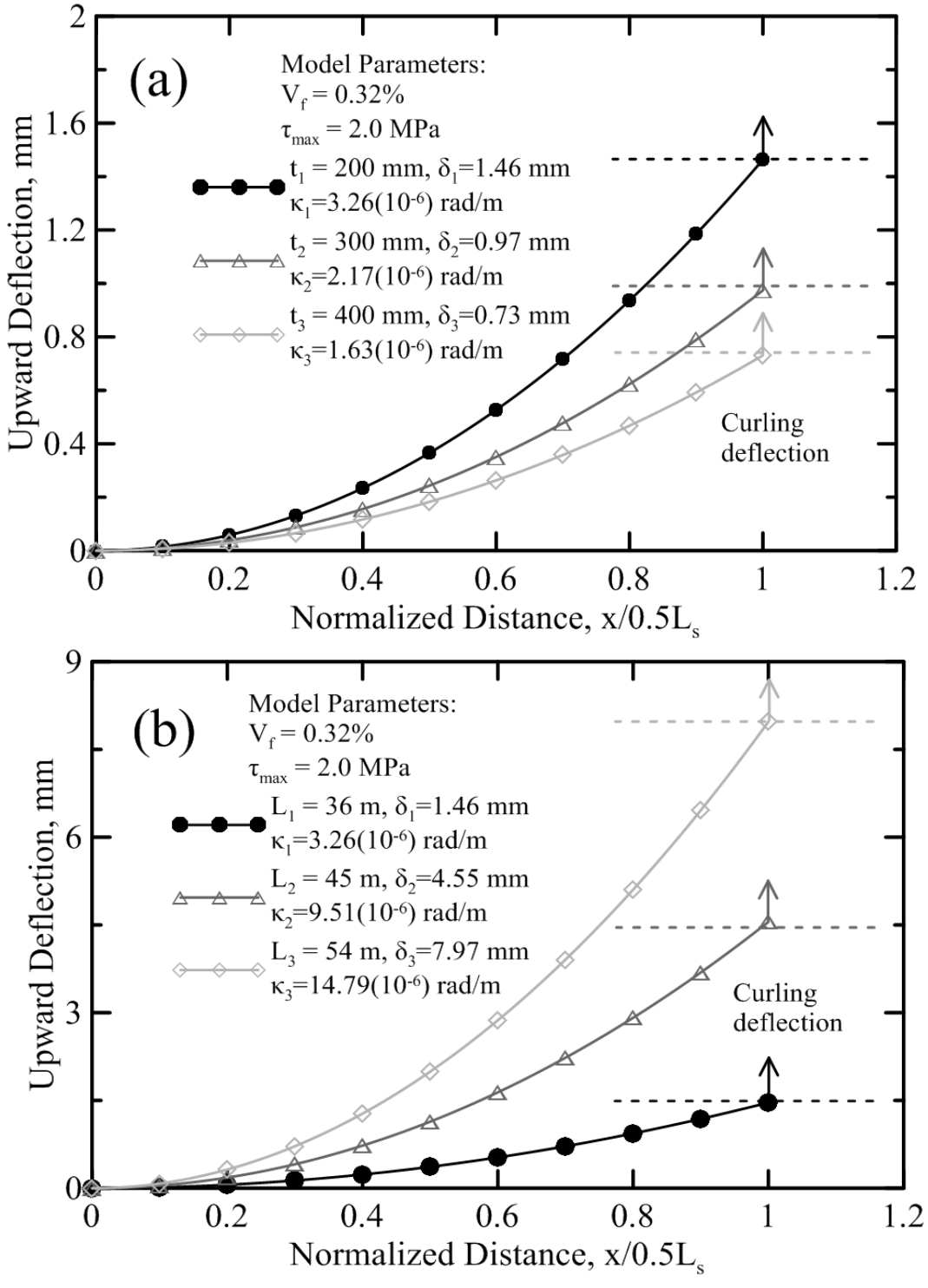

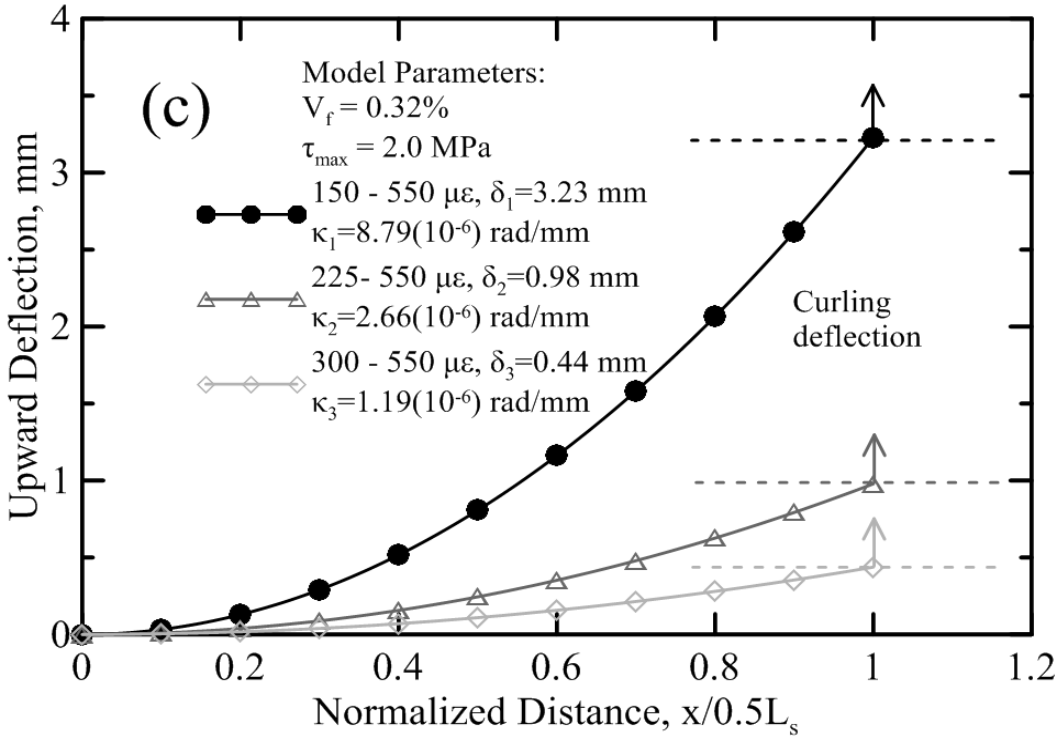

Figure 3-14 The Effects of (a) Slab Thickness, (b) Slab Length, and (c) Imposed Free Shrinkage Strain Gradient on the Curling [142].

4. ANALYTICAL MODEL AND DESIGN FOR FLEXURAL BEHAVIORS

4.1 Introduction

Post-cracking tensile behavior of FRC materials have been simulated by either a stress–strain (σ-ε) relationship in a smeared crack continuum model, or a stress–crack width (σ-w) discrete model using nonlinear fracture mechanics. The original discrete crack approach by Hillerborg [179] has been modified by many researchers [180,181,182]. It does not address crack formation and propagation, but instead uses a stress-crack width (σ-ω) response as an input parameter in the post peak tensile zone [183,184]. A representative volume element of a cracked section of a flexural beam with length *Lp* and depth *h* is shown in Figure 4-1. The section is characterized by compression and tensile sections. The tensile zone is represented by two regions; an elastic tensile strain as well as a bridged crack in opening mode. The stresses carried by fibers across the crack in tension are represented as a function of crack opening and the method is widely used in simulation and design of quasi-brittle materials [53, 185, 186]. One of the main parameters of these models is a characteristic length parameter defined as *Lp*, which prevents mesh dependency of the results in finite element models as it relates the crack width to strain [187, 188]. In smeared crack models, characteristic length parameter determines the width of localization and prevents snap-back and other numerical instabilities [189]. In the present paper the length of localization zone has been used as a constant length parameter that affects the postpeak descending response of the load deformation curve where cracks are localized. The σ-ε approach is more suitable for HRC elements since distributed cracking and tension stiffening are expected [190]. For example, application of superposition to add the contribution of reinforcement and fibers by updating the stress crack width relationship in

the tensile zone of multiple cracks in under-reinforced flexural sections is challenging. Furthermore, reinforcement ratio affects rebar stress and affects crack opening which will in turn affect fiber phase's contribution.

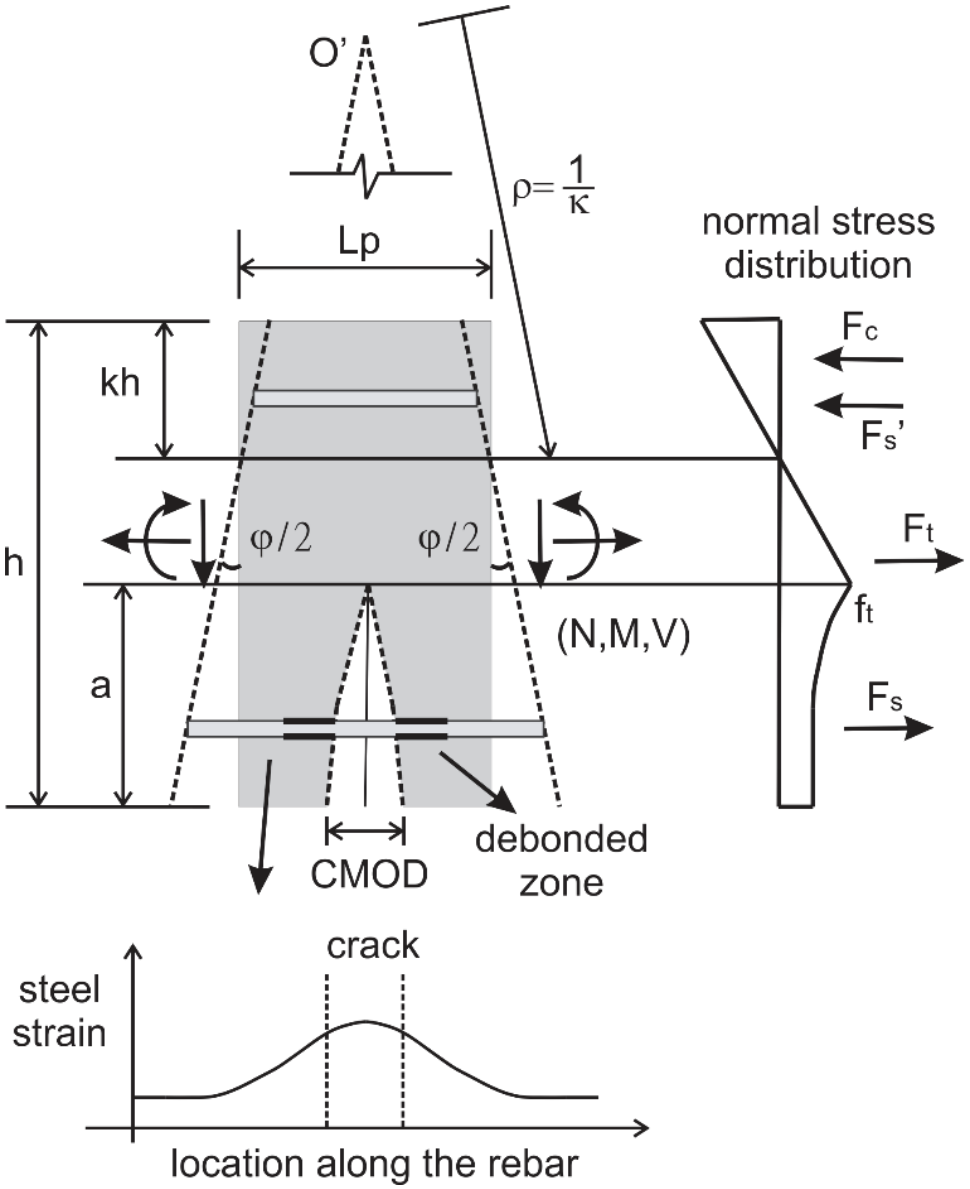

Figure 4-1 Schematic Presentation of Localized Zone for a Beam Section as a Nonlinear Hinge, Normal Stress Distribution and Strain Distribution in Steel Rebar.

In the present work analytical solutions for moment-curvature, load-deflection relationships, and minimum flexural reinforcement ratio are derived to address the synergy between continuous and fiber reinforcements. Derivations are presented as analytical

flexural behavior of beam and slab systems and support equivalent design charts based on a given deformation of composite systems for conventional, fiber reinforced, and hybrid reinforced concrete.

4.2 Derivation of Analytical Moment-Curvature Response

Figure 4-1 shows the schematic 2-D representation of the representative element of a cracked beam section as a nonlinear hinge during an incremental state of cracking. The element is represented by characteristics of length L_p, depth h, crack length a, angle of rotation φ, nominal curvature κ, normal stress distribution, and steel strain distribution. As the flexural crack extends, the steel rebar debonds and carries more stress at the flexural crack. However, in order to convert the 2-D representation into a 1-D cross sectional model, it is assumed that the average strain in the steel rebar can be represented by the nominal strain distribution at the rebar level of the section using the assumption of plane section remaining plane. The cross section may be of a variable shape and by integrating stresses over the area forces, bending moments, and neutral axis kh can be computed. The next step is to use the moment-curvature formulation in the analysis of a specific structures by means of analytical solutions or finite element approach. Templates for predicting load-deflection of elements with different boundary conditions are then developed.

Figure 6-2 presents three distinct material models used in the derivation of parametric response of HRC beams. Material parameters are described as two intrinsic parameters: tensile modulus E and the first cracking tensile strain ε_{cr} while other variables are normalized with respect to these intrinsic parameters. Figure 4-2(a) shows an idealized tension model with an elastic range of stress increases linearly with E up to the first cracking tensile strength of coordinates (ε_{cr}, σ_{cr}). In the post-crack region, the stress is

constant at $\sigma_p = \mu\sigma_{cr} = \mu\varepsilon_{cr}E$ and terminates at the ultimate tensile strain $\varepsilon_{tu} = \beta_{tu}\varepsilon_{cr}$. Figure 4-2(b) shows the elastic-perfectly plastic compression response with a modulus $E_c = \gamma E$. The plastic range initiates at strain $\varepsilon_{cy} = \omega\varepsilon_{cr}$ corresponding to yield stress $\sigma_{cy} = \omega\gamma\varepsilon_{cr}E$ and terminated at $\varepsilon_{cu} = \lambda_{cu}\varepsilon_{cr}$. Figure 4-2(c) is the elastic-perfectly plastic steel model using yield strain and stress of $\varepsilon_{sy} = \kappa\varepsilon_{cr}$ and $f_{sy} = \kappa n\varepsilon_{cr}E$ as defined by normalized parameters: κ and n. No termination level is specified for steel strain. Geometrical parameters are also normalized with the beam dimensions of width b and full depth h as shown in Figure 4-2(d) with steel parameters defined as area $A_s = \rho_g bh = \rho_g bd/\alpha$ at the reinforced depth $d = \alpha h$. The depth of compression steel $d = (1-\alpha)h$, and parameter ζ is introduced such that the area is $A_s' = \zeta A_s = \zeta\rho_g bh$. The reinforcement ratio ρ_g is defined per gross sectional area bh, and differs slightly from the conventional definition based on term bd used in reinforced concrete nomenclature. The material models for tension and compression of FRC and the model for steel rebar are presented as:

$$\sigma_t(\varepsilon_t) = \begin{cases} E\varepsilon_t & 0 \le \varepsilon_t \le \varepsilon_{cr} \\ \mu E\varepsilon_{cr} & \varepsilon_{cr} < \varepsilon_t \le \varepsilon_{tu} \\ 0 & \varepsilon_t > \varepsilon_{tu} \end{cases} \quad ; \quad \frac{\sigma_t(\beta)}{E\varepsilon_{cr}} = \begin{cases} \beta & 0 \le \beta \le 1 \\ \mu & 1 < \beta \le \beta_{tu} \\ 0 & \beta > \beta_{tu} \end{cases} \qquad \text{Equation 4-1}$$

$$\sigma_c(\varepsilon_c) = \begin{cases} E_c\varepsilon_c & 0 \le \varepsilon_c \le \varepsilon_{cy} \\ E_c\varepsilon_{cy} & \varepsilon_{cy} < \varepsilon_c \le \varepsilon_{cu} \\ 0 & \varepsilon_c > \varepsilon_{cu} \end{cases} \quad ; \quad \frac{\sigma_c(\lambda)}{E\varepsilon_{cr}} = \begin{cases} \gamma\lambda & 0 \le \lambda \le \omega \\ \gamma\omega & \omega < \lambda \le \lambda_{cu} \\ 0 & \lambda > \lambda_{cu} \end{cases} \qquad \text{Equation 4-2}$$

$$f_s(\varepsilon_s) = \begin{cases} E_s\varepsilon_s & 0 \le \varepsilon_s \le \varepsilon_{sy} \\ E_s\varepsilon_{sy} & \varepsilon_s > \varepsilon_{sy} \end{cases} \quad ; \quad \frac{f_s(\chi)}{E\varepsilon_{cr}} = \begin{cases} n\chi & 0 \le \chi \le \kappa \\ n\kappa & \chi > \kappa \end{cases} \qquad \text{Equation 4-3}$$

where normalized strains are defined as $\beta = \varepsilon_t/\varepsilon_{cr}$, $\lambda = \varepsilon_c/\varepsilon_{cr}$ and $\chi = \varepsilon_s/\varepsilon_{cr}$. Variable λ as top compressive fiber ε_{ctop} is used in the derivation of moment-curvature diagram and other

variables such as tensile strain in concrete and steel strain are obtained using the expressions derived based on the present formulation.

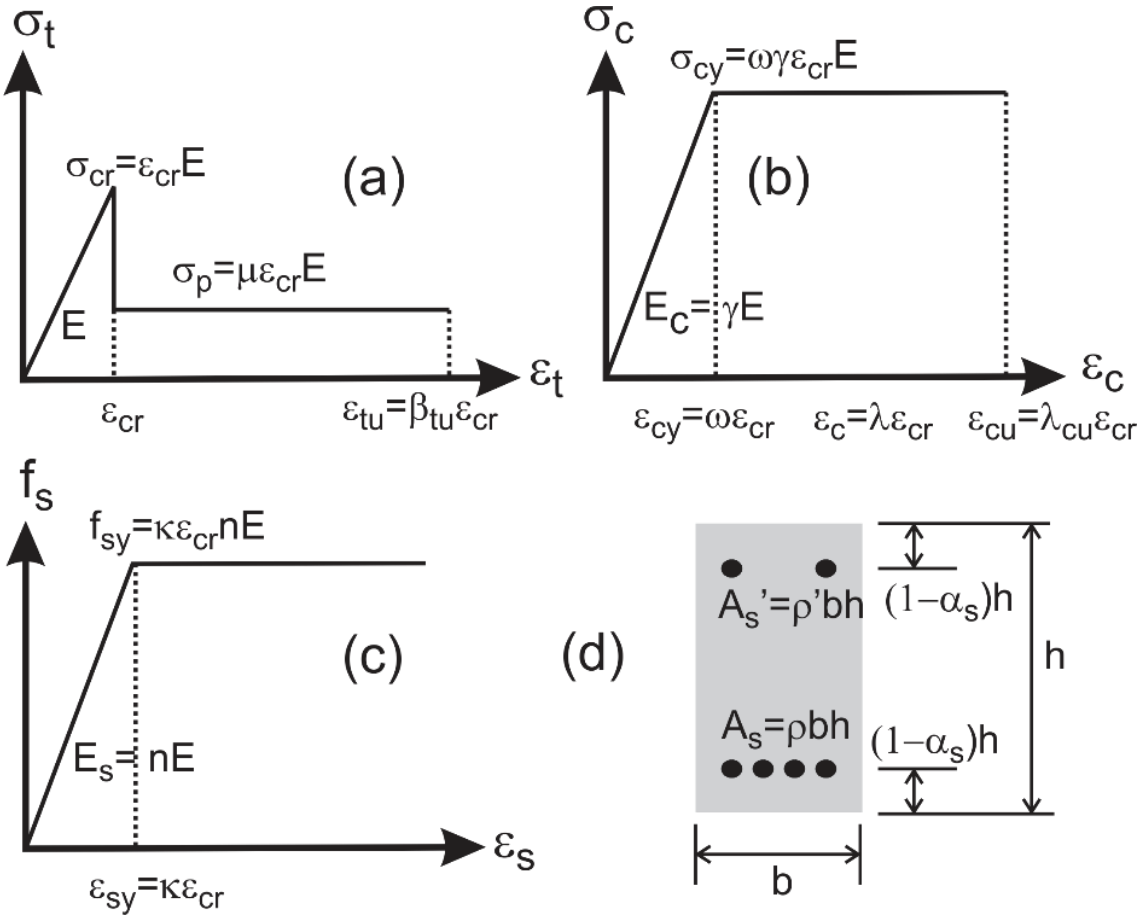

Figure 4-2 Material Model for Single Reinforced Concrete Design (a) Tension Model; (b) Compression Model; (c) Steel Model; (d) Beam Cross Section.

3.2. Moment-Curvature Diagram

In derivation of moment-curvature for a beam with rectangular cross section, the assumption of plane section remaining plane is assumed. By applying linear strain distribution across the depth, ignoring shear deformation, and using material models of Equations 4-1 to 4-3 and Figure 4-2(a)-(c), the stress distributions as shown in Figure 4-3 are obtained. The normalized compressive strain at the top concrete fiber λ is used as an independent variable to incrementally impose flexural deformation for three distinct stages.

The first stage ($0 < \lambda \leq \lambda_{R1}$) corresponds to elastic range until tensile strain at the bottom fiber reaches ε_{cr}. Stage 2 ($\lambda_{R1} < \lambda \leq \omega$) corresponds to an elastic compressive strain and the tensile strain in post-crack region. Finally, stage 3 ($\omega < \lambda \leq \lambda_{cu}$) corresponds to the plastic compressive strain while the tensile strain is in post-crack range. For stages 2 and 3 two possible scenarios exist: the steel is either elastic, or yielding, therefore stages 2 &3 are each divided into two sub-stages, 2.1, 2.2, or 3.1, and 3.2 where term 1 represents elastic and term 2 represents plastic response.

Three stages of stress distribution in Figure 4-3, show the height of compression and tension zones normalized with respect to the beam depth *h*, while stresses are normalized with respect to the first cracking strength $E\varepsilon_{cr}$ and presented in Tables 4-1 and 4-2, respectively. Forces and their lines of action are normalized with respect to cracking tensile force $bhE\varepsilon_{cr}$ and beam depth *h* as shown in Tables 4-3 and 4-4.

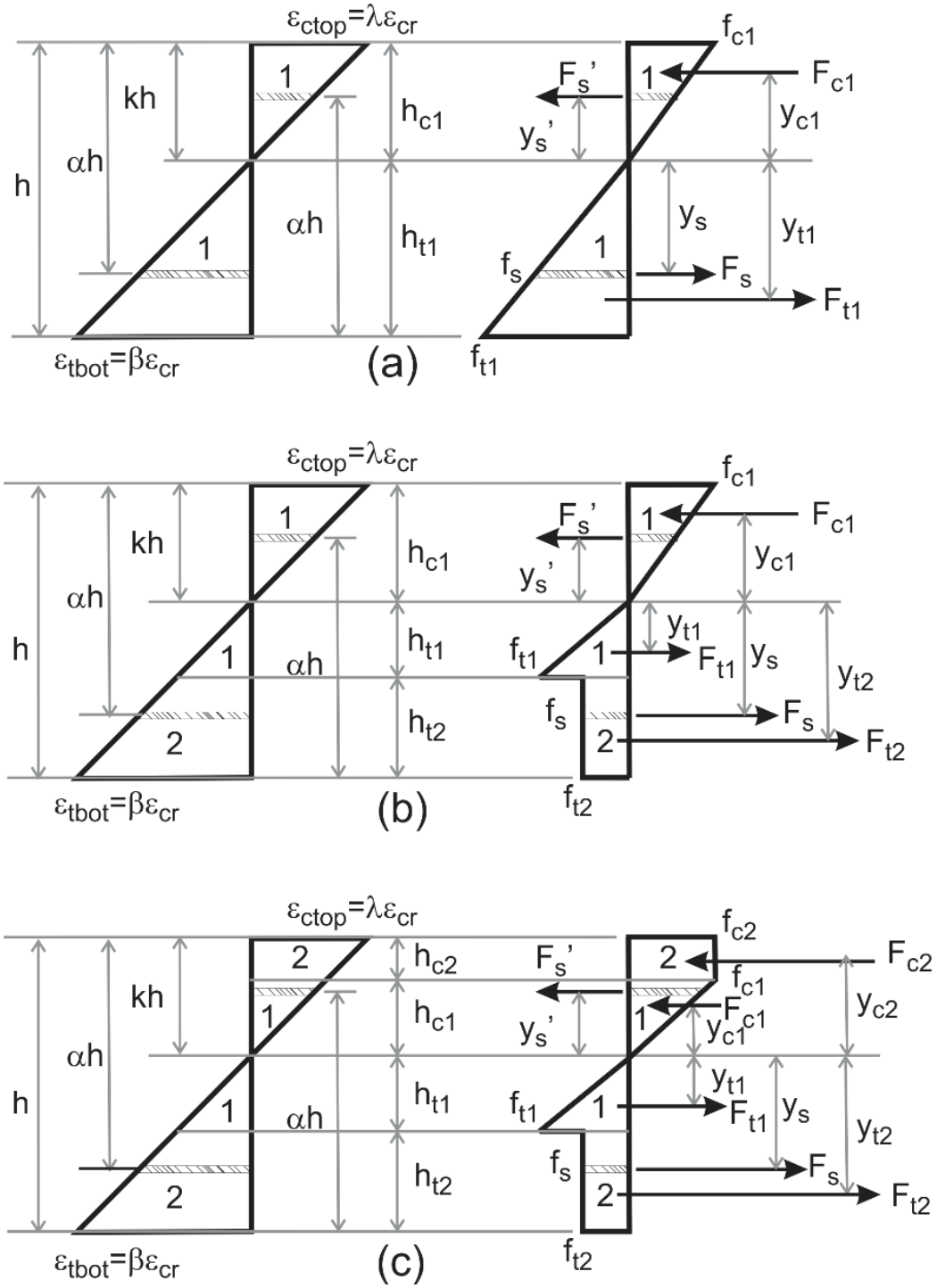

Figure 4-3 Strain and Stress Diagrams at Three Stage of Applied Compressive Strain at Top Fiber (λ); (a) Stage 1 ($0 < \lambda < \lambda_{R1}$) Elastic Compression-Elastic Tension; (b) Stage 2: $\lambda_{R1} < \lambda < \omega$ Elastic Compression-Post Crack Tension; (c) Stage 3: $\omega < \lambda < \lambda_{cu}$ Plastic Compression-Post Crack Tension.

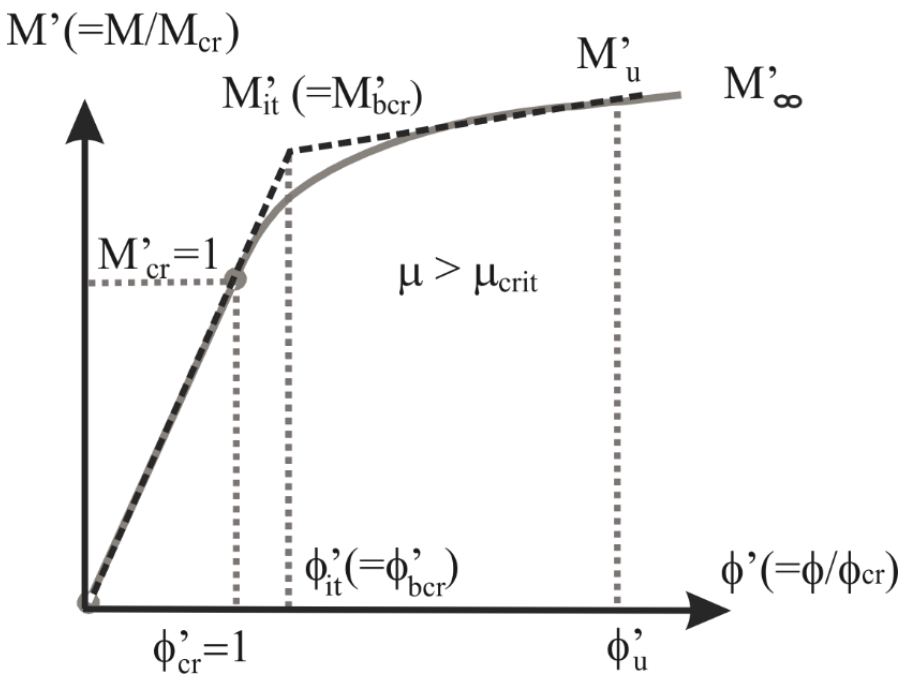

Figure 4-4 Normalized Moment-Curvature Diagram and Approximate Bilinear Model for Deflection Hardening ($\mu > \mu_{crit}$) [169].

The net section force is obtained as the difference between the tension and compression forces, and solved for internal equilibrium to obtain the normalized location of neutral axis, *k*. When steel is elastic in stages 1, 2.1 and 3.1, the expressions for net force are in the quadratic forms and result in two possible solutions for *k*. With a large scale of numerical tests covering the practical range of material parameters, only one solution yields the valid value in the range $0<k<1$. During stage 1, the singularity of k_1 for $\gamma = 1$, requires an asymptotic expression. When steel is in yield condition in stages 2.2 or 3.2, there is a unique solution for *k* as presented in Table 4-5. Internal moment is obtained by integrating the force components using the distance to the neutral axis as the moment arm, and the curvature is represented as the ratio of compressive fiber strain ($\varepsilon_{ctop} = \lambda\varepsilon_{cr}$) to the depth of neutral axis *kh*. Effective flexural stiffness is defined as the ratio of the moment to the

curvature at any given imposed λ. By normalizing the moment M_i, curvature ϕ_i and stiffness K_i for each stage i, using the cracking values M_{cr}, ϕ_{cr} and K_{cr} are expressed as analytical expressions M_i', ϕ_i' and K_i' as presented in Table 4-5.

$$M_i = M_i' M_{cr}; \qquad M_{cr} = \frac{1}{6} bh^2 E \varepsilon_{cr} \qquad \text{Equation 4-4}$$

$$\phi_i = \phi_i' \phi_{cr}; \qquad \phi_{cr} = \frac{2\varepsilon_{cr}}{h} \qquad \text{Equation 4-5}$$

$$K_i = K_i' K_{cr}; \qquad K_{cr} = \frac{1}{12} bh^3 \qquad \text{Equation 4-6}$$

The compressive strain corresponding to end of elastic region 1 (λ_{R1}) is determined from the strain gradient diagram shown in Figure 4-3(a).

$$\frac{\lambda_{R1}\varepsilon_{cr}}{kh} = \frac{\varepsilon_{cr}}{(1-k)h} \qquad \text{Equation 4-7}$$

By substituting k_1 from Table 4-5 for k in Equation 4-7 and solving for λ_{R1}, one obtains:

$$\lambda_{R1} = \begin{cases} -\dfrac{1+n\rho_g\zeta+n\rho_g-\sqrt{(n\rho_g\zeta+n\rho_g+1)^2-(\gamma-1)[2n\rho_g(\alpha\zeta-\alpha-\zeta)-1]}}{2+n\rho_g\zeta+n\rho_g+\sqrt{(n\rho_g\zeta+n\rho_g+1)^2-(\gamma-1)[2n\rho_g(\alpha\zeta-\alpha-\zeta)-1]}} & \text{when } \gamma \neq 1 \\ -\dfrac{2n\rho_g(\zeta\alpha-\alpha-\zeta)-1}{2n\rho_g(\zeta\alpha-\alpha+1)+1} & \text{when } \gamma = 1 \end{cases}$$

Equation 4-8

The yield condition for tensile steel is checked by first assuming that it yields and then using k_{22} or k_{32} in Table 4-5 for k in Equation 4-9 to calculate the steel strain ε_s:

$$\varepsilon_s = \frac{\alpha - k}{k} \lambda \varepsilon_{cr} \qquad \text{Equation 4-9}$$

If ε_s is greater than ε_{sy}, the assumption is correct, otherwise steel has not yielded and one has to use k_{21} or k_{31}. Using the values in Table 4-5 and Equations 4-4 to 4-6 analytical expressions for moment-curvature response and flexural stiffness are calculated.

By considering an under-reinforced section, one can solve for the balanced reinforcement ratio $\rho_{g,bal}$, representing compression failure and steel reaching its yield limit defined as ($\varepsilon_c = \varepsilon_{cu}$ & $\varepsilon_s = \varepsilon_{sy}$). The strain gradient in stage 3.2 of Figure 4-3(c), represents a plastic compressive strain and tensile strain in the post-crack region as:

$$\frac{\lambda_{cu}\varepsilon_{cr}}{kh} = \frac{\kappa\varepsilon_{cr}}{(\alpha - k)h} \qquad \text{Equation 4-10}$$

By substituting λ_{cu} in the expression for k_{32} in Table 4-5 and following with k in Equation 4-10, one can solve for the balance reinforcement ratio as:

$$\rho_{g,bal} = \frac{\alpha[\alpha\omega\xi(\omega - 2\lambda_{cu}) + 2\mu(\kappa - \alpha) + 2\mu\lambda_{cu}(1-\alpha) + \alpha]}{2n[\kappa^2(\zeta\alpha - \zeta - \alpha) + \kappa\lambda_{cu}(3\zeta\alpha - 2\zeta - \alpha) + \zeta\lambda_{cu}^2(2\alpha - 1)]} \qquad \text{Equation 4-11}$$

For single reinforced section with tensile rebar only, i.e., $\zeta = 0$, eqn. (xx) is simplified to:

$$\rho_{g,bal} = \frac{2\mu\left(\lambda_{cu}(\alpha - 1) + \alpha - \kappa\right) + \alpha\gamma\omega(2\lambda_{cu} - \omega) - \alpha}{2n\kappa(\lambda_{cu} + \kappa)} \qquad \text{Equation 4-12}$$

3.3. Simplified Analytical Solutions for Load-Deflection Response

Load-deflection response of various geometries is obtained from the analytical moment and curvature distribution expressions for a few loading cases. The first step is to simplify and represent the normalized moment-curvature as a bilinear response as shown by the dashed line in Figure 4-4 for the case of a deflection hardening beam [61]. By applying the moment-area method to the bilinear moment-curvature diagrams, mid-span deflection can be derived explicitly. For 3PB, additional parameter for plastic length L_p at the vicinity of

the load is needed to simulate the zone undergoing localization in postpeak response while the non-localized zone is elastically unloading. For the 4PB, the distance between the two load points was used as the plastic length L_p. The load-deflection response is affected by the residual tensile strength. The transition from deflection softening to deflection hardening is obtained at a threshold postpeak tensile capacity $\mu_{crit} = \omega/(3\omega\text{-}1) \approx 0.35$, and equations for mid-span deflection δ of 3PB at first bilinear cracking δ_{bcr}, and at ultimate δ_u are presented in Eqs. 14 and 15, (a-c), [61].

$$\delta_{bcr} = \frac{1}{12} L^2 \phi_{bcr}$$

$$\delta_u = \frac{L^2}{24 M_u^2}\left[\left(2M_u^2 - M_u M_{bcr} - M_{bcr}^2\right)\phi_u + \left(M_u^2 + M_u M_{bcr}\right)\phi_{bcr}\right] \quad \mu > \mu_{crit} \qquad \text{Equation 4-13}$$

$$\delta_u = \frac{\phi_u L_p}{8}\left(2L - L_p\right) + \frac{M_u \phi_{bcr} L}{12 M_{bcr}}\left(L - 2L_p\right) \quad \mu < \mu_{crit}$$

Similarly, a set of equations for 4PB can be written as:

$$\delta_{bcr} = \frac{23}{216} L^2 \phi_{bcr}$$

$$\delta_u = \frac{L^2}{216 M_u^2}\left[\left(23M_u^2 - 4M_u M_{bcr} - 4M_{bcr}^2\right)\phi_u + \left(4M_u^2 + 4M_u M_{bcr}\right)\phi_{bcr}\right] \qquad \text{Equation 4-14}$$

$$\mu > \mu_{crit}$$

$$\delta_u = \frac{5L^2 \phi_u}{72} + \frac{M_u L^2 \phi_{bcr}}{27 M_{bcr}} \quad \mu < \mu_{crit}$$

Table 4-1 Normalized Height of Compression (C) and Tension Zones (T) for Each Stage of Normalized Compressive Strain at Top Fiber (λ)

Zone	Normalized height	Stage 1 $0 < \lambda \leq \lambda_{R1}$	Stage 2 $\lambda_{R1} < \lambda \leq \omega$		Stage 3 $\omega < \lambda \leq \lambda_{cu}$	
			2.1 $\varepsilon_s \leq \varepsilon_{sy}$	2.2 $\varepsilon_s > \varepsilon_{sy}$	3.1 $\varepsilon_s \leq \varepsilon_{sy}$	3.2 $\varepsilon_s > \varepsilon_{sy}$
C	$\frac{h_{c2}}{h}$	-	-		$\frac{k(\lambda-\omega)}{\lambda}$	
	$\frac{h_{c1}}{h}$	k	k		$\frac{\omega k}{\lambda}$	
T	$\frac{h_{t1}}{h}$	$1-k$	$\frac{k}{\lambda}$		$\frac{k}{\lambda}$	
	$\frac{h_{t2}}{h}$	-	$\frac{\lambda-(\lambda+1)k}{\lambda}$		$\frac{\lambda-(\lambda+1)k}{\lambda}$	

Table 4-2 Normalized Stress at Vertices in the Stress Diagram for Each Stage of Normalized Compressive Strain at Top Fiber (λ)

Zone	Normalized stress	Stage 1 $0 < \lambda \leq \lambda_{R1}$	Stage 2 $\lambda_{R1} < \lambda \leq \omega$		Stage 3 $\omega < \lambda \leq \lambda_{cu}$	
			2.1 $\varepsilon_s \leq \varepsilon_{sy}$	2.2 $\varepsilon_s > \varepsilon_{sy}$	3.1 εs < εsy	2.1 $\varepsilon_s \leq \varepsilon_{sy}$
C	$\frac{f_{c2}}{E\varepsilon_{cr}}$	-	-		$\gamma\omega$	
	$\frac{f_{c1}}{E\varepsilon_{cr}}$	$\gamma\lambda$	$\gamma\lambda$		$\gamma\omega$	
T	$\frac{f_{t1}}{E\varepsilon_{cr}}$	$\frac{(1-k)\lambda}{k}$	1		1	
	$\frac{f_{t2}}{E\varepsilon_{cr}}$	-	μ		μ	
	$\frac{f_s}{E\varepsilon_{cr}}$	$\frac{n\lambda(a-k)}{k}$	$\frac{n\lambda(a-k)}{k}$	$n\kappa$	$\frac{n\lambda(a-k)}{k}$	$n\kappa$

Table 4-3 Normalized Force Component for Each Stage of Normalized Compressive Strain at Top Fiber (λ)

Zone	Normalized force component	Stage 1 $0 < \lambda < \lambda_{R1}$	Stage 2 $\lambda_{R1} < \lambda < \omega$		Stage 3 $\omega < \lambda < \lambda_{cu}$	
			2.1 $\varepsilon_s < \varepsilon_{sy}$	2.2 $\varepsilon_s > \varepsilon_{sy}$	3.1 $\varepsilon_s < \varepsilon_{sy}$	3.2 $\varepsilon_s > \varepsilon_{sy}$
C	$\frac{F_{c2}}{bhE\varepsilon_{cr}}$	-	-		$\frac{\gamma\omega k(\lambda-\omega)}{\lambda}$	
	$\frac{F_{c1}}{bhE\varepsilon_{cr}}$	$\frac{1}{2}\gamma\lambda k$	$\frac{1}{2}\gamma\lambda k$		$\frac{\gamma\omega^2 k}{2\lambda}$	
T	$\frac{F_{t1}}{bhE\varepsilon_{cr}}$	$\frac{\lambda}{2k}(k-1)^2$	$\frac{k}{2\lambda}$		$\frac{k}{2\lambda}$	
	$\frac{F_{t2}}{bhE\varepsilon_{cr}}$	-	$\frac{\mu}{\lambda}(\lambda-k\lambda-k)$		$\frac{\mu}{\lambda}(\lambda-k\lambda-k)$	
	$\frac{F_s}{bhE\varepsilon_{cr}}$	$\frac{\rho_g n\lambda}{k}(\alpha-k)$	$\frac{\rho_g n\lambda}{k}(\alpha-k)$	$\rho_g n\kappa$	$\frac{\rho_g n\lambda}{k}(\alpha-k)$	$\rho_g n\kappa$

Table 4-4 Normalized Moment Arm of Force Component for Each Stage of Normalized Compressive Strain at Top Fiber (λ)

Zone	Normalized moment arm	Stage 1 $0 < \lambda < \lambda_{R1}$	Stage 2 $\lambda_{R1} < \lambda < \omega$		Stage 3 $\omega < \lambda < \lambda_{cu}$	
			2.1 $\varepsilon_s < \varepsilon_{sy}$	2.2 $\varepsilon_s > \varepsilon_{sy}$	3.1 $\varepsilon_s < \varepsilon_{sy}$	3.2 $\varepsilon_s > \varepsilon_{sy}$
C	$\frac{y_{c2}}{h}$	-	-		$\frac{k(\omega+\lambda)}{2\lambda}$	
	$\frac{y_{c1}}{h}$	$\frac{2}{3}k$	$\frac{2}{3}k$		$\frac{2\omega k}{3\lambda}$	
T	$\frac{y_{t1}}{h}$	$\frac{2}{3}(1-k)$	$\frac{2k}{3\lambda}$		$\frac{2k}{3\lambda}$	
	$\frac{y_{t2}}{h}$	-	$\frac{\lambda+(1-\lambda)k}{2\lambda}$		$\frac{\lambda+(1-\lambda)k}{2\lambda}$	
	$\frac{y_s}{h}$	$\alpha-k$	$\alpha-k$		$\alpha-k$	

Table 4-5 Normalized Neutral Axis, Moment, Curvature and Stiffness for Each Stage of Normalized Compressive Strain at Top Fiber (λ).

Stage	k	M'	ϕ'	K'
1	$k_1 = \frac{B_1 + \sqrt{B_1^2 - (\gamma-1)(B_2-1)}}{\gamma - 1}$	$MM_1' = C_1 k^2 + C_2 k + C_3 - 6\lambda + \frac{C_4 + 2\lambda}{k}$	$\phi_1' = \frac{\lambda}{2k_1}$	$K_1' = \frac{M_1'}{\phi_1'}$
2.1	$k_{21} = \frac{B_3 + \sqrt{B_3^2 - B_2 B_4 \lambda}}{B_4}$	$MM_{21}' = C_5 k^2 + C_6 k + C_3 + \frac{C_4}{k}$	$\phi_{21}' = \frac{\lambda}{2k_{21}}$	$K_{21}' = \frac{M_{21}'}{\phi_{21}'}$
2.2	$k_{22} = \frac{B_5 + \sqrt{B_5^2 - B_4 B_6 \lambda}}{B_4}$	$MM_{22}' = C_7 k^2 + C_8 k + C_9 + \frac{C_{10}}{k}$	$\phi_{22}' = \frac{\lambda}{2k_{22}}$	$K_{22}' = \frac{M_{22}'}{\phi_{22}'}$
3.1	$k_{31} = \frac{B_3 + \sqrt{B_3^2 - B_2 B_7 \lambda}}{B_7}$	$MM_{31}' = C_{11} k^2 + C_{12} k + C_3 + 3\mu + \frac{C_4}{k}$	$\phi_{31}' = \frac{\lambda}{2k_{31}}$	$K_{31}' = \frac{M_{31}'}{\phi_{31}'}$
3.2	$k_{32} = \frac{B_5 + \sqrt{B_5^2 - B_6 B_7 \lambda}}{B_7}$	$MM_{32}' = C_{11} k^2 + C_8 k + C_9 + \frac{C_{10}}{k}$	$\phi_{32}' = \frac{\lambda}{2k_{32}}$	$K_{32}' = \frac{M_{32}'}{\phi_{32}'}$

where, the coefficients are:

$$B_1 = -(n\rho\zeta + n\rho + 1);\ B_2 = 2n\rho(\alpha\zeta - \alpha - \zeta);\ B_3 = -(n\rho\zeta\lambda + n\rho\lambda - \mu);\ B_4 = \frac{\xi\lambda^2 + 2\mu\lambda + 2\mu - 1}{\lambda};$$

$$B_5 = -(n\rho\zeta\lambda - \kappa\rho\lambda - \mu);\ B_6 = 2n\rho\zeta(\alpha - 1);\ B_7 = \frac{2\omega\xi\lambda - \omega^2\xi + 2\mu\lambda + 2\mu - 1}{\lambda};$$

$$C_1 = 2\lambda(\xi - 1);\ C_2 = 6\lambda(n\rho\zeta + n\rho + 1);\ C_3 = 12n\rho\lambda[\zeta(\alpha - 1) - \alpha];\ C_4 = 6n\rho\lambda[\zeta(\alpha - 1)^2 + \alpha^2];\ C_5 = \frac{2(\xi\lambda^3 + 1)}{\lambda^2};$$

$$C_6 = 6n\rho(\zeta + 1)\lambda;\ C_7 = \frac{2\xi\lambda^3 + 3\mu\lambda^2 - 3\mu + 2}{\lambda^2};\ C_8 = 6(n\rho\zeta\lambda - \kappa n\rho - \mu)k;\ C_9 = 12n\rho\zeta\lambda(\alpha - 1) + 6n\rho\kappa\alpha + 3\mu;$$

$$C_{10} = 6n\rho\zeta\lambda(\alpha - 1)^2;\ C_{11} = \frac{3\omega\xi\lambda^2 - \omega^3\xi + 3\mu\lambda^2 - 3\mu + 2}{\lambda^2};\ C_{12} = 6(n\rho\zeta\lambda + n\rho\lambda - \mu)$$

4.3 Parametric Studies

Parametric studies of post-crack tensile strength and reinforcement ratio as two main reinforcing factors were conducted. Changes in the location of neutral axis, moment-curvature response, and stiffness degradation of a beam are normalized with respect to first cracking parameters of plain FRC. In addition to the two baseline parameters: E =24 GPa

and ε_{cr} =125 μstr, typical material models for SFRC and steel rebar were used that include: β_{tu} = 160, γ = 1, ω = 8.5, λ_{cu} = 28, n = 8.33, κ = 16 and α = 0.8. The variables of the study were: residual tensile strength parameter $0.0 \leq \mu \leq 1.0$ and reinforcement ratio $0.0 \leq \rho_g \leq 0.03$.

Figure 4-5 illustrates the effects of parameters μ and ρ_g on the normalized moment-curvature diagram. Figure 4-5(a) shows the effect of increasing the residual tensile strength from brittle (μ = 0) to ductile (μ = 1) in plain FRC. Noted that at a level μ = 0.33 which is sufficiently close to μ_{crit} = 0.35, the flexural response is almost perfectly-plastic, beyond which the deflection softening shifts to hardening. The elastic-plastic tensile response of FRC (μ = 1) yields an upper bound normalized moment capacity of 2.7. With a main flexural reinforcement of ρ_g = 0.01 (Figure 4-5(b)), the normalized moment capacity of 5.8 is achieved. Note that as ρ_g increases, the response eventually changes from a ductile under-reinforced to over-reinforced. Figure 4-5(c) reveals the effect of residual tensile strength (μ = 0.0–1.0) for a fixed reinforcement ratio of 0.01 while Figure 4-5(d) shows the marginal benefit of FRC with μ = 0.33 compared to the reinforced concrete system. The moment capacity slightly increases in comparison with the reinforced concrete without any fibers (Figure 4-5(b)). The present analysis ignores the contribution of the fiber phase to the compression response in the context of internal confinement, however than can be easily incorporated in the input parameters.

The neutral axis depth ratio k and the normalized secant stiffness K' are also affected by changes in μ and ρ_g. The neutral axis starts at a slightly higher value than 0.5 for a conventional reinforced concrete system (μ = 0, $\rho_g \geq 0$), since a larger compressive zone is needed to balance the summation of tensile forces of concrete and steel. The neutral axis

location, k decreases as the compressive strain at top fiber λ increases as functions of μ and ρ_g. This shift diminishes as ρ_g or μ increase, indicating the role of fiber and reinforcement in maintaining the tensile force after cracking. For plain FRC with low fiber contents, the normalized secant stiffness K' equals to 1.0 in elastic range ($\phi' \leq 1.0$) while K' is larger than 1.0 in conventional reinforced concrete systems as shown in Figure 4-6. Figure 4-6(a) shows that for the same reinforcement ratio, the rate of stiffness degradation decreased with addition of fibers (μ increased) as the curvature increases since the crack is bridged by distributed fibers through its depth. Figure 4-6(b) shows that for a given fiber residual tensile strength, μ = 0.33 higher ρ_g levels in conventional reinforced concrete efficiently reduces the rate of stiffness reduction and retains the post-crack stiffness. More details on the effect of parameters have been discussed elsewhere [191].

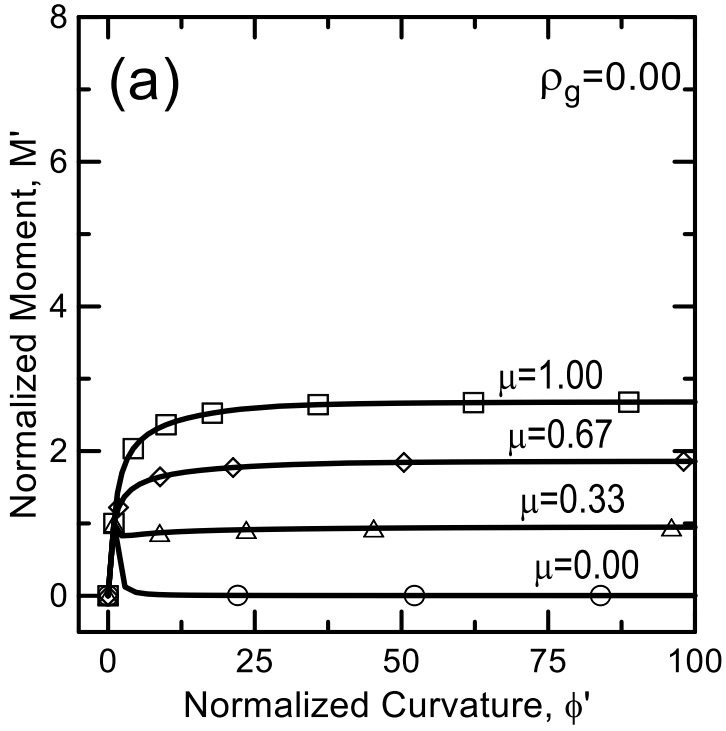
(a)
ρ_g=0.00
μ=1.00
μ=0.67
μ=0.33
μ=0.00
Normalized Moment, M'
Normalized Curvature, ϕ'
0
2
4
6
8
0
25
50
75
100

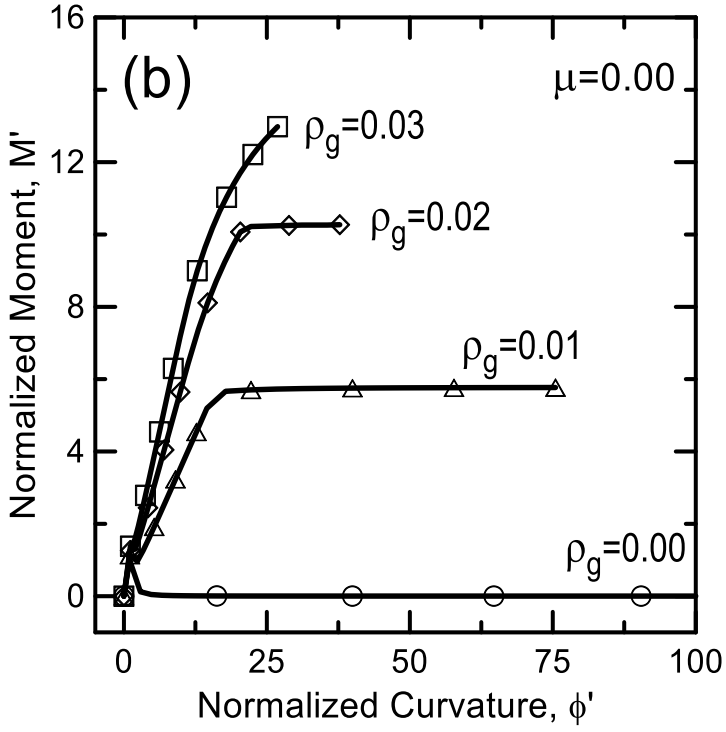
(b)
μ=0.00
ρ_g=0.03
ρ_g=0.02
ρ_g=0.01
ρ_g=0.00
Normalized Moment, M'
Normalized Curvature, ϕ'
0
4
8
12
16
0
25
50
75
100

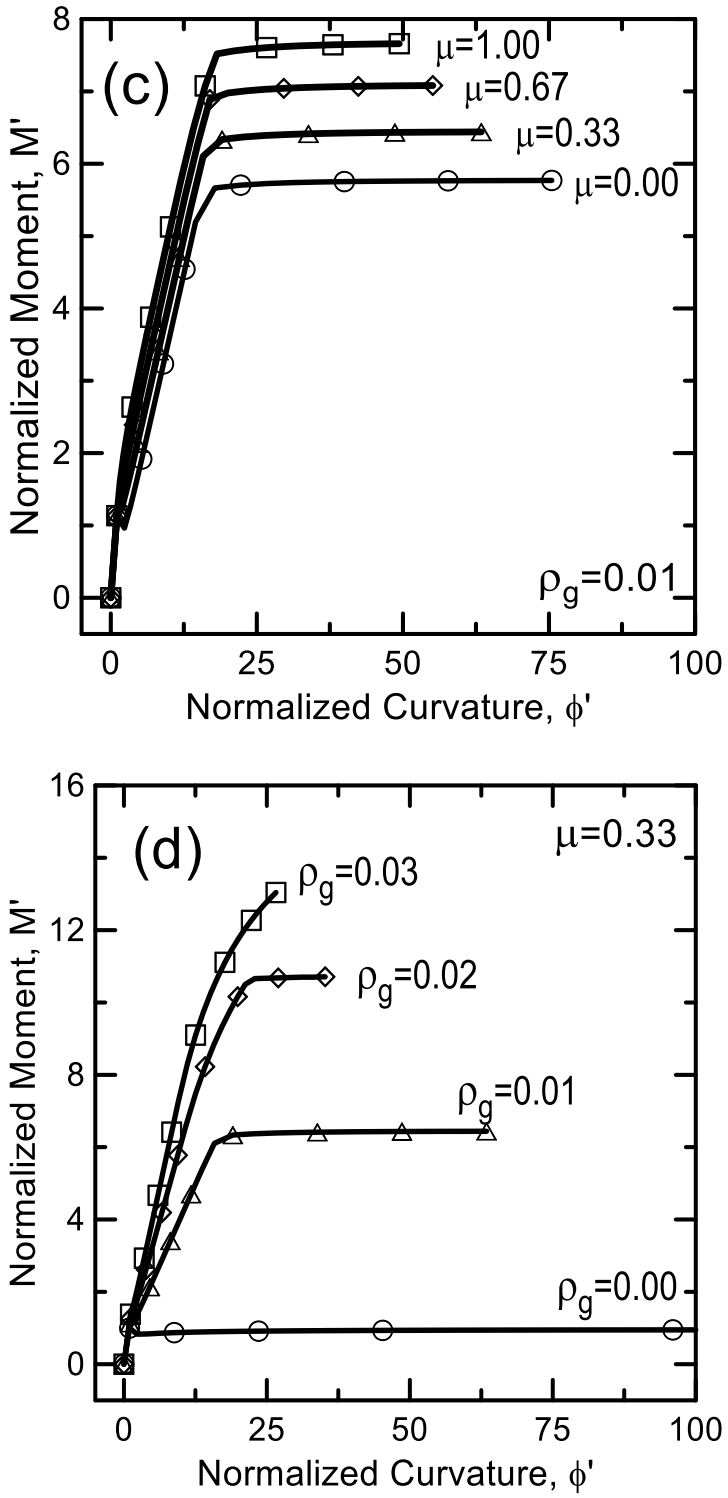

Figure 4-5 Parametric Studies of Normalized-Moment Curvature Diagram for Different Levels of Post Crack Tensile Strength Parameter μ and Reinforcement Ratio ρ_g [169].

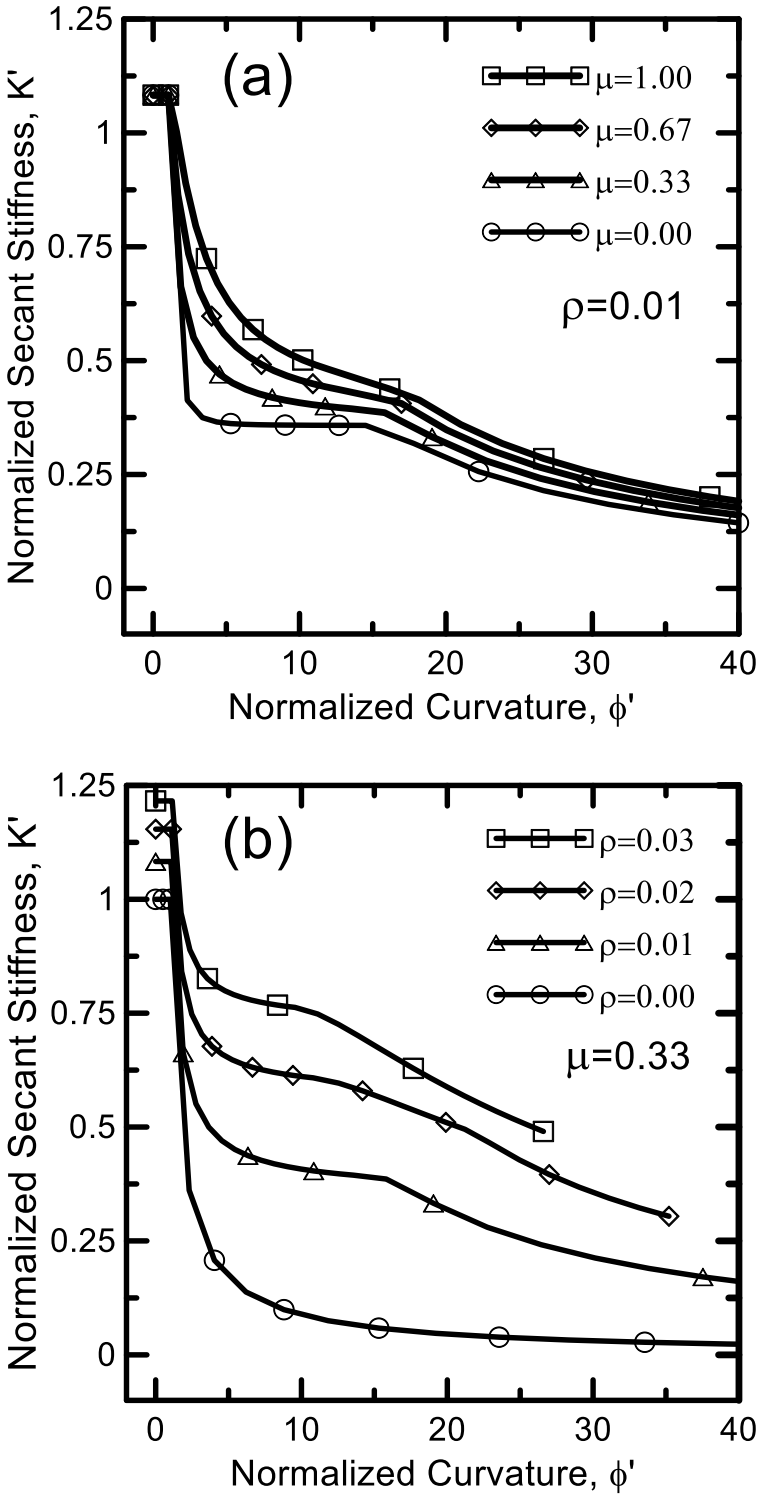

Figure 4-6 Parametric Studies of Normalized Secant Stiffness for Different Levels of Reinforcement Ratio ρ_g and Residual Tensile Strength Parameter μ [169].

4.4 Design

The ultimate moment capacity as a function of residual tensile strength and reinforcement ratio can be used as a convenient design tool for combinations of reinforcements. A limiting case of ductile moment-curvature response of under-reinforced section (Figure 4-5) is obtained at ($\lambda \to \infty$) by applying L'Hopital's rule in the limit case of compressive strain failure ($\lambda = \lambda_{cu} = \infty$). Thus, the ultimate moment M_u is reasonably approximated by the moment at infinite compressive strain M_∞ for under-reinforced section ($\rho_g < \rho_{g,bal}$). The yielding condition of steel is obtained by comparing it to the reinforcement ratio at balance failure as defined by Equation 4-12. Normalized moment at infinite M'_∞, is found by substituting the expression for k_{32} into the M'_{32} in Table 4-5, followed by taking the limit of λ to ∞, which results in:

$$M'_\infty = \lim_{\lambda_{cu}\to\infty} M'_{32} = \frac{3\kappa n\rho[\kappa n\rho(\zeta-1)^2 - 2\omega\gamma(\zeta\alpha-\zeta+\alpha) - 2\mu(\zeta\alpha+\alpha-1)] - 3\mu\omega\gamma}{\omega\gamma+\mu}$$

Equation 4-15

And the corresponding ultimate moment capacity M_u:

$$M_u \approx M'_\infty M_{cr} = \frac{3\kappa n\rho[\kappa n\rho(\zeta-1)^2 - 2\omega\gamma(\zeta\alpha-\zeta+\alpha) - 2\mu(\zeta\alpha+\alpha-1)] - 3\mu\omega\gamma}{\omega\gamma+\mu} M_{cr}$$

Equation 4-16

For single reinforced section:

$$M'_\infty = \lim_{\lambda_{cu}\to\infty} M'_{32} = \frac{6\rho_g n\kappa\left(\mu\alpha-\mu+\alpha\omega\right) + 3\omega\mu - 3\left(\rho_g n\kappa\right)^2}{\omega+\mu}$$

Equation 4-17

And the corresponding ultimate moment capacity M_u:

$$M_u \approx M'_\infty M_{cr} = \frac{6\rho_g n\kappa\left(\mu\alpha-\mu+\alpha\omega\right) + 3\omega\mu - 3\left(\rho_g n\kappa\right)^2}{\omega+\mu} M_{cr}$$

Equation 4-18

For a plain FRC beam without any flexural reinforcement ($\rho_g = 0$) and modulus of FRC are equal in compression and tension ($\gamma = E_c/E = 1$), Equation 4-16 reduces to $M_\infty' = 3\omega\mu/(\omega+\mu)$ reported previously [61]. The applicability of Equation 4-16 is limited to the sections that fail in a ductile manner only when flexural steel reinforcement ratio is below the balance failure $\rho_{g,bal}$ defined in Equation 4-12.

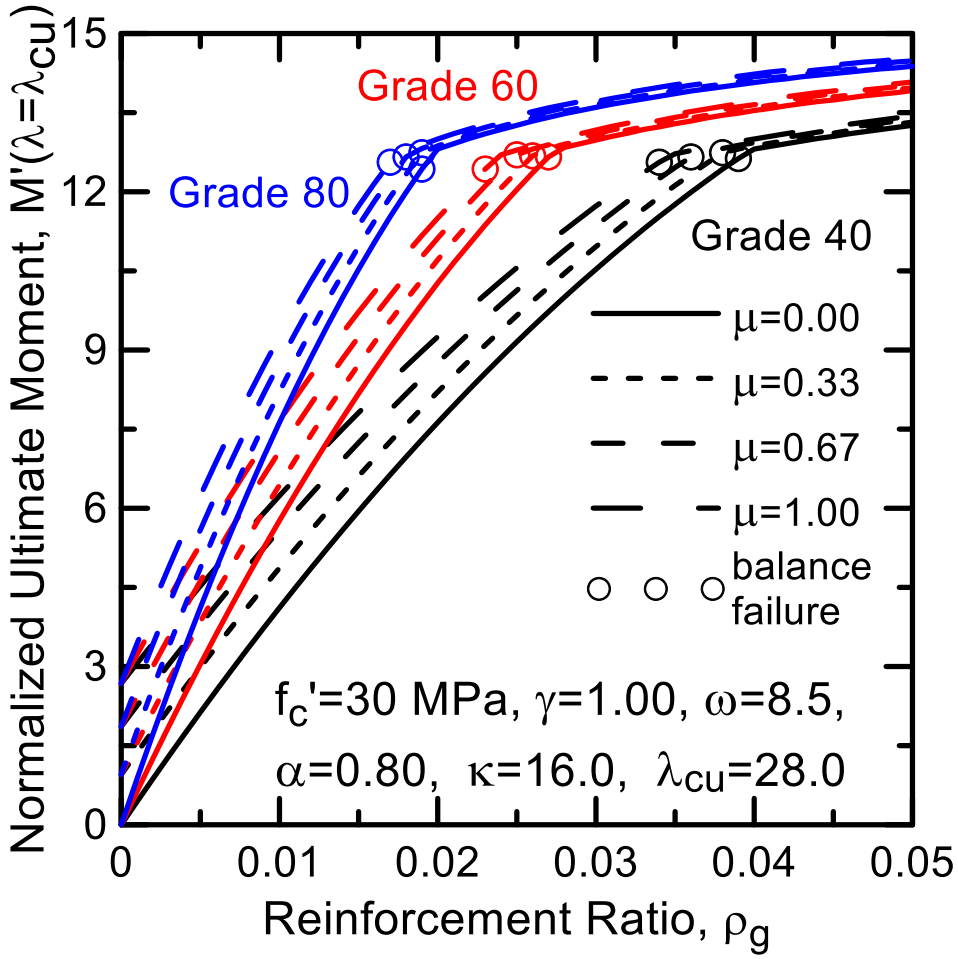

Figure 4-7 Design Chart of Normalized Ultimate Moment Capacity (Determined at $\lambda = \lambda_{cu}$) for Different Levels of Post Crack Tensile Strength μ and Reinforcement Ratio ρ_g [169].

Figure 4-7 shows a design chart for the numerical model used in the parametric studies with various grades of steel as defined by ASTM A615 [192]. The moment capacity is strongly dependent on the amount of reinforcement ratio whereas the residual tensile

strength provides extra capacity. Under-reinforced sections are shown by the curves below the balance failure points ($\rho_g \leq \rho_{g,bal}$, shown as hollow circles), as the moment capacity increases proportional to the reinforcement ratio. When $\rho_g > \rho_{g,bal}$, the strength of all curves marginally increases as the steel fails to reach yield strength. Effect of fiber contribution becomes negligible as the failure is governed by compression failure of concrete. Figure 4-7 also shows that as the steel grade increases from 40 to 80 (280 MPa to 550 MPa), the balanced failure is obtained at much lower reinforcement ratio, from about 0.035 to 0.015. To design flexural HRC members with this chart, the ultimate moment M_u due to factored load is determined and then normalized with cross sectional geometry while the cracking moment of the plain matrix M_{cr} is employed to obtain demand ultimate moment capacity M_u'. The chart is then used to select any combination of normalized residual tensile strength μ, grade of steel, and reinforcement ratio ρ_g that meets the demand for M_u'.

As a comparison with the customary design approach, one can develop a parameter representing coefficient of resistance R as a design chart [193], and proceed to determine a beam size for a given required moment. The normalized moment design chart in Figure 4-8 is equivalent to the well-established R-chart for single under-reinforced concrete design nominal moment capacity M_n as:

$$M_n = Rbd^2 = \rho f_{sy}\left(1 - 0.59\rho\frac{f_{sy}}{f_c'}\right)bd^2 \qquad \text{Equation 4-19}$$

where d is the effective depth, $\rho = A_s/bd$ is the reinforcement ratio. For the proposed model, the moment equations are represented as ratio of ultimate moment to cracking moment and reinforcing depth to full depth $\alpha = d/h$ as:

$$R = \frac{M(\lambda_{cu})}{bd^2} = \frac{M'(\lambda_{cu})M_{cr}}{bd^2} = \frac{M'(\lambda_{cu})}{bd^2}\frac{1}{6}bh^2\varepsilon_{cr}E = \frac{\varepsilon_{cr}E}{6\alpha^2}M'(\lambda_{cu}) \qquad \text{Equation 4-20}$$

Therefore, R is the normalized moment $M'(\lambda_{cu})$ by a factor of $\varepsilon_{cr}E/(6\alpha^2)$. In order to use equivalent set of input parameters, the compressive constitutive relationship is calibrated using parabolic stress-strain curve of Hognestad [194] up to the ultimate strain εcu = 0.003 to obtain equivalent areas under both curves:

$$\int_0^{\varepsilon_{cu}} 2\left(\frac{\varepsilon_c}{\varepsilon_{c0}}\right) - \left(\frac{\varepsilon_c}{\varepsilon_{c0}}\right)^2 d\varepsilon_c = \frac{1}{2}\varepsilon_{cy}\sigma_{cy} + \left(\varepsilon_{cu} - \varepsilon_{cy}\right)\sigma_{cy} \qquad \text{Equation 4-21}$$

By substituting $\varepsilon_{cu} = 1.5\varepsilon_{c0}$ and $\sigma_{cy} = 0.85f_c'$ in Equation 4-22, the compressive yield strain ε_{cy} and compressive modulus E_c can be estimated as.

$$\varepsilon_{cy} = \frac{6}{17}\varepsilon_{c0}; \qquad E_c = \frac{\sigma_{cy}}{\varepsilon_{cy}} = \frac{289\,f_c'}{120\varepsilon_{c0}} \qquad \text{Equation 4-22}$$

Three concrete strength f_c' = 30, 43 and 55 MPa and two grades of steel 280 and 420 MPa with Young's modulus E_s of 200 GPa were used to compare the coefficient of resistance defined by the ACI approach (Equation 4-19) and the proposed method (Equation 4-20]. Other assumed parameters were the first cracking strain ε_{cr} = 0.0001, compressive strain at peak stress ε_{c0} = 0.002, normalized depth of steel reinforcement α = 0.8, and assumption of no softening range for plain concrete (μ=0). For the proposed method, a set of material parameters of concrete and steel are used to calculate $\rho_{g,bal}$ by Equation 4-12 and compared it to the reinforcement ratio ρ_g used in a beam section. For $\rho_g < \rho_{g,bal}$, the expression k_{31} and M_{31}' in Table 4-5 are used to determine moment at ultimate compressive strain $M(\lambda_{cu})'$. For $\rho_g > \rho_{g,bal}$, the expression k_{32} and M_{32}' in Table 4-5 are used instead. Finally, by

substituting the calculated $M(\lambda_{cu})'$ in Equation 4-20 one obtains the R value for the proposed method.

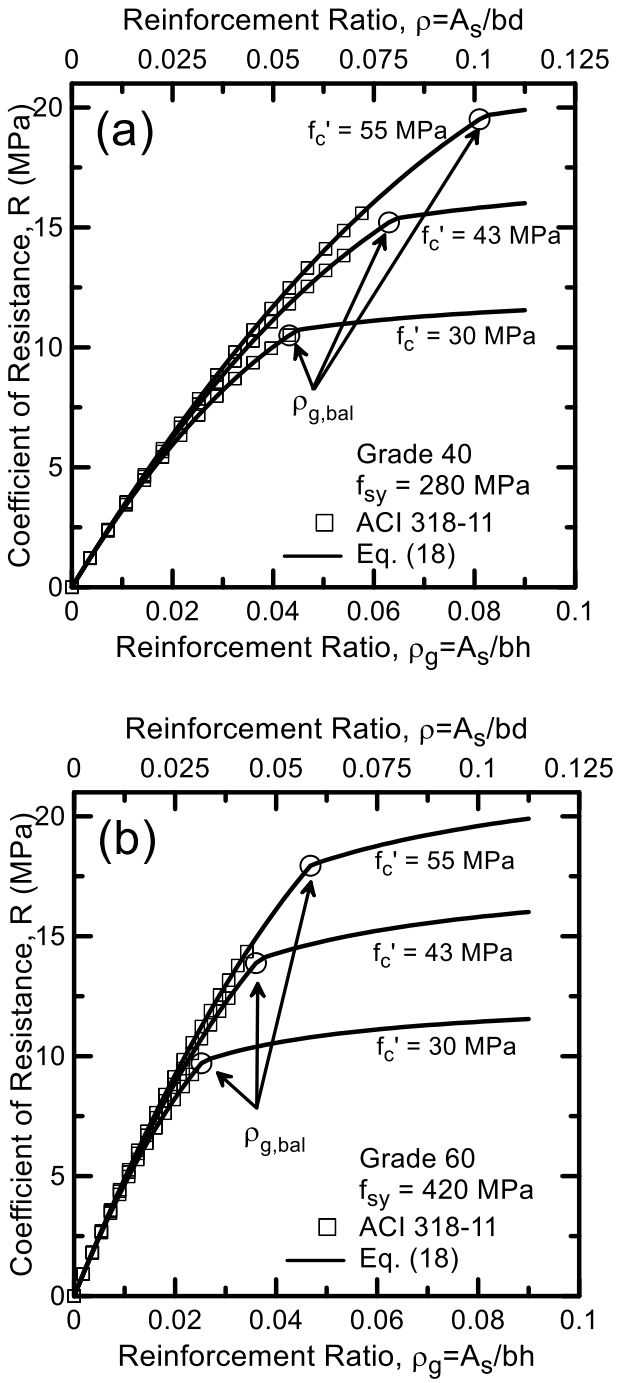

Figure 4-8 Comparison of Coefficient of Resistance Using ACI Stress Block Method and the Equation 4-20; (a) Steel Grade 40 (280 MPa); (b) Steel Grade 60 (420 MPa) [169].

Figure 4-8 compares the two methods showing excellent agreement for the reinforcement ratio up to the ACI balance failure (Equation 4-20). These points are generally lower than the balance failure points $\rho_{g,bal}$ defined by Equation 4-12 as marked by a circle symbol. The discrepancy between these two balanced failures is due to the fact that ACI approach uses a conservative empirical parameter β_1 in the calculation of the reinforcement ratio at balance failure while the $\rho_{g,bal}$ is analytically determined by Equation 4-12. Note that the applicable range of the *R* by ACI approach is terminated at the balance failure whereas the current method predicts a wider range in both under- and over-reinforced beam sections.

5.2. Minimum Reinforcement Ratio

A reinforced concrete beam can fail abruptly if its residual strength is less than the cracking moment of unreinforced concrete section computed from its modulus of rupture. In order to prevent such failures, the minimum reinforced ratio is defined as level of reinforcement to ensure that residual capacity is equal to the cracking moment, and is determined in accordance with ACI 318-11 Section 10.5 [195] and Eurocode 2 [196]. The minimum required reinforcement is empirically stipulated to be a function of concrete strength, yield limit of steel, as well as the beam size [197, 198, 199]. An analytical expression for minimum reinforcement ratio $\rho_{g,min}$ is derived explicitly by setting the moment from Equation 4-16 at infinity to unity, $M'_{\infty} = 1$. A quadratic equation is obtained such that the root satisfying $\rho_{min} \leq \rho_{bal}$ is valid and expressed as:

$$\rho_{\min} = -\frac{L_1 - \sqrt{L_2 + L_1^2}}{3n\kappa(\zeta - 1)^2} \qquad \text{Equation 4-23}$$

where $L_1 = 3(1-\alpha)(\zeta\omega\gamma + \mu) - 3\alpha(\zeta\mu + \omega\gamma)$,

$L_2 = 3\zeta^2(3\mu\omega\gamma - \omega\gamma - \mu) - 3\omega\gamma(6\zeta\mu + 2\zeta + 3\mu) + 3(2\zeta\mu - \omega\gamma - \mu)$

For single reinforced:

$$\rho_{\min} = \frac{3G_1 - \sqrt{G_2 + 9G_1^2}}{3\alpha n\kappa} \qquad \text{Equation 4-24}$$

where $G_1 = \mu(\alpha - 1) + \alpha\gamma\omega, G_2 = 3\gamma\omega(3\mu - 1) - 3\mu$ and parameter α in the denominator is introduced to express and correlate the present formulation that is based on the gross section *bh* to the effective cross section *bd*. The equation is further simplified as an analytical minimum reinforcement ratio for conventional reinforced concrete system by substituting parameters: μ=0, γ = 3/4 and ω = 6 into Equation 4-24.

$$\rho_{\min} = \frac{9\alpha - \sqrt{81\alpha^2 - 6}}{2\alpha n\kappa} \qquad \text{Equation 4-25}$$

Figure 4-9 shows minimum reinforcement ratio as a function μ and α, and compared to specifications of ACI 318-11 and Eurocode 2 (EC2) with varying grades of steel. For an assumed value of α=0.5-0.9, the trend shows that as the residual tensile strength μ increases, the required minimum reinforcement $\rho_{min,rc}$ decreases indicating the role of steel fibers in substitution of reinforcement. Additionally, the effect of α is diminishing gradually and all the curves converge when $\mu \rightarrow \mu_{crit}$ =0.35 in accordance with the onset of deflection hardening, where no longitudinal reinforcement is required to meet the minimum strength requirement.

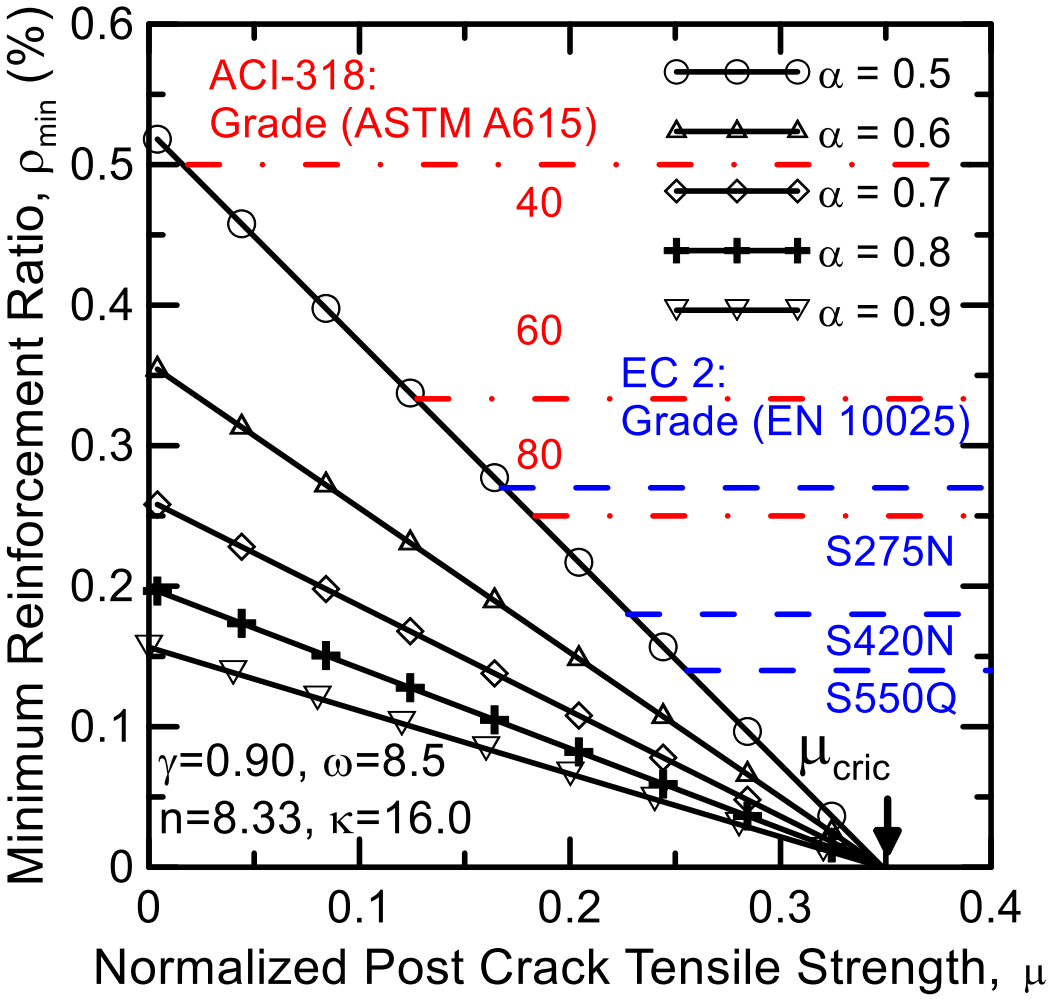

Figure 4-9 Comparison of Minimum Reinforcement Ratio ρ_{min} Between Proposed Method and Design Codes: ACI 318-11 and Eurocode 2 (EC 2) [169].

4.5 Application to Flanged Beams

Besides the rectangular beams, flanged sections are widely used in engineering applications as well, such as the beam-slab system, bridge girder, and recently developed UHPC pi-girder [200]. The use of flanged beams made of high performance concrete materials as an economical and effective solution reduces the materials consumption, self-weight, as well as improves the mechanical strength, ductility and durability due to the superior material properties.

Figure 4-10 presents three distinct material models used in the derivation of parametric response of HRC beams. Material parameters are described as two intrinsic parameters: tensile modulus E and the first cracking tensile strain ε_{cr} while other variables are normalized with respect to these intrinsic parameters. Figure 4-10(a) shows an idealized tension model with an elastic range of stress increases linearly with E up to the first cracking tensile strength of coordinates (ε_{cr}, σ_{cr}). In the post-crack region, the stress is constant at $\sigma_p = \mu\sigma_{cr} = \mu\varepsilon_{cr}E$ and terminates at the ultimate tensile strain $\varepsilon tu = \beta tu\varepsilon cr$. Figure 4-10(b) shows the elastic-perfectly plastic compression response with a modulus $Ec = \gamma E$. The plastic range initiates at strain $\varepsilon cy = \omega\varepsilon cr$ corresponding to yield stress $\sigma cy = \omega\gamma\varepsilon crE$ and terminated at $\varepsilon_{cu} = \lambda_{cu}\varepsilon_{cr}$. Figure 4-10(c) is the elastic-perfectly plastic steel model using yield strain and stress of $\varepsilon_{sy} = \kappa\varepsilon_{cr}$ and $f_{sy} = \kappa n\varepsilon_{cr}E$ as defined by normalized parameters: κ and n. No termination level is specified for steel strain. The debonding of steel is characterized by a reduced modulus after reaching a certain stress level f_{sdb} where the interface starts to debond. As a result of relative displacement between steel rebar and concrete matrix, the level of strain in rebar is lower than the nominal strain in cross section at the same level. Geometrical parameters are also normalized with the beam dimensions of width b and full depth h as shown in Figure 4-10(d) with steel parameters defined as area $A_s = \rho_g bh = \rho_g bd/\alpha$ at the reinforced depth $d = \alpha h$. The reinforcement ratio ρ_g is defined per gross sectional area bh, and differs slightly from the conventional definition based on term bd used in reinforced concrete nomenclature. The material models for tension and compression of FRC and the model for steel rebar are presented as:

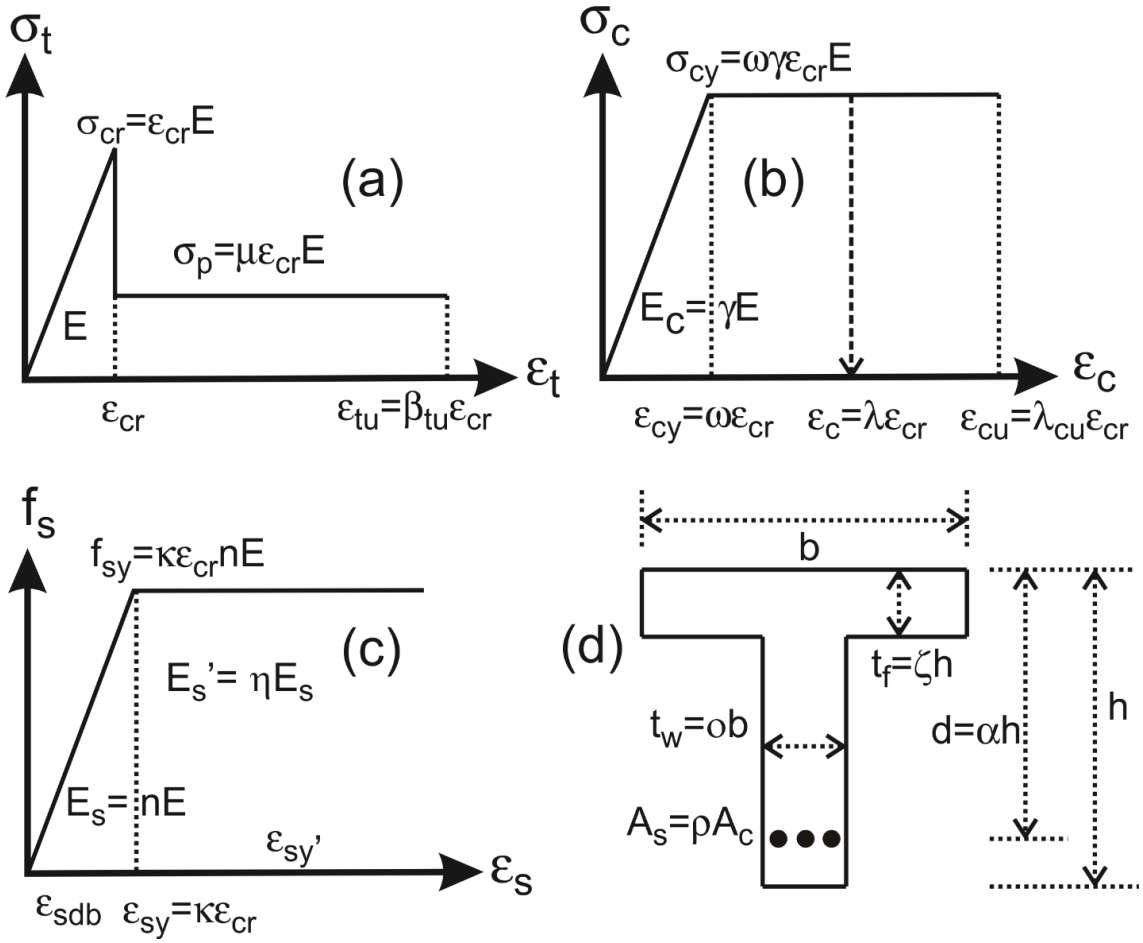

Figure 4-10 Material Model for Single Reinforced Concrete Design (a) Tension Model; (b) Compression Model; (c) Steel Model; (d) Beam Cross Section.

In derivation of moment-curvature for a beam with T-section, the assumption of plane section remaining plane is assumed. By applying linear strain distribution across the depth, ignoring shear deformation, and using material models of Eqs. (1)-(3) and Figure 4-10, the stress distributions as shown in Figure 4-11 are obtained. The normalized compressive strain at the top concrete fiber λ is used as an independent variable to incrementally impose flexural deformation for three distinct stages. The first stage ($0 < \lambda \leq \lambda_{R1}$) corresponds to elastic range until tensile strain at the bottom fiber reaches ε_{cr}. Stage 2 ($\lambda_{R1} < \lambda \leq \omega$) corresponds to an elastic compressive strain and the tensile strain in post-crack region. Finally, stage 3 ($\omega < \lambda \leq \lambda_{cu}$) corresponds to the plastic compressive strain while the tensile

strain is in post-crack range. For stages 2 and 3 two possible scenarios exist: the steel is either elastic, or yielding, therefore stages 2 &3 are each divided into two sub-stages, 2.1, 2.2, or 3.1, and 3.2 where term 1 represents elastic and term 2 represents plastic response. For the sake of simplification, the compression force contributed by the web section is not considered as the area is much smaller compared to the flange section (shown as the shaded region in Figure 4-11(a)).

Three stages of stress distribution in Figure 4-11, show the height of compression and tension zones normalized with respect to the beam depth h, while stresses are normalized with respect to the first cracking strength $E\varepsilon_{cr}$ and presented in Tables 4-6 and 7, respectively. Forces and their lines of action are normalized with respect to cracking tensile force $bhE\varepsilon_{cr}$ and beam depth h as shown in Tables 4-8 and 9.

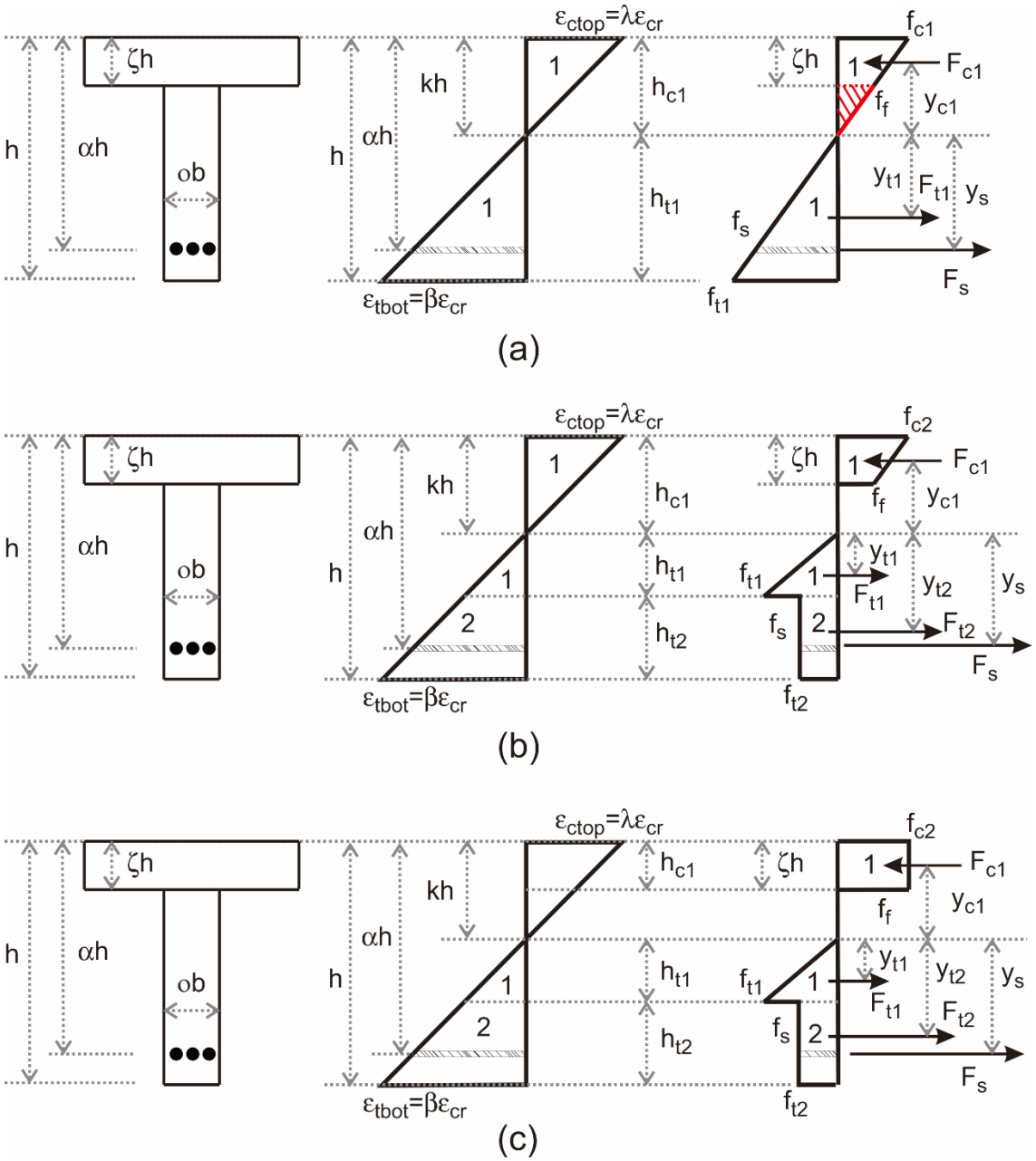

Figure 4-11 Strain and Stress Diagram at Three Stage of Applied Compressive Strain at Top Fiber (λ); (a) Stage 1 ($0 < \lambda < \lambda_{R1}$) Elastic Compression-Elastic Tension; (b) Stage 2:$\lambda_{R1} < \lambda < \omega$, Elastic Compression–Post Crack Tension; (c) Stage 3: $\omega < \lambda < \lambda_{cu}$ Plastic Compression–Post Crack Tension.

The net section force is obtained as the difference between the tension and compression forces, and solved for internal equilibrium to obtain the normalized location of neutral axis, *k*. When steel is elastic in stages 1, 2.1 and 3.1, the expressions for net force are in the

quadratic forms and result in two possible solutions for k. With a large scale of numerical tests covering the practical range of material parameters, only one solution yields the valid value in the range $0<k<1$. During stage 1, the singularity of k_1 for $\gamma = 1$, requires an asymptotic expression. When steel is in yield condition in stages 2.2 or 3.2, there is a unique solution for k as presented in Table 4-10. Internal moment is obtained by integrating the force components using the distance to the neutral axis as the moment arm, and the curvature is represented as the ratio of compressive fiber strain ($\varepsilon_{ctop} = \lambda\varepsilon_{cr}$) to the depth of neutral axis kh. Effective flexural stiffness is defined as the ratio of the moment to the curvature at any given imposed λ. By normalizing the moment M_i, curvature ϕ_i and stiffness K_i for each stage i, using the cracking values M_{cr}, ϕ_{cr} and K_{cr} are expressed as analytical expressions M_i', ϕ_i' and K_i' as presented in Table 4-11. Unlike the rectangular beam where the cracking moment can be simply calculated as $M_{cr}=bh^2E\varepsilon_{cr}/6$, the expression for T-section is complicated. However, parametric studies (see Figure 4-12) show that the cracking moment of T-section is not sensitive to the changing of flange thickness ζ, but almost linearly related to the web thickness o. Therefore, it is assumed that the cracking moment is a linear function of o in a practical range from 0.05 to 0.30, and the least square fit yields the equation $M_{cr}=(o/5+1/200)\, bh^2E\varepsilon_{cr}$.

$$
\begin{aligned}
&F_i = F_i' F_{cr}; \qquad F_{cr} = (\zeta + o - \zeta o) bh E\varepsilon_{cr} \\
&\phi_i = \phi_i' \phi_{cr}; \qquad \phi_{cr} = \frac{2\varepsilon_{cr}}{h} \\
&\frac{M_{cr}}{bh^2 E\varepsilon_{cr}} = \frac{1}{5}o + \frac{1}{200}; \; M_{cr} = \left(\frac{1}{5}o + \frac{1}{200}\right) bh^2 E\varepsilon_{cr} \\
&K_i = K_i' K_{cr}; \qquad K_{cr} = \frac{1}{12} bh^3
\end{aligned}
$$

Equation 4-26

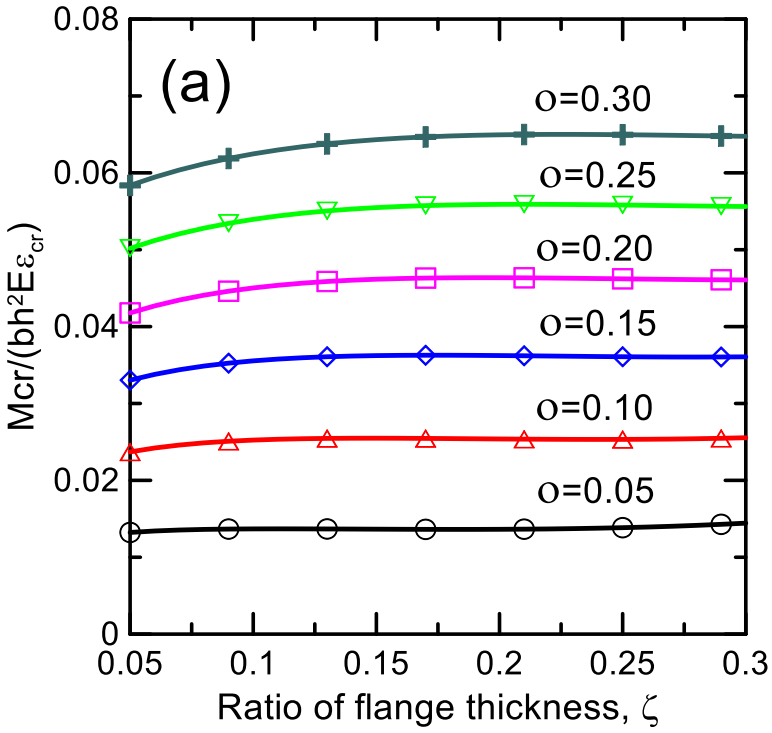
(a)
o=0.30
o=0.25
o=0.20
o=0.15
o=0.10
o=0.05
Mcr/(bh²Eεcr)
Ratio of flange thickness, ζ
0.08
0.06
0.04
0.02
0
0.05
0.1
0.15
0.2
0.25
0.3

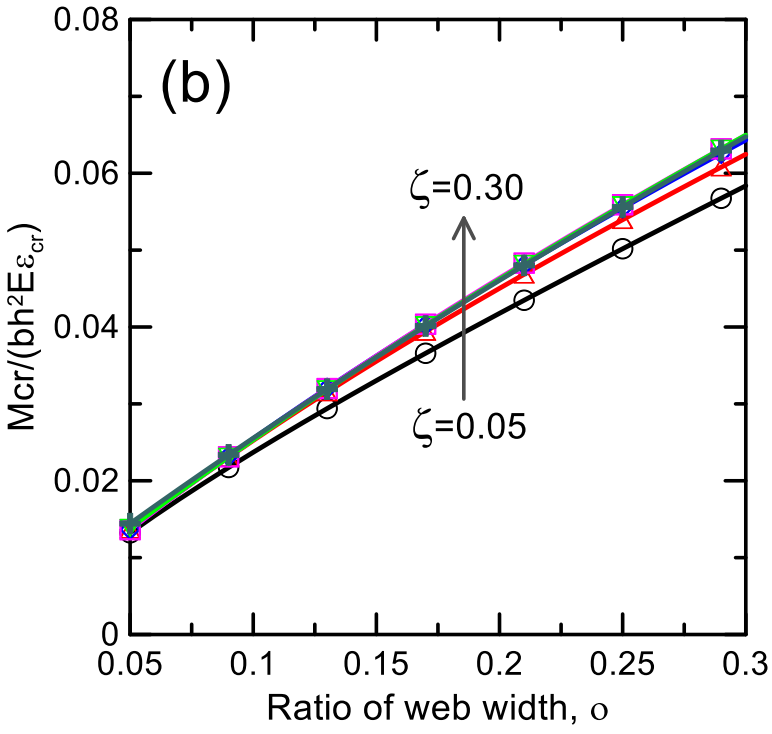
(b)
ζ=0.30
ζ=0.05
Mcr/(bh²Eεcr)
Ratio of web width, o
0.08
0.06
0.04
0.02
0
0.05
0.1
0.15
0.2
0.25
0.3

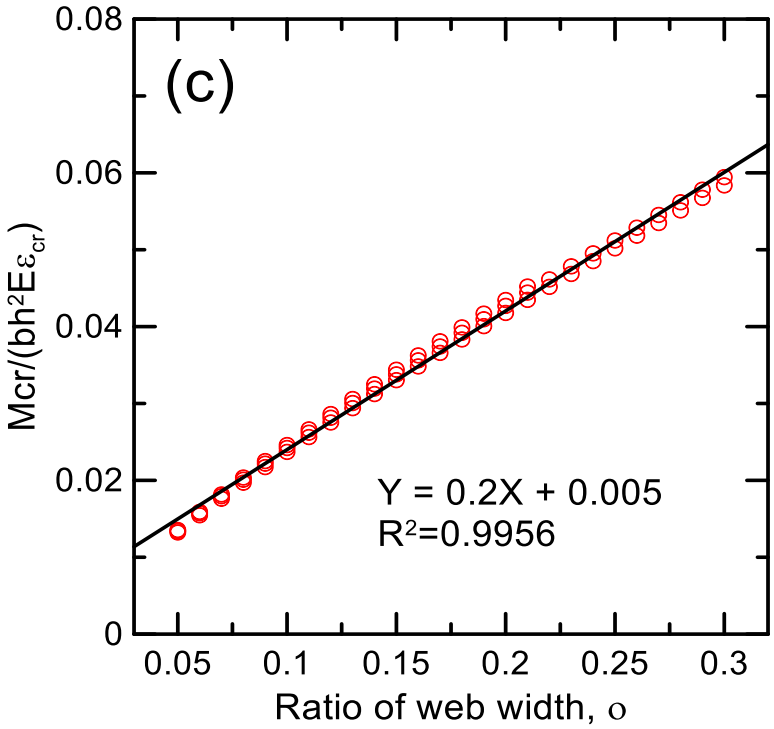

Figure 4-12 Normalized Cracking Moment Versus (a) Ratio of Flange Thickness and (b) Ratio of Web Width; (c) Linear Correlation Between M_{cr} and Ratio of Web Width.

The compressive strain corresponding to end of elastic region 1 (λ_{R1}) is determined from the strain gradient diagram shown in Figure 4-11(a).

$$\frac{\lambda_{R1}\varepsilon_{cr}}{kh} = \frac{\varepsilon_{cr}}{(1-k)h}$$

$$\lambda_{R1} = \frac{k_1}{1-k_1}$$

Equation 4-27

The yield condition for tensile steel is checked by first assuming that it yields and then using k_{22} or k_{32} in Table 4-10 for k in Equation 4-28 to calculate the steel strain ε_s:

$$\varepsilon_s = \frac{\alpha - k}{k}\lambda\varepsilon_{cr}$$

Equation 4-28

If ε_s is greater than ε_{sy}, the assumption is correct, otherwise steel has not yielded and one has to use k_{21} or k_{31}. Using the values in Table 4-10 and Eqs. (4) - (6) analytical expressions for moment-curvature response and flexural stiffness are calculated.

By considering an under-reinforced section, one can solve for the balanced reinforcement ratio $\rho_{g,bal}$, representing compression failure and steel reaching its yield limit defined as ($\varepsilon_c = \varepsilon_{cu}$ & $\varepsilon_s = \varepsilon_{sy}$). The strain gradient in stage 3.2 of Figure 4-11(c), represents a plastic compressive strain and tensile strain in the post-crack region as:

$$\frac{\lambda_{cu}\varepsilon_{cr}}{kh} = \frac{\kappa\varepsilon_{cr}}{(\alpha - k)h} \qquad \text{Equation 4-29}$$

By substituting λ_{cu} in the expression for k_{32} in Table 4-10 and following with k in Equation 4-29, one can solve for the balance reinforcement ratio as:

$$\rho_{g,bal} = -\frac{2\zeta\gamma\omega(\kappa + \lambda_{cu}) + 2\mu o\lambda_{cu}(\alpha - 1) + 2\mu o(\alpha - \kappa) - \alpha o}{2n\kappa(\zeta o - \zeta - o)(\lambda_{cu} + \kappa)} \qquad \text{Equation 4-30}$$

The coefficients of B_i, C_i of these equations are provided in Table 4-11. Load-deflection response of various geometries is obtained from the analytical moment and curvature distribution expressions using the step shown in the previous chapter.

Table 4-6 Normalized Height of Compression (C) and Tension (T) Zones for Each Stage of Normalized Compressive Strain at Top Fiber (λ).

Zone	Normalized height	Stage 1 $0 < \lambda \leq \lambda_{R1}$	Stage 2 $\lambda_{R1} < \lambda \leq \omega$		Stage 3 $\omega < \lambda \leq \lambda_{cu}$	
			2.1 $\varepsilon_s \leq \varepsilon_{sy}$	2.2 $\varepsilon_s > \varepsilon_{sy}$	3.1 $\varepsilon_s \leq \varepsilon_{sy}$	3.2 $\varepsilon_s > \varepsilon_{sy}$
C	$\frac{h_{c1}}{h}$	k	k		ζ	
T	$\frac{h_{t1}}{h}$	$1-k$	$\frac{k}{\lambda}$		$\frac{k}{\lambda}$	
	$\frac{h_{t2}}{h}$	-	$-\frac{k\lambda + k - \lambda}{\lambda}$		$-\frac{k\lambda + k - \lambda}{\lambda}$	

Table 4-7 Normalized Stress at Vertices in the Stress Diagram for Each Stage of Normalized Compressive Strain at Top Fiber (λ).

Zone	f'	Stage 1 $0 < \lambda \leq \lambda_{R1}$	Stage 2 $\lambda_{R1} < \lambda \leq \omega$		Stage 3 $\omega < \lambda \leq \lambda_{cu}$	
			2.1 $\varepsilon_s \leq \varepsilon_{sy}$	2.2 $\varepsilon_s > \varepsilon_{sy}$	3.1 $\varepsilon_s \leq \varepsilon_{sy}$	3.2 $\varepsilon_s > \varepsilon_{sy}$
C	$\frac{f_{c1}}{\sigma_{cr}}$	$\gamma\lambda$	$\gamma\lambda$		$\gamma\omega$	
T	$\frac{f_{t1}}{\sigma_{cr}}$	$\frac{(1-k)\lambda}{k}$	1		1	
	$\frac{f_{t2}}{\sigma_{cr}}$	-	μ		μ	
	$\frac{f_s}{\sigma_{cr}}$	$\frac{n(a-k)\lambda}{k}$	$\frac{n(a-k)\lambda}{k}$	$n\kappa$	$\frac{n(a-k)\lambda}{k}$	$n\kappa$
Junction	$\frac{f_f}{\sigma_{cr}}$	$\frac{(k-\zeta)\gamma\lambda}{k}$	$\frac{(k-\zeta)\gamma\lambda}{k}$		$\gamma\omega$	

Table 4-8 Normalized Force Component for Each Stage of Normalized Compressive Strain at Top Fiber (λ).

Zone	F'	Stage 1 $0 < \lambda \leq \lambda_{R1}$	Stage 2 $\lambda_{R1} < \lambda \leq \omega$		Stage 3 $\omega < \lambda \leq \lambda_{cu}$	
			2.1 $\varepsilon_s \leq \varepsilon_{sy}$	2.2 $\varepsilon_s > \varepsilon_{sy}$	3.1 $\varepsilon_s \leq \varepsilon_{sy}$	3.2 $\varepsilon_s > \varepsilon_{sy}$
C	$\frac{F_{c1}}{F_{cr}}$	$\frac{\gamma\lambda(2k-\zeta)\zeta}{2k(\zeta+o-\zeta o)}$	$\frac{\gamma\lambda(2k-\zeta)\zeta}{2k(\zeta+o-\zeta o)}$		$\frac{\gamma\omega\zeta}{\zeta+o-\zeta o}$	
	$\frac{F_{t1}}{F_{cr}}$	$\frac{\lambda o(k-1)^2}{2k(\zeta+o-\zeta o)}$	$\frac{ko}{2\lambda(\zeta+o-\zeta o)}$		$\frac{ko}{2\lambda(\zeta+o-\zeta o)}$	
T	$\frac{F_{t2}}{F_{cr}}$	-	$-\frac{\mu o(k\lambda+k-\lambda)}{\lambda(\zeta+o-\zeta o)}$		$-\frac{\mu o(k\lambda+k-\lambda)}{\lambda(\zeta+o-\zeta o)}$	
	$\frac{F_s}{F_{cr}}$	$\frac{\rho_g n\lambda(\alpha-k)}{k}$	$\frac{\rho_g n\lambda(\alpha-k)}{k}$	$\rho_g n\kappa$	$\frac{\rho_g n\lambda(\alpha-k)}{k}$	$\rho_g n\kappa$

Table 4-9 Normalized Moment Arm (y') of Force Component for Each Stage of Normalized Compressive Strain at Top Fiber (λ).

Zone	y'	Stage 1 $0 < \lambda \leq \lambda_{R1}$	Stage 2 $\lambda_{R1} < \lambda \leq \omega$ 2.1 $\varepsilon_s \leq \varepsilon_{sy}$	 2.2 $\varepsilon_s > \varepsilon_{sy}$	Stage 3 $\omega < \lambda \leq \lambda_{cu}$ 3.1 $\varepsilon_s \leq \varepsilon_{sy}$	 3.2 $\varepsilon_s > \varepsilon_{sy}$
C	$\frac{y_{c1}}{h}$	$\frac{2(3k^2-3k\zeta+\zeta^2)}{3(2k-\zeta)}$	$\frac{2(3k^2-3k\zeta+\zeta^2)}{3(2k-\zeta)}$		$k-\frac{\zeta}{2}$	
	$\frac{y_{t1}}{h}$	$\frac{2}{3}(1-k)$	$\frac{2k}{3\lambda}$		$\frac{2k}{3\lambda}$	
T	$\frac{y_{t2}}{h}$	-	$-\frac{k\lambda-k-\lambda}{2\lambda}$		$-\frac{k\lambda-k-\lambda}{2\lambda}$	
	$\frac{y_s}{h}$	$\alpha-k$	$\alpha-k$		$\alpha-k$	

Table 4-10 Normalized Height of Neutral Axis for Each Stage.

Location of neutral axis	Stage	k
Web	1	$k_1 = -\dfrac{[B_8 - B_1] + \sqrt{[B_8 - B_1]^2 - o[2\alpha B_1 - \gamma\zeta^2 - o]}}{o}$
	2.1	$k_{21} = -\dfrac{[B_5 - B_1\lambda] + \sqrt{[B_5 - B_1\lambda]^2 - B_2[2\alpha B_1 - \gamma\zeta^2]}}{B_2}\lambda$
	2.2	$k_{22} = -\dfrac{[\kappa B_1 + B_5] - \sqrt{[\kappa B_1 + B_5]^2 + B_2\gamma\zeta^2}}{B_2}\lambda$
	3.1	$k_{31} = \dfrac{[B_1\lambda + B_6] + \sqrt{[B_1\lambda + B_6]^2 - 2\alpha B_1 B_2}}{B_2}\lambda$
	3.2	$k_{32} = -\dfrac{2(\kappa B_1 - B_6)\lambda}{B_2}$
Flange	1	$k_1 = -\dfrac{[B_9 - B_1] + \sqrt{[B_9 - B_1]^2 - \gamma[2\alpha B_1 + o(\zeta^2 - 1)]}}{\gamma}$
	2.1	$k_{21} = \dfrac{[B_1\lambda + B_7] + \sqrt{[B_1\lambda + B_7]^2 - B_3[2\alpha B_1 + o\zeta^2]}}{B_3}\lambda$
	2.2	$k_{22} = -\lambda\dfrac{[\kappa B_1 - B_7] - \sqrt{[\kappa B_1 - B_7]^2 - B_3 o\zeta^2}}{B_3}$
	3.1	$k_{31} = \dfrac{[B_1\lambda + B_7] + \sqrt{[B_1\lambda + B_7]^2 - B_4[2\alpha B_1 + o\zeta^2]}}{B_4}\lambda$
	3.2	$k_{32} = -\dfrac{[\kappa B_1 - B_7] - \sqrt{[\kappa B_1 - B_7]^2 - B_4 o\zeta^2}}{B_4}\lambda$

Where $B_1 = n\rho(o\zeta - o - \zeta)$, $B_2 = o(2\lambda\mu + 2\mu - 1)$, $B_3 = (\gamma + o)\lambda^2 + 2\mu o(\lambda + 1) - o$,

$B_4 = o\lambda^2 + 2\gamma\omega\lambda + 2\mu o\lambda + 2\mu o - o$ $B_5 = \gamma\zeta\lambda - \mu o$, $B_6 = -\gamma\omega\zeta + \mu o$, $B_7 = o\zeta\lambda + \mu o$,

$B_8 = \gamma\zeta + o$, $B_9 = o(1 - \zeta)$

Table 4-11 Normalized Moment of Neutral Axis for Each Stage.

Location of neutral axis	Stage	M'
Web	1	$M_1^{'} = -2o\lambda k^2 - 6[C_1 - \gamma\zeta - o]\lambda k + 6[2\alpha C_1 - \gamma\zeta^2 - o]\lambda - \frac{C_{11}}{k}$
	2.1	$M_{21}^{'} = C_2 k^2 - 6[C_1\lambda + C_8]k + 12\alpha C_1\lambda + C_5 - \frac{6\alpha^2 C_1 - 2\gamma\zeta^3}{k}\lambda$
	2.2	$M_{22}^{'} = C_2 k^2 + 6[\kappa C_1 - C_8]k - 6\kappa\alpha C_1 + C_5 + \frac{2\gamma\zeta^3\lambda}{k}$
	3.1	$M_{31}^{'} = C_2 k^2 - 6[C_1\lambda + C_9]k + 12\alpha C_1\lambda + C_6 - \frac{6\alpha^2 C_1\lambda}{k}$
	3.2	$M_{32}^{'} = C_2 k^2 + 6[\kappa C_1 - C_9]k - 6\kappa\alpha C_1 + C_6$
Flange	1	$M_1^{'} = -2\gamma\lambda k^2 - 6[C_1 - o(\zeta + 1)]\lambda k + 6[2\alpha C_1 + o(\zeta^2 - 1)]\lambda - \frac{C_{12}\lambda}{k}$
	2.1	$M_{21}^{'} = C_3 k^2 - 6[C_1\lambda + C_{10}]k + 12\alpha C_1\lambda + C_7 - \frac{6\alpha^2 C_1 + 2o\zeta^3}{k}\lambda$
	2.2	$M_{22}^{'} = C_3 k^2 + 6[\kappa C_1 - C_{10}]k - 6\kappa\alpha C_1 + C_7 - \frac{2o\zeta^3\lambda}{k}$
	3.1	$M_{31}^{'} = C_4 k^2 - 6[C_1\lambda + C_{10}]k + 12\alpha C_1\lambda + C_7 - \frac{6\alpha^2 C_1 + 2o\zeta^3}{k}\lambda$
	3.2	$M_{32}^{'} = C_4 k^2 + 6[\kappa C_1 - C_{10}]k - 6\kappa\alpha\lambda C_1 + C_7 - \frac{2o\zeta^3\lambda}{k}$

Where $C_1 = n\rho(o\zeta - o - \zeta)$, $C_2 = \frac{(3\mu\lambda^2 - 3\mu + 2)o}{\lambda^2}$, $C_3 = \frac{2(\gamma + o)\lambda^3 + 3\mu o(\lambda^2 - 1) + 2o}{\lambda^2}$,

$C_4 = \frac{2o\lambda^3 + 3\mu o\lambda^2 + 3\lambda^2\omega\gamma - 3\mu o + 2o}{\lambda^2}$, $C_5 = -6\gamma\zeta^2\lambda + 3\mu o$, $C_6 = -3\gamma\omega\zeta^2 + 3\mu o$,

$C_7 = 6o\zeta^2\lambda + 3\mu o$, $C_8 = -\gamma\zeta\lambda + \mu o$, $C_9 = -\gamma\omega\zeta + \mu o$, $C_{10} = o\zeta\lambda + \mu o$,

$C_{11} = 2[3\alpha^2 C_1 - \gamma\zeta^3 - o]\lambda$, $C_{12} = 2[3\alpha^2 C_1 + o(\zeta^3 - 1)]\lambda$

Parametric studies of post-crack tensile strength and reinforcement ratio as two main reinforcing factors were conducted. Changes in the location of neutral axis, moment-curvature response, and stiffness degradation of a beam are normalized with respect to first cracking parameters of plain FRC. In addition to the two baseline parameters: E =25 GPa and ε_{cr} =90 μstr, typical material models for SFRC and steel rebar were used that include: $\beta_{tu} = 160$, $\gamma = 1$, $\omega = 8.5$, $\lambda_{cu} = 28$, $n = 8.33$, $\kappa = 16$ and $\alpha = 0.8$. The variables of the study were: residual tensile strength parameter $0.0 \leq \mu \leq 1.0$ and reinforcement ratio $0.0 \leq \rho_g \leq 0.03$.

Figure 4-13 illustrates the effects of parameters μ and ρ_g on the normalized moment-curvature diagram. Figure 4-13(a) shows the effect of increasing the residual tensile strength from brittle ($\mu = 0$) to ductile ($\mu = 1$) in plain FRC. Noted that at a level $\mu = 0.33$ which is sufficiently close to $\mu_{crit} = 0.35$, the flexural response is almost perfectly-plastic, beyond which the deflection softening shifts to hardening. The elastic-plastic tensile response of FRC ($\mu = 1$) yields an upper bound normalized moment capacity of 2.7. With a main flexural reinforcement of $\rho_g = 0.01$ (Figure 4-13(b)), the normalized moment capacity of 5.8 is achieved. Note that as ρ_g increases, the response eventually changes from a ductile under-reinforced to over-reinforced. Figure 4-13(c) reveals the effect of residual tensile strength ($\mu = 0.0$–1.0) for a fixed reinforcement ratio of 0.01 while Figure 4-13(d) shows the marginal benefit of FRC with $\mu = 0.33$ compared to the reinforced concrete system. The moment capacity slightly increases in comparison with the reinforced concrete without any fibers (Figure 4-13(b)). The present analysis ignores the contribution of the fiber phase to the compression response in the context of internal confinement, however than can be easily incorporated in the input parameters.

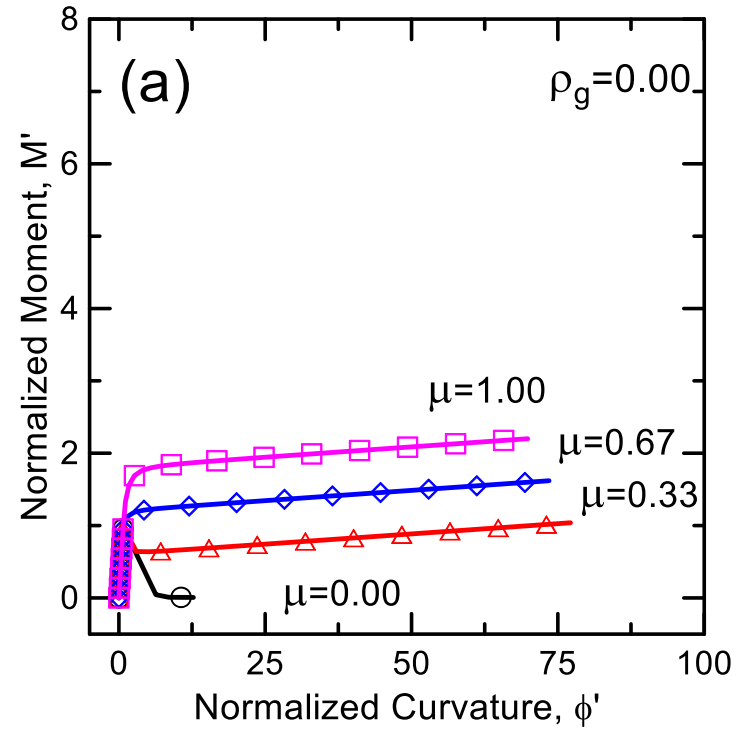
(a)
ρ_g=0.00
Normalized Moment, M'
Normalized Curvature, ϕ'
μ=1.00
μ=0.67
μ=0.33
μ=0.00
0
2
4
6
8
0
25
50
75
100

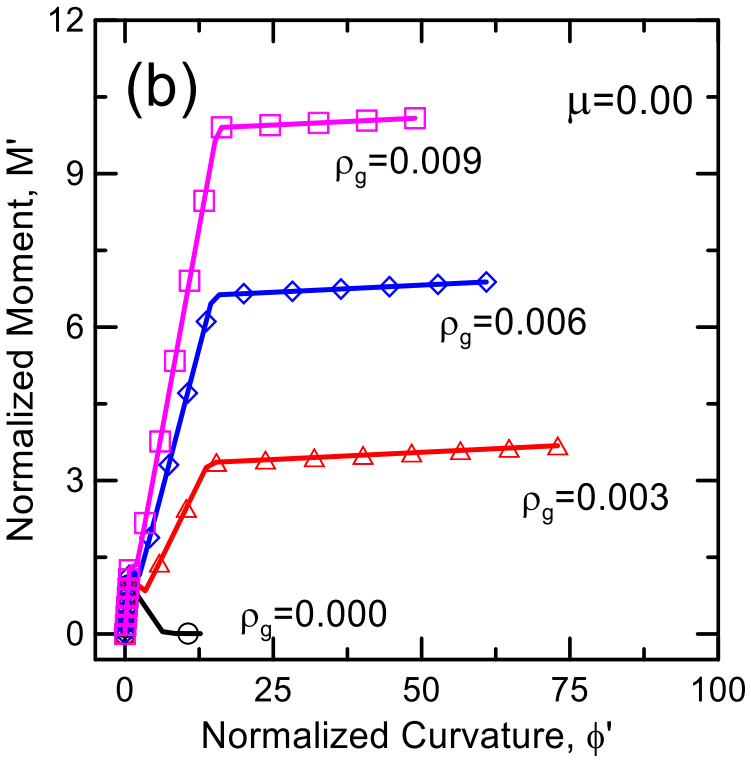
(b)
μ=0.00
Normalized Moment, M'
Normalized Curvature, ϕ'
ρ_g=0.009
ρ_g=0.006
ρ_g=0.003
ρ_g=0.000
0
3
6
9
12
0
25
50
75
100

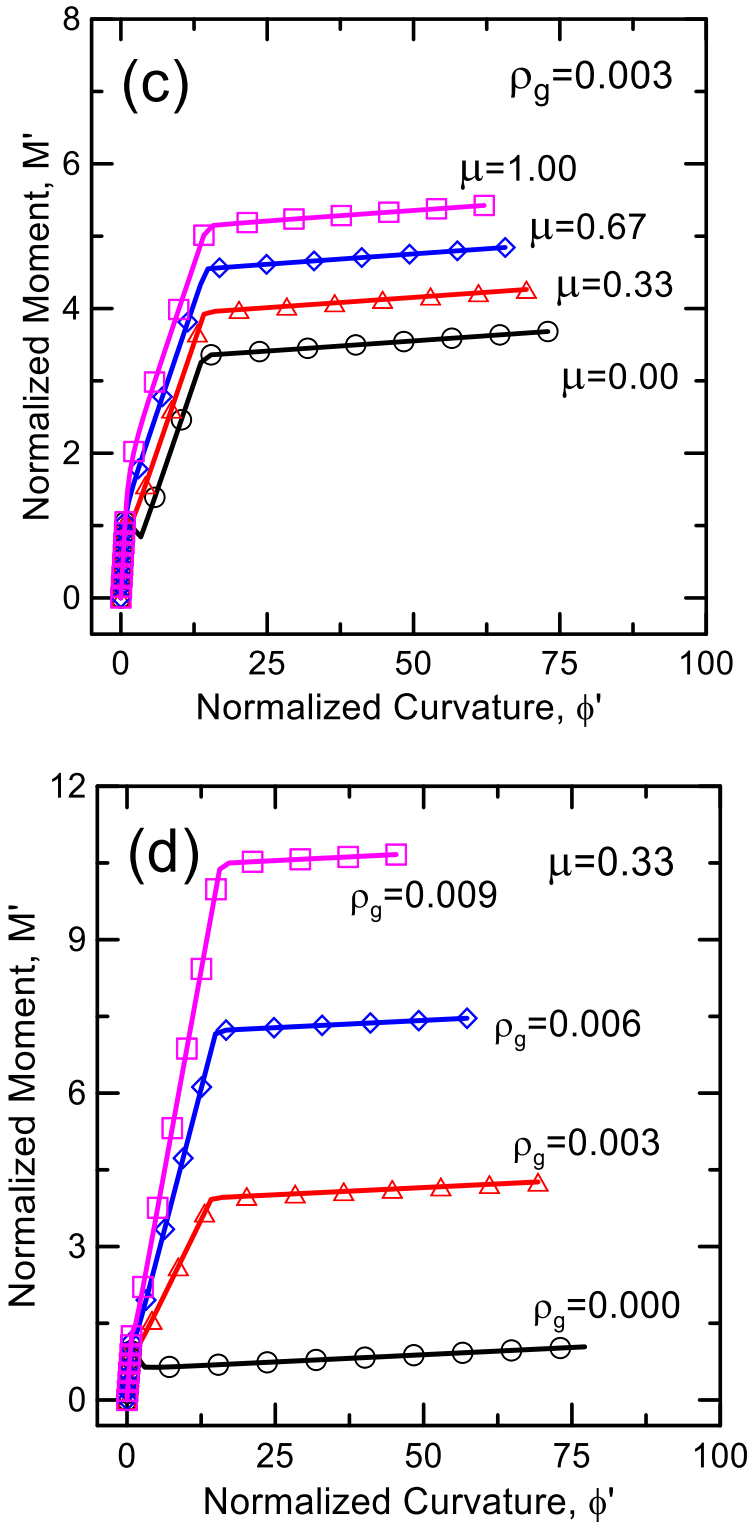

Figure 4-13 Parametric Studies of Normalized Moment Curvature Diagram for Different Levels of Post Crack Tensile Strength Parameter μ and Reinforcement Ratio ρ_g.

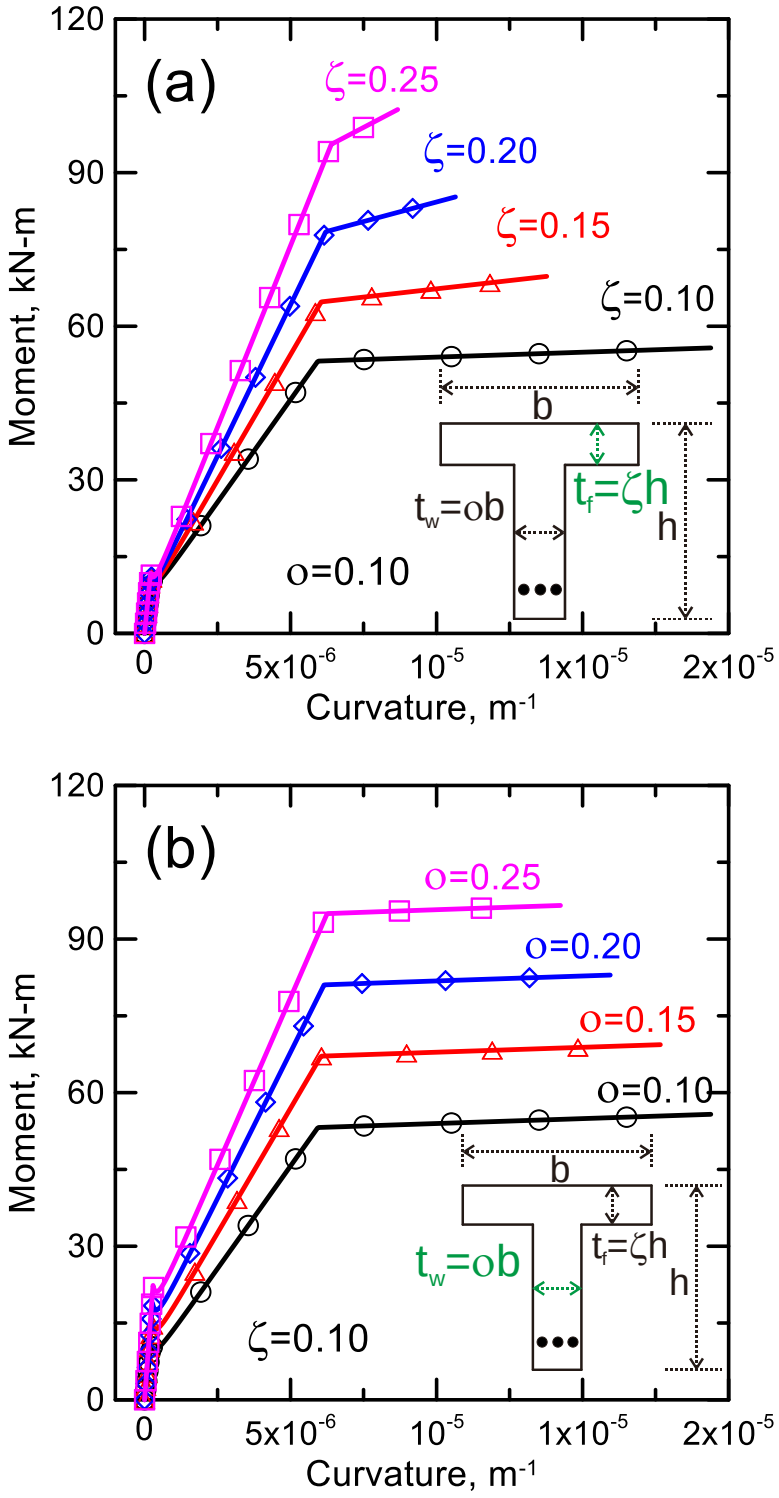

Figure 4-14 Parametric Studies of Normalized Moment-Curvature Diagram for Different Ratios of Flange Thickness (ζ) and Web Width (o).

On another set of comparison, the changing parameters were selected as the sectional geometries o and ζ, as shown in Figure 4-14. Since the two parameters are related to the geometries, i.e., cracking moment M_{cr}, moment curvature with dimensions are compared using a cross section of b=500mm, d=600mm, span of 3000mm, μ=0.33, ρ_g=0.3% (other material parameters are same). The two ratios o and ζ are both changing from 0.1 to 0.25 to cover a practical range. The moment capacities in both increase for about 80% while the mechanisms are different. The role of ζ is primarily shown as the improvement of post-crack stiffness by providing additional compression forces, while the effect on cracking moment is not apparent. On the other hand, as o increases from 0.1 to 0.25, the cracking moment increases as much as twice, which agrees with the trend shown in Figure 4-14. Nevertheless, the improvement in post-cracking stiffness is marginal since the tensile forces are primarily contributed by the rebars.

4.6 Experimental Verification of Flexural Model

4.6.1 Rectangular Beams

Full scale beam tests from the Brite/Euram project BRPR-CT98-0813 “Test and design methods for steel fibre reinforced concrete” by Dupont were used for model verification [201]. The experimental program studied the effects of four variables: concrete strength, fiber dosage, span length and longitudinal reinforcement ratio. Table 4-12 provides the details of the 12 beam series, each with 2 replicates, of two grades of normal (NSC), and high strength concrete (HSC). Normal strength concrete used fiber type RC 65/60 BN at 25 and 50 kg/m^3 while HSC used fiber type RC 80/60 BP at 60 kg/m^3. All beams had a cross section of 0.20 x 0.20 m, with two different span lengths of 1.0 and 2.0 m and tested

under four-point bending set up with a constant spacing between the two point loads at 0.2 m. The first half of the series (B1 – B6) contains no rebar and the other half (B7 – B12) contained two rebars of size 8, 12 and 16 mm. Steel parameters were Young modulus of 200 GPa, yield strength of 560 MPa, and a concrete cover of 15 mm.

The load-deflection responses of the 12 beam series were simulated by the algorithm proposed and compared with Updated RILEM method [201] as reference. The material model parameters used were obtained by fitting the tension and compression models shown in Figs. 6-1 to the models shown in Figs. 6-10 and summarized in Table 4-13. The residual tensile strength μ corresponds to average response of the RILEM method. Ultimate tensile strain of 0.025 was used for both models [57].

Figure 4-16 shows the simulations of the 6 plain SFRC beams without flexural reinforcement representing the effect of concrete strength, fiber content, and span length. Average test results of two replicate samples of each series is also shown and compared to the simulation curves. The simulations compare favorably to the experimental results while underestimating the RILEM method. This is attributed to the differences between the tensile responses used by the two models. The RILEM model specified two points (σ_2, ε_2) and (σ_3, ε_3) to express the descending branch (Figure 4-15(a)) as opposed to a constant residual strength σ_p with a lower bound estimation of the residual strength in the proposed model with a single step drop from σ_{cr} to $\sigma_p < \sigma_2$ (Figure 4-2(a)). This is also shown in Table 4-13 and results in lower predicted load at fiber contents of 25 and 50 kg/m^3 (Figure 4-15(a) and (b)). For the high fiber content, residual strengths used in two models are identical and thus similar load-deflection responses obtained (Figure 4-15(c)). It is also noteworthy that both models underestimate the post-crack response of beam B1 but

overestimate the response of beam B2. Since the same model parameters are used for beams of different lengths, the simulations demonstrate the nature of size effect of properties obtained from smaller specimens. Larger specimens indicate the apparent size effect observed in experiments with the descending parts that behave differently from smaller beams.

Figure 4-17 presents load-deflection responses for the 6 HRC beams with flexural reinforcement of ρ=0.13% - 0.20%. Both models simulate the experimental results with the discrepancy in the flexural stiffness after cracking for the HSC beams in Figure 4-17(c). The present model assumes cracks to be uniformly distributed throughout the mid-zone between the two loading points used as the localized zone. However additional cracks form outside the mid-zone in HSC beams in the shear span region due to tension stiffening effects which results in a larger localized zone. Since the deflection correlates with the double integration of curvature, additional cracking over a larger section will inherently result in a larger localization zone, and higher deflections at the same loading level. The limit-state load capacity is insensitive to the length of localization zone as shown by Bakhshi et. al [202], and the size effect due to span in HRC beams is not as pronounced as the FRC samples. Finally, the difference between the predictability of the two methods diminishes since they both use the same elastic-perfectly plastic steel model.

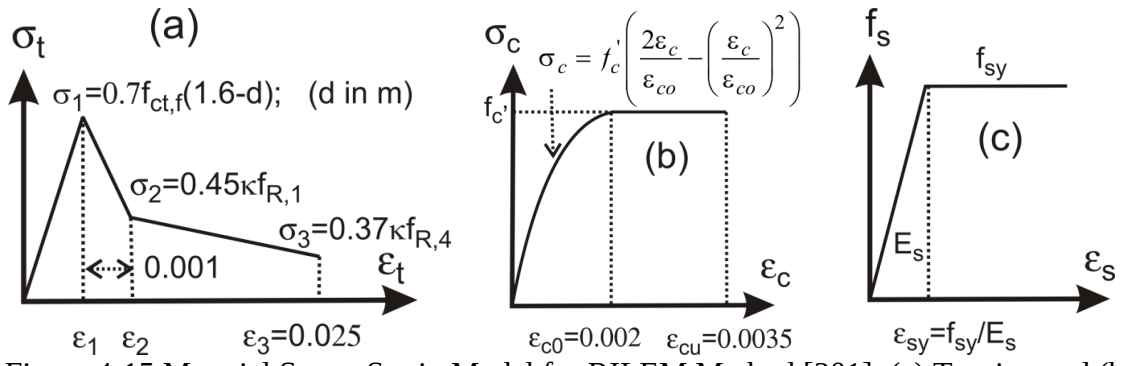

Figure 4-15 Material Stress-Strain Model for RILEM Method [201]; (a) Tension and (b) Compression Model for SFRC; (c) Steel Model.

Table 4-12 Beam Test Series [169]

Beam	Mix	Fiber content kg/m^3	Span m	Rebar
B1	NSC	25	1.0	-
B2	NSC	25	2.0	-
B3	NSC	50	1.0	-
B4	NSC	50	2.0	-
B5	HSC	60	1.0	-
B6	HSC	60	2.0	-
B7	NSC	25	1.0	2-ϕ8
B8	NSC	25	2.0	2-ϕ8
B9	NSC	50	1.0	2-ϕ12
B10	NSC	50	2.0	2-ϕ12
B11	HSC	60	1.0	2-ϕ16
B12	HSC	60	2.0	2-ϕ16

Table 4-13 Steel Fiber Reinforced Concrete Parameters for RILEM and Proposed Models [169]

Beam Type			SFRC			HRC		
Fiber content		kg/m^3	25	50	60	25	50	60
RILEM	E	GPa	31.8	30.6	38.4	30.5	30.3	39
	f_c'	MPa	30	26	53	26.4	26.1	55.4
	σ_1	MPa	3.5	4.2	6.2	3.2	3.8	6.3
	σ_2	MPa	1.1	2	3.1	1.3	1.8	3.8
	σ_3	MPa	0.8	1.2	3.1	0.9	1.1	3.2
	ε_1	%	0.011	0.014	0.016	0.011	0.013	0.016
	ε_2	%	0.21	0.24	0.26	0.21	0.23	0.26
	ε_3	%	0.25	0.25	0.25	0.25	0.25	0.25
Proposed	E_c	GPa	22.6	20	39.7	20	20	41
	σ_{cy}	MPa	30.2	26.6	52.9	26.4	26.1	55.4
	σ_{cr}	MPa	3.5	4.2	6.2	3.2	3.8	6.3
	σ_p	MPa	1	1.6	3.1	1.1	1.5	3.5
	ε_{cr}	%	0.011	0.014	0.016	0.011	0.013	0.016
	ε_{tu}	%	0.25	0.25	0.25	0.25	0.25	0.25
	μ		0.273	0.382	0.501	0.345	0.383	0.557

*strain at peak stress, ε_{c0} = 0.2%, at compressive yield stress, ε_{cy} = 0.133%, and ultimate compressive strain, ε_{cu} = 0.35% for all mixes.

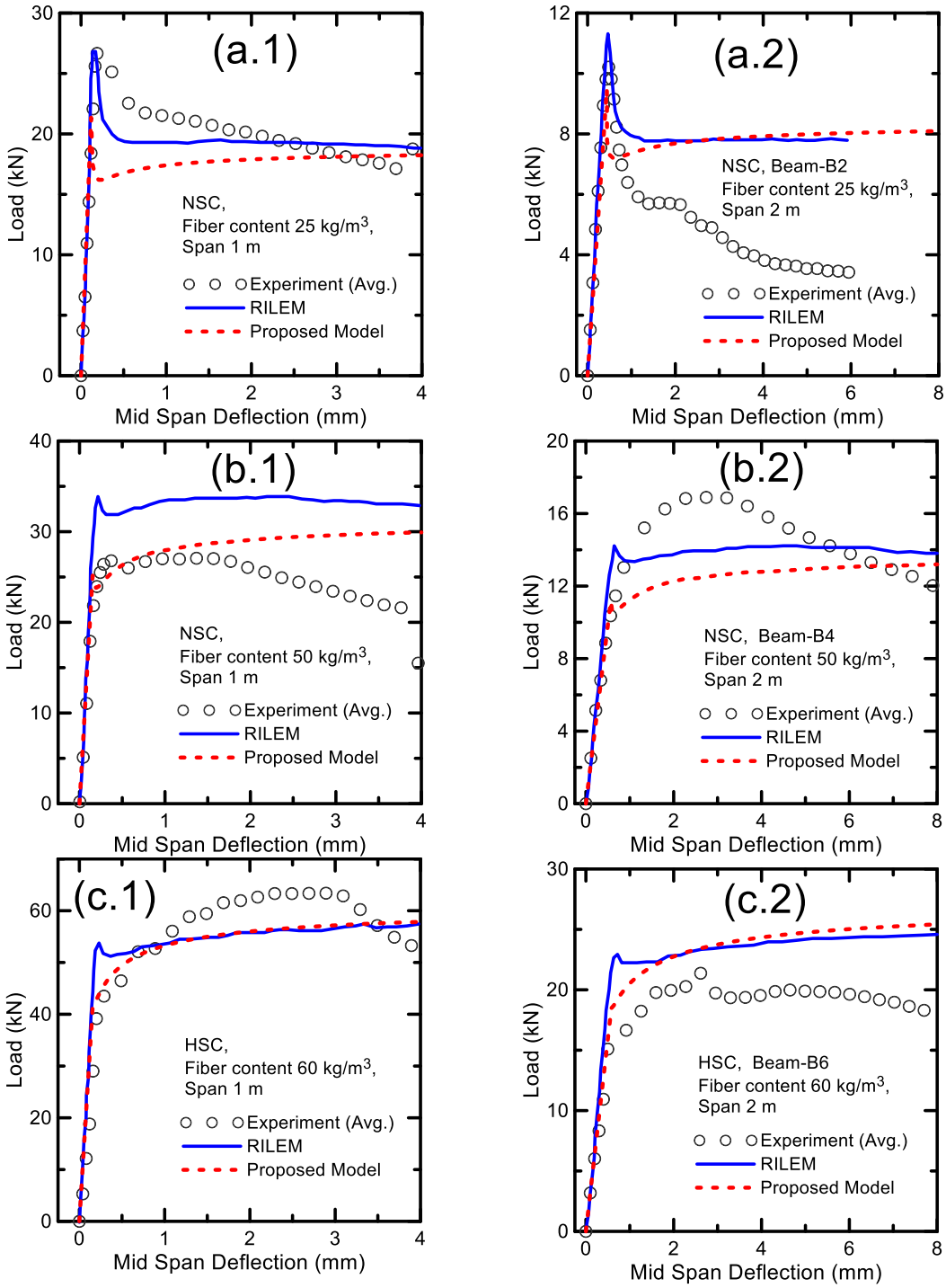

Figure 4-16 Load Deflection Responses of SFRC Beams at Three Levels of Fiber Contents (25 kg/m^3, 50 kg/m^3 and 60 kg/m^3). RILEM Refers to the Updated RILEM Stress-Strain Model [169,201].

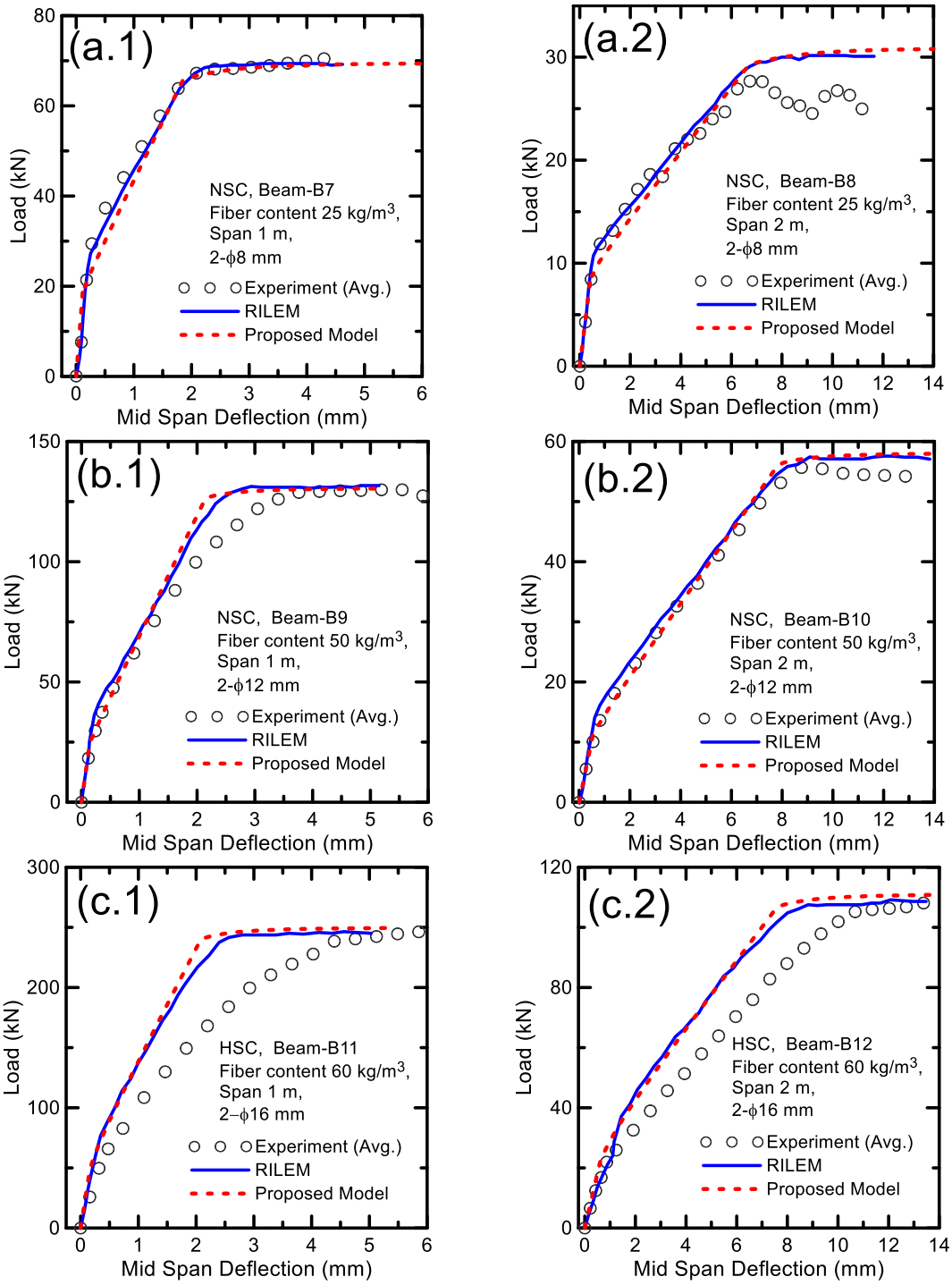

Figure 4-17 Load Deflection Responses of HRC Beams at Three Levels of Fiber Contents (25 kg/m^3, 50 kg/m^3 and 60 kg/m^3). RILEM Refers to the Updated RILEM Stress-Strain Model [169,201].

4.6.2 Flanged Beams

Demir et al. [203] conducted four-point bending test on T-section beams using an alternative diagonal shear reinforcement. The geometries and reinforcement diagram are shown in Figure 4-18(a). The material parameters are as follows: f_c'=26.4 MPa, f_{cr}=2.9 MPa, ε_{cr}=78 με, E_c=24 GPa, f_y=414 MPa, E_s=205 GPa. The ratio of web and flange thickness are o=0.33 and ζ=0.21, respectively. Figure 4-18(b) compares the experimental data and model simulation using the given parameters. It can be seen that the predicted curve is quite favorable up to the yield of tensile rebar.

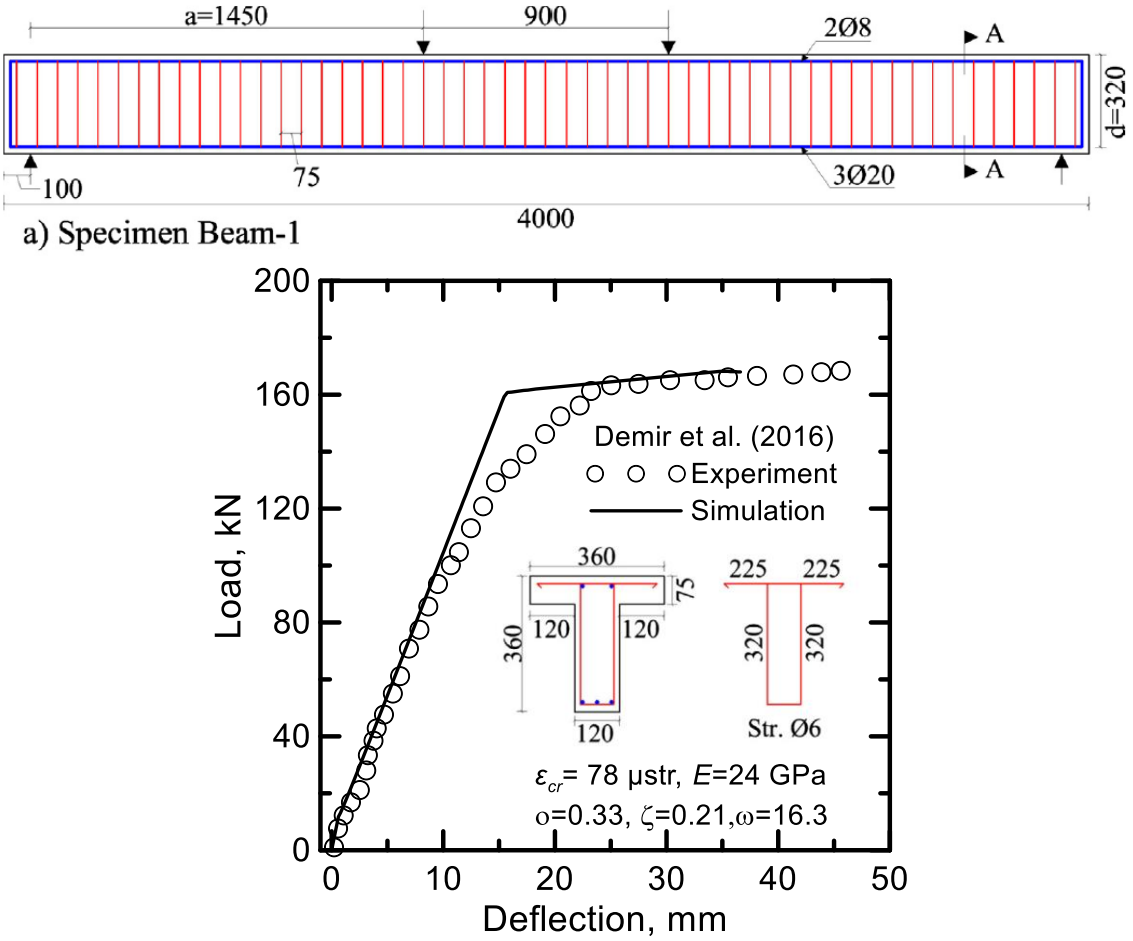

Figure 4-18 (a) Details of the Specimens [203], (b) Comparison Between Experimental Data and Model Simulation.

Abdul-Ahad and Aziz et al. [204] studied the T-beams reinforced by both rebars and steel fibers up to a volume fraction of 1.5%. The geometries and reinforcement diagram are shown in Figure 4-19(a). The material parameters are as follows: f_c'=21 MPa, f_{cr}=1.8 MPa, ε_{cr}=90 με, E_c=20 GPa, f_y=450 MPa, E_s=210 GPa. The ratio of web and flange thickness are o=0.4 and ζ=0.29, respectively. The model simulation agrees well with the experimental load-deflection response as shown in Figure 4-19(b).

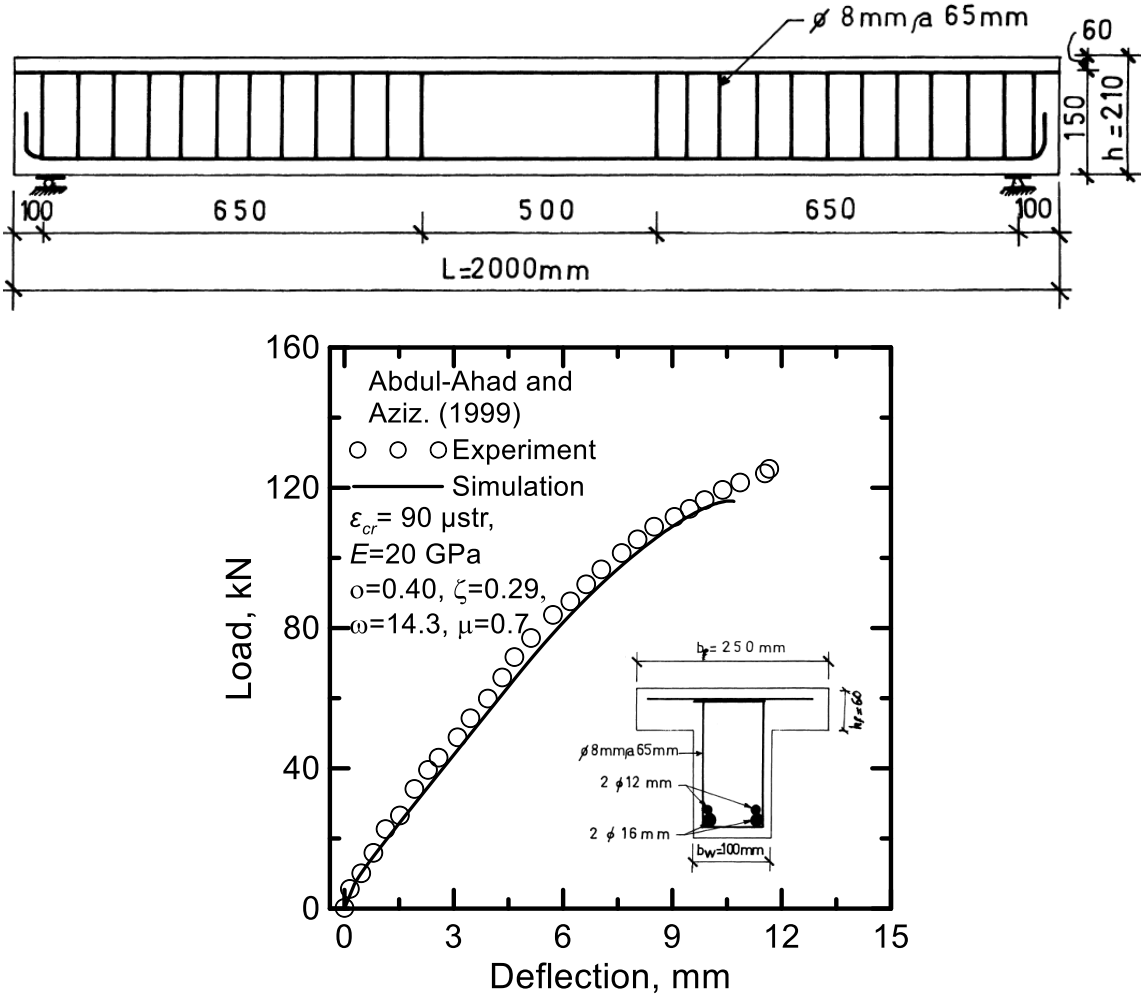

Figure 4-19 (a) Details of the Specimens [204], (b) Comparison Between Experimental Data and Model Simulation.

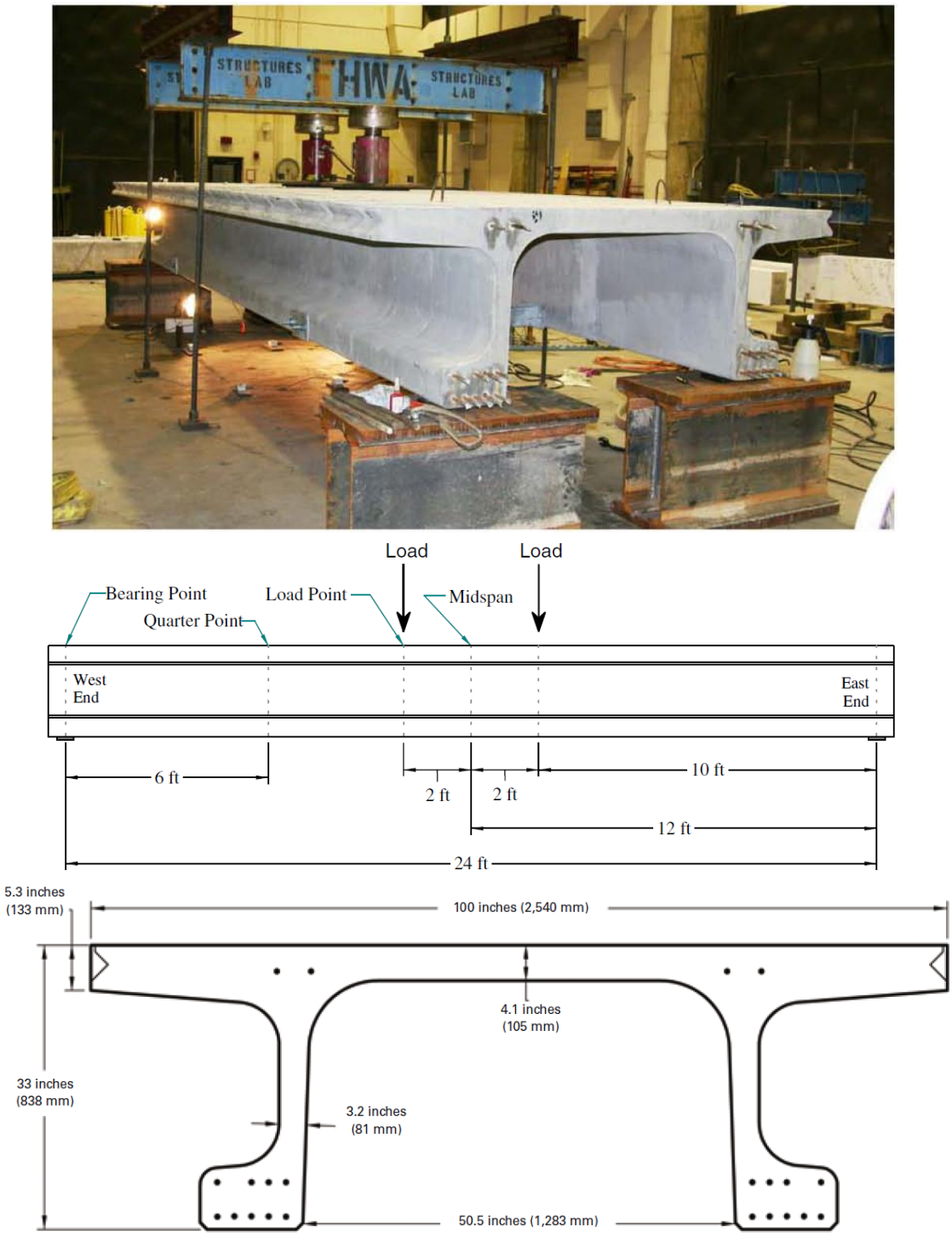

Figure 4-20 Bending Test Setup and Cross Sectional Properties of UHPC Pi-Girders [200,205].

Graybeal from FHWA [205] proposed a UHPC Pi-girder as decked girder members and the deployment of the concept was completed in a project in Buchanan County, IA. Chen and Graybeal [200] performed full scale four-point bending tests and finite element analysis of the UHPC Pi-girders with a span of 24ft. The sectional properties and test setup are shown in Figure 4-20.

In order to simulate the flexural response of Pi-girder, the cross section is converted into an equivalent T-section based as shown in Figure 4-21. The conversion is rational due symmetry in the Pi-girder and the two sections have same moment of inertia about the neutral axis. The T-section has same height, width and flange thickness with the original section, while the thickness of web is taken as the summation of the bulb width. Comparison of simulated and experimental load-deflection responses is shown in Figure 4-22. The material parameters are as follows: f_c'=97 MPa, ε_{cr}=73 με, E_c=53 GPa, f_y=1820 MPa, E_s=210 GPa. The ratio of web and flange thickness are o=0.24 and ζ=0.16, respectively. The model is able to accurately predict the flexural behavior of Pi-girder using the conversion procedure.

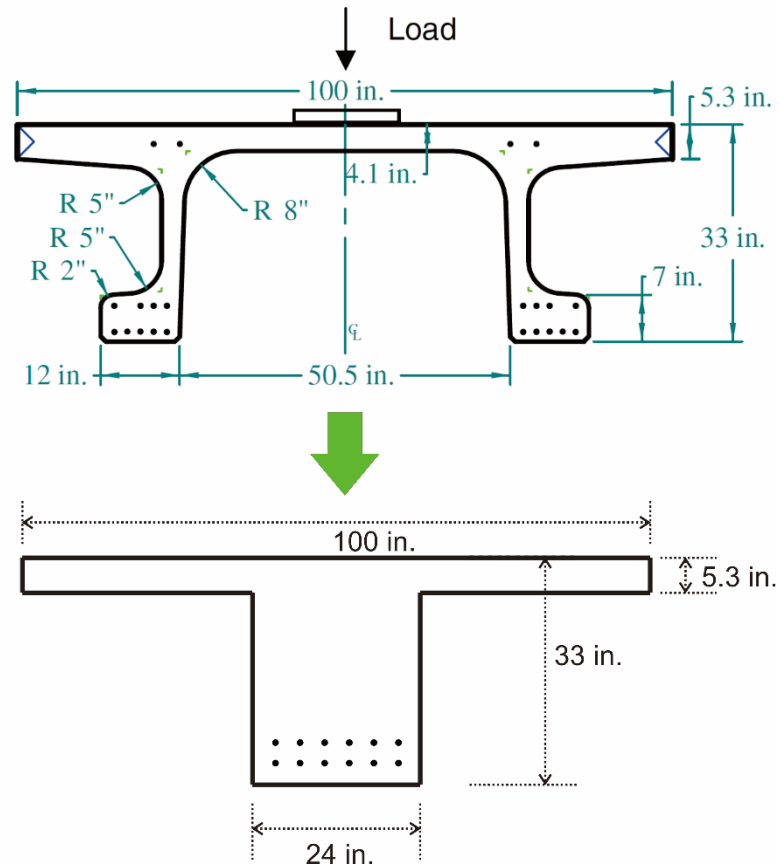

Figure 4-21 Conversion From Pi-Girder to an Equivalent T-Section.

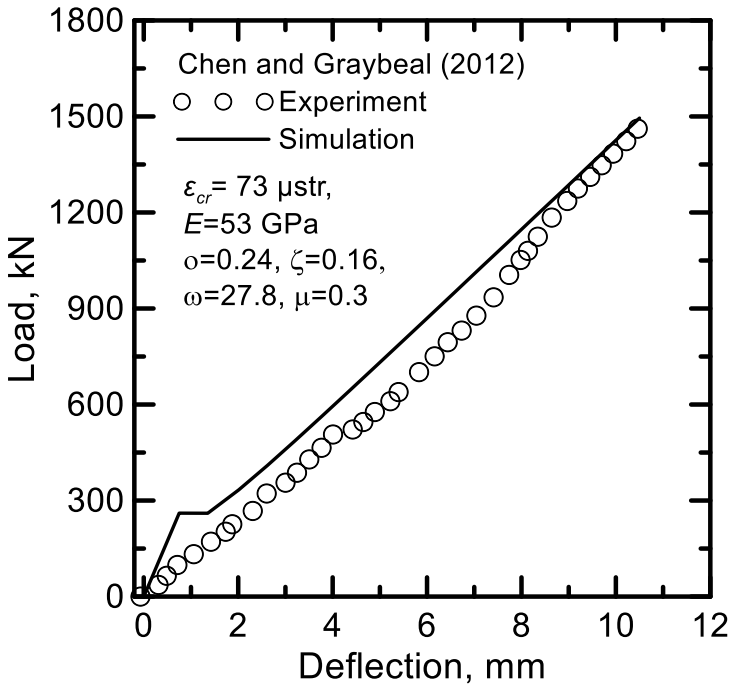

Figure 4-22 Comparison Between Experimental Data and Model Simulation.

4.6.3 Size Effects on Serviceability Limits

Since the present analytical model keeps track of the curvature distribution and allows the determination of load capacity at given deformation, it can be used to compare the results of beams of various sizes for a serviceability based criterion such as maximum allowable curvature, deflection, ductility or stress. Various parameters have been proposed and used to characterize the flexural toughness and residual strength of FRC from experimental data. For example, EN14651 uses equivalent flexural tensile strength $f_{eq,3}$ determined at a specific deflection level of δ = 2.5 mm; ASTM C1609 uses an equivalent flexural strength ratio $R_{e,3}$ at a similar value of deflection $\delta = L/150$. However, extraction of experimental results from small beams at a given deflection may be inappropriate for the design of full scale structures due to the size effect [206]. A study of size effect on the curvatures which correlates with maximum load at specified levels of deflection was thus conducted. In addition to Dupont's beam tests results discussed for spans of 1 and 2 m, additional simulations were conducted on the experiments by Kim et. al [207] and Mobasher et. al [208] on SFRC beams with spans of 0.45 m as well as Barros and Figuerias [209] on slab strips with 1.5 m span. Model parameters can be found elsewhere [210]. Once the load-deflection results were simulated based on the model, the magnitudes of maximum curvatures corresponding to the deflection $\delta = L/150$ were plotted as a function of span length and summarized in Figure 4-23. The size effect can be observed that the curvature limit required to fit the experimental data is independent of the amount of fibers used. The maximum curvature decreased by almost 80% as the span increased from 0.45 m to 2 m which is the range of many experimental data conducted in the literature. The simulated curvatures of large beams using the same material parameters are much lower than those

of smaller beams at equivalent levels of deflection. This points out that the trend of specifying parameters such as $R_{e,3}$ which occur at quite a large deflection and curvature for small specimens in order to design and construct large beams is too conservative as the curvatures obtained by the small samples may not be obtained under real size geometries.

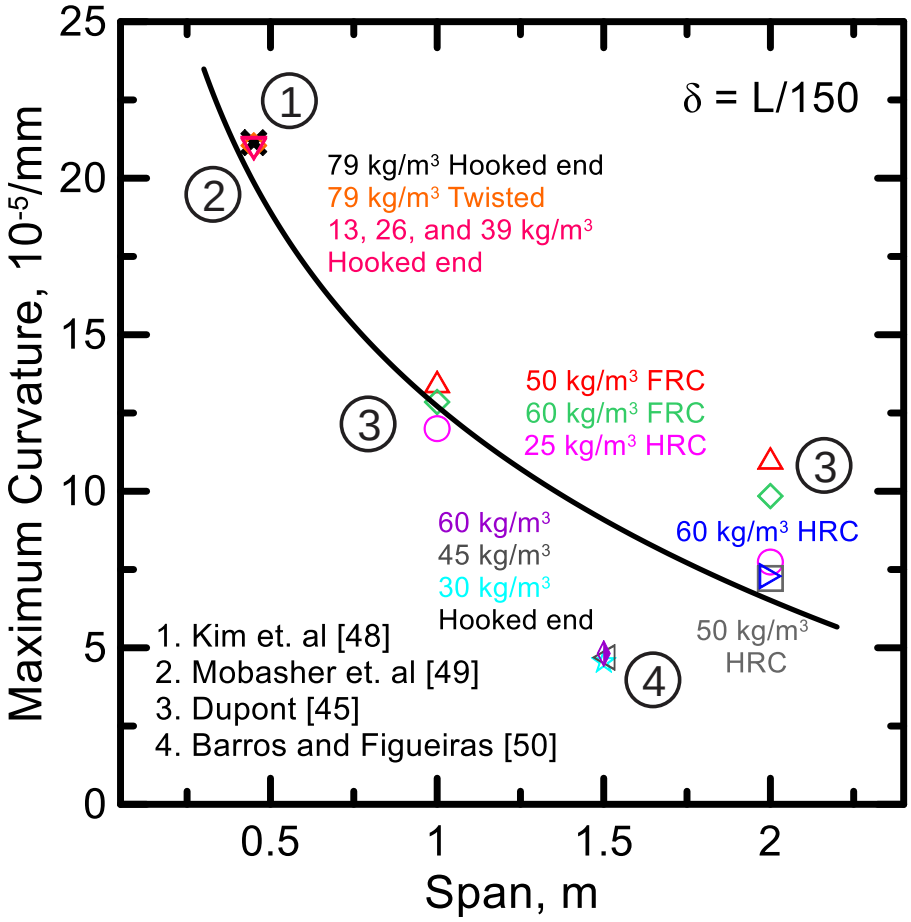

Figure 4-23 Simulated Curvatures Corresponding to Deflection of δ = L/150 for Various Materials and Beam Sizes [169].

Material characteristics of HRC are idealized using elastic-residual-tensile strength for tension and elastic-perfectly plastic for compression and an elastic-perfectly plastic reinforcing steel. Analytical solutions for neutral axis depth, moment-curvature, and effective stiffness at each stage of flexural deformation are obtained. Analytical expressions for load-deflection response are explicitly derived based on simplified bilinear

moment-curvature curves. Parametric studies demonstrate that the use of discrete fibers to increase residual tensile strength is not as effective as continuous reinforcement in improving the moment capacity, however the ability of fibers to distribute cracking leads to higher stiffness and strength than plain reinforced concrete.

The derivations are used in terms of design charts representing the normalized ultimate moment capacity as a function of residual tensile strength and reinforcement ratio and are applicable to conventional-, fiber-, and hybrid-reinforced concrete. Results are further converted to coefficient of resistance R by stress block approach, nominal strength, and minimum reinforcement ratio. Numerical tests covering materials and geometrical ranges as a well as comparison with available experimental data confirmed the proposed equations against the original equations.

Notation

A_s = area of steel rebar

b = beam width

d = effective depth at location of steel rebar

E = elastic tensile modulus of concrete

E_c = elastic compressive modulus of concrete

E_s = elastic modulus of steel

f'_c = cylindrical ultimate compressive strength of concrete

f = stress

F = force components in stress diagram

h = full height of a beam section or height of each compression and tension zone in stress diagram

K = effective flexural stiffness of a beam section

k = neutral axis depth ratio

M = moment

M_n = nominal moment capacity

M_u = ultimate moment

n = modulus ratio (E_s/E)

R = coefficient of resistance

y = moment arm from force component to neutral axis

α = normalized depth of steel reinforcement (d/h)

β = normalized tensile strain ($\varepsilon_t/\varepsilon_{cr}$)

β_1 = coefficient for the depth of ACI rectangular stress block

ε = strain

ε_c = concrete compressive strain

ε_{c0} = concrete compressive strain at peak stress

ε_{ctop} = concrete compressive strain at top fiber

ε_t = concrete tensile strain

ε_{tbot} = concrete tensile strain at bottom fiber

ϕ = curvature

γ = normalized concrete compressive modulus (E_c/E)

κ = normalized steel yield strain ($\varepsilon_{sy}/\varepsilon_{cr}$)

λ = normalized compressive strain ($\varepsilon_c/\varepsilon_{cr}$)

λ_{R1} = normalized compressive strain at the end of elastic region 1

μ = normalized residual tensile strength (σ_p/σ_{cr})

μ_{crit} = the critical normalized residual tensile strength that change deflection-softening to deflection-hardening

ρ = steel reinforcement ratio per effective area

ρ_{bal} = steel reinforcement ratio per effective area at balance failure

ρ_g = steel reinforcement ratio per gross area

$\rho_{g,bal}$ = steel reinforcement ratio per gross area at balance failure

$\rho_{g,min}$ = minimum flexural reinforcement per gross section

$\rho_{g,min,rc}$ = minimum flexural reinforcement per gross section for conventional reinforced concrete

ρ_{min} = minimum flexural reinforcement ratio per effective section

$\rho_{min,rc}$ = minimum flexural reinforcement ratio per effective section for conventional reinforced concrete

σ = concrete stress

σ_c = concrete compressive stress

σ_p = residual tensile strength

σ_t = concrete tensile stress

ω = normalized concrete compressive yield strain ($\varepsilon_{cy}/\varepsilon_{cr}$)

χ = normalized steel strain ($\varepsilon_s/\varepsilon_{cr}$)

Subscripts

1 = at stage 1, elastic compression – elastic tension

21 = at stage 2.1, elastic compression – residual tension, steel is elastic

22 = at stage 2.2, elastic compression – residual tension, steel is yield

31 = at stage 3.1, plastic compression – residual tension, steel is elastic

32 = at stage 3.2, plastic compression – residual tension, steel is yield

c1 = elastic compression zone 1 in stress diagram

c2 = plastic compression zone 2 in stress diagram

cr = at first cracking

cu = at ultimate concrete compressive strain

cy = at concrete compressive yielding

i = at stage *i* of normalized concrete compressive strain and tensile steel condition

s = refer to steel

sy = at steel yielding

t1 = elastic tension zone 1 in stress diagram

t2 = residual tension zone 2 in stress diagram

tu = at concrete ultimate tensile stain

cu = at concrete ultimate compressive strain

∞ = at concrete compressive strain approach infinity

Supper scripts

’ = normalizing symbol

5. ANALYTICAL MODEL FOR COMBINED AXIAL-BENDING LOADS

5.1 Introduction

Structural members such as columns, beam-column joints, footings and tunnel lining segments are subjected to combined loads of axial compression and bending moment. The combined effects may be induced by different factors, such as unbalanced moments at connecting beams, vertical misalignment, lateral forces resulting from wind or seismic activity, or curved shape of the member itself [211]. P-M interaction diagrams were presented originally by Whitney and Cohen [212] in 1956 and continue to be widely used today in the design of these structural members, which represents the interaction of axial load and moment on ultimate strength [213]. These diagrams provide solutions for the reinforcement required to resist a specified combination of axial load and moment.

The development of interaction diagrams of reinforced concrete (RC) rectangular sections have been investigated extensively by numerous researchers [214,215,216,217,218,219]. However, most of the work was carried out using the Whitney's rectangular stress block for the concrete in compression and assumed no contribution by tensile zone of concrete. Second-degree parabolic stress-strain models to describe the compression behavior were employed by Marin [220], as well as Rodriguez and Aristizabal-Ochoa [221], who presented closed-form expressions for ultimate loads and bending moments. But programming involving nonlinear numerical solver is needed which may not be applicable as design equations. Mobasher et al. [169] derived analytical flexural load-deflection solutions of HRC beams subjected to pure bending using a parametric material tensile and compression constitutive model, as well as steel model. The contribution of fiber was addressed by the parameter of residual tensile strength, which may be obtained by standard

flexural tests [57] and back-calculation procedure [61,62]. The expressions of minimum reinforcement ratio and ultimate moment capacity including the effect of residual strength were explicitly derived which can be used in a simplified design procedure for cement composites. Moreover, analytical equations can be used for selection of variables using a design automation procedure; hence gradient-based optimization algorithms can be conducted much faster.

This chapter presents analytical solutions to construct a full range P–M interaction diagram of HRC sections that consider the contributions of fibers in the post-cracking strength. The proposed methodology covers all the control modes in the structural members subjected to the axial compression and bending loads. The model simulates are verified with experimental results and analysis from literature for columns and tunnel lining segments. The proposed P–M diagram could be used by engineers as a design tool in different types of applications.

5.2 Material Models

The objective of this study is to develop the analytical solutions of the P-M interaction diagram of the HRC section. Figure 5-1 presents three distinct material models used in the derivation of parametric response of HRC beams. Material parameters are described as two intrinsic parameters: tensile modulus E and the first cracking tensile strain ε_{cr} while other variables are normalized with respect to these intrinsic parameters. Figure 5-1(a) shows an idealized tension model with an elastic range of stress increases linearly with E up to the first cracking tensile strength of coordinates (ε_{cr}, σ_{cr}). In the post-crack region, the stress is constant at $\sigma_p = \mu\sigma_{cr} = \mu\varepsilon_{cr}E$ and terminates at the ultimate tensile strain $\varepsilon_{tu} = \beta_{tu}\varepsilon_{cr}$. Figure 5-1(b) shows the elastic-perfectly plastic compression response with a modulus $E_c = \gamma E$.

The plastic range initiates at strain $\varepsilon_{cy} = \omega\varepsilon_{cr}$ corresponding to yield stress $\sigma_{cy} = \omega\gamma\varepsilon_{cr}E$ and terminated at $\varepsilon_{cu} = \lambda_{cu}\varepsilon_{cr}$. The effect of lateral ties on the compressive behavior is characterized by an improved compressive strength $\sigma_{cy}' = (\omega+\omega')\gamma\varepsilon_{cr}E$. Figure 5-1(c) is the elastic-perfectly plastic steel model using yield strain and stress of $\varepsilon_{sy} = \kappa\varepsilon_{cr}$ and $f_{sy} = \kappa n\varepsilon_{cr}E$ as defined by normalized parameters: κ and n. No termination level is specified for steel strain. Geometrical parameters are also normalized with the cross sectional dimensions of width b and full depth h as shown in Figure 5-1(d) with steel parameters defined as area $A_s = \rho_g bh$ at the reinforced depth αh for both compression and tension rebars. The compression reinforcement ratio ρ_g' is assumed equal to the tension reinforcement ratio ρ_g throughout the study.

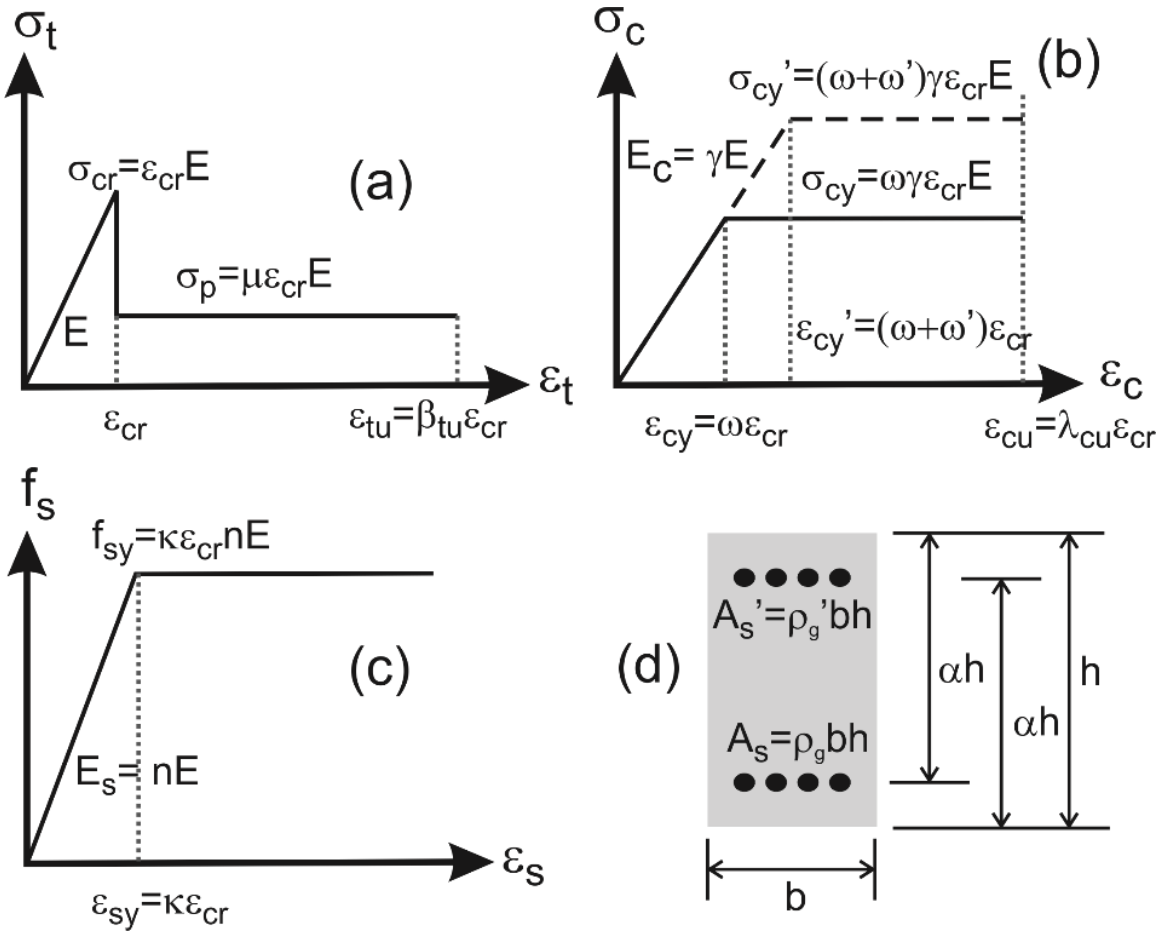

Figure 5-1 Material Models Including (a) Tensile Model, (b) Compressive Model, (c) Steel Model, (d) Cross Section.

The material models for tension and compression of FRC and the model for steel rebar are presented as:

$$\sigma_t(\varepsilon_t)=\begin{cases} E\varepsilon_t & 0\le\varepsilon_t\le\varepsilon_{cr} \\ \mu E\varepsilon_{cr} & \varepsilon_{cr}<\varepsilon_t\le\varepsilon_{tu} \\ 0 & \varepsilon_t>\varepsilon_{tu} \end{cases} \quad ; \quad \frac{\sigma_t(\beta)}{E\varepsilon_{cr}}=\begin{cases} \beta & 0\le\beta\le 1 \\ \mu & 1<\beta\le\beta_{tu} \\ 0 & \beta>\beta_{tu} \end{cases} \qquad \text{Equation 5-1}$$

unconfied :

$$\sigma_c(\varepsilon_c)=\begin{cases}E_c\varepsilon_c & 0\le\varepsilon_c\le\varepsilon_{cy}\\ E_c\varepsilon_{cy} & \varepsilon_{cy}<\varepsilon_c\le\varepsilon_{cu}\\ 0 & \varepsilon_c>\varepsilon_{cu}\end{cases};\quad \frac{\sigma_c(\lambda)}{E\varepsilon_{cr}}=\begin{cases}\gamma\lambda & 0\le\lambda\le\omega\\ \gamma\omega & \omega<\lambda\le\lambda_{cu}\\ 0 & \lambda>\lambda_{cu}\end{cases}$$

confined :

$$\sigma_c'(\varepsilon_c)=\begin{cases}E_c\varepsilon_c & 0\le\varepsilon_c\le\varepsilon_{cy}'\\ E_c\varepsilon_{cy}' & \varepsilon_{cy}<\varepsilon_c\le\varepsilon_{cu}\\ 0 & \varepsilon_c>\varepsilon_{cu}\end{cases};\ \frac{\sigma_c'(\lambda)}{E\varepsilon_{cr}}=\begin{cases}\gamma\lambda & 0\le\lambda\le\omega+\omega'\\ \gamma(\omega+\omega') & \omega+\omega'<\lambda\le\lambda_{cu}\\ 0 & \lambda>\lambda_{cu}\end{cases}$$

Equation 5-2

$$f_s(\varepsilon_s)=\begin{cases}E_s\varepsilon_s & 0\le\varepsilon_s\le\varepsilon_{sy}\\ E_s\varepsilon_{sy} & \varepsilon_s>\varepsilon_{sy}\end{cases};\quad \frac{f_s(\chi)}{E\varepsilon_{cr}}=\begin{cases}n\chi & 0\le\chi\le\kappa\\ n\kappa & \chi>\kappa\end{cases}$$ Equation 5-3

where normalized strains are defined as $\beta = \varepsilon_t/\varepsilon_{cr}$, $\lambda = \varepsilon_c/\varepsilon_{cr}$ and $\chi = \varepsilon_s/\varepsilon_{cr}$.

5.3 Confinement Effects

Mansur et al. [222] performed compression tests on plan concrete and FRC to investigate the effects of tie confinements. Empirical equations to predict the compressive stress-strain behaviors were proposed based on the experimental results. Specifically, the effects of confinement on the compressive strength can be described by the equations below:

for plain concrete

$$\frac{f_0'}{f_0}=1+0.60\left(\frac{\rho_s f_y}{f_0}\right)^{1.23}$$ Equation 5-4

for FRC

$$\frac{f_0'}{f_0}=1+11.63\left(\frac{\rho_s f_y}{f_0}\right)^{1.23}$$ Equation 5-5

where f_0 is original compressive strength, f_0' is the confined strength, ρ_s is the reinforcement ratio of the ties, f_y is the yield strength of steel. Parametric studies covering some typical

materials including Grade 60 (60 ksi) and 80 steel (80 ksi), as well as normal strength (5000 psi) and high strength (7000 psi) concrete are conducted. Figure 5-2 shows the effect of confinement for these combinations as reinforcement ratio increases from 0 to 0.3%. The results indicate that the ratio of confined strength over original strength, i.e. f_0'/f_0 or $(\omega+\omega')/\omega$, can be as high as 1.37 within the range of study. While the actual confinement ratio used in the model will depend on the details of case study.

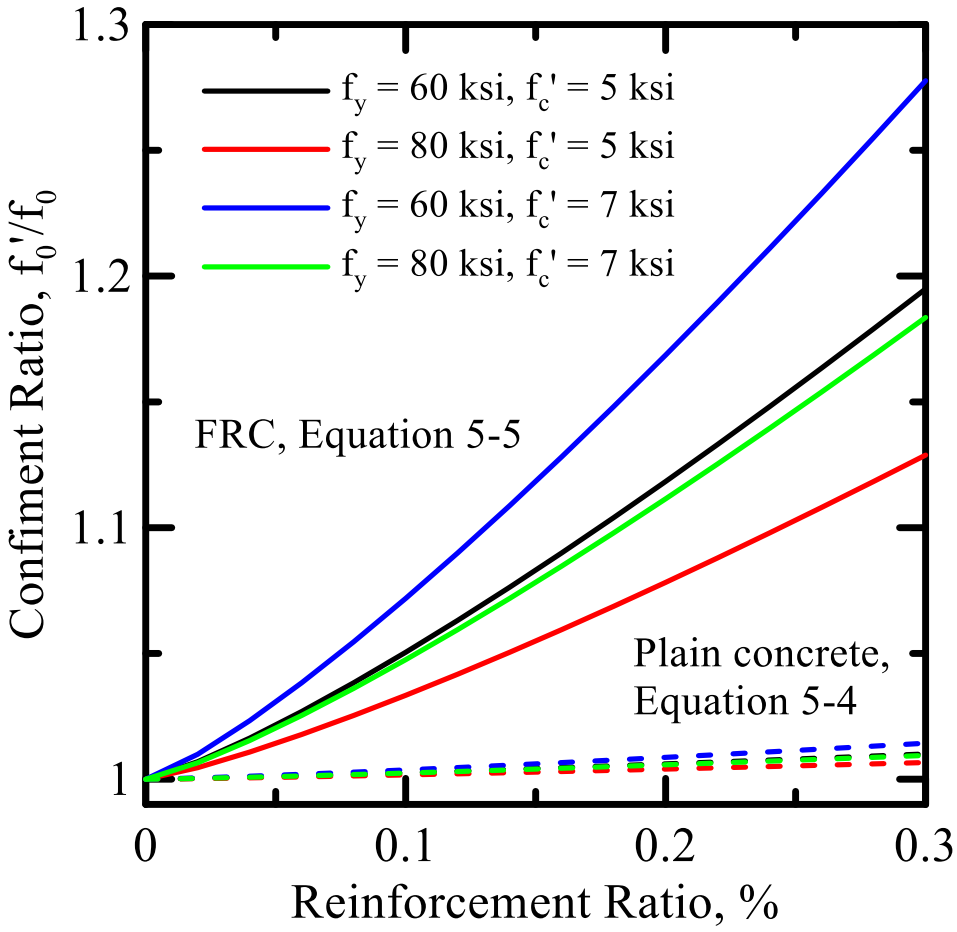

Figure 5-2 Effects of Confinement on the Compressive Strength for FRC and Plain Concrete.

5.4 Derivations

5.4.1 Strain and Stress Diagrams

In derivation of axial force (P) and bending moment (M) for a rectangular cross section, the assumption of plane section remaining plane is assumed. By applying linear strain distribution across the depth, ignoring shear deformation, and using material models of Eqs. (1)-(3) and Figure 5-1(a)-(c), the stress distributions as shown in Figure 5-3 are obtained. The normalized strain at the bottom concrete fiber is used as an independent variable to incrementally impose axial and flexural deformations for three modes of failure. Specifically, letter λ represents the bottom strain in compression while β refers to tensile strain. In the present study, the compressive strain is defined as positive, and the terms of stress, force follow the same sign convention. The Mode 1 corresponds to range where the entire cross section is under compression, where two sub-modes exist: 1.1 bottom concrete fiber yield in compression ($\lambda \geq \omega$), 1.2 bottom concrete fiber does not yield ($0 < \lambda < \omega$); Mode 2 corresponds to compression controlled failure where the steel in tensile region is not yielded ($-\kappa \leq \chi \leq 0$), which also includes two sub-modes: 2.1 no tension crack ($-1 \leq \beta \leq 0$) and 2.2 tension crack ($\beta < -1$). Finally, Mode 3 corresponds to the tension controlled failure ($-0.005/\varepsilon_{cr} < \chi \leq -\kappa$) with two scenarios existing in each sub-stage: 3.1 the compression steel is elastic or 3.2 yielding. In modes 2 and 3, where the bottom fiber is in tension ($\beta < 0$), a parameter k is introduced to represent the normalized height of natural axis:

$$kh = h_{c1} + h_{c2}$$
$$\frac{\lambda_{cu}\varepsilon_{cr}}{kh} = \frac{-\beta\varepsilon_{cr}}{h-kh} \quad or \quad \beta = -\frac{1-k}{k}\lambda_{cu} \qquad \text{Equation 5-6}$$

Theoretically, these two scenarios could exist in other modes as well, but quick examinations for practical considerations showed that the compression still is yielded in most of the cases in compression controlled zones. Therefore, it is assumed that the steel in compression is yielded all time in Modes 1 and 2 in this study as a rational simplification.

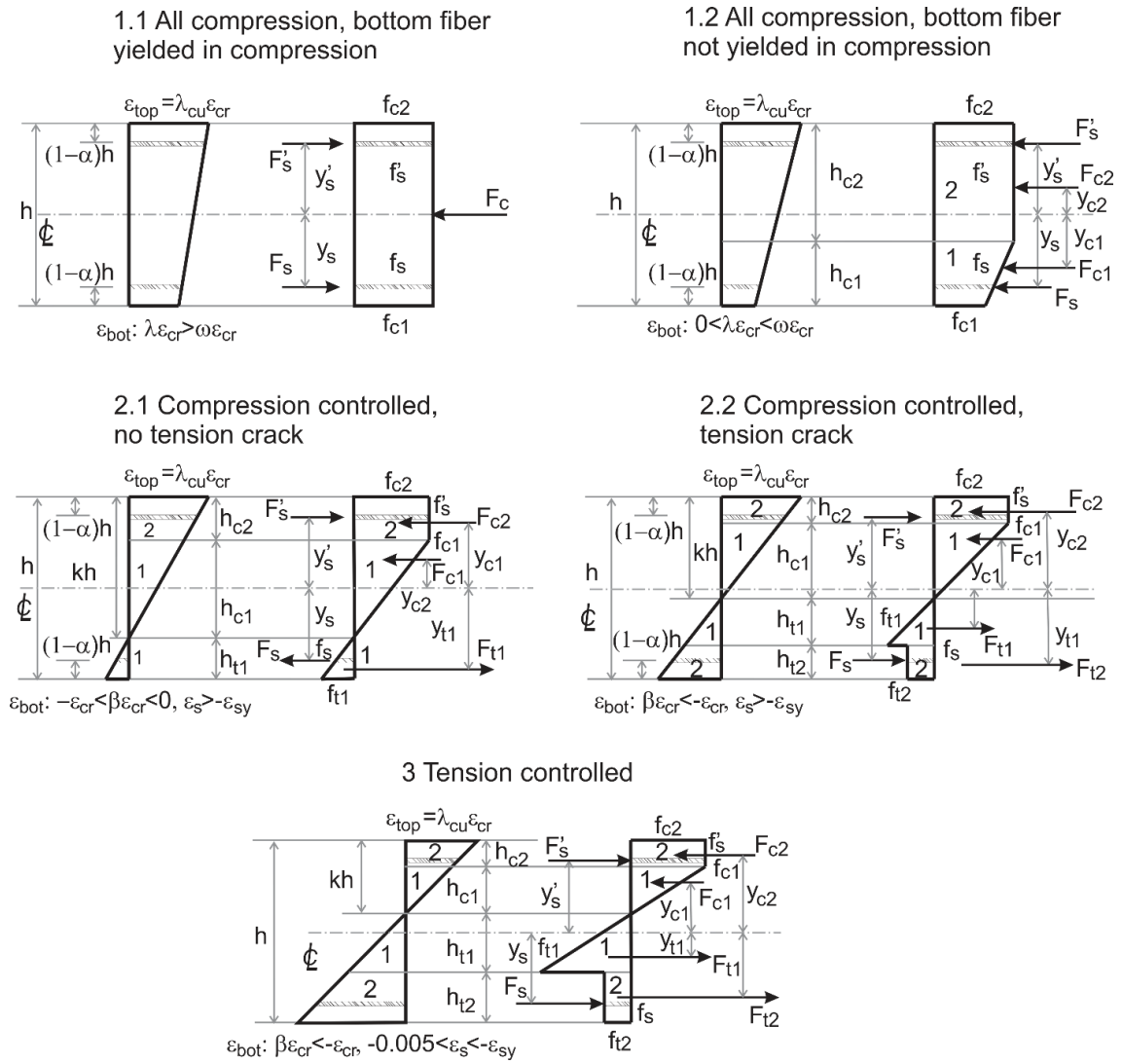

Figure 5-3 Strain and Stress Diagrams at Three Modes: (a) All Compression, (b) Compression Controlled Failure, (c) Tension Controlled Failure.

5.4.2 Calculations of Force and Moment

Three modes of stress distribution in Figure 5-3, show the height of compression and tension zones normalized with respect to the beam depth *h*, while stresses are normalized with respect to the first cracking strength $E\varepsilon_{cr}$ and presented in Tables 5-1 and 2, respectively.

Forces are normalized with respect to cracking tensile force $bhE\varepsilon_{cr}$ as shown in Table 3. The net section force is obtained as the difference between the tension and compression forces. Internal moment is obtained by integrating the force components using the distance to the center line as the moment arm. By normalizing the moment M_i using the cracking value M_{cr} are expressed as analytical expressions M_i' as presented in Table 5-4.

$$P_i = P_i' P_{cr}; \qquad P_{cr} = bhE\varepsilon_{cr}$$
$$M_i = M_i' M_{cr}; \qquad M_{cr} = \frac{1}{6} bh^2 E\varepsilon_{cr} \qquad \text{Equation 5-7}$$

Table 5-1 Normalized Height of Compression (C) and Tension (T) Zones for Each Mode.

Zone	Normalized height	Mode 1 ($\chi > 0$)		Mode 2 ($-\kappa \le \chi \le 0$)		Mode 3 ($0.005/\varepsilon_{cr} < \chi \le -\kappa$)	
		1.1	1.2	2.1	2.2	3.1	3.2
C	$\frac{h_{c2}}{h}$	-	$\frac{\lambda_{cu}-\omega}{\lambda_{cu}-\lambda}$		$\frac{k(\lambda_{cu}-\omega)}{\lambda_{cu}}$		$\frac{k(\lambda_{cu}-\omega)}{\lambda_{cu}}$
	$\frac{h_{c1}}{h}$	-	$\frac{\omega-\lambda}{\lambda_{cu}-\lambda}$		$\frac{\omega k}{\lambda_{cu}}$		$\frac{\omega k}{\lambda_{cu}}$
T	$\frac{h_{t1}}{h}$	-	-	$1-k$	$\frac{k-1}{\beta}$		$\frac{k-1}{\beta}$
	$\frac{h_{t2}}{h}$	-	-	-	$\frac{(1-k)(1+\beta)}{\beta}$		$\frac{(1-k)(1+\beta)}{\beta}$

Table 5-2 Normalized Stress at Vertices in the Stress Diagram for Each Mode.

Zone	Normalized Stress	Mode 1 ($\chi > 0$)		Mode 2 ($-\kappa \le \chi \le 0$)		Mode 3 ($0.005/\varepsilon_{cr} < \chi \le -\kappa$)	
		1	2	1	2	1	2
C	$\frac{f_{c2}}{E\varepsilon_{cr}}$	$\gamma\omega$		$\gamma\omega$		$\gamma\omega$	
	$\frac{f_{c1}}{E\varepsilon_{cr}}$	$\gamma\omega$	$\gamma\lambda$	$\gamma\omega$		$\gamma\omega$	
	$\frac{f_s'}{E\varepsilon_{cr}}$	$n\kappa$		$n\kappa$		$n\kappa$	$n\chi$
T	$\frac{f_{t1}}{E\varepsilon_{cr}}$	-	-	β	1	1	
	$\frac{f_{t2}}{E\varepsilon_{cr}}$	-	-	-	μ	μ	
	$\frac{f_s}{E\varepsilon_{cr}}$	$n\kappa$	$n\chi$	$n\chi$		$n\kappa$	

Table 5-3 Normalized Force Component for Each Mode.

Zone	Normalized Force	Mode 1 ($\chi > 0$)		Mode 2 ($-\kappa \le \chi \le 0$)		Mode 3 ($0.005/\varepsilon_{cr} < \chi \le -\kappa$)	
		1	2	1	2	1	2
C	$\frac{F_{c2}}{bhE\varepsilon_{cr}}$	-	$\frac{\lambda_{cu}-\omega}{\lambda_{cu}-\lambda}\gamma\omega$	$\frac{\gamma k\omega(\lambda_{cu}-\omega)}{\lambda_{cu}}$	-	-	
	$\frac{F_{c1}}{bhE\varepsilon_{cr}}$	$\gamma\omega$	$\frac{\omega^2-\lambda^2}{\lambda_{cu}-\lambda}\gamma\omega$	$\frac{\gamma k\omega^2}{2\lambda_{cu}}$	$\gamma\omega$	$\gamma\omega$	
	$\frac{F_s'}{bhE\varepsilon_{cr}}$	$\rho_g n\kappa$	$\rho_g n\kappa$	$\rho_g n\kappa$	$\rho_g n\kappa$	$\rho_g n\kappa$	$\rho_g n\chi$
T	$\frac{F_{t1}}{bhE\varepsilon_{cr}}$	-	-	$\frac{\beta(1-k)}{2}$	$\frac{(1-k)}{2\beta}$	$\frac{(1-k)}{2\beta}$	
	$\frac{F_{t2}}{bhE\varepsilon_{cr}}$	-	-	-	$\frac{(k-1)(1+\beta)\mu}{\beta}$	$\frac{(k-1)(1+\beta)\mu}{\beta}$	
	$\frac{F_s}{bhE\varepsilon_{cr}}$	$\rho_g n\chi$		$\rho_g n\chi$		$\rho_g n\kappa$	

Table 5-4 Normalized Force and Moment for Each Mode.

	Mode	P'
Force	1.1	$P_{11}^{'} = 2\kappa n\rho_g + \omega\gamma$
	1.2	$P_{12}^{'} = \dfrac{(\lambda^2 + \omega^2 - 2\omega\lambda_{cu})\gamma + 2n\rho_g(\chi+\kappa)(\lambda-\lambda_{cu})}{2(\lambda-\lambda_{cu})}$
	2.1	$P_{21}^{'} = -\dfrac{(\omega^2\gamma - 2\omega\gamma\lambda_{cu} + \beta\lambda_{cu})k}{2\lambda_{cu}} + n\rho_g(\chi+\kappa) + \dfrac{\beta}{2}$
	2.2	$P_{22}^{'} = (-\dfrac{\omega^2\gamma}{2\lambda_{cu}} + \omega\gamma)k + \dfrac{2\beta\mu + 2\mu - 1}{2\beta}(k-1) + n\rho_g(\chi+\kappa)$
	3.1	$P_{31}^{'} = (-\dfrac{\omega^2\gamma}{2\lambda_{cu}} + \omega\gamma)k + \dfrac{2\beta\mu + 2\mu - 1}{2\beta}(k-1)$
	3.2	$P_{32}^{'} = (-\dfrac{\omega^2\gamma}{2\lambda_{cu}} + \omega\gamma)k + \dfrac{2\beta\mu + 2\mu - 1}{2\beta}(k-1) - n\rho_g(\lambda_{cu}-\kappa) + \dfrac{n\rho_g(\alpha-1)}{k}\lambda_{cu}$
Moment	1.1	$M_{11}^{'} = 0$
	1.2	$M_{12}^{'} = \dfrac{\mathrm{C}_1\lambda_{cu}^{\ 2} + \mathrm{C}_2\lambda_{cu} + \mathrm{C}_3\beta^2 + 2\omega^3\gamma}{2(\beta-\lambda_{cu})^2}$
	2.1	$M_{21}^{'} = C_4k^2 + C_5k + C_6$
	2.2	$M_{22}^{'} = \mathrm{C}_7k^2 + \mathrm{C}_8k + \mathrm{C}_9(\chi-\kappa) + \mathrm{C}_{10}$
	3.1	$M_{31}^{'} = \mathrm{C}_7k^2 + \mathrm{C}_8k - 2\mathrm{C}_9 + \mathrm{C}_{10}$
	3.2	$M_{32}^{'} = \mathrm{C}_7k^2 + \mathrm{C}_8k + C_{11} + \dfrac{\mathrm{C}_{12}}{k}$

where $k = \dfrac{\lambda_{cu}}{\beta+\lambda_{cu}}$, $\mathrm{C}_1 = 6n\rho_g(2\alpha-1)(\chi-\kappa)$,

$\mathrm{C}_2 = 12\beta^2 n\rho_g(2\alpha+1)(\kappa-\chi) - 3\beta\gamma\omega(\omega-2\lambda_{cu})$, $\mathrm{C}_3 = \beta^2\mathrm{C}_1 - \gamma\omega^2(2\omega-3\lambda_{cu})$,

$C_4 = -\dfrac{\omega^3\gamma}{\lambda_{cu}^{\ 2}} + \dfrac{3\omega^2\gamma}{\lambda_{cu}} - 3\omega\gamma + \beta$, $C_5 = -\dfrac{1}{2}(\dfrac{3\omega^2\gamma}{\lambda_{cu}} - 6\omega\gamma + \beta)$,

$C_6 = 3n\rho_g(2\alpha-1)(\chi-\kappa) - \dfrac{\beta}{2}$, $\mathrm{C}_7 = -\dfrac{\omega-3\lambda_{cu}}{\lambda_{cu}^{\ 2}}\gamma\omega^2 - 3(\gamma\omega+\mu) - \dfrac{6\mu-3}{\beta} + \dfrac{3\mu-2}{\beta^2}$,

$\mathrm{C}_8 = -\dfrac{3\gamma\omega^2}{2\lambda_{cu}} + 3(\gamma\omega+\mu) + \dfrac{18\mu-9}{2\beta} + \dfrac{6\mu-4}{\beta^2}$, $\mathrm{C}_9 = -3n\rho_g(2\alpha-1)$,

$\mathrm{C}_{10} = -\dfrac{6\mu-3}{2\beta} - \dfrac{3\mu-2}{\beta^2}$, $\mathrm{C}_{11} = \mathrm{C}_{10} - \mathrm{C}_9(\kappa+\lambda_{cu})$, $C_{12} = C_9(1-\alpha)\lambda_{cu}$

5.4.3 Ultimate and Balanced Point

The ultimate axial load can be obtained at concentric loading case:

$$P_u' = 2\kappa n\rho_g + \gamma\omega \qquad \text{Equation 5-8}$$

The axial load and bending moment at balanced point can be determined by substituting $k_b = \frac{\alpha\lambda_{cu}}{\lambda_{cu}+\kappa}$ into equations at mode 3.1, i.e. P_{31}' and M_{31}':

$$P_b' = (\frac{1}{3}C_8 + \mu + \frac{1}{2}C_{13})\frac{\alpha\lambda_{cu}}{\lambda_{cu}+\kappa} + \frac{1}{2}C_{13} + \frac{n\rho_g(\alpha-1)(\kappa+\lambda_{cu})}{\alpha} + n\rho_g(\lambda_{cu}-\kappa) - \mu$$

$$M_b' = (\frac{\alpha\lambda_{cu}}{\lambda_{cu}+\kappa})^2[-\frac{\omega^3}{\lambda_{cu}^2} - C_8 - 3C_{13} + C_{14}] + \frac{\alpha\lambda_{cu}}{\lambda_{cu}+\kappa}[C_8 - \frac{9}{2}C_{13} - 2C_{14}] + C_{14} + \frac{3}{2}C_{13} - 2\kappa C_9$$

Equation 5-9

Where $C_{13} = \frac{\alpha(2\mu-1)}{\alpha\lambda_{cu}-\lambda_{cu}-\kappa}$, $C_{14} = \frac{\alpha^2(2-3\mu)}{(\alpha\lambda_{cu}-\lambda_{cu}-\kappa)^2}$.

5.5 Parametric Study

Using the equations summarized in Table 5-4, generating of numeric P-M interaction diagram is feasible. A matlab code is developed to implement the analytical expressions using concrete strain at bottom fiber β as the changing variable. A base numerical model is used as illustration with the parameters: E =25 GPa and ε_{cr} =110 μstr, μ =*0.33,* ε_{cu} = 0.003, β_{tu} = 160, γ = 1.0, ω = 12, λ_{cu} = 27, n = 8, κ = 18, and α = 0.85. The normalized interaction diagram obtained is shown in Figure 5-4, where all the different stages are identified. Strength reduction factor φ is also calculated using the following Equation 5-10 and a comparison between P_u-M_u and φP_u-φM_u is shown in Figure 5-5.

$$\begin{aligned} \phi &= 0.65, && \varepsilon_t \le 0.002 \\ \phi &= 0.65 + 83.3(\varepsilon_t - 0.002), && \varepsilon_{sy} < \varepsilon_t \le 0.005 \\ \phi &= 0.90, && \varepsilon_t > 0.005 \end{aligned} \qquad \text{Equation 5-10}$$

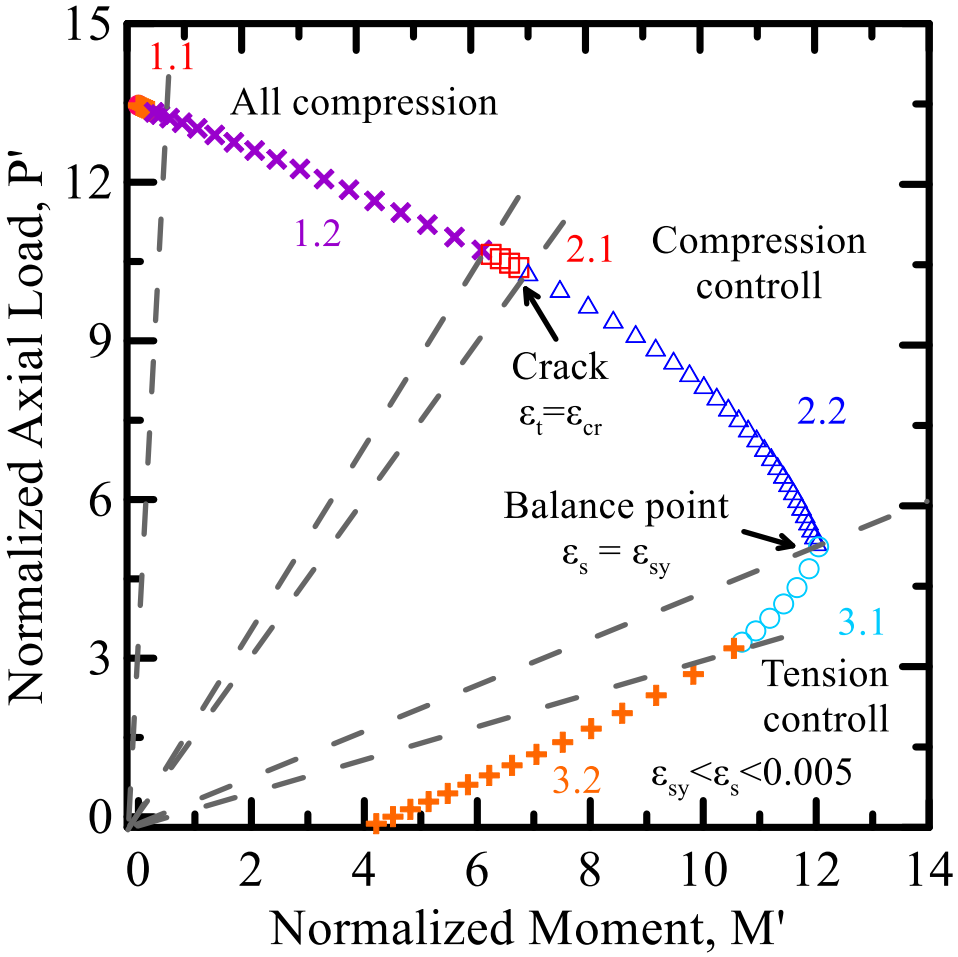

Figure 5-4 Normalized P-M Diagram Showing Different Modes.

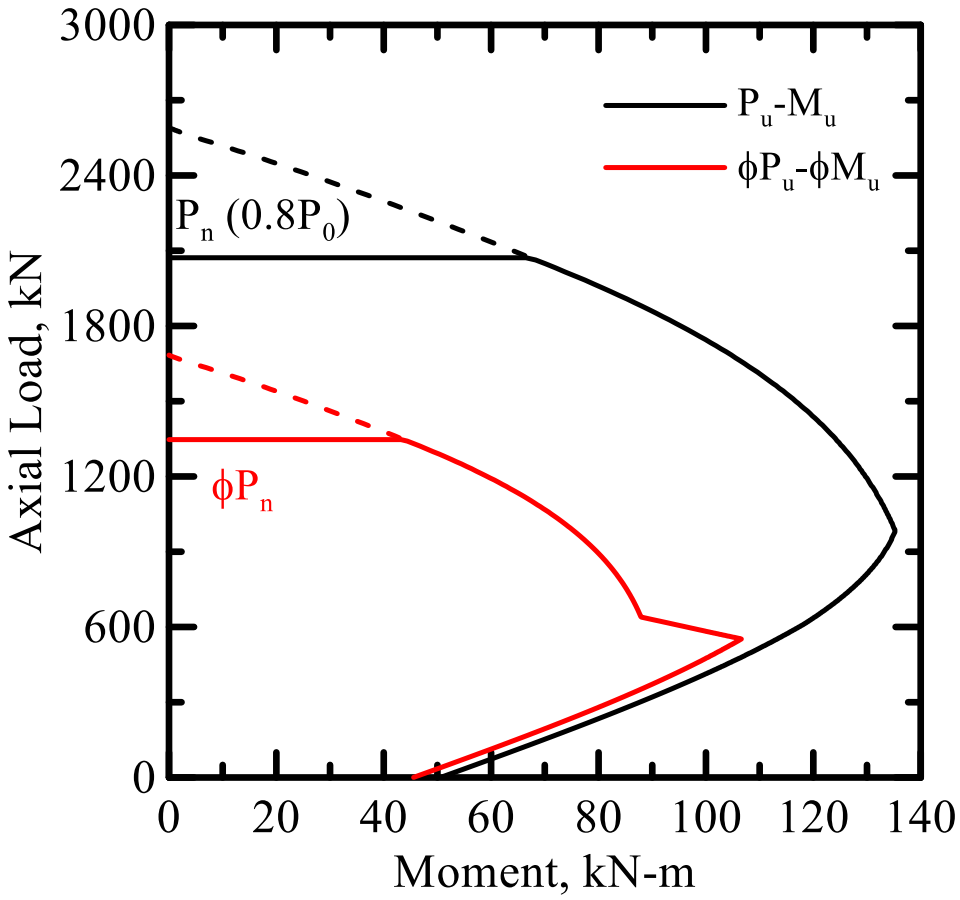

Figure 5-5 Comparison Between P_u-M_u and φP_u-φM_u for a Cross Section With b=200mm, h=350mm.

Parametric studies of post-crack tensile strength, confinement effect, reinforcement ratio and yield strength of rebar were conducted. The variables of the study were: residual tensile strength parameter $0.0 \leq \mu \leq 1.0$, improved compressive strength $0.0 \leq \omega'/\omega \leq 0.3$, (normalized compressive strength increases from ω to 1.3ω), reinforcement ratio $0.25\% \leq \rho \leq 1.0\%$, and yield strength f_{sy} increases from 400 MPa (Grade 60) to 485 MPa (Grade 70) and 550 MPa (Grade 80).

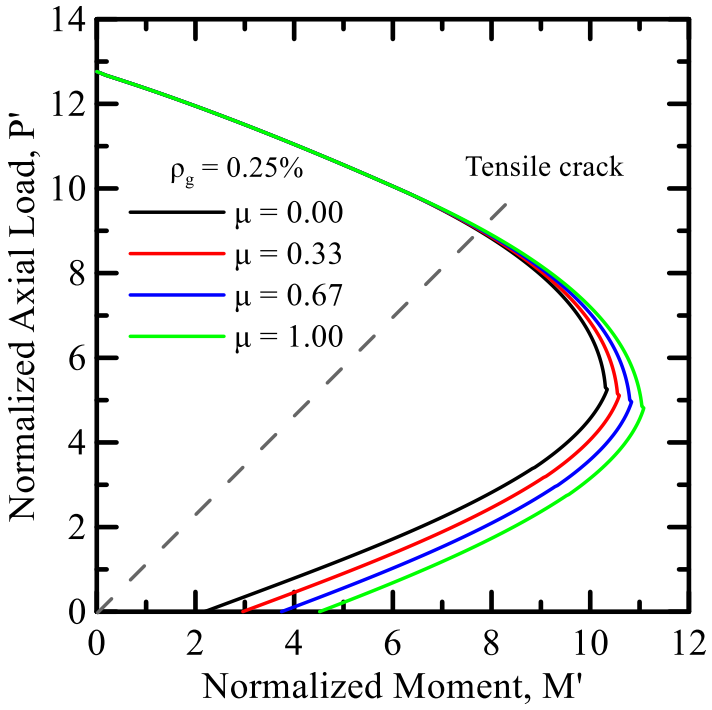
Normalized Axial Load, P'
Normalized Moment, M'
ρg = 0.25%
μ = 0.00
μ = 0.33
μ = 0.67
μ = 1.00
Tensile crack
0
2
4
6
8
10
12
14

(a)

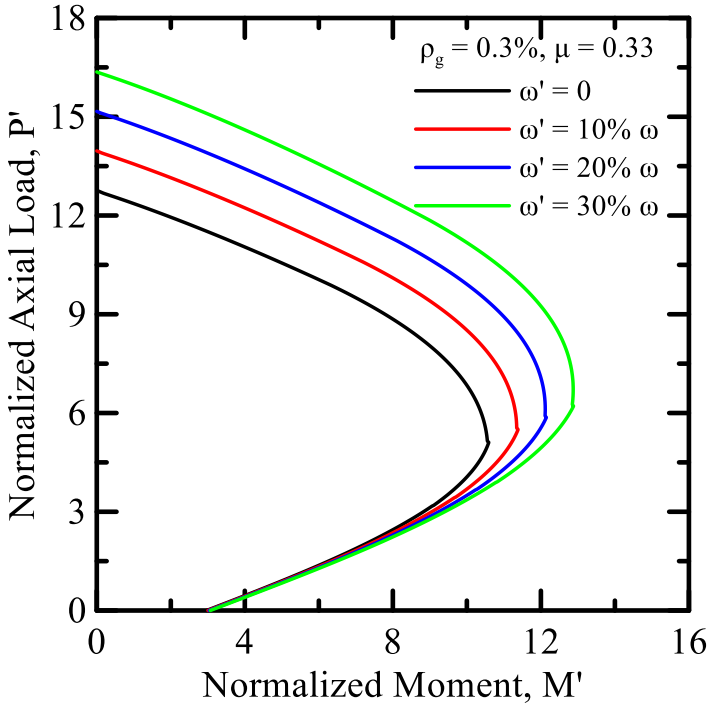
Normalized Axial Load, P'
Normalized Moment, M'
ρg = 0.3%, μ = 0.33
ω' = 0
ω' = 10% ω
ω' = 20% ω
ω' = 30% ω
0
3
6
9
12
15
18
0
4
8
12
16

(b)

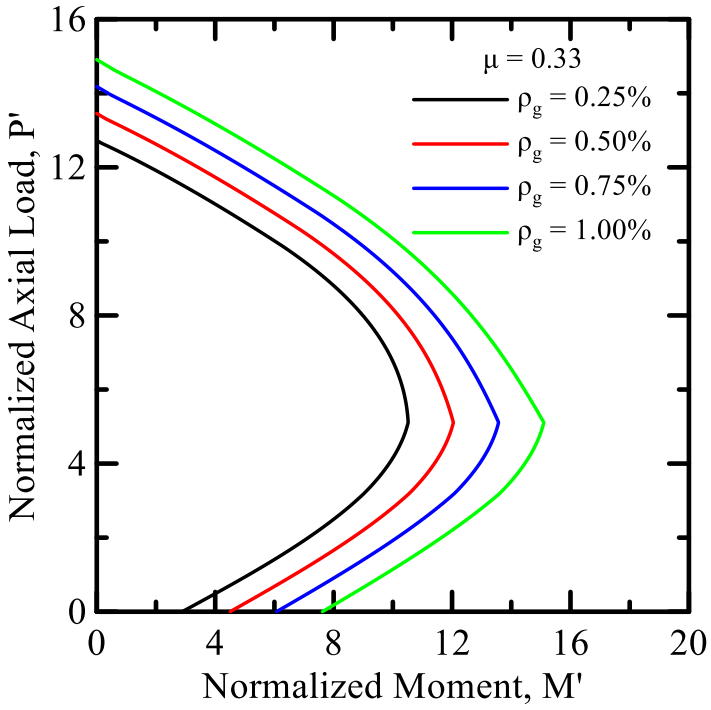

(c)

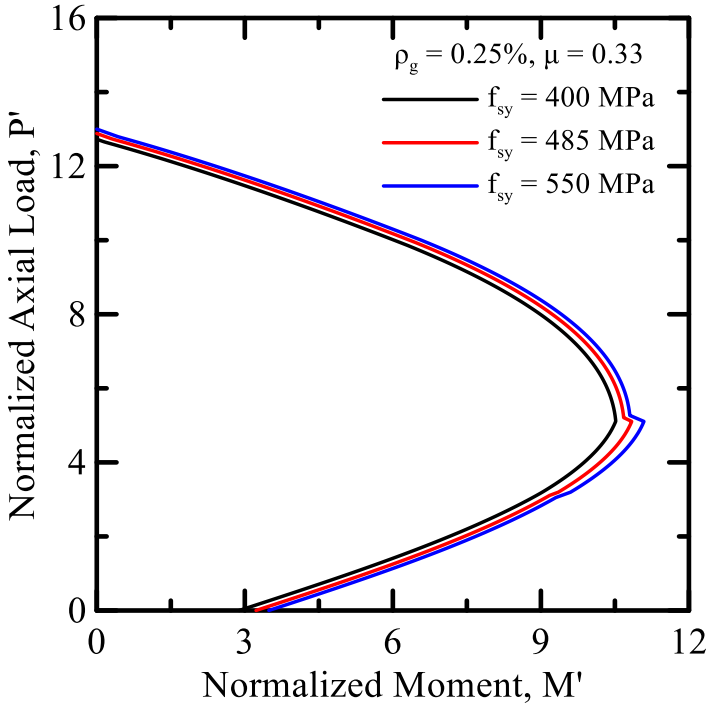

(d)

Figure 5-6 Parametric Study on the Effects of (a) Residual Tensile Strength μ, (b) Improved Compressive Strength ω' Due to Confinement, (c) Reinforcement Ratio ρ_g, and (d) Yield Strength f_{sy}.

Figure 5-6(a) shows the effect of residual tensile strength μ on the normalized interaction diagram. As a parameter governing the tensile properties, the ultimate axial load P_u' is therefore not affected. However, the moment capacity after cracking in tension starts to increase due to the improvement of the tensile force provided by fiber bridging mechanism. Specifically, the balance moment M_b' increases from 10.3 to 10.6, 10.8 and 11.1, when μ increases from 0 to 0.33, 0.67, and 1, respectively. The effect of confinement is evaluated by increasing the compressive strength for 10%, 20% and 30%, i.e. ω' changes from 0 to 0.1ω, 0.2ω, and 0.3ω. A clear improvement in P_u', P_b' and M_b' can be observed in Figure 5-6(b) while the moment capacity at pure bending is not affected (intersection with x-axis). The effects of longitudinal reinforcement properties in terms of reinforcement ratio and rebar yield strength are illustrated in Figures 5-6(c) and (d), respectively. Increases in ρ_g and f_{sy} can improve the overall cross sectional properties in ultimate load, balance load and moment and moment capacity under pure bending, especially by increasing reinforcement ratio.

5.6 Model Verification

Chaallal and Shahawy [223] evaluated the performance of RC columns under combined axial-flexrual loading and obtained experimental interaction diagrams. The column had cross section of b = 203mm and d = 356 mm. Two #6 rebars were placed on each side with a cover of 50 mm, which results in a reinforcement ratio of ρ_g = 0.8% and reinforcement depth parameter α = 0.86. The rebar was Grade 60 steel with a yield strength of f_{sy} = 414 MPa and the concrete compressive strength was σ_{cy} = 25.0 MPa. In additional to the geometrical and mechanical properties, other model parameters used including: E =30 GPa, ε_{cr} =110 μstr, μ =*0.5,* ε_{cu} = 0.003, β_{tu} = 181, γ = 0.9, ω = 7.6, λ_{cu} = 27, γ = *0.9*, n = 7, and

κ = 18. A comparison of experimental and simulated results is shown in Figure 5-7 where a good agreement can be observed. Note that the nominal capacity P_n and M_n are used without considering the reduction factor ϕ.

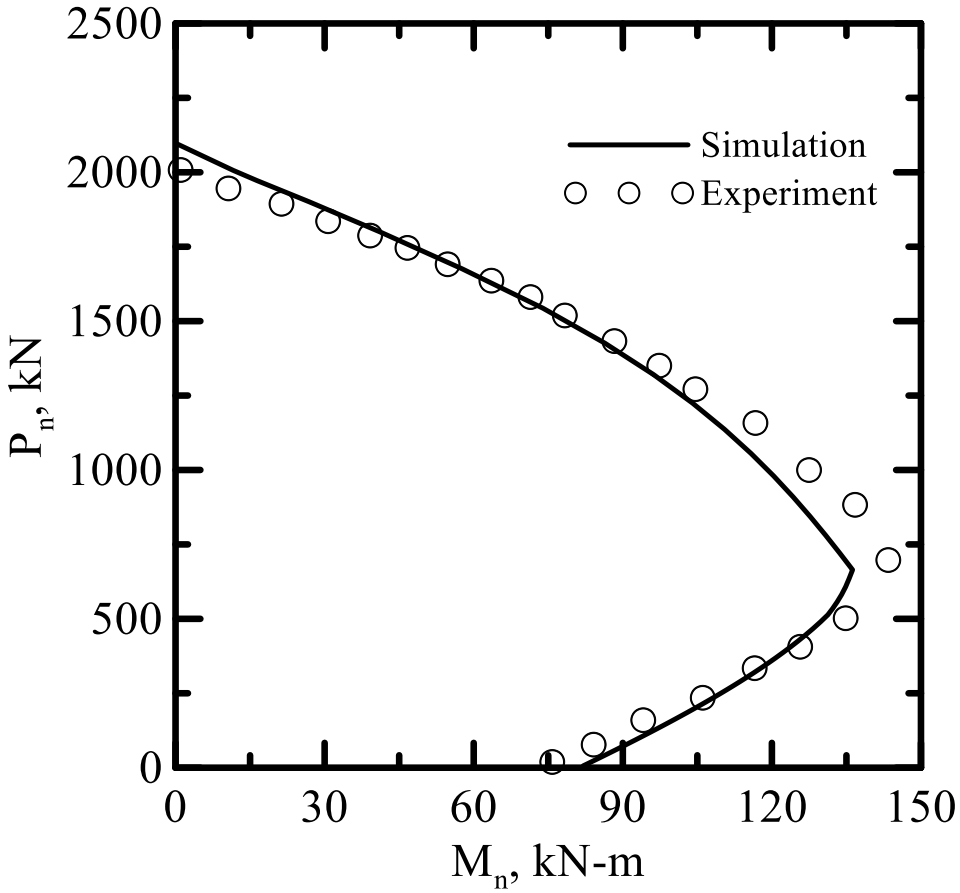

Figure 5-7 Comparison of Simulated and Experimentally Determined P-M Diagram of a RC Column.

de la Fuene et al. [224] presented the successful experiences regarding the use of fibers as the main reinforcement in precast segmental linings in the metropolitan area of Barcelona. It is known that the addition of structural fibers improves the mechanical behavior of the structure during its construction, especially in cases such as the thrust of the jacks, and on the other hand it leads to a reduction of the global costs by reducing the conventional passive reinforcement. The case discussed in present study consists in two parallel rail

tunnels built in the urban area of Terrassa as the extension of the Ferrocarriles de la Generalitat de Catalunya (FGC). Both tunnels have been excavated successively with a total length of 4510 m each. The tunnels consist of segmental rings with an internal diameter of 6.0 m, formed by 6 + 1 RC-SFRC precast concrete C30/37 segments with a width of 1.5 m and a thickness of 0.30 m as shown in Figure 5-8.

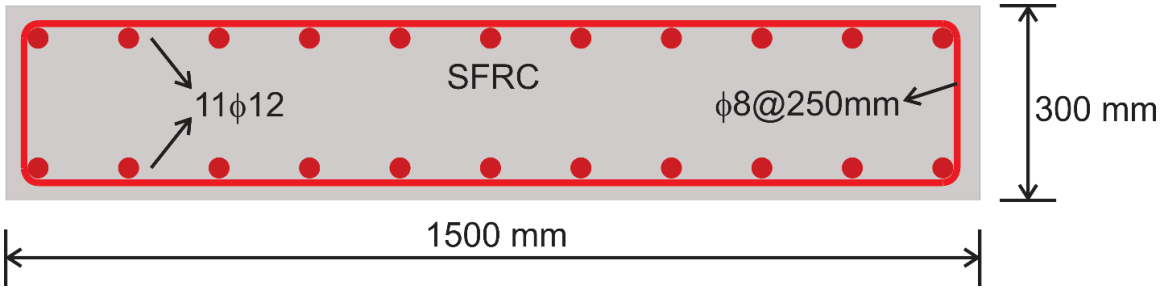

Figure 5-8 Cross Section of RC-SFRC Precast Segment.

Figure 5-9 shows the interaction diagrams for the section with the RC-SFRC precast segment obtained by proposed model and original analysis. The parameters for proposed model are as follows: E =30 GPa, ε_{cr} =200 μstr, ε_{cu} = 0.003, β_{tu} = 250, γ = 0.9, ω = 5.0, λ_{cu} = 17.5, γ = *0.9*, ρ = 0.28%, n = 7, and κ = 11.9. The yielding strength and modulus of rebar are 500 MPa and 210 GPa. The residual strength parameter μ was selected as 0, 0.15, and 0.3 for the fiber contents of 0, 15 and 30 kg/m^3, respectively. The contribution and effects of steel fibers on the interaction diagram of the precast segments are therefore revealed. The interaction diagram is divided into compression and the tension controlled zones as illustrated in Figure 5-4. It is evident from the Figure 5-9(a) that the changing in fiber content does not affect in most of compression controlled region while the ultimate moment starts to increase after cracking and becomes more pronounced in the tension controlled region. The phenomenon can be traced back to the role of fibers in the concrete matrix which primarily enhances the post-cracking and residual strengths in tension by bridging

the cracks. This mechanism is predicted by the proposed model by increasing the normalized residual strength factor μ.

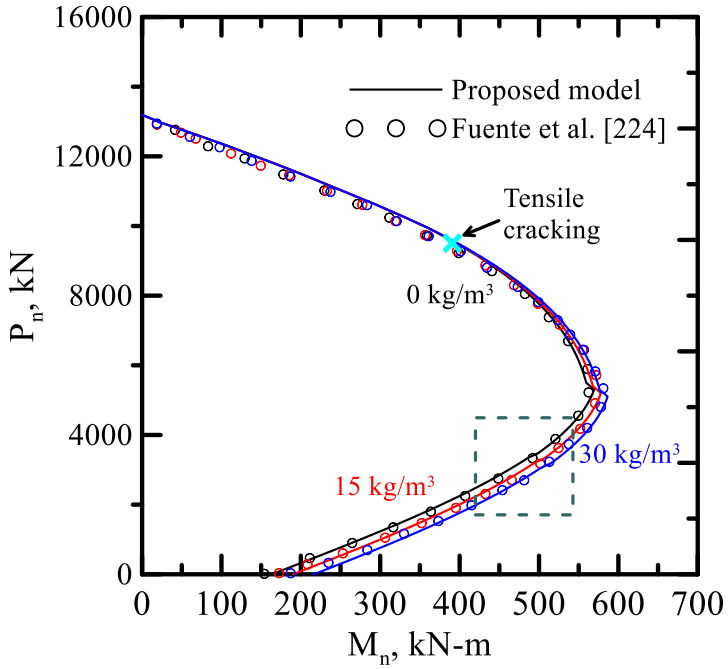

(a)

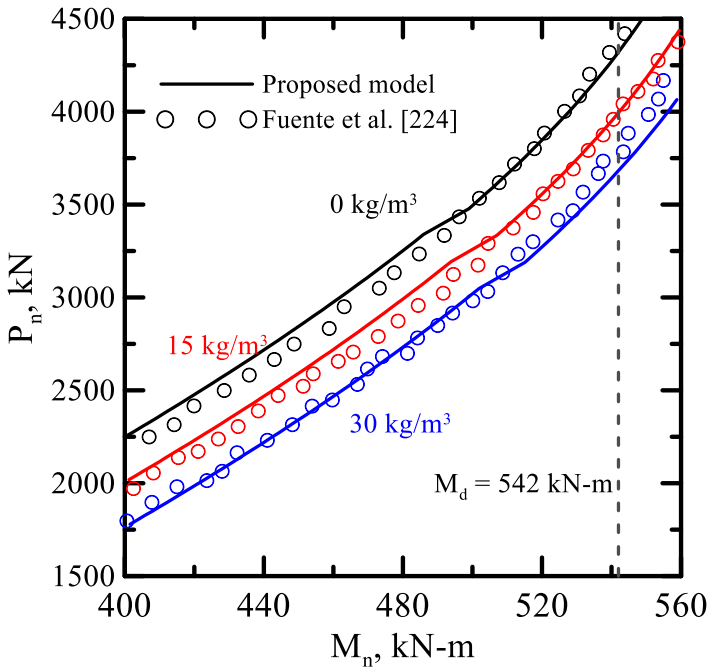

(b)

Figure 5-9 (a) P-M Diagram for the Tunnel Lining Segment With a Cross Section of 11φ12 and Varying Amount of Fibers; (b) Closer Look at the Range Indicated.

On the basis of the results presented in Figure 5-9(b), it is observed that with a fiber content of 15 kg/m^3, the design moment M_d of 542 kN-m in service stage is already exceeded [224]. Likewise, it should be noted that the maximum increase of M_u does not exceed 5% (30 kg/m^3) with regard to the RC precast segment (0 kg/m^3) if N_d = 4209 kN. In other words, in this case the rebars perform the main resistance function in failure, whereas the fibres play a more important role in the crack width control.

Tiberti [225] performed numerical analysis on different case studies of the tunneling segments with internal diameters ranging from 7.25 m to 14.9 m. The effect of steel fiber was considered in the study by using a similar concept of residual tensile strength "χ" that ranges from 0 to 0.75. The studies of each case were performed in two configurations: plain SFRC and HRC sections with a reinforcement ratio of ρ=0.2% (note that ρ_g defined as reinforcement ratio per gross area in present study is different from ρ, which depends on the cross sectional geometries and steel configuration). The design compressive strength of the concrete f_{cd} = 22.7 MPa, tensile strength f_{cld} = 1.6 MPa, concrete modulus E = 35 GPa, design yielding strength of steel f_{yd} = 391 MPa, steel modulus E_s = 200 GPa. Two case studies, "Malpensa-Saronno lining" with smaller diameter of 7.25 and "Highway tunnel lining" with larger diameter of 14.9 m are presented in this work by comparing the original analysis with the proposed model.

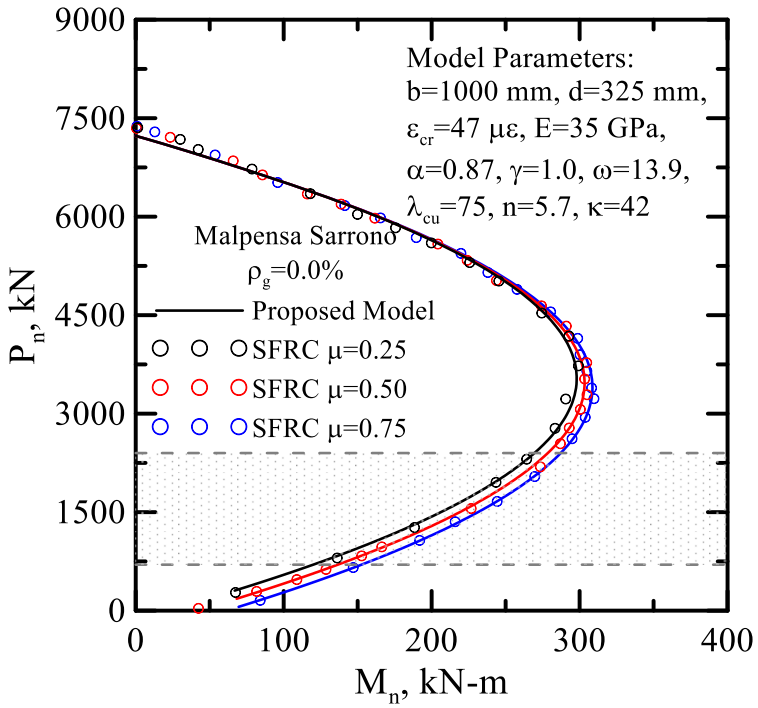

(a)

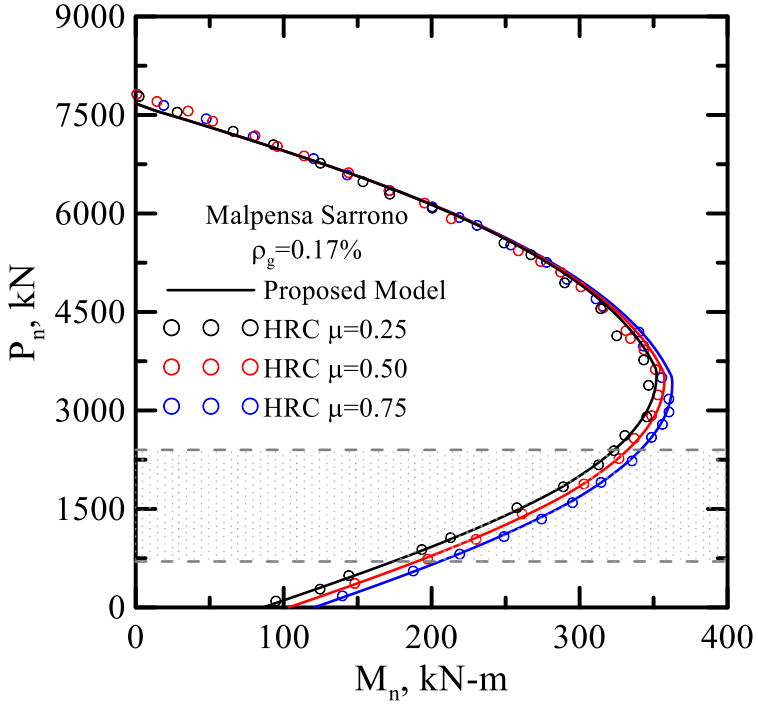

(b)

Figure 5-10 P-M Diagram for the Malpensa-Saronno Lining Configuration (a) Plain SFRC Section, and (b) HRC Section [225].

Figures 5-10 and 5-11 compare the interaction diagrams for the sections made of plain SFRC and HRC for the two case studies, respectively. The cross sectional geometries and model parameters are indicated in the figures. In order to address the residual strength used in the original study, same values are assigned to the parameter μ, which are 0.25, 0.50 and 0.75, respectively. Similarly, increments in the ultimate moment capacity are observed with increasing μ value. The shaded area represents the region of axial force under investigation which is referred to as the "normal ring force" defined in the original study (range of tunnel overburden considered from 1 to 4 times of the external diameter). It clearly turns out that for linings having small diameter (Malpensa-Saronno lining in Figure 5-10), the range of normal ring force investigated is located in a favorable region of the domains, where the fiber resistant is considerable. On the other hand, for the tunnel linings having large diameter (Highway tunnel lining in Figure 5-11), the shaded region moves to high normal ring force exhibiting a less pronounced contribution due to fibers. For instance, referring to the Highway tunnel, the normal force investigated exceeds the maximum resistant bending moment of the domain. It is therefore known that, in this case the sectional lining behavior is governed by the concrete compressive strength [225].

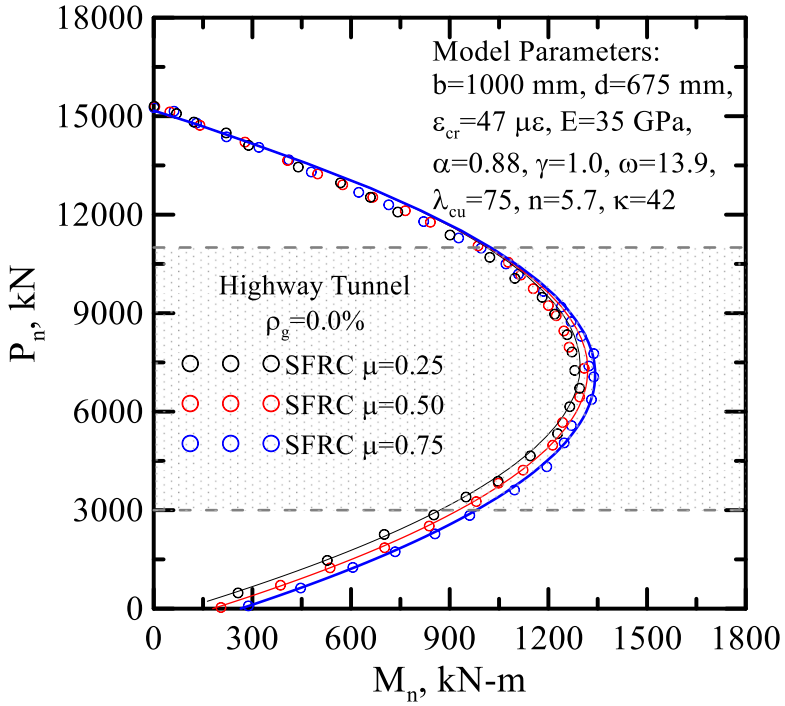

(a)

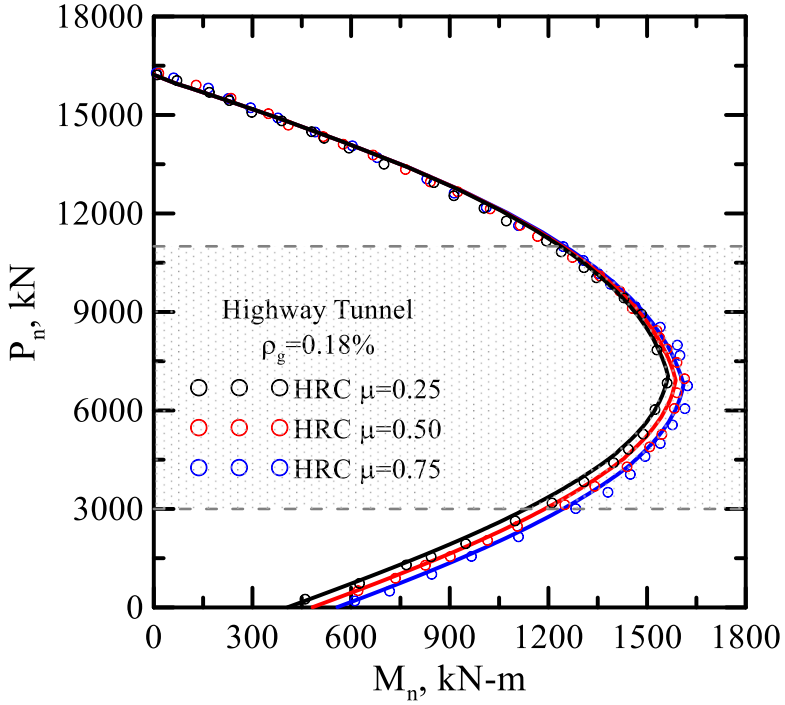

(b)

Figure 5-11 P-M Diagram for the Highway Tunnel Lining Configuration (a) Plain SFRC Section, and (b) HRC Section [225].

Besides the precast segment, cast-in-situ application is also investigated. Chiaia et al. [226] proposed a numerical block model that evaluates the cracking information in RC and HRC members, which was applied to the design of Faver-S.S. 612 tunnel lining in Italy. The segment has a cross section of 1000 mm by 500 mm with reinforcement area A_s = 800 mm^2. Concrete compressive strength and steel yield strength are 25 MPa and 430 MPa, respectively. Steel fibers at dosage of 35 kg/m^3 were added to the mix. The applied loads (M_{sd}-N_{sd}) and bending moments were obtained from multi-stage 2D finite element model. The ultimate limit states of the cross-section were defined by two interaction diagrams for plain SFRC (ρ_g=0.0%) section using the material model specified by RILEM TC 162-TDF [57] and HRC (ρ_g=0.16%) section derived by Chiaia et al. [227].

The applied actions M_{sd}-N_{sd} and are compared to the computed interaction diagrams as shown in Figure 5-12. For the considered cross-sections, the ultimate limit states are reached in the tensile zones, since the couples M_{sd}-N_{sd} generally fall in the tension-controlled zones of the interaction curves. In addition, most of the applied actions fall within the range of plain SFRC section indicating the sufficient resistance provided by the designed section for most cases. However, some of the points M_{sd}-N_{sd} fall outside the computed design diagrams of SFRC section where the axial action is dominated by tension. In these zones, the rebars are needed to provide necessary tensile resistance where a ρ_g value of 0.16% (ρ=0.2%) as a minimum reinforcement ratio is sufficient [227].

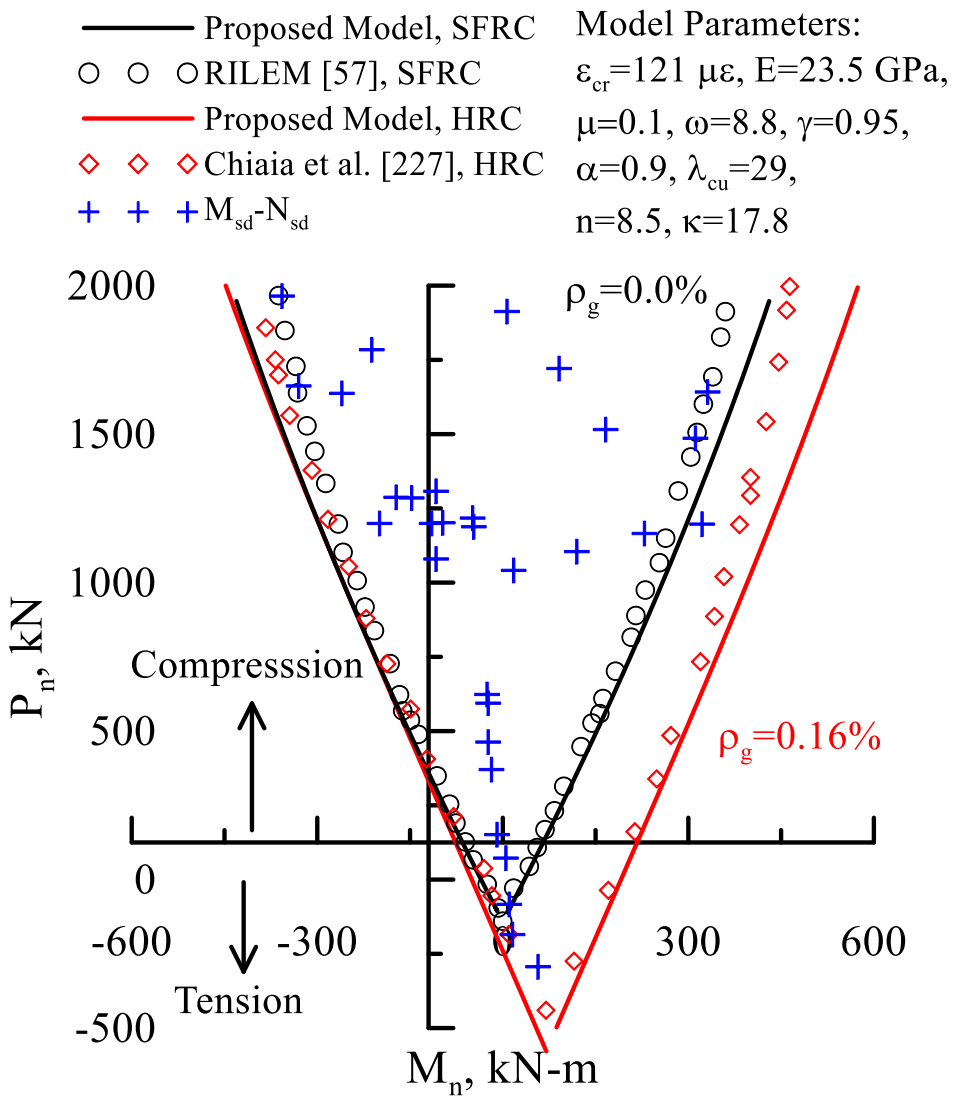

Figure 5-12 Comparison Between Applied Actions and the Design Interaction Diagrams Obtained by Different Methods.

Notation

A_s= area of steel rebar

b= beam width

$C_{1\text{-}11}$= coefficients for normalized moment in Table 5-4

d = effective depth at location of steel rebar

E= elastic tensile modulus of concrete

E_c= elastic compressive modulus of concrete

E_s= elastic modulus of steel

f'_c= cylindrical ultimate compressive strength of concrete

f= stress

F= force components in stress diagram

d= full height of a beam section or height of each compression and tension zone in stress diagram

k= neutral axis depth ratio

M= moment

M_n= nominal moment capacity

n= modulus ratio (E_s/E)

y= moment arm from force component to neutral axis

α= normalized depth of steel reinforcement

β= normalized tensile strain ($\varepsilon_t/\varepsilon_{cr}$)

ε= strain

ε_c= concrete compressive strain

ε_t= concrete tensile strain

γ= normalized concrete compressive modulus (E_c/E)

κ= normalized steel yield strain ($\varepsilon_{sy}/\varepsilon_{cr}$)

λ= normalized compressive strain ($\varepsilon_c/\varepsilon_{cr}$)

μ= normalized residual tensile strength (σ_p/σ_{cr})

ρ= steel reinforcement ratio per effective area

σ = concrete stress

σ_p= residual tensile strength

ω= normalized concrete compressive yield strain ($\varepsilon_{cy}/\varepsilon_{cr}$)

χ= normalized steel strain ($\varepsilon_s/\varepsilon_{cr}$)

φ= strength reduction factor

Subscripts

c1= elastic compression zone 1 in stress diagram

c2= plastic compression zone 2 in stress diagram

cr= at first cracking

cu= at ultimate concrete compressive strain

cy= at concrete compressive yielding

i= at stage *i* of normalized concrete compressive strain and tensile steel condition

s= refer to steel

sy= at steel yielding

t1= elastic tension zone 1 in stress diagram

t2= residual tension zone 2 in stress diagram

tu= at concrete ultimate tensile stain

cu= at concrete ultimate compressive strain

Supper scripts

'= normalizing symbol

6. SHEAR FAILURE IN BEAMS

6.1 Introduction

Since the shear strength of concrete is dominated by its ability to resist diagonal tension [228, 229], use of steel fibers may provide sufficient shear resistance and partly or even fully replace web reinforcements. It is well known that the use of even modest amounts of diffused steel fiber reinforcement significantly increases the post-cracking toughness and ductility of concrete [230,231,232,233,234], increases tensile strength to varying degrees [235], and reduces the width and spacing of cracks [149,236,237,238]. According to Dinh et al. [239], fiber reinforcement enhances shear resistance by transferring tensile stresses across diagonal cracks and improves aggregate interlock by reducing the spacing and width of diagonal cracks. Based on a comprehensive review of test data related to the use of steel fibers as shear reinforcement [229], Parra-Montesinos [240] has reported an average shear stress of $0.3\sqrt{f_c'}$ MPa ($3.5\sqrt{f_c'}$ psi) to represent a lower bound to the shear strength of beams reinforced with deformed steel fibers when volume fractions V_f greater than or equal to 0.75%. Subsequently, a new provision was first introduced in ACI 318-08 and reaffirmed in the 2011 ACI Building Code allowing the use of deformed steel fibers in volume fractions greater than or equal to 0.75% as minimum shear reinforcement in normal-strength concrete beams. In addition to the specified minimum fiber content, the ACI Building Code also prescribes a flexural performance criteria based on the ASTM C1609 four-point bend test for the acceptance of steel fibers as minimum shear reinforcement.

Shear failure is not considered in the proposed flexural model which sometimes may lead to inaccurate predictions. For example, Figure 6-2(b) shows that the model simulation overestimates the experimental results reported by Ding et al. [241] to a great extent, which

can only be explained by the different modes of failure. As shown in Figure 6-2(c), the beams are subjected to shear failure companied by dominating diagonal cracks, which occurs prior to the flexural failures such as rebar yielding or compression failure. Therefore, the goal of this section is to determine the shear stress using a rational method based on 2D stress analysis approach, and construct the shear failure criteria in HRC beams without stirrups.

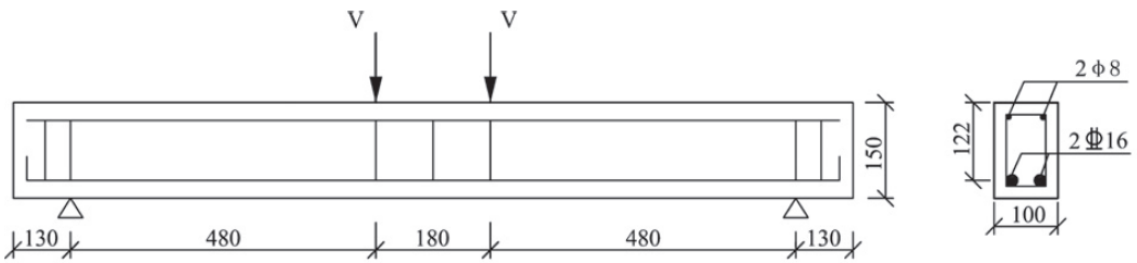

(a)

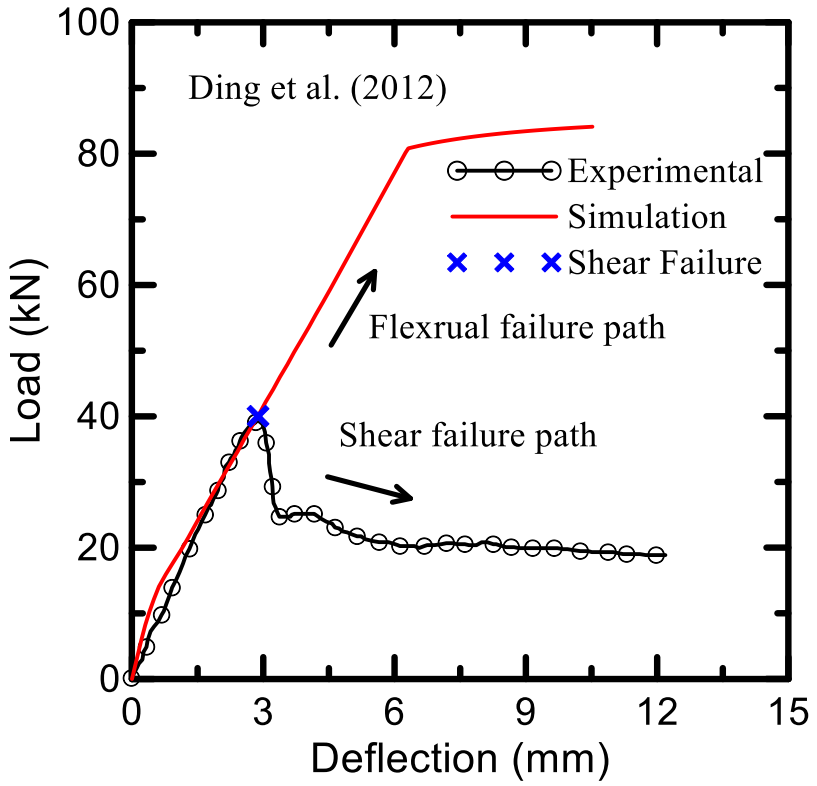

(b)

(c)

Figure 6-1 (a) Details of the Beam Subjected to Four-Point Bending, (b) Comparison Between Flexural Model Simulation and Experimental Data, (c) Shear Failure in the Tested Beams.

6.2 Stress Analysis Based Calculation

The nature of the analytical based cross sectional analysis enables the track of full field distribution of normal strain and stress across the entire beam. The first step is to determine the distribution of bending moment along the beam based on equilibrium; then the curvature and normalized strain at extreme fiber can be extracted from moment-curvature and moment-strain curves; once the strain at extreme fiber is obtained, the strain and stress distribution can be reconstructed based on Figure 6-3.

Figure 6-3(a) shows the stress and strain distribution along a certain cross section in cracked stage. Once the full field distribution is obtained, a thin element can then be investigated as shown in Figure 6-3(b). The shear stress at location of (x,y) can be calculated by solving equilibrium equations, as shown in Figure 6-3(c). Note that in the example figure, tensile stress below the location of rebar is a constant $\mu\varepsilon_{cr}$ on both sides of the free body. Thus the shear stress below location of tensile rebar is zero.

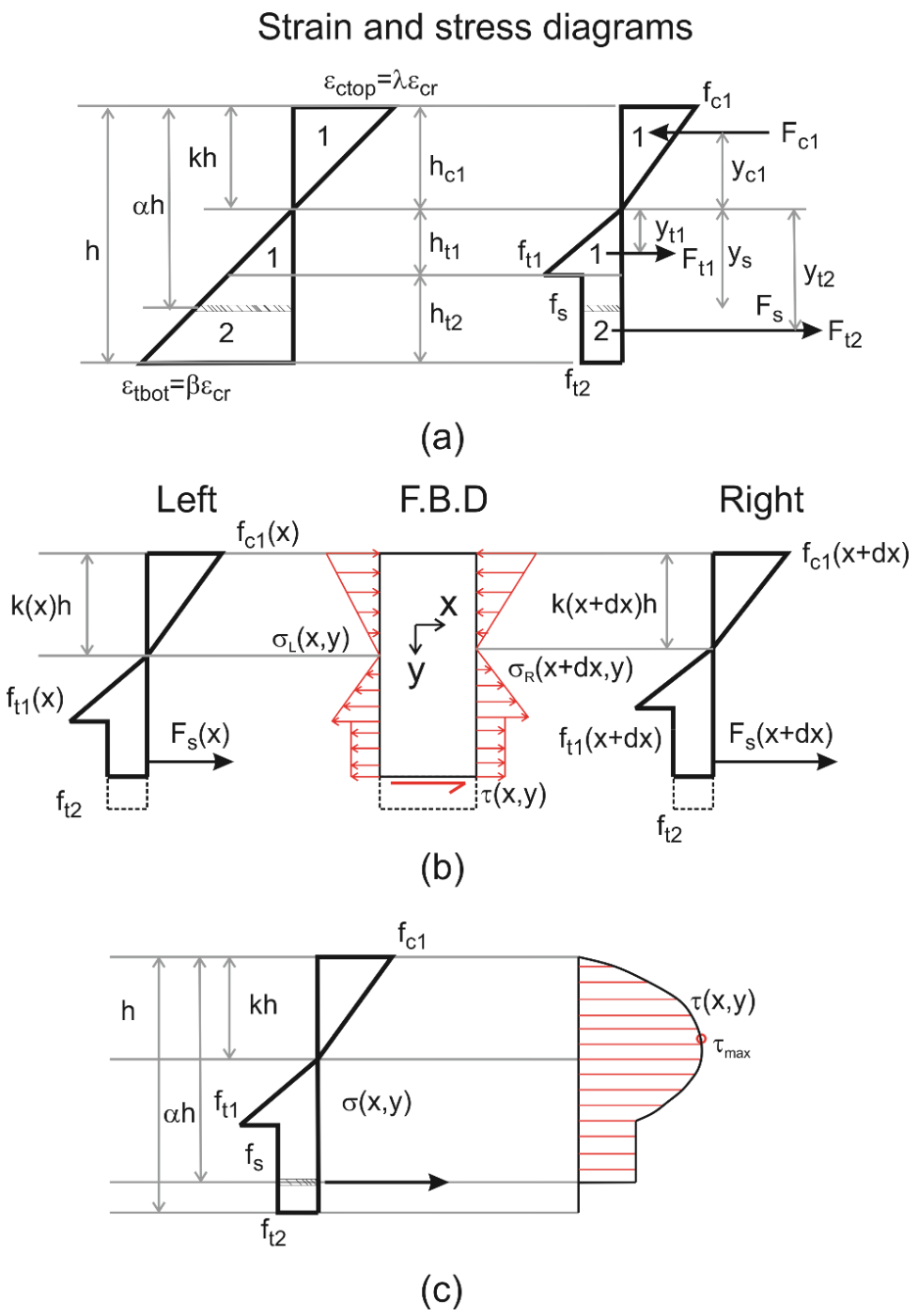

Figure 6-2 (a) Normal Stress Distribution of A HRC Cross Section in Cracked Stage, (b) Free Body Diagram of a Thin Element, (c) Distribution of Shear Stress.

6.3 Structural Analysis Using Distributed Hinges

Figure 6-4 schematically presents the development of flexural-shear cracks in a RC beam subjected to shear failure. At early stage of the test, the first crack initiates and grows at the mid-span where the maximum bending moment is at. As load keeps increasing, multiple cracking starts to form and spread from the mid-span towards the far field. As a result of combined tensile and shear stresses, the principle stress σ_1 turns into an inclined direction near the crack tip, which subsequently leads to the growth of vertical cracks along the diagonal directions. The diagonal cracks initiated from the flexural cracks eventually merged and form a dominated shear crack that results in the failure.

Based on the experimental study of multiple cracking mechanisms discussed in Chapter 2, the distributed cracking as a result of tension stiffening locate at approximately regular intervals. It is therefore reasonable to model the multiple cracks are equally distributed along the beam. The significant parameter crack spacing can be either obtained from experimental observation or tension stiffening model. In order to address the distributed cracking using a smeared cracking material model, the distributed hinges (Figure 4-1) are assumed to be formed sequentially along the beam as the tensile strain attains cracking strain. The length of the hinge L_p is assumed to be equal to the crack spacing.

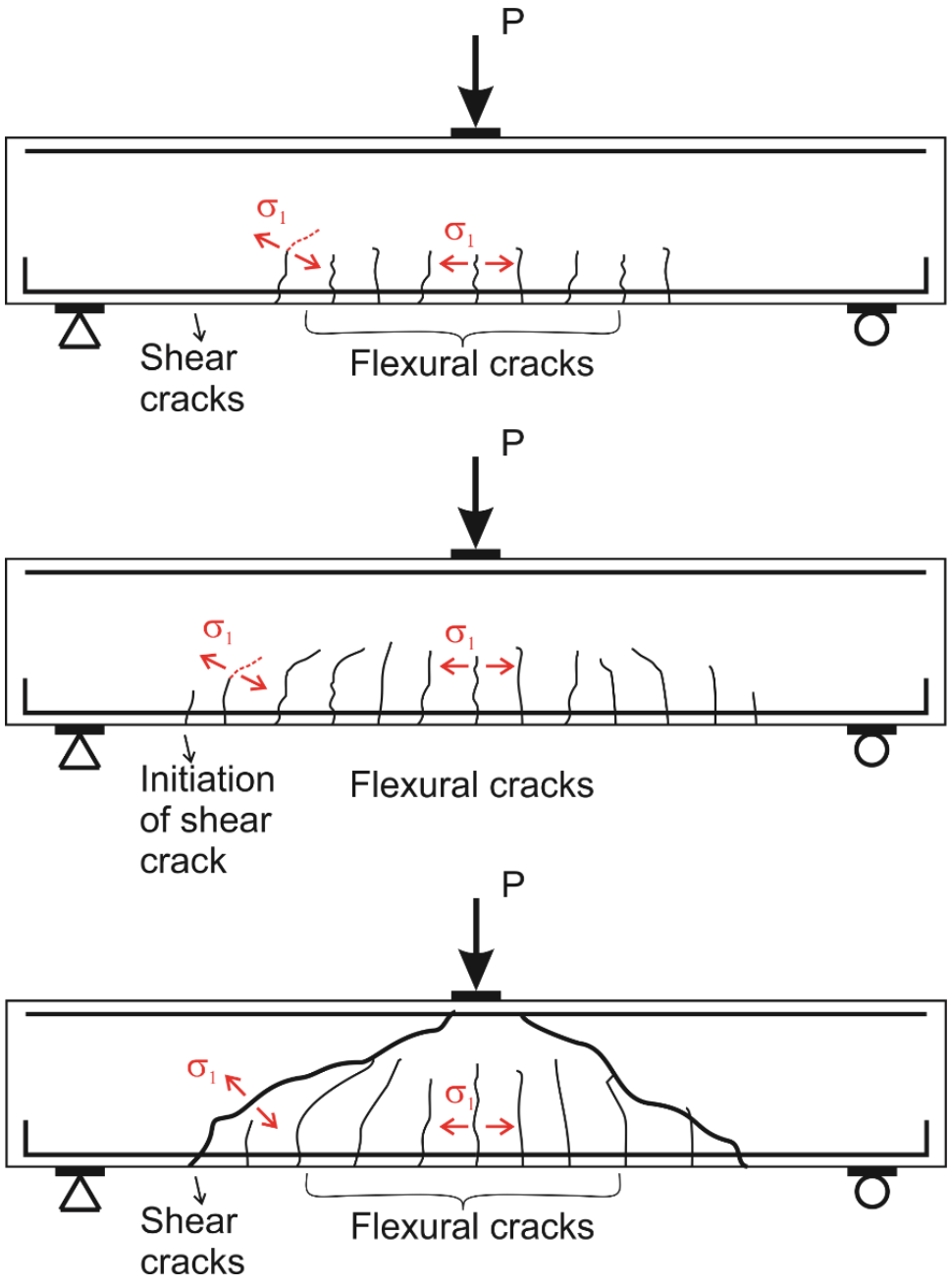

Figure 6-3 Development of Flexural and Shear Cracks in a RC Beam Dominated by Shear Failure.

Figure 6-5 shows the distributed hinges in a beam subjected to four-point bending (only half of the beam is shown due to symmetry). The location of flexural crack is assumed to be at the center of each hinge such that when the tensile strain at the mid-section of the pre-assigned hinge area reaches the cracking strain, a new hinge is formed. It is shown in the

DIC observation (Chapter 2) that the tensile strain is localized across the cracks while the far field strain is uniformly distributed at low values. In order to implement the smeared cracking model, the tensile strain is assumed to be a constant within each hinge by equating the displacement, i.e., converting crack opening into nominal strain through characteristic length, which in this case refers to crack spacing l_{cs} or the hinge length L_p [53]. Subsequently, the curvature is also averaged over each hinge and the mid-span deflection can be obtained by numerical integrate of the curvature over the length.

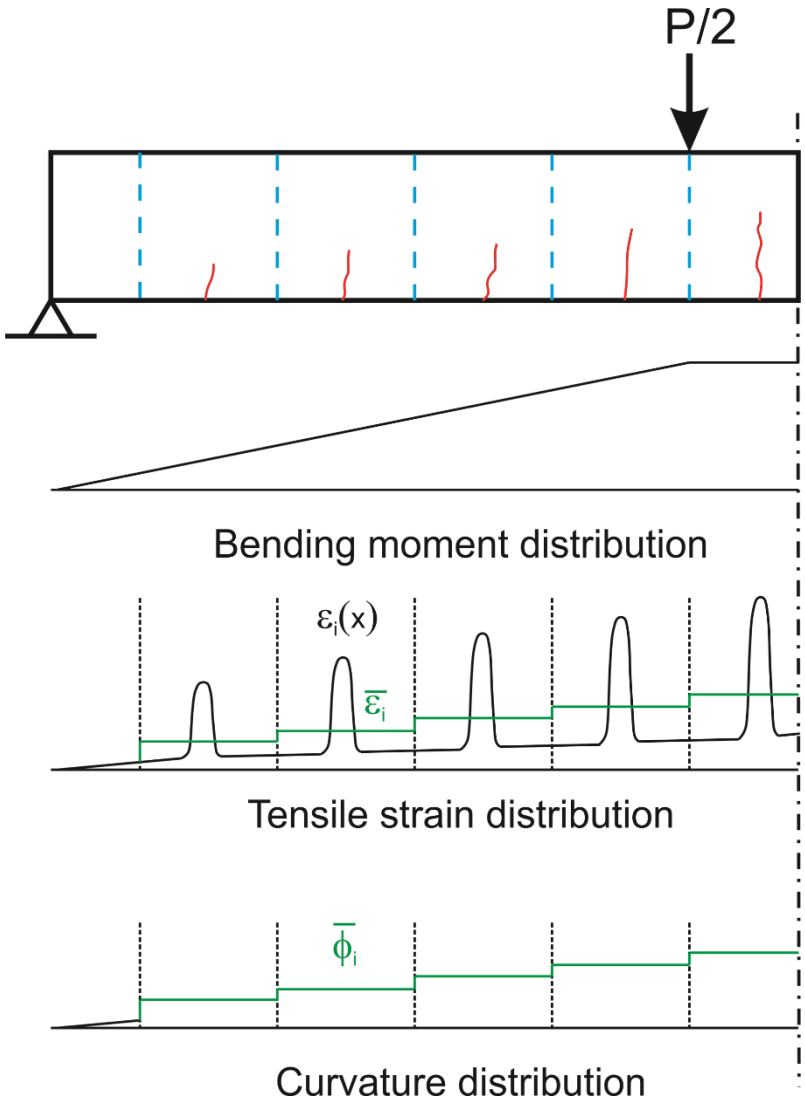

Figure 6-4 Averaged Tensile Strain and Curvature of Each Nonlinear Hinge.

With the discrete damage methodology introduced above, a numerical beam model of the example shown in Figure 6-2 is used to illustrate the stress and strain distributions. The beam subjected to four-point bending has dimensions of b=100mm, d=150mm, L=1140mm. Material parameters used in the model are as follows: The material parameters are as follows: f_c'=41 MPa, f_{cr}=3 MPa, ε_{cr}=111 με, E_c=27 GPa, f_y=430 MPa, E_s=210 GPa, ρ_g=2.7%. Figure 6-6 demonstrates the 2D distributions of normal strain, stress, shear stress and principle directions (θ_{P1}) at load level of 40 kN where shear failure occurs. The principle stress and direction are calculated based on normal and shear stresses using following equations:

$$\sigma_{1,2} = \frac{\sigma_x + \sigma_y}{2} \pm \sqrt{\left(\frac{\sigma_x - \sigma_y}{2}\right)^2 + \tau_{xy}^2} \qquad \text{Equation 6-1}$$

$$cos\,2\theta_{P1} = \frac{\sigma_x - \sigma_y}{2R}$$

As shown in Figure 6-6(a) and (b), the compression and tension zones can be clearly identified at the upper and lower half of the beam, respectively. Shear stress map shown in Figure 6-6(c) reveals a non-uniform distribution pattern along the length of the beam, which is against the conventional calculation of average shear stress using shear force. As previously mentioned, the shear stresses below tensile rebar is zero due to constant residual strength. Also the region near left support shows very low shear stress since the nonlinear hinge is not formed and the normal stresses are relatively low as well. The maximum shear stress is found to be 2.2 MPa, which is higher than the average shear stress $v_u = Vu / bd = 1.6MPa$.

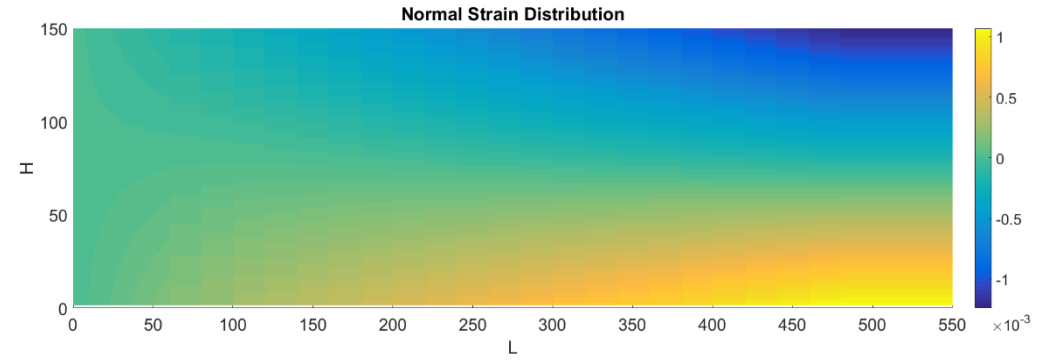

(a)

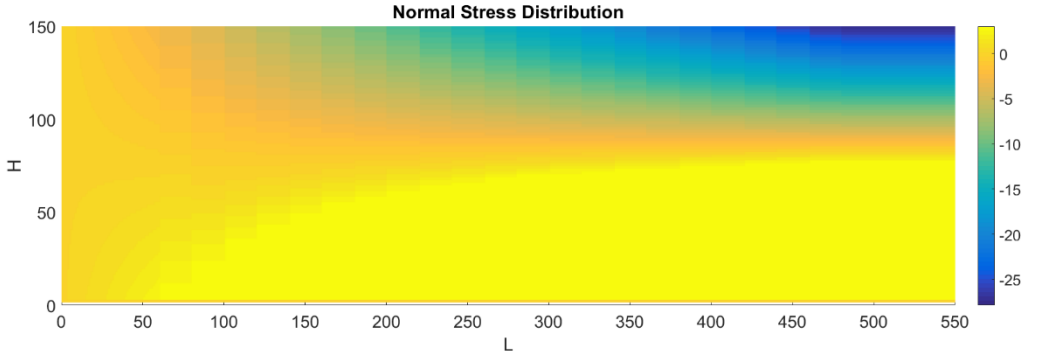

(b)

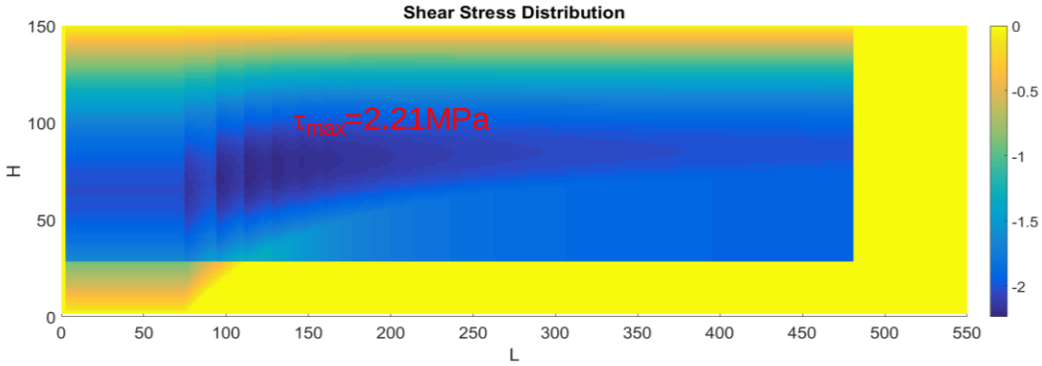

(c)

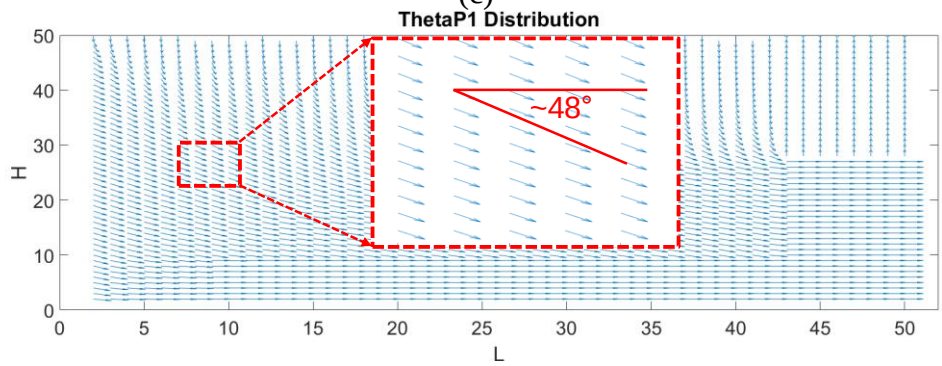

(d)

Figure 6-5 2D Distributions of (a) Normal Strain, (b) Normal Stress, (c) Shear Stress, (d) θ_{P1}.

6.4 Experimental Calibration

Minelli et al. [242] carried out an experimental campaign on HRC beams under shear loading: nine full scale beams, having a height varying from 500 to 1500 mm, were tested for investigating the effect of steel fibers on key parameters influencing the shear response of concrete members. All tested members contained no conventional shear reinforcement and different amounts of steel fibers: 0, 0.64 and 1 % by volume. The beam details and rebar configuration are shown in Figure 6-7.

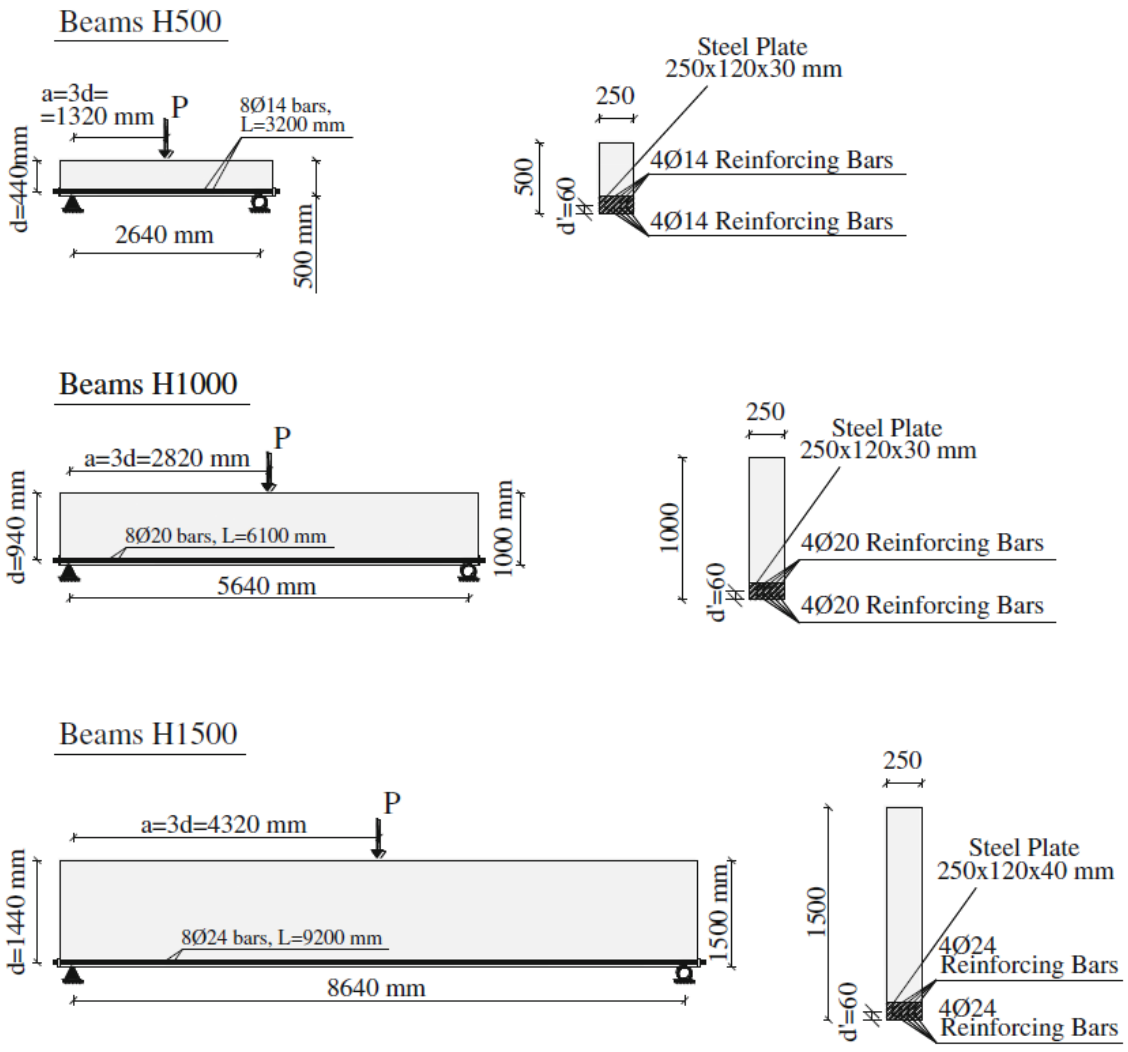

Figure 6-6 Beam and Cross Section Details [242].

Figure 6-8 presents the model simulation and experimental data for the beam with a height of 500 mm, where the ultimate shear force V_u is 443 kN and corresponding maximum shear stress is 2.94 MPa. A plasticity stage is used at a constant load to show the shear failure path against the flexural failure path. Distributions of shear and principle stresses are shown in Figure 6-9. In addition to the stress distribution, the discrete hinges are also presented in terms of the nominal crack in Figure 6-10. The vertical bars represent the locations of hinges mid-section while the height equals to the height of cracked zone h_{t2}, as shown in Figure 4-3.

Table 6-1 summarizes the model parameters, calculated shear stress as well as the average shear stress of all the samples. Empirical equations are used in present design guidelines as a function of compressive strength f_c', for example, ACI-ASCE Committee 426 report suggested the following equation to specify the shear strength for the beam without web reinforcement:

$$v_c = 59(f_c'\rho\frac{d}{a})^{1/3} \qquad \text{Equation 6-2}$$

However, the use of steel fiber can greatly improve the shear strength of the concrete beams and the empirical methods is based on an average stress calculation and may not be appropriate for HRC beams. Figure 6-11 compares the maximum shear stress determined by the proposed method and the average stress based on the results of 26 beams with reinforcement ratio ranging from 1 to 2.7%. The beam height varies from 430 mm to 1500 mm while the span is from 1310 mm to 8640 mm. A clearly improvement of shear strength is observed as the longitudinal reinforcement ratio increases. The maximum shear stresses

calculated by the proposed method are larger than the average shear stresses, as well as the strength indicated by empirical equations.

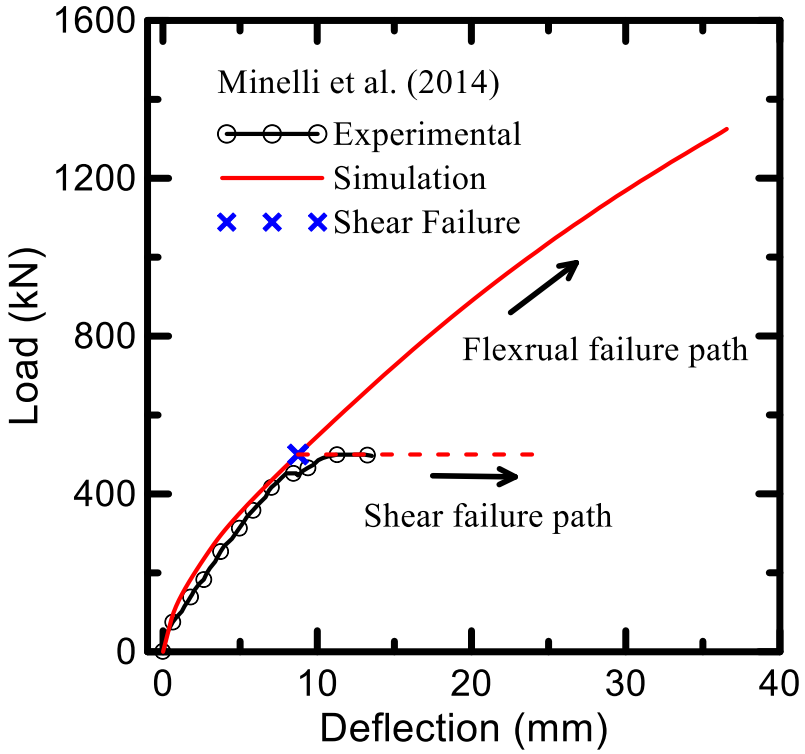

Figure 6-7 Identification of Shear Failure by Comparing Model Simulation and Experimental Data.

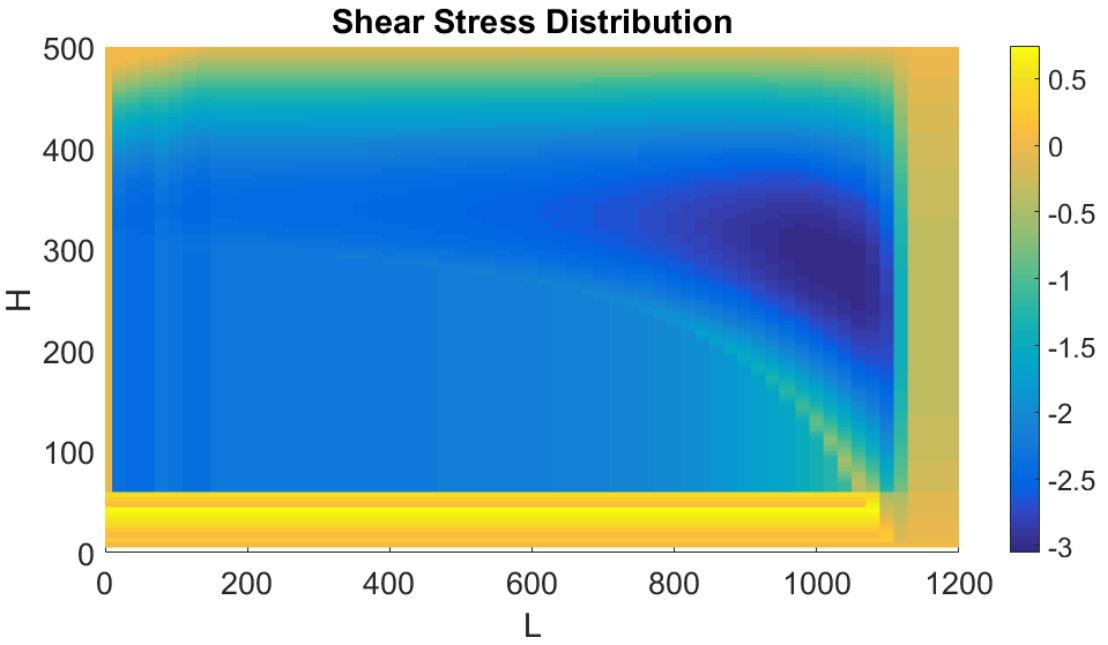

(a)

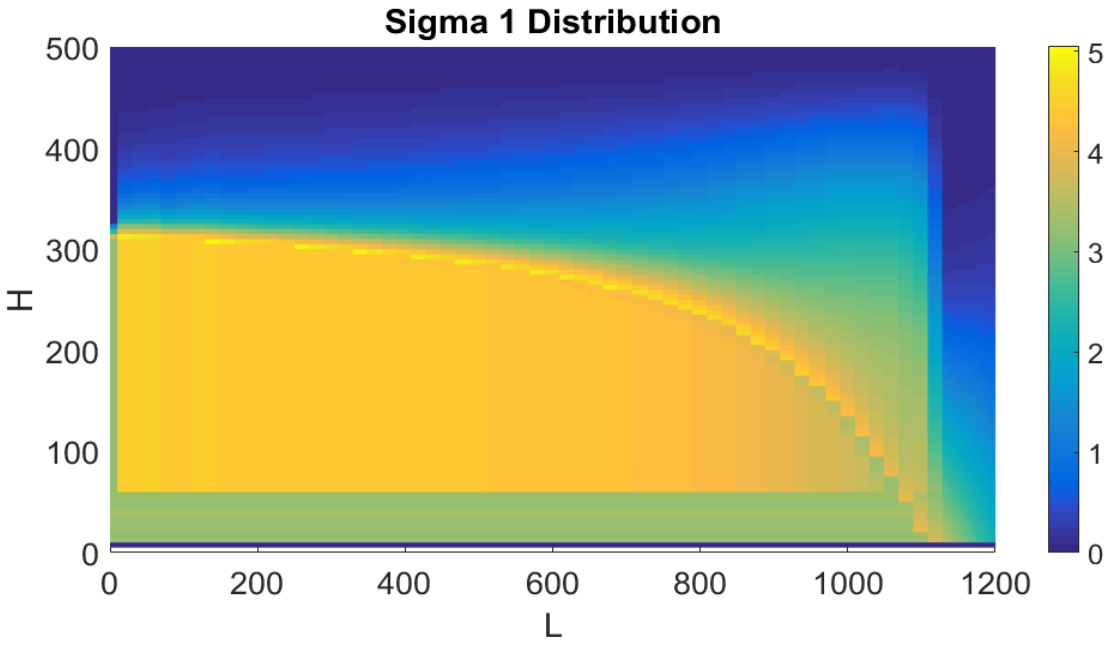

(b)

Figure 6-8 Distributions of (a) Shear Stress and (b) First Principal Stress.

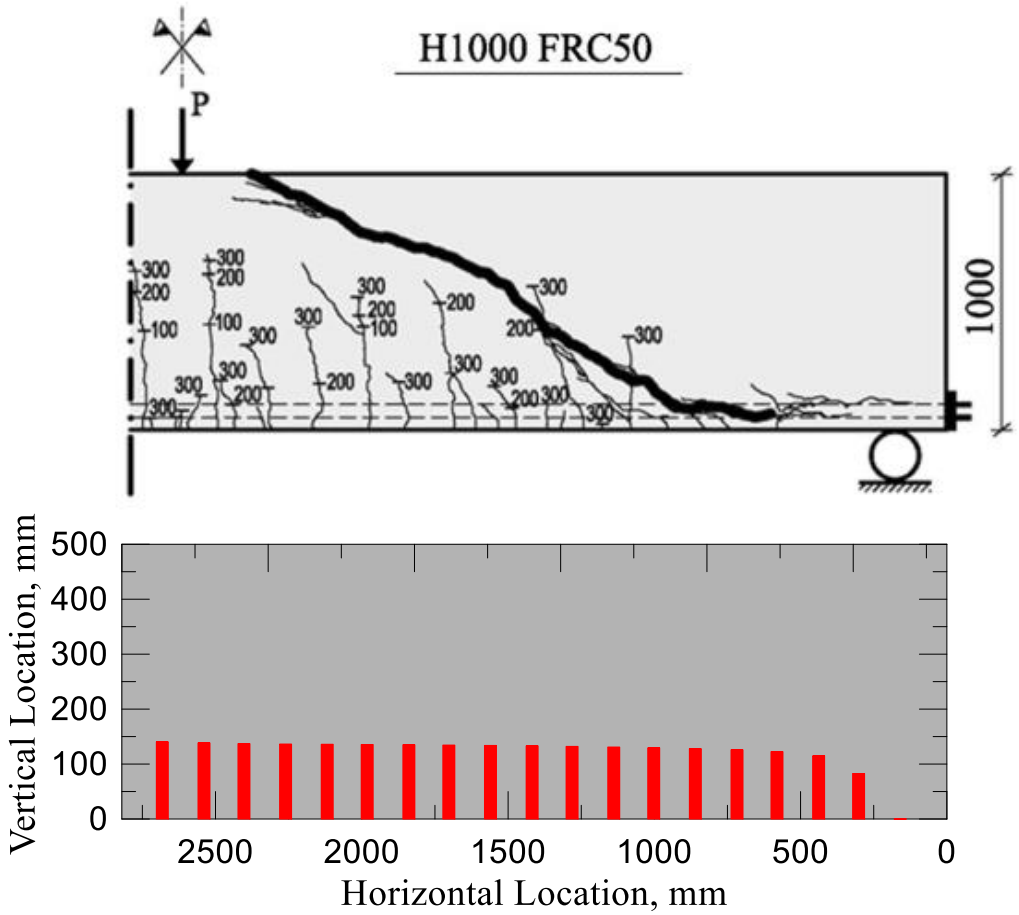

Figure 6-9 Comparison of Experimentally Observed Cracking Pattern With Distribution of Nominal Cracks Predicted by Analytical Model.

Table 6-1 Model Parameters and Shear Stress

Beam ID	d	V_f	ρ	f_c'	μ	L_p	V_u	τ_{max}	$\tau_{max}/(f_c')^{0.5}$	θp_1	v_u	$v_u/(f_c')^{0.5}$
	mm	%	%	MPa		mm	kN	MPa		°	MPa	
H500	440	0.64	1.12	32.1	0.7	140	443	2.94	0.52	48.1	2.18	0.38
H500	440	1	1.12	33.1	0.8	140	457	2.96	0.51	47.5	2.13	0.37
H1000	940	0.64	1.07	32.1	0.7	140	500	1.76	0.31	48.6	1.16	0.20
H1000	940	1	1.07	33.1	0.8	140	673.6	2.17	0.38	49.7	1.49	0.26
H1500	1440	0.64	1.01	32.1	0.7	140	879	1.91	0.34	50.2	1.34	0.24
H1500	1440	1	1.01	33.1	0.8	140	1025	2.17	0.38	48.7	1.54	0.27

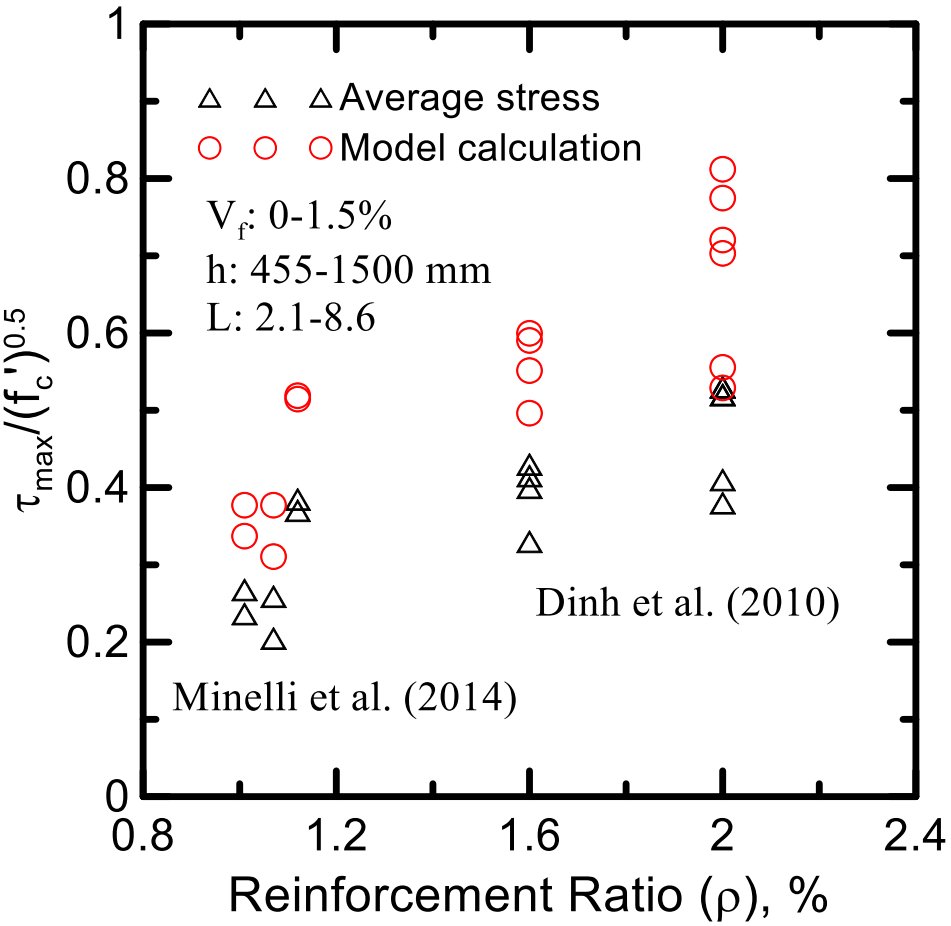

Figure 6-10 Normalized Shear Stress Versus Longitudinal Reinforcement Ratio.

6.5 Verification With Finite Element Method (FEM)

Even though the stress analysis based approach is proposed to determine the shear strength of HRC beams, the analytical model is limited by the 1D cross sectional analysis while the growth of inclined damage cannot be addressed. In order to verify the methodology and extend the study, FE analysis is performed to further reveal the failure mechanisms. The FE analysis is conducted using LS-Dyna V971 [243]. Modeling of concrete structures involves potential displacement localization in the post-peak and softening load-deformation response. Both methods of implicit or explicit analysis differ by convenience or computational efficiency but yield comparable results if the models are appropriately

calibrated. In some cases, however, only one option is open because the other choice does not produce the results because of uniqueness of solution or loss of positive definiteness of the global structural stiffness matrix. When stress state at integration points of an element moves beyond its maximum level and enters the softening region, the effective material stiffness becomes negative, subsequently leading to a negative global stiffness. Standard matrix inversion tools that are used for solution of systems of equation fail, and a negative eigenvalue warning is issued. This implies that the global stiffness matrix is not positive definite, leading to non-uniqueness of solution, and convergence problems especially when the algorithm encounters highly nonlinear stage. Concrete with cracking model presents such a highly nonlinear problem, making implicit approaches an incessant nuance.

Explicit analysis is preferred for modeling problems with both ascending and softening responses because it does not form a global stiffness matrix but solves dynamic equilibrium one equation at a time. The total time step required to complete the analysis is divided to several smaller time steps. The solution at each step is solved explicitly on the basis of the previous stress state such that the iterative procedure is not necessary.

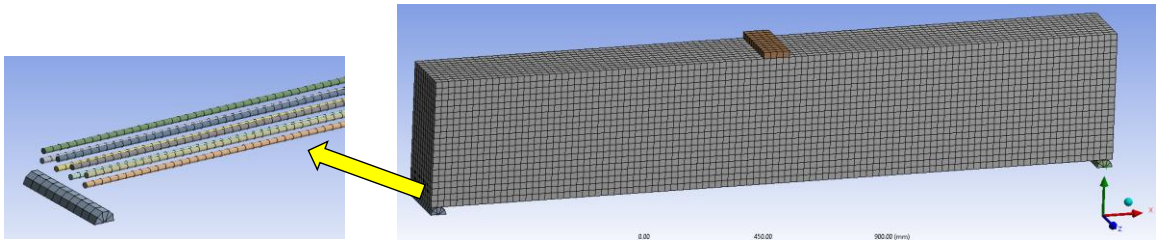

Figure 6-11 FEM Mesh of the RC Beam

Figure 6-12 shows the mesh of the HRC beam and rebar model under three-point bending. Fixed boundary conditions are applied at the bottom surfaces of the two supports. Solid element is used for the concrete, support and load pad, while beam element is used for the rebars. A total displacement of 20mm is applied on the top surface of the load pad in the

middle of the beam. Concrete material model MAT159 [244,245] is used in the present study to model the concrete beam. The concrete model is commonly referred to as a smooth or continuous surface cap model. Hence, model 159 is implemented in keyword format as MAT_CSCM for Continuous Surface Cap Model. A smooth and continuous intersection is formulated between the failure surface and hardening cap as shown in Figure 6-13. The main features of the model are: (a) Isotropic constitutive equations; (b) three stress invariant yield surface with translation for prepeak hardening; (c) a hardening cap that expands and contracts; (d) damage-based softening with erosion and modulus reduction; (e) rate effects for increasing strength in high-strain rate applications.

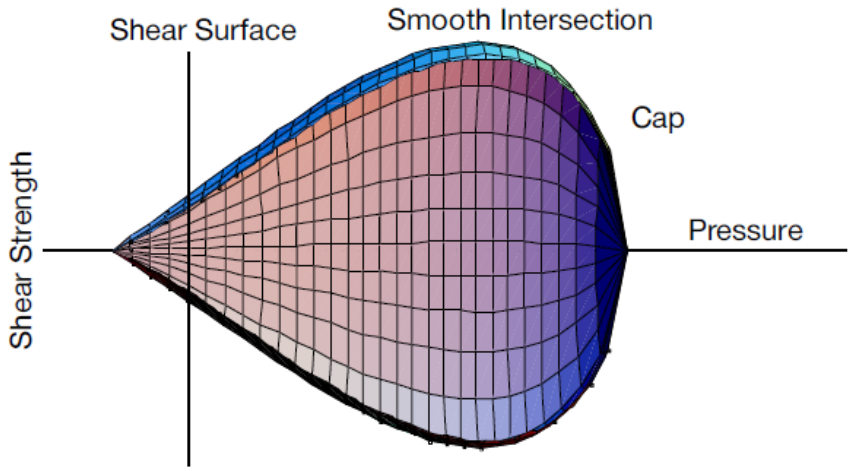

Figure 6-12 General Shape of Concrete Model Yield Surface in Two Dimensions [243].

The steel reinforcement is modelled using MAT 024, MAT_PIECEWISE_ LINEAR_PLASTICITY. This is an elasto-plastic material that an arbitrary stress versus strain curve and arbitrary strain rate dependency can be defined. Also, failure based on a plastic strain or a minimum time step size can be defined [243]. It is available for beam, shell, and solid elements. The interface between concrete and rebar is assumed to be perfectly bonded using CONSTRAINED_LAGRANGE_IN_SOLID.

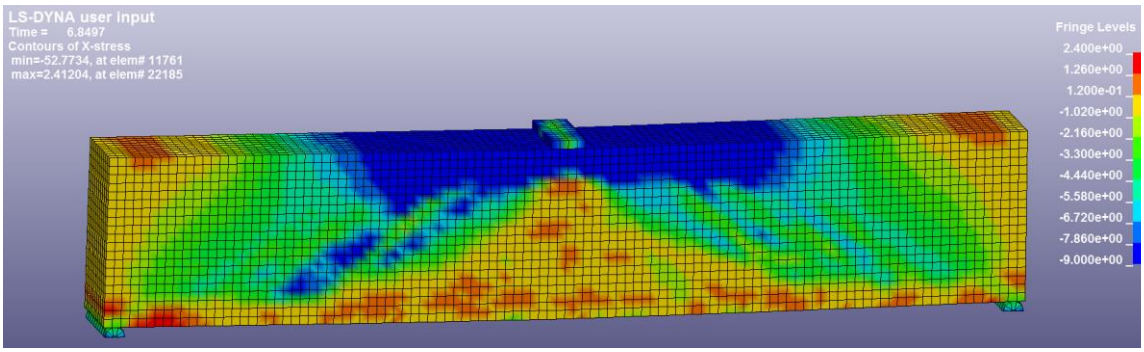

(a)

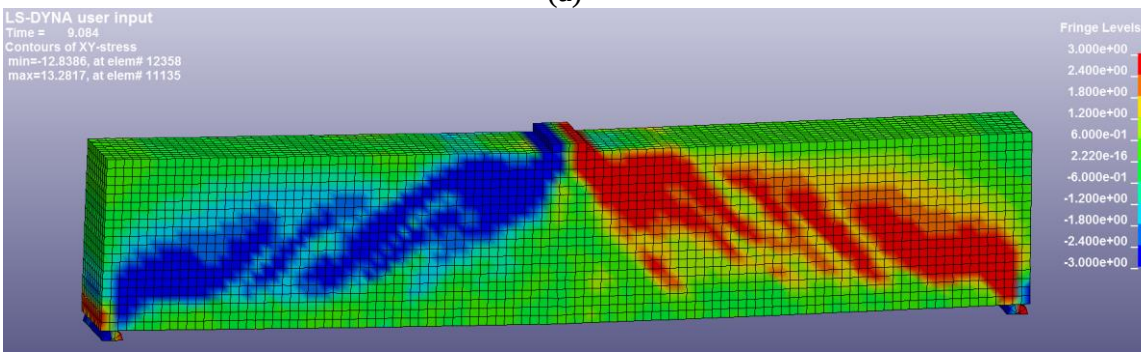

(b)

Figure 6-13 Distribution of (a) Normal Stress and (b) Shear Stress Obtained by FE Analysis.

Figure 6-14 illustrates the FE results in terms of normal and shear stress distributions, which generally agrees with the trends shown by the analytical model. Figure 6-15(a) illustrates the development of damages which is defined as the concrete exhibiting softening in the tensile and low to moderate compressive regimes. It can be seen that at the beginning of the process, few vertical damaged zones form near the mid-span of the beam. As the load increases, the damage zones grow upwards companied by the formation of new damages. In addition, the damage zones which are farther from the mid-span starts to propagate along inclined direction as a result of shear effects. The final stage of demonstrates distributed damages along diagonal directions, which are similar to the final crack pattern of the beam as shown in Figure 6-15(b). The comparison shown in Figure 6-

16 of the load-deflection responses between experiment and FE analysis further validates the accuracy of model predictions.

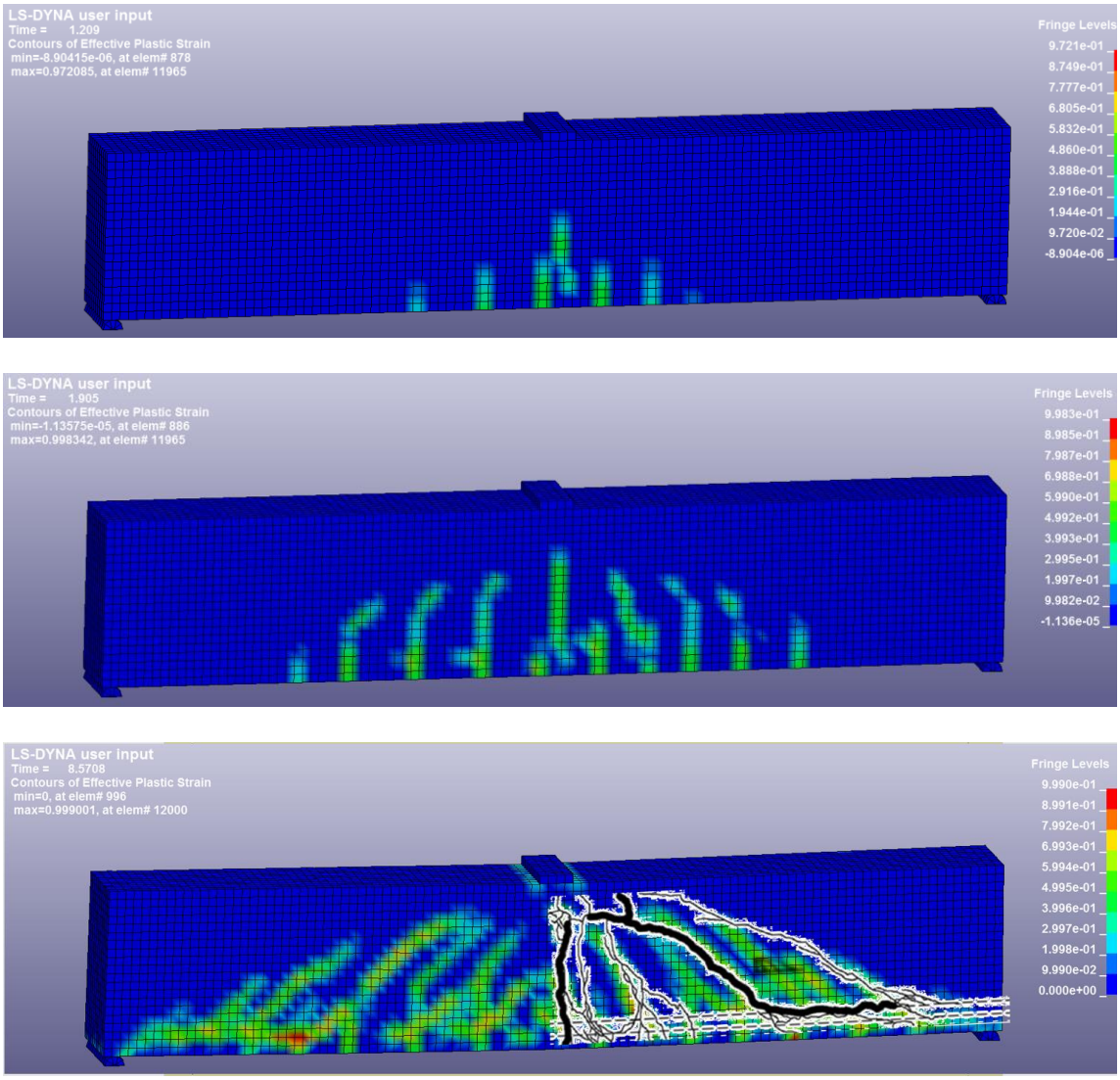

(a)

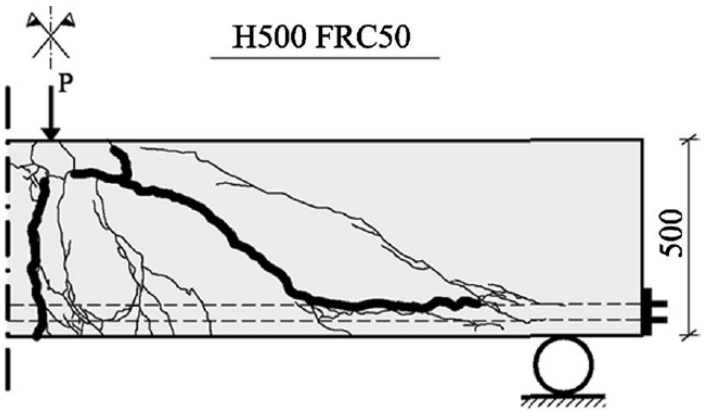

(b)

Figure 6-14 (a) Distributed of Damages and (b) Experimental Cracking Pattern.

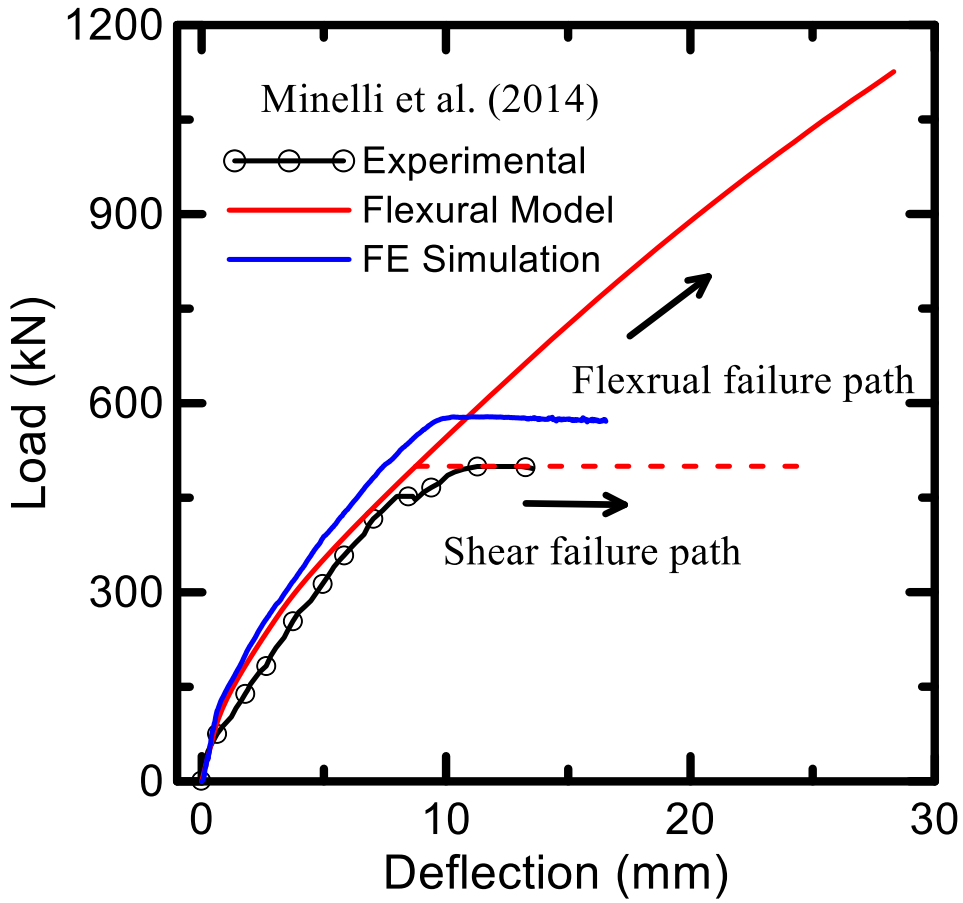

Figure 6-15 Comparison of Analytical Model and FE Simulations With Experimental Data.

7. RELIABILITY ANALYSIS

7.1 Introduction

The philosophy of limit states design is based on the assumption of equilibrium between applied loads and structural response (resistance of the structure). The safety margin is the difference between the two sides of the equilibrium equation formulated as a limit state function. Limit state functions can be formulated for each possible failure mode for design and during service life of the considered structure. The load and resistance parameters may involve a considerable degree of uncertainty and should be treated as random variables. Therefore, reliability is a rational measure of structural performance. The design process, known as Limit States Design, requires a set of load and resistance factors for each appropriate limit state. The objective of the code calibration is to select these factors so that the reliability of designed structures is consistent with the predetermined target level.

Load and resistance parameters are random variables; therefore, it is convenient to measure the structural performance in terms of the reliability index β. Various procedures for calculation of b are presented by Nowak and Collins [246]. The general format of the limit state function g is

$$g() = R - Q < 0 \qquad \text{Equation 7-1}$$

where g = safety margin; R = resistance; and Q = load effect. In this study, Q is a combination of load components.

The reliability index β can be considered as a function of the probability of failure PF

$$\beta = -\Phi^{-1}(P_F) \qquad \text{Equation 7-2}$$

where Φ^{-1} = inverse standard normal distribution function.

The reliability analysis procedure includes the following steps: (1) perform deterministic design using load and resistance factors: γ_D, γ_L, γ_S, γ_W, γ_E, and ϕ, and the calculations are carried out for several possible values of ϕ; (2) calculate load parameters: the mean total load, the corresponding coefficient of variation, and the standard deviation; (3) Determine the statistical parameters of R using Monte Carlo Simulation (MCS) or First Order Reliability Methods (FORM); (4) calculate the reliability index β

$$\beta = \frac{m_R - m_Q}{\sqrt{\sigma_R^2 + \sigma_R^2}} \qquad \text{Equation 7-3}$$

where m_R = mean value of resistance; m_Q = mean value of the total load effect; σ_R = standard deviation of resistance; and σ_Q = standard deviation of the total load effect.

7.2 Deterministic Design of Concrete Beams in Bending

A study of a simple beam subjected to uniformly distributed load is used to illustrate the design procedure using proposed model and reliability analysis. The loads applied on the structure may include the live load and dead load which is contributed from the self-weight of beams, columns, slabs, roof, walls and partitions. Consider the location of this building is in Tempe, Arizona, as well as its total height, the earthquake load, wind load, flood load, rain load and snow load are not considered in the analysis and design. The nominal resistance is calculated using the load combination specified by ASCE 7-10 [247]:

$$1.2D + 1.6L < \phi R \qquad \text{Equation 7-4}$$

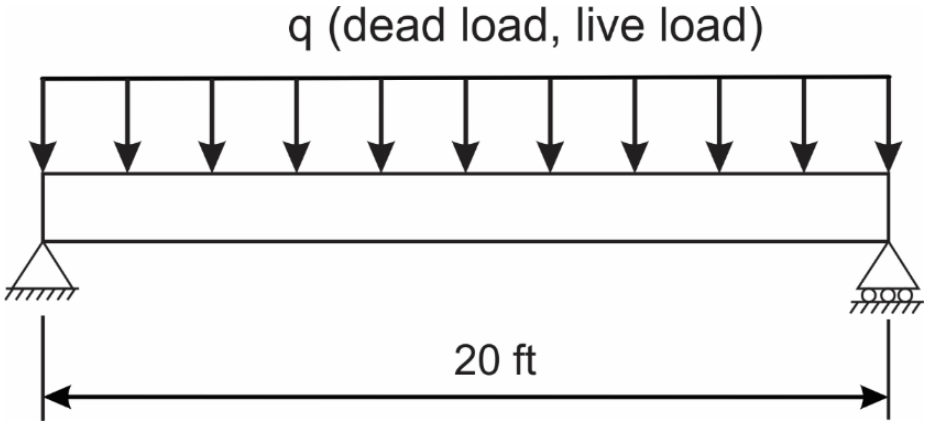

Figure 7-1 Simple Beam Subjected to Uniformly Distributed Load.

The loads taken by the beams include the self-weight of slab and beam, weight of walls/partitions and live loads. According to ASCE 7-10 [247], the live load of an office building is taken as 50 psf and the live load on the roof is 16 psf. In order to satisfy the deflection limit, the minimum thickness of the slab should yield $h = l/20$, where l is the span [248]. In this study, the thickness t is selected is selected as 12 in. The self-weight per unit area is:

$$W_{Slab} = 150\,lb/\,ft^3 * 1\,ft * 120in. = 125\,lbs/in.$$

$$LL = 50\,psf * 120in. = 41.7\,lbs/in.$$

In the present study, one-way slab is employed and the tributary area is shown in Figure 7-2. Besides the load from slab, the self-weight of the beam and weight of walls and partitions are computed as:

$$W_{Beam} = 150\,lb/\,ft^3 * 12in. * 18in. = 18.75\,lbs/in.$$
$$W_{Wall} = 12\,psf * 12in. = 12\,lbs/in$$
$$W_{Partitions} = 8\,psf * 12in. = 8\,lbs/in$$

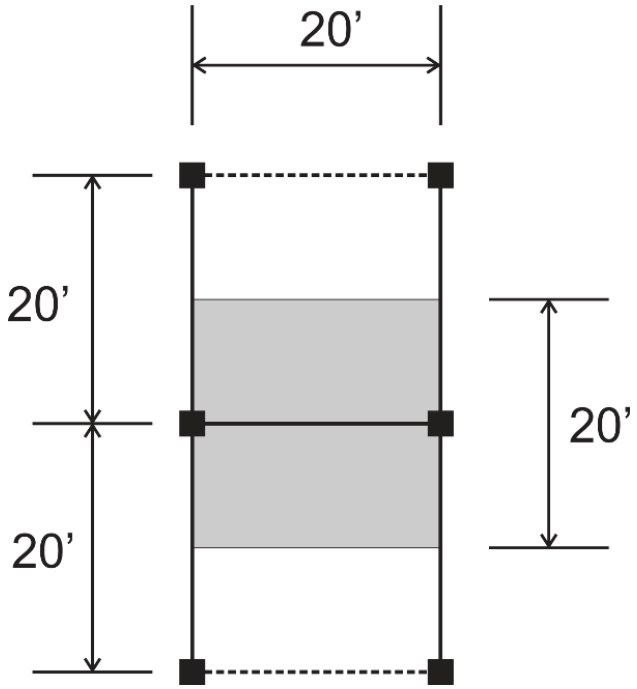

Figure 7-2 Tributary Area.

Therefore, the total load distributed load per unit length that is transferred to the beam can be calculated as:

$$q = 1.2(W_{Slab} + W_{Beam} + W_{Wall}) + 1.6LL = 458.3 lbs / in.$$

The maximum moment is:

$$M_{\max} = \frac{ql^2}{8} = \frac{360.08 * 240^2}{8} = 3299.7\ kip - in.$$

Closed form equations for moment capacity M_u:

Singly reinforced

$$M_u \approx M'_{\infty} M_{cr} = \frac{6\rho_g n\kappa\left(\mu\alpha - \mu + \alpha\gamma\omega\right) + 3\gamma\omega\mu - 3\left(\rho_g n\kappa\right)^2}{\omega\gamma + \mu} M_{cr} \quad \text{Equation 7-5}$$

Doubly reinforced

$$M_u \approx M'_\infty M_{cr} = \frac{3\kappa n\rho_g[\kappa n\rho_g(\zeta-1)^2 - 2\omega\gamma(\zeta\alpha-\zeta+\alpha) - 2\mu(\zeta\alpha+\alpha-1)] - 3\mu\omega\gamma}{\omega\gamma+\mu} M_{cr}$$

Equation 7-6

By checking the moment resistance using the design equations, a singly reinforced section with 4 #7 rebars shown in Figure 7-3 is sufficient. However, double reinforcement with 2 #7 compression rebars is also considered for the demonstration purposes. Note that the beam height of 20 in. obtained at the strength reduction factor ϕ=0.85. In this study reduction factor of 0.90 and 0.95 are also investigated which correspond to beam height of 19 and 18 in., respectively. The residual strength parameter μ is taken as 0.5.

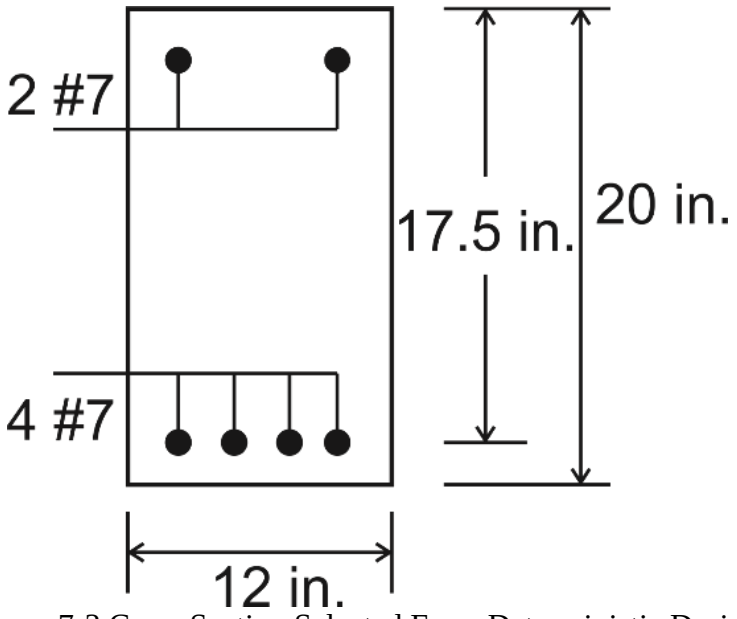

Figure 7-3 Cross Section Selected From Deterministic Design.

7.3 Random Variables

Nowak and Szerszen [249] compiled the test data for ordinary, high-strength, and lightweight concretes which were obtained from ready-mix companies and precasting plants. The statistical parameters of concrete strength fc' were calculated from the cumulative distribution functions (CDFs). The CDF curves include all the available

samples obtained from different sources (concrete industry) and were plotted separately for each file from the database. Then, the distributions were plotted for all files representing the same nominal concrete strength.

Uncertainties in member geometry are functions of care and quality control exercised during construction [250]. Based on an extensive study on the variations in dimensions of reinforced concrete members from field data, Mirza and McGregor [251] recommend normal distributions as probability models for all geometric imperfections. Since mean deviations from nominal dimensions are small, they are neglected in this study, and the designed values are taken as the mean values. The c.o.v's for the various geometric variables have been adapted from [251] and are listed in Table 7-1.

Table 7-1 Description of Random Variables (Data From [249,250,251])

Xi		Description	Distribution	Mean	C.O.V
Geometries	t, in.	Slab thickness		Design value	0.07
	h, in.	Beam height		Design value	0.01
	d, in.	Effective beam depth		Design value	0.02
	b, in.	Beam width		Design value	0.01
Material properties	fy, psi	Yield strength of steel	Lognormal	69850.2	0.05
	fc', psi	Compressive strength of concrete		4936.6	0.145
	ρ	Reinforcement ratio		Design value	0.04
	μ	Residual strength		0.5	0.2
Load	DD	Dead load		Design value	0.10
	LL	Live load		Design value	0.65

7.4 Monte Carlo Simulation

Monte Carlo simulation is performed to obtain the statistical parameters of the applied load and resistance for the following limit state equation:

$$g() = M_u - \frac{ql^2}{8} = 0 \qquad \text{Equation 7-7}$$

The reliability index β is calculated for different reduction factor using the procedure introduced above. The reliability indices for the singly reinforced section at three level of reduction factor are 3.402, 4.056, 5.378, respectively. The values of doubly reinforced section are larger due to higher moment resistance, which are 4.411, 4.904 and 5.378, respectively. Target reliability indices are shown in Table 7-2 as a reference, which indicates the expected performance level of proposed design section. Figure 7-4 shows the probability density functions of applied moment and resistance for different reduction factors. Higher nominal values are observed in the case of double reinforcement which agrees with the higher indices. But the variabilities are also larger which may be caused by the compression rebar related randomness.

Table 7-2 Target Reliability Indices (US Army Corps of Engineers 1997) [252]

β	pf	Expected performance level
5	3e-7	High
4	3e-5	Good
3	0.001	Above average
2.5	0.006	Below average
2.0	0.023	Poor
1.5	0.07	Unsatisfactory
1.0	0.16	Hazardous

In actual structures, the portion of dead/live load varies with real world scenarios. The practical range of dead load ratio D/(D+L) is between 0.3 to 0.9 [253]. Therefore, reliability analysis is performed for a full range from 0 to 1, as shown in Figures 7-5 and 7-6. It is shown that β increases with increasing dead load ratio and reaches maximum at when D/(D+L) is about 0.76. This trend can be explained by the fact that live load has higher variability (cov=0.18) compared to dead load (cov=0.10). While the dead load ratio is about 0.76 for the case illustrated in deterministic design, which may indicate the most reliable scenario.

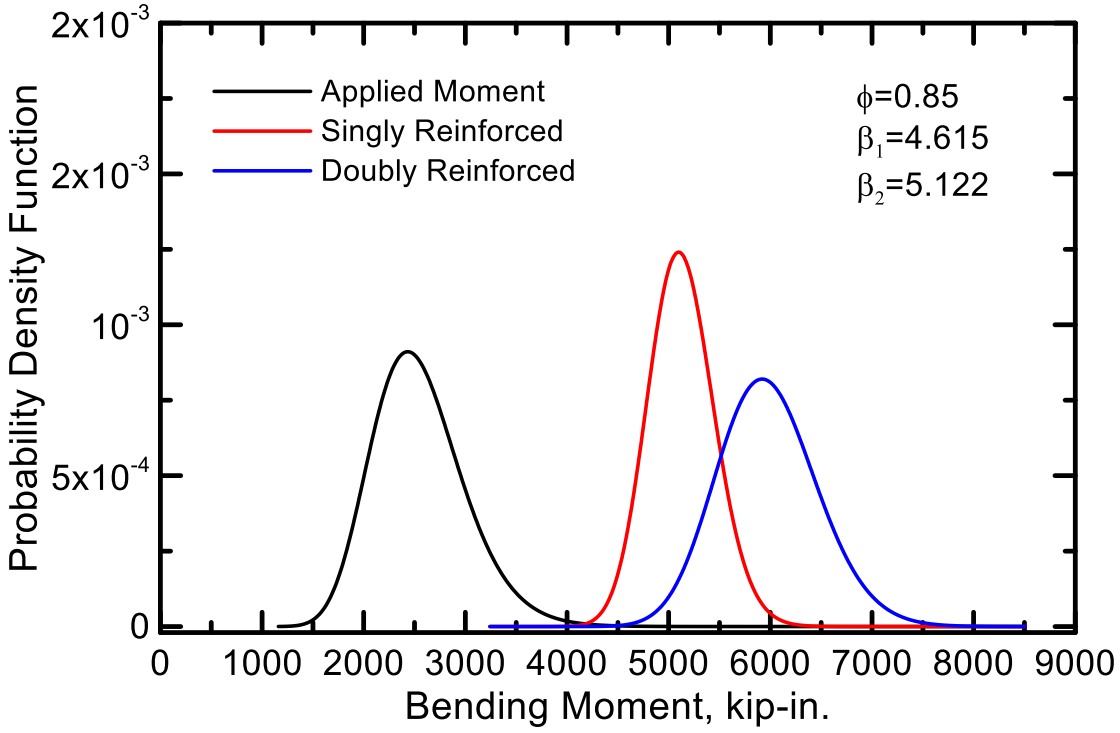
Probability Density Function
2x10-3
2x10-3
10-3
5x10-4
0
Applied Moment
Singly Reinforced
Doubly Reinforced
ϕ=0.85
β1=4.615
β2=5.122
0
1000
2000
3000
4000
5000
6000
7000
8000
9000
Bending Moment, kip-in.

(a)

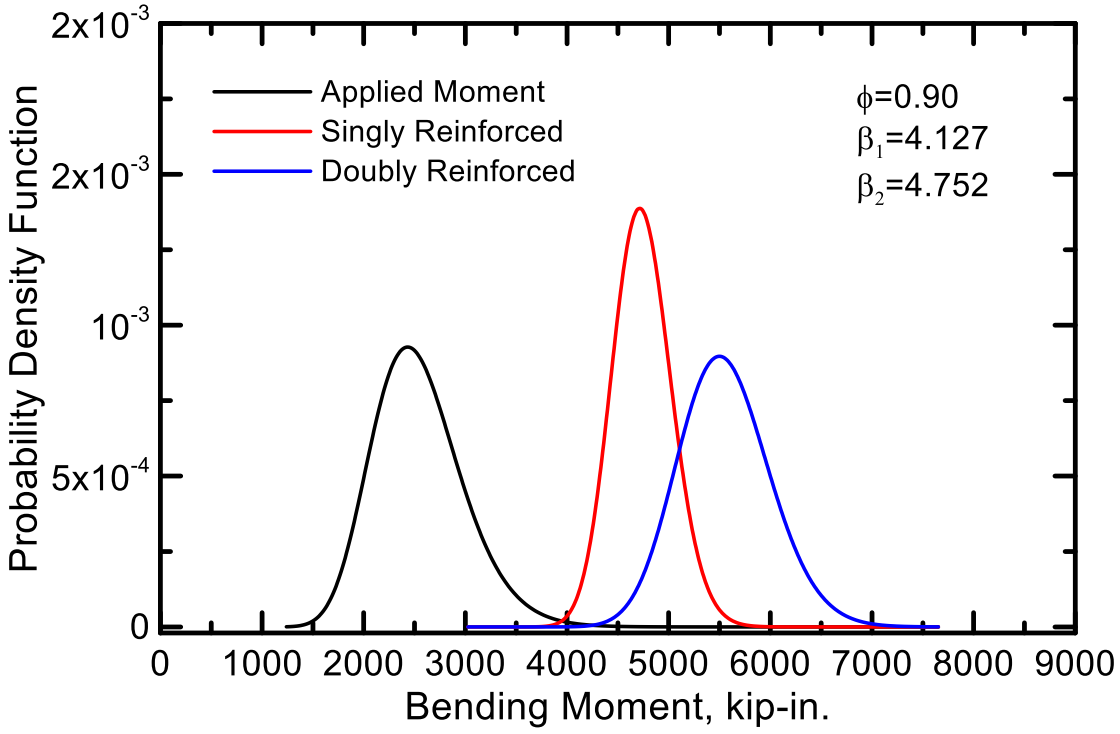
Probability Density Function
2x10-3
2x10-3
10-3
5x10-4
0
Applied Moment
Singly Reinforced
Doubly Reinforced
ϕ=0.90
β1=4.127
β2=4.752
0
1000
2000
3000
4000
5000
6000
7000
8000
9000
Bending Moment, kip-in.

(b)

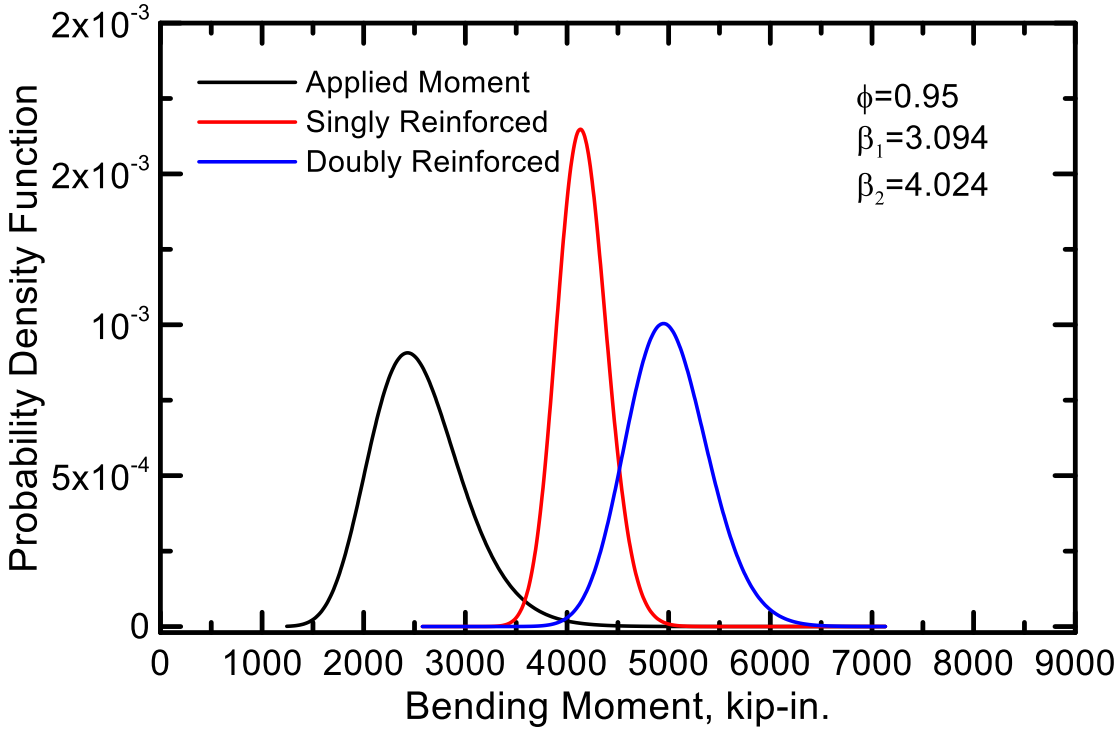

(c)

Figure 7-4 Probability Density Functions of Applied Moment and Resistance for Different Strength Reduction Factors: (a) φ=0.95, (a) φ=0.90, (a) φ=0.85.

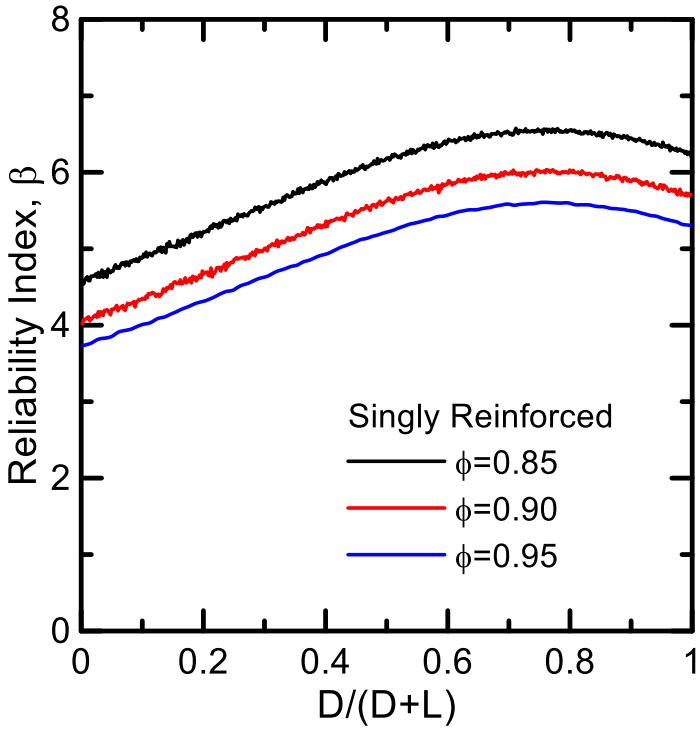

Figure 7-5 Reliability Index (β) Versus Dead Load Ratio for Singly Reinforced Section.

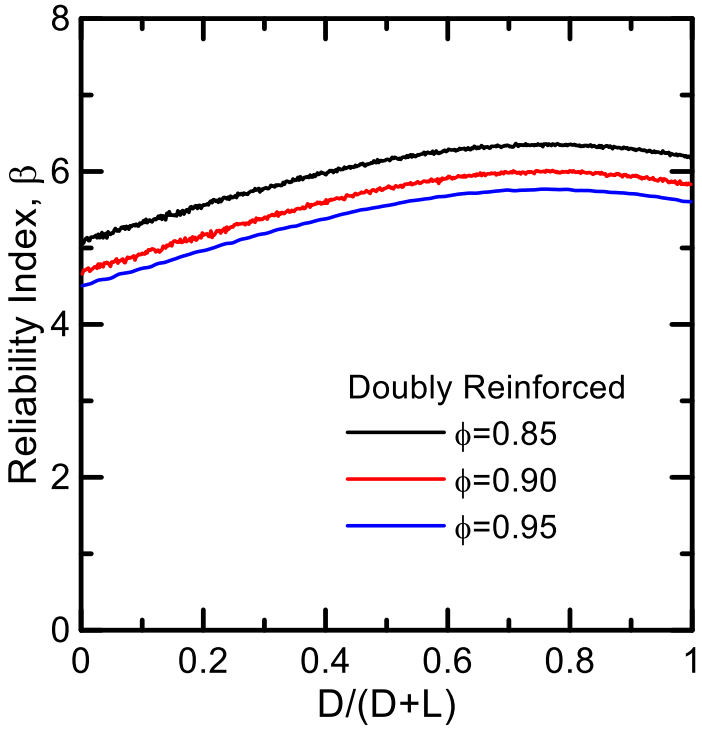

Figure 7-6 Reliability Index (β) Versus Dead Load Ratio for Doubly Reinforced Section.

8. SUMMARY AND FUTURE WORK

8.1 Summary

In this study, distributed cracking mechanisms were experimentally investigated following a sequence of reinforcing materials, cement composites with localized damage and finally the composites exhibiting distributed damages. Tensile properties were evaluated under varying strain rates from quasi-static to high speed (up to 100 s^{-1}) and varying temperature from -25 to 100 °C. Strain rates effects were observed in terms of tensile strength, ductility and toughness, while the saturated crack spacing was found to be independent of strain rate. On the other hand, a decreasing trend was observed in the post-crack stiffness with increasing temperature, which indicates the dependence of stiffening mechanisms on the testing temperature.

The DIC measurements of the complex strain fields represented a non-uniform distribution of longitudinal strain consisting of three main zones: localization, shear lag and uniform strain. The strain behavior in each zone was addressed by means of three competing models: stress-crack width, bond stress-slip, and composite stress-strain relationships. These models were eventually used as the damage criteria for the finite difference model. Important parameters localization zone width (h_L) and saturated crack spacing (s) for modelling of distributed cracking behaviors were directly measured using DIC method. Both these measures decreased with the addition of short fibers, indicating the improvement in bond characteristics.

A tension stiffening model based on finite difference method were used to simulate the tensile behaviors including stress-strain, crack spacing-strain and matrix degradation. The model addresses the multiple aspects of distributed mechanisms including a matrix strength

model, fiber tension model, interface bond-slip model and nonlinear spring model for transvers restriction. The finite difference model is further extended to simulate the sequential cracking procedure in SFRC joint free slabs on grade. The primary parameters affecting drying shrinkage including free shrinkage strain, friction of grade and fiber volume are addressed by the model. An empirical equation was proposed to predict the crack opening of a restrained slab on grade and compared with the numerical model. Parametric study showed that the predicted crack opening was reduced with higher level of restraint by increasing fiber volume fraction, base friction, and bond strength. This indicates the role of fiber and base course in controlling the crack opening by restricting the movement of cracked slab segments.

Based on the experimental characterization, an elastic-residual-tensile strength model for tension and elastic-perfectly plastic model for compression behaviors are proposed to model the flexural behavior of HRC beams that exhibit hardening and multiple cracking. Analytical solutions for neutral axis depth, moment-curvature, and effective stiffness at each stage of flexural deformation are obtained. Analytical expressions for load-deflection response are explicitly derived based on simplified bilinear moment-curvature curves. The derivations are used in terms of design charts representing the normalized ultimate moment capacity as a function of residual tensile strength and reinforcement ratio and are applicable to conventional-, fiber-, and hybrid-reinforced concrete. In addition, a stress analysis based method was proposed to determine multiple components including shear stress, principle stress and principle directions. A structural analysis approach based on assumption of equally distributed nonlinear hinges was used together with the stress analysis. The method was applied to experimental data from literature to determine the ultimate shear stress in

the HRC beams without conventional shear reinforcement. Results are further converted to coefficient of resistance R by stress block approach, nominal strength, and minimum reinforcement ratio. Numerical tests covering materials and geometrical ranges as a well as comparison with available experimental data confirmed the proposed equations against the original equations.

The theoretical framework was extended to model the bending behavior of T-beam and structural members subjected to combined axial-bending loads. Analytical solutions for the moment-curvature and load-deflection responses for T-beam were derived. On the other hand, the equations constructing interaction diagram (P-M) were also analytically expressed, that addresses all the models of failure with the effects of fibers. These analytical models greatly extend the proposed methodologies to wide engineering applications such as the beam-slab floor system, deck-girder, new generation UHPC Pi-girder, short columns and tunnel lining segments.

As a demonstration and verification of the design procedure using the proposed methodologies, reliability analysis was performed using Monte Carlo simulation. Reliability indices were calculated for different strength reduction factors and dead load ratios in order to cover more practical problems. The reliability index remains confined in a relatively narrow band and varies slowly over a wide realistic range of dead load ratio. This indicates the proposed design equations may approach a uniform reliability for the design cases presented here, while extensive studies to cover more design parameters and structures are desired for further verification.

8.2 Recommendations for Future Work

In the current study of analytical model approach, the analysis is limited to the axial and flexural behaviors of an independent structural member, it is therefore highly desired to extend the approach to a structural analysis framework. Similarly, the reliability analysis shall be applied to more design cases and a structural performance evaluation will be of interest. On the other hand, Finite element analysis (FEA) will be employed to further investigate the flexural and shear behavior in strain hardening cement composites. Another study of interest is to extend the modelling technique to dynamic and impact loads. Impact flexural tests of FRC and sandwich systems have been conducted while modeling and simulation of the experimental data are demanded.

Short-term properties have been studied through this dissertation, while long-term performance of this class of materials is also significant in the serviceability design of structures, which mostly are subjected to sustained load. However, long-term behavior of FRC has not been considered in codes yet. Studies on creep of FRC in compression indicate that fibers restrain creep strains when compared to plain mortar and concrete. As FRC contribution to structural load-bearing capacity is based on its flexural response, and mainly in the cracked state, the capacity of the material to keep the crack opening values low enough to guarantee the reinforcement effectiveness should be assessed. Creep testing equipment have been developed and preliminary data are being collected. Future work will focus on the analysis and modelling techniques on creep flexural behaviors.

References

1. Damtoft, J. S., Lukasik, J., Herfort, D., Sorrentino, D., & Gartner, E. M. (2008). Sustainable development and climate change initiatives. *Cement and concrete research*, *38*(2), 115-127.

2. Yunovich, M., Thompson, N. G., & Virmani, Y. P. (2004). Corrosion of Highway Bridges: Economic Impact and Life-Cycle Cost Analysis. In *The 2004 Concrete Bridge Conference*.

3. Roy, D. M. (1999). Alkali-activated cements opportunities and challenges. *Cement and Concrete Research*, *29*(2), 249-254.

4. Hammond, G. P., & Jones, C. I. (2008). Embodied energy and carbon in construction materials. *Proceedings of the Institution of Civil Engineers-Energy*, *161*(2), 87-98.

5. Paul, S. C., Pirskawetz, S., Van Zijl, G. P. A. G., & Schmidt, W. (2015). Acoustic emission for characterising the crack propagation in strain-hardening cement-based composites (SHCC). *Cement and Concrete Research*, 69, 19-24.

6. Li, V. C. (2003). On engineered cementitious composites (ECC). *Journal of advanced concrete technology*, 1(3), 215-230.

7. Yang, E. H., & Li, V. C. (2014). Strain-rate effects on the tensile behavior of strain-hardening cementitious composites. *Construction and Building Materials*, 52, 96-104.

8. Yang, E. H., Yang, Y., & Li, V. C. (2007). Use of high volumes of fly ash to improve ECC mechanical properties and material greenness. *ACI materials journal*, 104(6), 620-628.

9. Gupta, P., Banthia, N., & Yan, C. (2000). Fiber reinforced wet-mix shotcrete under impact. *Journal of materials in civil engineering*, 12(1), 81-90.

10. Banthia, N., Bindiganavile, V., & Mindess, S. (2004). Impact and blast protection with fiber reinforced concrete. In *Conference Proceedings-BEFIB, Veronna, Italy, RILEM* (Vol. 39, pp. 31-44).

11. Meyers, M. A. (1994). *Dynamic behavior of materials*. John wiley & sons.

12. Nicholas, T. (1981). Tensile testing of materials at high rates of strain. *Experimental Mechanics*, 21(5), 177-185.

13. Hoge, K. G. (1966). Influence of strain rate on mechanical properties of 6061-T6 aluminum under uniaxial and biaxial states of stress. *Experimental Mechanics*, 6(4), 204-211.

14. Zabotkin, K., O'Toole, B., & Trabia, M. (2003, July). Identification of the dynamic properties of materials under moderate strain rates. In *16th ASCE Engineering Mechanics Conference, Seattle, WA*.

15. Bruce, D. M., Matlock, D. K., Speer, J. G., & De, A. K. (2004). *Assessment of the strain-rate dependent tensile properties of automotive sheet steels* (No. 2004-01-0507). SAE Technical Paper.

16. Xiao, X. (2008). Dynamic tensile testing of plastic materials. *Polymer Testing*, 27(2), 164-178.

17. Fitoussi, J., Meraghni, F., Jendli, Z., Hug, G., & Baptiste, D. (2005). Experimental methodology for high strain-rates tensile behaviour analysis of polymer matrix composites. *Composites Science and Technology*, 65(14), 2174-2188.

18. Mechtcherine, V., Silva, F. D. A., Butler, M., Zhu, D., Mobasher, B., Gao, S. L., & Mäder, E. (2011). Behaviour of strain-hardening cement-based composites under high strain rates. *Journal of Advanced Concrete Technology*, *9*(1), 51-62.

19. Society of Automotive Engineers (SAE). (2008). *High Strain Rate Tensile Testing of Polymers*. J2749.

20. Yan, B., Kuriyama, Y., Uenishi, A., Cornette, D., Borsutzki, M., & Wong, C. (2006). *Recommended Practice for Dynamic Testing for Sheet Steels-Development and Round Robin Tests* (No. 2006-01-0120). SAE Technical Paper.

21. ISO 18872:2007. (2007). *Plastics—Determination of Tensile Properties at High Strain Rates*.

22. Bharatkumar, B. H., & Shah, S. P. (2004, March). Impact resistance of hybrid fiber reinforced mortar. In *K. Kovler K, Marchand J, Mindess S, Weiss J, editors. International RILEM symposium on concrete science and engineering: a tribute to Arnon Bentur, Evanston, IL.*

23. Dey, V., Bonakdar, A., & Mobasher, B. (2014). Low-velocity flexural impact response of fiber-reinforced aerated concrete. *Cement and Concrete Composites*, 49, 100-110.

24. Destree, X. P., & Lazzari, A. A. (1987). *U.S. Patent No. 4,640,648*. Washington, DC: U.S. Patent and Trademark Office.

25. Ytterberg, R. F. (1987). Shrinkage and Curling of Slabs on Grade--Part 1.*Concrete international*, *9*(4), 22-30.

26. Alexandre, E., & Bouhon, B. (2010). Jointless steel fiber-reinforced concrete slabs-on-grade and on piles. *Special Publication*, *268*, 89-102.

27. Kwon, S. J., Na, U. J., Park, S. S., & Jung, S. H. (2009). Service life prediction of concrete wharves with early-aged crack: Probabilistic approach for chloride diffusion. *Structural Safety*, *31*(1), 75-83.

28. Yoon, I. S., Schlangen, E., Rooij, M. R. D., & Van Breugel, K. (2007). The effect of cracks on chloride penetration into concrete. In *Key Engineering Materials* (Vol. 348, pp. 769-772). Trans Tech Publications.

29. Lura, P., Pease, B., Mazzotta, G. B., Rajabipour, F., & Weiss, J. (2007). Influence of shrinkage-reducing admixtures on development of plastic shrinkage cracks. *ACI Materials Journal*, *104*(2), 187.

30. Jafarifar, N., Pilakoutas, K., & Bennett, T. (2014). Moisture transport and drying shrinkage properties of steel–fibre-reinforced-concrete. *Construction and building materials*, *73*, 41-50.

31. Zhang, J., Hou, D., & Gao, Y. (2013). Calculation of shrinkage stress in early-age concrete pavements. II: Calculation of shrinkage stress. *Journal of Transportation Engineering*, *139*(10), 971-980.

32. Brooks, J. (2015). Shrinkage of concrete. *Concrete and Masonry Movements, Butterworth-Heinemann*, 137-185. Butterworth Heinemann, Oxford, U.K.

33. Foster, S. J., Voo, Y. L., & Chong, K. T. (2006). FE analysis of steel fiber reinforced concrete beams failing in shear: variable engagement model.*Special Publication*, *237*, 55-70.

34. Foster, S. (2010, December). 12 Design of FRC beams for shear using the VEM and the draft Model Code approach. In *Shear and Punching Shear in RC and FRC Elements: Technical Report: Proceedings of a Workshop Held on 15-16 October 2010, in Salò, Lake Garda, Italy* (Vol. 57, p. 195). fib Fédération internationale du béton.

35. Narayanan, R., & Darwish, I. (1987). "Use of steel fibers as shear reinforcement", *ACI Structural Journal*,84 (3), 2066-2079.

36. Al-Ta'an, S. A., & Al-Feel, J. R. (1990). Evaluation of shear strength of fibre-reinforced concrete beams. *Cement and Concrete Composites*, *12*(2), 87-94.

37. Khuntia, M., Stojadinovic, B., & Goel, S. C. (1999). Shear strength of normal and high-strength fiber reinforced concrete beams without stirrups. *Structural Journal*, *96*(2), 282-289.

38. Sahoo, D. R., & Sharma, A. (2014). Effect of steel fiber content on behavior of concrete beams with and without stirrups. *ACI Structural Journal*, *111*(5), 1157.

39. Meda, A., Minelli, F., & Plizzari, G. A. (2012). Flexural behaviour of RC beams in fibre reinforced concrete. *Composites Part B: Engineering*, *43*(8), 2930-2937.

40. Destrée, X. (2006). Concrete free suspended elevated slabs reinforced with only steel Fibers: Full scale testing results and conclusions–design examples. *RILEM Proceedings PRO49*, 287-294.

41. Salehian, H., & Barros, J. A. (2015). Assessment of the performance of steel fibre reinforced self-compacting concrete in elevated slabs. *Cement and Concrete Composites*, *55*, 268-280.

42. Salehian, H., Barros, J. A., & Taheri, M. (2014). Evaluation of the influence of post-cracking response of steel fibre reinforced concrete (SFRC) on load carrying capacity of SFRC panels. *Construction and Building Materials*, *73*, 289-304..

43. Mobasher, B., Peled, A., & Pahilajani, J. (2006). Distributed cracking and stiffness degradation in fabric-cement composites. *Materials and structures*,*39*(3), 317-331.

44. Zhu, D., Peled, A., & Mobasher, B. (2011). Dynamic tensile testing of fabric–cement composites. *Construction and Building Materials*, *25*(1), 385-395.

45. de Andrade Silva, F., Butler, M., Mechtcherine, V., Zhu, D., & Mobasher, B. (2011). Strain rate effect on the tensile behaviour of textile-reinforced concrete under static and dynamic loading. *Materials Science and Engineering: A*, *528*(3), 1727-1734.

46. Yao, Y., Bonakdar, A., Faber, J., Gries, T., & Mobasher, B. (2016). Distributed cracking mechanisms in textile-reinforced concrete under high speed tensile tests. *Materials and Structures*, *49*(7), 2781-2798.

47. Hawkins, N. M., & Mitchell, D. (1979, July). Progressive collapse of flat plate structures. In *ACI Journal Proceedings* (Vol. 76, No. 7, pp. 775-808).

48. Sasani, M., & Sagiroglu, S. (2008). Progressive collapse of reinforced concrete structures: a multihazard perspective. *ACI Structural Journal*,*105*(1), 96.

49. Udilovich, K. V., Shleykov, I. B., & Banchuzhnyy, M. V. (2010). Design of Flat-Plate Floors for Progressive Collapse Using Yield-Line Analysis.*Concrete international*, *32*(07), 37-44.

50. Fischer, G. (2004). Current US guidelines on fiber reinforced concrete and implementation in structural design. In *Proceeding of the North American/European Workshop on Advances in Fiber Reinforced Concrete* (pp. 13-22).

51. Teutsch, M. (2004). German guidelines on steel fiber concrete. In *Proceeding of the North American/European Workshop on Advances in Fiber Reinforced Concrete* (pp. 23-28).

52. Barr, B., & Lee, M. K. (2004). FRC Guidelines in the UK, with Emphasis on SFRC in Floor Slabs. In *Proceeding of the North American/European Workshop on Advances in Fiber Reinforced Concrete* (pp. 29-38).

53. Di Prisco, M., Plizzari, G., & Vandewalle, L. (2009). Fibre reinforced concrete: new design perspectives. *Materials and Structures*, *42*(9), 1261-1281. doi: 10.1617/s11527-009-9529-4.

54. Taheri, M., Barros, J. A., & Salehian, H. (2011). A design model for strain-softening and strain-hardening fiber reinforced elements reinforced longitudinally with steel and FRP bars. *Composites Part B: Engineering*,*42*(6), 1630-1640.

55. Lim, T. Y., Paramisivam, P., & Lee, S. L. (1987). Bending behavior of steel-fiber concrete beams. *Structural Journal*, *84*(6), 524-536.

56. Lok, T. S., & Pei, J. S. (1998). Flexural behavior of steel fiber reinforced concrete. *Journal of Materials in Civil Engineering*, *10*(2), 86-97.

57. Vandewalle, L., Nemegeer, D., Balazs, L., Barr, B., Barros, J., Bartos, P., & Falkner, H. (2003). RILEM TC162-TDF: test and design methods for steel fibre reinforced concrete: sigma-epsilon design method (final recommendation). *Materials and Structures*, *36*(262), 560-567.

58. du Béton, F. I. (2013). fib model code for concrete structures 2010. *Wilhelm Ernst & Sohn., Berlin*.

59. di Prisco, M., Plizzari, G., & Vandewalle, L. (2014). Structural design according to fib MC 2010: comparison between RC and FRC elements. In*Proceedings of FRC*.

60. Kooiman, A. G. (2000). *Modelling steel fibre reinforced concrete for structural design*. TU Delft, Delft University of Technology.

61. Soranakom, C., & Mobasher, B. (2007). Closed-form solutions for flexural response of fiber-reinforced concrete beams. *Journal of engineering mechanics*, *133*(8), 933-941.

62. Soranakom, C., & Mobasher, B. (2008). Correlation of tensile and flexural responses of strain softening and strain hardening cement composites. *Cement and concrete Composites*, *30*(6), 465-477.

63. van Zijl, G. P. A. G., & Mbewe, P. B. K. (2013). Flexural modelling of steel fibre-reinforced concrete beams with and without steel bars. *Engineering Structures*, *53*, 52-62.

64. Meda, A., Plizzari, G. A., & Riva, P. (2004). Fracture behavior of SFRC slabs on grade. *Materials and Structures*, *37*(6), 405-411.

65. Belletti, B., Cerioni, R., Meda, A., & Plizzari, G. (2008). Design aspects on steel fiber-reinforced concrete pavements. *Journal of Materials in Civil Engineering*, *20*(9), 599-607.

66. Jacob, G. C., Starbuck, J. M., Fellers, J. F., Simunovic, S., & Boeman, R. G. (2004). Strain rate effects on the mechanical properties of polymer composite materials. *Journal of Applied Polymer Science*, *94*(1), 296-301.

67. Soutis, C. (2005). Carbon fiber reinforced plastics in aircraft construction.*Materials Science and Engineering: A*, *412*(1), 171-176.

68. Brameshuber, W. (2006). *Report 36: Textile Reinforced Concrete-State-of-the-Art Report of RILEM TC 201-TRC* (Vol. 36). RILEM publications.

69. Babaeidarabad, S., Arboleda, D., Loreto, G., & Nanni, A. (2014). Shear strengthening of un-reinforced concrete masonry walls with fabric-reinforced-cementitious-matrix. *Construction and Building Materials*, *65*, 243-253.

70. Babaeidarabad, S., Loreto, G., & Nanni, A. (2014). Flexural strengthening of RC beams with an externally bonded fabric-reinforced cementitious matrix.*Journal of Composites for Construction*, *18*(5), 04014009.

71. Wang, Y., & Xia, Y. (2000). Dynamic tensile properties of E-glass, Kevlar49 and polyvinyl alcohol fiber bundles. *Journal of materials science letters*,*19*(7), 583-586.

72. Zhou, Y., Wang, Y., Xia, Y., & Jeelani, S. (2010). Tensile behavior of carbon fiber bundles at different strain rates. *Materials Letters*, *64*(3), 246-248.

73. Hou, Y., Hu, H., Sun, B., & Gu, B. (2013). Strain rate effects on tensile failure of 3-D angle-interlock woven carbon fabric. *Materials & Design*, *46*, 857-866.

74. Sanborn, B., & Weerasooriya, T. (2014). Quantifying damage at multiple loading rates to Kevlar KM2 fibers due to weaving, finishing, and pre-twist.*International Journal of Impact Engineering*, *71*, 50-59.

75. Wang, Y., & Xia, Y. (1998). The effects of strain rate on the mechanical behaviour of Kevlar fibre bundles: an experimental and theoretical study.*Composites Part A: Applied Science and Manufacturing*, *29*(11), 1411-1415.

76. Wagner, H. D., Aronhime, J., & Marom, G. (1990, April). Dependence of the tensile strength of pitch-based carbon and para-aramid fibres on the rate of strain. In *Proceedings of the Royal Society of London A: Mathematical, Physical and Engineering Sciences* (Vol. 428, No. 1875, pp. 493-510). The Royal Society.

77. Cheng, M., Chen, W., & Weerasooriya, T. (2005). Mechanical properties of Kevlar® KM2 single fiber. *Journal of Engineering Materials and Technology*,*127*(2), 197-203.

78. Dooraki, B. F., Nemes, J. A., & Bolduc, M. (2006, August). Study of parameters affecting the strength of yarns. In *Journal de Physique IV (Proceedings)* (Vol. 134, pp. 1183-1188). EDP sciences.

79. Lim, J., Zheng, J. Q., Masters, K., & Chen, W. W. (2011). Effects of gage length, loading rates, and damage on the strength of PPTA fibers.*International Journal of Impact Engineering*, *38*(4), 219-227.

80. Joshi, S. V., Drzal, L. T., Mohanty, A. K., & Arora, S. (2004). Are natural fiber composites environmentally superior to glass fiber reinforced composites?. *Composites Part A: Applied science and manufacturing*, *35*(3), 371-376.

81. Fiore, V. I. N. C. E. N. Z. O., Di Bella, G., & Valenza, A. (2011). Glass–basalt/epoxy hybrid composites for marine applications. *Materials & Design*,*32*(4), 2091-2099.

82. Fiore, V., Scalici, T., Di Bella, G., & Valenza, A. (2015). A review on basalt fibre and its composites. *Composites Part B: Engineering*, *74*, 74-94.

83. Dhand, V., Mittal, G., Rhee, K. Y., Park, S. J., & Hui, D. (2015). A short review on basalt fiber reinforced polymer composites. *Composites Part B: Engineering*, *73*, 166-180.

84. Sarasini, F., Tirillò, J., Ferrante, L., Valente, M., Valente, T., Lampani, L., ... & Sorrentino, L. (2014). Drop-weight impact behaviour of woven hybrid basalt–carbon/epoxy composites. *Composites Part B: Engineering*, *59*, 204-220.

85. Dehkordi, M. T., Nosraty, H., Shokrieh, M. M., Minak, G., & Ghelli, D. (2013). The influence of hybridization on impact damage behavior and residual compression strength of intraply basalt/nylon hybrid composites. *Materials & Design*, *43*, 283-290.

86. Deák, T., & Czigány, T. (2009). Chemical composition and mechanical properties of basalt and glass fibers: a comparison. *Textile Research Journal*, *79*(7), 645-651.

87. Zhu, L., Sun, B., Hu, H., & Gu, B. (2010). Constitutive equations of basalt filament tows under quasi-static and high strain rate tension. *Materials Science and Engineering: A*, *527*(13), 3245-3252.

88. Zhu, L., Sun, B., & Gu, B. (2011). Frequency features of basalt filament tows under quasi-static and high strain rate tension. *Journal of Composite Materials*, 0021998311417648.

89. Yao, Y., Zhu, D., Zhang, H., Li, G., & Mobasher, B. (2016). Tensile Behaviors of Basalt, Carbon, Glass, and Aramid Fabrics under Various Strain Rates. *Journal of Materials in Civil Engineering*, 04016081.

90. Ou, Y., & Zhu, D. (2015). Tensile behavior of glass fiber reinforced composite at different strain rates and temperatures. Construction and Building Materials, 96, 648-656.

91. Montgomery, D. C. (2008). *Design and analysis of experiments*. John Wiley & Sons.

92. Amroune, S., Bezazi, A., Belaadi, A., Zhu, C., Scarpa, F., Rahatekar, S., & Imad, A. (2015). Tensile mechanical properties and surface chemical sensitivity of technical fibres from date palm fruit branches (Phoenix dactylifera L.). *Composites Part A: Applied Science and Manufacturing*, 71, 95-106.

93. Qi, Y., Li, J., & Liu, L. (2014). Tensile properties of multilayer-connected biaxial weft knitted fabric reinforced composites for carbon fibers. *Materials & Design*, 54, 678-685.

94. Misnon, M. I., Islam, M. M., Epaarachchi, J. A., & Lau, K. T. (2015). Analyses of woven hemp fabric characteristics for composite reinforcement. *Materials & Design*, 66, 82-92.

95. Zohdi, T. I., & Steigmann, D. J. (2002). The toughening effect of microscopic filament misalignment on macroscopic ballistic fabric response. *International journal of fracture*, 118(4), 71-76.

96. Lu, C., & Leung, C. K. (2016). A new model for the cracking process and tensile ductility of Strain Hardening Cementitious Composites (SHCC). *Cement and Concrete Research*, 79, 353-365.

97. Mechtcherine, V., Millon, O., Butler, M., & Thoma, K. (2011). Mechanical behaviour of strain hardening cement-based composites under impact loading. *Cement and Concrete Composites*, *33*(1), 1-11.

98. Kim, S. W., & Yun, H. D. (2011). Crack-damage mitigation and flexural behavior of flexure-dominant reinforced concrete beams repaired with strain-hardening cement-based composite. *Composites Part B: Engineering*, 42(4), 645-656.

99. Kim, S. W., Park, W. S., Jang, Y. I., Feo, L., & Yun, H. D. (2015). Crack damage mitigation and shear behavior of shear-dominant reinforced concrete beams repaired with strain-hardening cement-based composite. *Composites Part B: Engineering*, 79, 6-19.

100. Mechtcherine, V., de Andrade Silva, F., Müller, S., Jun, P., & Toledo Filho, R. D. (2012). Coupled strain rate and temperature effects on the tensile behavior of strain-hardening cement-based composites (SHCC) with PVA fibers. *Cement and Concrete Research*, 42(11), 1417-1427.

101. Curosu, I., Mechtcherine, V., & Millon, O. (2016). Effect of fiber properties and matrix composition on the tensile behavior of strain-hardening cement-based composites (SHCCs) subject to impact loading. *Cement and Concrete Research*, 82, 23-35.

102. Soe, K. T., Zhang, Y. X., & Zhang, L. C. (2013). Impact resistance of hybrid-fiber engineered cementitious composite panels. *Composite Structures*, 104, 320-330.

103. Li, Z., Mu, B., & Chui, S. N. (2001). Static and dynamic behavior of extruded sheets with short fibers. *Journal of Materials in Civil Engineering*, 13(4), 248-254.

104. Secrieru, E., Mechtcherine, V., Schröfl, C., & Borin, D. (2016). Rheological characterisation and prediction of pumpability of strain-hardening cement-based-composites (SHCC) with and without addition of superabsorbent polymers (SAP) at various temperatures. *Construction and Building Materials*, 112, 581-594.

105. Boshoff, W. P., Mechtcherine, V., & van Zijl, G. P. (2009). Characterising the time-dependant behaviour on the single fibre level of SHCC: Part 2: The rate effects on fibre pull-out tests. *Cement and Concrete Research*, 39(9), 787-797.

106. Zhu, D., Mobasher, B., & Rajan, S. D. (2010). Dynamic tensile testing of Kevlar 49 fabrics. *Journal of Materials in Civil Engineering*, 23(3), 230-239.

107. Sutton, M. A., Wolters, W. J., Peters, W. H., Ranson, W. F., & McNeill, S. R. (1983). Determination of displacements using an improved digital correlation method. *Image and Vision Computing*, 1(3), 133-139.

108 Bruck, H. A., McNeill, S. R., Sutton, M. A., & Peters Iii, W. H. (1989). Digital image correlation using Newton-Raphson method of partial differential correction. *Experimental mechanics*, 29(3), 261-267.

109. Giancane, S., Panella, F. W., Nobile, R., & Dattoma, V. (2010). Fatigue damage evolution of fiber reinforced composites with digital image correlation analysis. *Procedia Engineering*, 2(1), 1307-1315.

110. Destrebecq, J. F., Toussaint, E., & Ferrier, E. (2011). Analysis of cracks and deformations in a full scale reinforced concrete beam using a digital image correlation technique. *Experimental Mechanics*, 51(6), 879-890.

111. Shah, S. G., & Kishen, J. C. (2011). Fracture properties of concrete–concrete interfaces using digital image correlation. *Experimental Mechanics*, 51(3), 303-313.

112. Koerber, H., Xavier, J., & Camanho, P. P. (2010). High strain rate characterisation of unidirectional carbon-epoxy IM7-8552 in transverse compression and in-plane shear using digital image correlation. *Mechanics of Materials*, 42(11), 1004-1019.

113. Gao, G., Huang, S., Xia, K., & Li, Z. (2015). Application of digital image correlation (DIC) in dynamic notched semi-circular bend (NSCB) tests. *Experimental Mechanics*, 55(1), 95-104.

114. Pan, B., Qian, K., Xie, H., & Asundi, A. (2009). Two-dimensional digital image correlation for in-plane displacement and strain measurement: a review. *Measurement Science and Technology*, *20*(6), 062001.

115. Yao, Y., Silva, F. A., Butler, M., Mechtcherine, V., & Mobasher, B. (2015). Tension stiffening in textile-reinforced concrete under high speed tensile loads. *Cement and Concrete Composites*, *64*, 49-61.

116. de Andrade Silva, F., Zhu, D., Mobasher, B., Soranakom, C., & Toledo Filho, R. D. (2010). High speed tensile behavior of sisal fiber cement composites.*Materials Science and Engineering: A*, *527*(3), 544-552.

117. Peled, A., Sueki, S., & Mobasher, B. (2006). Bonding in fabric–cement systems: effects of fabrication methods. *Cement and Concrete Research*,*36*(9), 1661-1671.

118. Peled, A., Cohen, Z., Pasder, Y., Roye, A., & Gries, T. (2008). Influences of textile characteristics on the tensile properties of warp knitted cement based composites. *Cement and Concrete Composites*, *30*(3), 174-183.

119. Peled, A., & Mobasher, B. (2007). Tensile behavior of fabric cement-based composites: pultruded and cast. *Journal of Materials in Civil Engineering*, 19(4), 340-348.

120. Peled, A., Mobasher, B., & Cohen, Z. (2009). Mechanical properties of hybrid fabrics in pultruded cement composites. *Cement and Concrete Composites*, *31*(9), 647-657.

121. Yao, Y. (2013). *Application of 2-D Digital Image Correlation (DIC) method to Damage Characterization of Cementitious Composites under Dynamic Tensile Loads*. Arizona State University.

122. Zhu, D., Rajan, S. D., Mobasher, B., Peled, A., & Mignolet, M. (2011). Modal analysis of a servo-hydraulic high speed machine and its application to dynamic tensile testing at an intermediate strain rate. *Experimental Mechanics*, *51*(8), 1347-1363.

123. Peled, A., & Bentur, A. (2000). Geometrical characteristics and efficiency of textile fabrics for reinforcing cement composites. *Cement and Concrete Research*, *30*(5), 781-790.

124. Barhum, R., & Mechtcherine, V. (2012). Effect of short, dispersed glass and carbon fibres on the behaviour of textile-reinforced concrete under tensile loading. *Engineering Fracture Mechanics*, 92, 56-71.

125. Barhum, R., & Mechtcherine, V. (2013). Influence of short dispersed and short integral glass fibres on the mechanical behaviour of textile-reinforced concrete. *Materials and Structures*, 46(4), 557-572.

126. Bhat, P. S., Chang, V., & Li, M. (2014). Effect of elevated temperature on strain-hardening engineered cementitious composites. *Construction and Building Materials*, 69, 370-380.

127. de Andrade Silva, F., Butler, M., Hempel, S., Toledo Filho, R. D., & Mechtcherine, V. (2014). Effects of elevated temperatures on the interface properties of carbon textile-reinforced concrete. *Cement and Concrete Composites*, 48, 26-34.

128. Kravaev, P., Janetzko, S., Gries, T., Kang, B. G., Brameshuber, W., Zell, M., & Hegger, J. (2009). Commingling yarns for reinforcement of concrete.

129. Peled, A., & Mobasher, B. (2006). Properties of fabric–cement composites made by pultrusion. *Materials and Structures*, 39(8), 787-797.

130. Mobasher, B., Dey, V., Cohen, Z., & Peled, A. (2014). Correlation of constitutive response of hybrid textile reinforced concrete from tensile and flexural tests. *Cement and Concrete Composites*, *53*, 148-161.

131. Butler, M., Hempel, S., & Mechtcherine, V. (2011). Modelling of ageing effects on crack-bridging behaviour of AR-glass multifilament yarns embedded in cement-based matrix. *Cement and Concrete Research*, *41*(4), 403-411.

132. Ferreira, T., & Rasband, W. (2012). ImageJ user guide. *IJ1. 46r. Natl. Inst. Health, Bethesda, MD. http://rsb.info.nih.gov/ij/docs/guide/user-guide.pdf*

133. Soranakom, C., & Mobasher, B. (2010). Modeling of tension stiffening in reinforced cement composites: Part I. Theoretical modeling. *Materials and Sstructures*, 43(9), 1217-1230.

134. Soranakom, C., & Mobasher, B. (2010). Modeling of tension stiffening in reinforced cement composites: Part II. Simulations versus experimental results. *Materials and Structures*, *43*(9), 1231-1243.

135. Portal, N. W., Perez, I. F., Thrane, L. N., & Lundgren, K. (2014). Pull-out of textile reinforcement in concrete. *Construction and Building Materials*, *71*, 63-71.

136. Tuyan, M., & Yazıcı, H. (2012). Pull-out behavior of single steel fiber from SIFCON matrix. *Construction and Building Materials*, *35*, 571-577.

137. Naaman, A. E., Namur, G. G., Alwan, J. M., & Najm, H. S. (1991). Fiber pullout and bond slip. I: Analytical study. *Journal of Structural Engineering*,*117*(9), 2769-2790.

138. Sueki, S., Soranakom, C., Mobasher, B., & Peled, A. (2007). Pullout-slip response of fabrics embedded in a cement paste matrix. *Journal of Materials in Civil Engineering*, *19*(9), 718-727.

139. Cohen, Z., & Peled, A. (2010). Controlled telescopic reinforcement system of fabric–cement composites—Durability concerns. *Cement and Concrete Research*, *40*(10), 1495-1506.

140. Banholzer, B., Brockmann, T., & Brameshuber, W. (2006). Material and bonding characteristics for dimensioning and modelling of textile reinforced concrete (TRC) elements. *Materials and Structures*, *39*(8), 749-763.

141. Soranakom, C., & Mobasher, B. (2009). Geometrical and mechanical aspects of fabric bonding and pullout in cement composites. *Materials and Structures*, *42*(6), 765-777.

142. Destrée, X., Yao, Y., & Mobasher, B. (2015). Sequential Cracking and Their Openings in Steel-Fiber-Reinforced Joint-Free Concrete Slabs. *Journal of Materials in Civil Engineering*, 28(4), 04015158.

143. Zhang, J., Hou, D., & Gao, Y. (2012). Calculation of shrinkage stress in early-age concrete pavements. I: Calculation of shrinkage strain. *Journal of Transportation Engineering*, *139*(10), 961-970.

144. Meininger, R. C. (1966). Drying shrinkage of concrete. *Engineering Report No. RD3 (A Summary of Joint Research Laboratory Series J–135, J–145, 173, and, 143* (pp. 22). National Ready Mixed Concrete Association, Silver Spring, MD.

145. Zhang, W., Zakaria, M., & Hama, Y. (2013). Influence of aggregate materials characteristics on the drying shrinkage properties of mortar and concrete.*Construction and Building Materials*, *49*, 500-510.

146. Mangat, P. S., & Azari, M. M. (1988). Shrinkage of steel fibre reinforced cement composites. *Materials and Structures*, *21*(3), 163-171.

147. Gribniak, V., Kaklauskas, G., Kliukas, R., & Jakubovskis, R. (2013). Shrinkage effect on short-term deformation behavior of reinforced concrete–when it should not be neglected. *Materials & Design*, *51*, 1060-1070.

148. Güneyisi, E., Gesoğlu, M., Mohamadameen, A., Alzeebaree, R., Algın, Z., & Mermerdaş, K. (2014). Enhancement of shrinkage behavior of lightweight aggregate concretes by shrinkage reducing admixture and fiber reinforcement. *Construction and Building Materials*, *54*, 91-98.

149. Shah, S. P., Weiss, W. J., & Yang, W. (1998). Shrinkage Cracking--Can It Be Prevented?. *Concrete International*, *20*(4), 51-55.

150. Voigt, T., Bui, V. K., & Shah, S. P. (2004). Drying shrinkage of concrete reinforced with fibers and welded-wire fabric. *Materials Journal*, *101*(3), 233-241.

151. Silfwerbrand, J. (2004). Design of Steel Fibre Reinforced Concrete Slabs on Grade for Restrained Loading. In *6th RILEM Symposium on Fibre Reinforced Concrete, Varenna, Italy* (pp. 975-984).

152. Bakhshi, M., & Mobasher, B. (2011). Experimental observations of early-age drying of Portland cement paste under low-pressure conditions. *Cement and Concrete Composites*, *33*(4), 474-484.

153. Bakhshi, M., Mobasher, B., & Soranakom, C. (2012). Moisture loss characteristics of cement-based materials under early-age drying and shrinkage conditions. *Construction and Building Materials*, *30*, 413-425.

154. Chia, W. S., McCullough, B. F., & Burns, N. H. (1986). Field evaluation of subbase friction characteristics. Center for Transportation Research, Univ. of Texas at Austin, Austin, TX.

155. Lee, S. W. (2000). Characteristics of friction between concrete slab and base. *KSCE Journal of Civil Engineering*, *4*(4), 265-275.

156. Maitra, S. R., Reddy, K. S., & Ramachandra, L. S. (2009). Experimental evaluation of interface friction and study of its influence on concrete pavement response. *Journal of Transportation Engineering*, *135*(8), 563-571.

157. Stott, J. P. (1961). Tests on materials for use in sliding layers under concrete road slabs. *KSCE Journal of Civil Engineering*, *56*(663), 1297-1299.

158. Friberg, B. F. (1954). Frictional resistance under concrete pavements and restraint stresses in long reinforced slabs. In *Highway Research Board Proceedings* (Vol. 33).

159. Sparkes, F. N. (1939). Stresses in concrete road slabs. *Struct. Engr*, 17(2), 98-116.

160. Chan Suh, Y., Woo Lee, S., & Soo Kang, M. (2002). Evaluation of subbase friction for typical Korean concrete pavement. *Transportation Research Record: Journal of the Transportation Research Board*, (1809), 66-73.

161. Venkatasubramanian, V. (1964*). Investigation on temperature and friction stresses in bonded cement concrete pavements.* Ph.D. dissertation, Indian Institute of Technology, Kharagpur, India.

162. Malmberg, B., & Skarendahl, A. (1978). Method of studying the cracking of fibre concrete under restrained shrinkage. In *RILEM Symposium on Testing and Test Methods of Fiber Cement Composites* (pp. 173-179).

163. Yang, S., & Chen, J. (1988). Bond-slip and crack width calculations of tension members. *Structural Journal*, *85*(4), 414-422.

164. Borosnyói, A., & Balázs, G. L. (2005). Models for flexural cracking in concrete: the state of the art. *Structural Concrete*, *6*(2), 53-62.

165. Georgiadi-Stefanidi, K., Mistakidis, E., Pantousa, D., & Zygomalas, M. (2010). Numerical modelling of the pull-out of hooked steel fibres from high-strength cementitious matrix, supplemented by experimental results.*Construction and Building Materials*, *24*(12), 2489-2506.

166. Tuma JJ. (1970). *Engineering mathematics handbook*, McGraw-Hill, New York.

167. Al-Saleh, S. A. (2014). Comparison of theoretical and experimental shrinkage in concrete. *Construction and Building Materials*, *72*, 326-332.

168. Yoo, D. Y., Min, K. H., Lee, J. H., & Yoon, Y. S. (2014). Shrinkage and cracking of restrained ultra-high-performance fiber-reinforced concrete slabs at early age. *Construction and Building Materials*, *73*, 357-365.

169. Mobasher, B., Yao, Y., & Soranakom, C. (2015). Analytical solutions for flexural design of hybrid steel fiber reinforced concrete beams. *Engineering Structures*, 100, 164-177.

170. Naaman, A. E., Namur, G. G., Alwan, J. M., & Najm, H. S. (1991). Fiber Pullout and Bond Slip. II: Experimental Validation. *Journal of Structural Engineering*, 117(9), 2791-2800.

171. Guo, E. H., Dong, M. M., Daiutolo, H., & Dong, M. M. (2005). Curling under different environmental variations as monitored in a single concrete slab. In *Eighth International Conference on Concrete Pavements* (pp. 14-18). Transportation Research Board, Washington, DC.

172. Daiutolo, H. (2008). Control of slab curling in rigid pavements at the FAA national airport pavement test facility. In *Proc., 3rd Int. Conf. on Accelerated Pavement Testing* (pp. 1-3).

173. Hiller, J. E., & Roesler, J. R. (2009). Simplified nonlinear temperature curling analysis for jointed concrete pavements. *Journal of Transportation Engineering*, *136*(7), 654-663.

174. Jeong, J. H., & Zollinger, D. G. (2005). Environmental effects on the behavior of jointed plain concrete pavements. *Journal of Transportation Engineering*, *131*(2), 140-148.

175. Rao, S., & Roesler, J. R. (2005). Characterizing effective built-in curling from concrete pavement field measurements. *Journal of Transportation Engineering*, 131(4), 320-327.

176. Rufino, D., & Roesler, J. (2006). Effect of slab-base interaction on measured concrete pavement responses. *Journal of Transportation Engineering*, 132(5), 425-434.

177. Ceylan, H., et al. (2005). "Impact of curling, warping, and other early-age behavior on concrete pavement smoothness: Early, frequent, and detailed (EFD) study." Iowa State Univ., National Concrete Pavement Technology Center, Ames, IA.

178. Heath, A., and Roesler, J. (1999). "Shrinkage and thermal cracking of fast setting hydraulic cement concrete pavements in Palmdale, California." Pavement Research Center, Institute of Transportation Studies, Univ. of California, Berkeley, CA.

179. Hillerborg, A., Modéer, M., & Petersson, P. E. (1976). Analysis of crack formation and crack growth in concrete by means of fracture mechanics and finite elements. *Cement and Concrete Research*, *6*(6), 773-781.

180. Zhang, J., & Stang, H. (1998). Applications of stress crack width relationship in predicting the flexural behavior of fibre-reinforced concrete. *Cement and Concrete Research*, *28*(3), 439-452.

181. Belytschko, T., & Black, T. (1999). Elastic crack growth in finite elements with minimal remeshing. *International journal for numerical methods in engineering*, *45*(5), 601-620.

182. Denneman, E., Wu, R., Kearsley, E. P., & Visser, A. T. (2011). Discrete fracture in high performance fibre reinforced concrete materials. *Engineering Fracture Mechanics*, *78*(10), 2235-2245.

183. Van Mier, J. G. (1996). *Fracture processes of concrete* (Vol. 12). New York, NY: CRC press.

184. Vandewalle, L. (2002). Design of steel fibre reinforced concrete using the sigma-w method: principles and applications. *Materials and Structures*,*35*(249), 262-278.

185. Minelli, F., & Plizzari, G. (2015). Derivation of a simplified stress–crack width law for Fiber Reinforced Concrete through a revised round panel test. *Cement and Concrete Composites*, *58*, 95-104.

186. Abrishambaf, A., Barros, J. A., & Cunha, V. M. (2015). Tensile stress–crack width law for steel fibre reinforced self-compacting concrete obtained from indirect (splitting) tensile tests. *Cement and Concrete Composites*, *57*, 153-165.

187. di Prisco, M., Colombo, M., & Dozio, D. (2013). Fibre-reinforced concrete in fib Model Code 2010: principles, models and test validation. *Structural Concrete*, *14*(4), 342-361.

188. di Prisco, M., Felicetti, R., & Gambarova, P. G. (1999). On the evaluation of the characteristic length in high strength concrete. In *First Engineering Foundation Conference on High Strength Concrete (pp. 377-390).*

189. Koeberl, B., & Willam, K. (2008). Question of tension softening versus tension stiffening in plain and reinforced concrete. *Journal of Engineering Mechanics*, *134*(9), 804-808.

190. Buratti, N., Ferracuti, B., & Savoia, M. (2013). Concrete crack reduction in tunnel linings by steel fibre-reinforced concretes. *Construction and Building Materials*, 44, 249-259.

191. Mobasher, B. (2011). *Mechanics of fiber and textile reinforced cement composites* (pp. 480). CRC press.

192. Subcommittee, A. S. T. M. *A01. 05. 2015. Standard Specification for Deformed and Plain Carbon-Steel Bars for Concrete Reinforcement*. ASTM A615/A615M-15. West Conshohocken, PA: ASTM International.

193. MacGregor, J. G., Wight, J. K., Teng, S., & Irawan, P. (1997). *Reinforced concrete: mechanics and design* (Vol. 3). Upper Saddle River, NJ: Prentice Hall.

194. Eivind, H. (1951). A study of combined bending and axial load in reinforced concrete members (pp. 128). *Bulletin Series*, (399). University of Illinois Engineering Experimental Station.

195. ACI Committee 318. 318-14: Building Code Requirements for Structural Concrete and Commentary, 2014.

196. No, E. (1992). 2, Design of Concrete Structures, Part 1: General Rules and Rules for buildings. *Commission of European Communities ENV*, 1-1.

197. Bosco, C., Carpinteri, A., & Debernardi, P. G. (1990). Minimum reinforcement in high-strength concrete. *Journal of Structural Engineering*,*116*(2), 427-437.

198. Bosco, C., Carpinteri, A., & Debernardi, P. G. (1990). Fracture of reinforced concrete: scale effects and snap-back instability. *Engineering Fracture Mechanics*, *35*(4-5), 665-677.

199. Ferro, G., Carpinteri, A., & Ventura, G. (2007). Minimum reinforcement in concrete structures and material/structural instability. *International Journal of Fracture*, *146*(4), 213-231.

200. Chen, L., & Graybeal, B. A. (2011). Modeling structural performance of second-generation ultrahigh-performance concrete pi-girders. *Journal of Bridge Engineering*, 17(4), 634-643.

201. Dupont, D. (2003). *Modelling and experimental validation of the constitutive law (σ-ε) and cracking behaviour of fibre reinforced concrete* (Doctoral dissertation, Ph. D. Thesis, Katholieke Universiteit Leuven).

202. Bakhshi, M., Barsby, C., & Mobasher, B. (2014). Comparative evaluation of early age toughness parameters in fiber reinforced concrete. *Materials and structures*, *47*(5), 853-872.

203. Demir, A., Caglar, N., Ozturk, H., & Sumer, Y. (2016). Nonlinear finite element study on the improvement of shear capacity in reinforced concrete T-Section beams by an alternative diagonal shear reinforcement. *Engineering Structures*, 120, 158-165.

204. Abdul-Ahad, R. B., & Aziz, O. Q. (1999). Flexural strength of reinforced concrete T-beams with steel fibers. *Cement and Concrete Composites*, 21(4), 263-268.

205. Graybeal, B. A. (2009). *Structural Behavior of a 2nd Generation UHPC Pi-girder*. US Department of Transportation, Federal Highway Administration, Research, Development and Technology, Turner-Fairbank Highway Research Center.

206. Jiang, Z., & Banthia, N. (2010). Size effects in flexural toughness of fiber reinforced concrete. *Journal of Testing and Evaluation*, 38(3), 1-7.

207. Kim, D. J., Naaman, A. E., & El-Tawil, S. (2010, May). Correlation between tensile and bending behavior of FRC composites with scale effect. In *Proceedings of FraMCoS-7, 7th international conference on fracture mechanics of concrete and concrete structures. Jeju Island, South Korea*.

208. Mobasher, B., Bakhshi, M., & Barsby, C. (2014). Backcalculation of residual tensile strength of regular and high performance fiber reinforced concrete from flexural tests. *Construction and Building Materials*, 70, 243-253.

209. Barros, J. A., & Figueiras, J. A. (1999). Flexural behavior of SFRC: testing and modeling. *Journal of Materials in Civil Engineering*, *11*(4), 331-339.

210. Soranakom, C. (2008). *Multi-scale modeling of fiber and fabric reinforced cement based composites.* Ph.D. Dissertation, Arizona State University.

211. Rocca, S., Galati, N., & Nanni, A. (2009). Interaction diagram methodology for design of FRP-confined reinforced concrete columns. *Construction and Building Materials*, 23(4), 1508-1520.

212. Whitney, C. S., & Cohen, E. (1956, November). Guide for ultimate strength design of reinforced concrete. In *ACI Journal Proceedings* (Vol. 53, No. 11, pp. 455-490).

213. Hernández-Montes, E., Gil-Martín, L. M., & Aschheim, M. (2005). Design of concrete members subjected to uniaxial bending and compression using reinforcement sizing diagrams. *ACI structural journal*, 102(1), 150.

214. Bresler, B. (1960, November). Design criteria for reinforced columns under axial load and biaxial bending. In *ACI Journal Proceedings* (Vol. 57, No. 11, pp. 481-490).

215. Meek, J. L. (1963, August). Ultimate strength of columns with biaxially eccentric loads. In *ACI Journal Proceedings* (Vol. 60, No. 8, pp. 1053-1064).

216. Pannell, F. N. (1963, January). Failure surfaces for members in compression and biaxial bending. In *ACI Journal Proceedings* (Vol. 60, No. 1, pp. 129-140).

217. Parme, A. L., Nieves, J. M., & Gouwens, A. (1966, September). Capacity of Reinorced Rectangular Columns Subject to Biaxial Bending. In *ACI Journal Proceedings* (Vol. 63, No. 9, pp. 911-924).

218. Weber, D. C. (1966, November). Ultimate strength design charts for columns with biaxial bending. In *ACI Journal Proceedings* (Vol. 63, No. 11, pp. 1205-1230).

219. Rotter, J. M. (1985). Rapid exact inelastic biaxial bending analysis. *Journal of Structural Engineering*, 111(12), 2659-2674.

220. Marin, J. (1979, November). Design aids for L-shaped reinforced concrete columns. In *ACI Journal Proceedings* (Vol. 76, No. 11, pp. 1197-1216).

221. Rodriguez, J. A., & Aristizabal-Ochoa, J. D. (1999). Biaxial interaction diagrams for short RC columns of any cross section. *Journal of Structural Engineering*, 125(6), 672-683.

222. Mansur, M. A., Chin, M. S., & Wee, T. H. (1997). Stress-strain relationship of confined high-strength plain and fiber concrete. *Journal of Materials in Civil engineering*, *9*(4), 171-179.

223. Chaallal, O., & Shahawy, M. (2000). Performance of fiber-reinforced polymer-wrapped reinforced concrete column under combined axial-flexural loading (pp. 659-668). *ACI Structural Journal*, *97*(4).

224. De la Fuente, A., Pujadas, P., Blanco, A., & Aguado, A. (2012). Experiences in Barcelona with the use of fibres in segmental linings. *Tunnelling and Underground Space Technology*, *27*(1), 60-71.

225. Tiberti, G. (2009). *Concrete tunnel segments with combined traditional and fiber reinforcement: optimization of the structural behaviour and design aspects* (Doctoral dissertation, PhD thesis, University of Brescia).

226. Chiaia, B., Fantilli, A. P., & Vallini, P. (2009). Combining fiber-reinforced concrete with traditional reinforcement in tunnel linings. *Engineering Structures*, 31(7), 1600-1606.

227. Chiaia, B., Fantilli, A. P., & Vallini, P. (2007). Evaluation of minimum reinforcement ratio in FRC members and application to tunnel linings. *Materials and Structures*, 40(6), 593-604.

228. Gesoğlu, M., Güneyisi, E. M., Güneyisi, E., Yılmaz, M. E., & Mermerdaş, K. (2014). Modeling and analysis of the shear capacity of adhesive anchors post-installed into uncracked concrete. *Composites Part B: Engineering*, 60, 716-724.

229. Singh, B., & Jain, K. (2014). Appraisal of steel fibers as minimum shear reinforcement in concrete beams. *ACI Structural Journal*, *111*(5), 1191.

230. Batson, G. (1976). Steel fiber reinforced concrete. *Materials Science and Engineering*, *25*, 53-58.

231. Vandewalle, L. (1999, May). Influence of Tensile Strength of Steel Fibre on the Toughness of High Strength Concrete. In *Third International Workshop" High Performance Fiber Reinforced Cement Composites"* (pp. 331-340).

232. Balaguru, P., Narahari, R., & Patel, M. (1992). Flexural toughness of steel fiber reinforced concrete. *Materials Journal*, *89*(6), 541-546.

233. Lee, S. C., Cho, J. Y., & Vecchio, F. J. (2011). Diverse embedment model for steel fiber-reinforced concrete in tension: Model development. *ACI Materials Journal*, *108*(5), 516-525.

234. Voo, J. Y., & Foster, D. S. J. (2003). *Variable engagement model for fibre reinforced concrete in tension*. University of New South Wales, School of Civil and Environmental Engineering. (pp.86)

235. Shah, S. P., & Rangan, B. V. (1971, February). Fiber reinforced concrete properties. In *ACI Journal Proceedings* (Vol. 68, No. 2, pp. 126-137).

236. Grzybowski, M., & Shah, S. P. (1990). Shrinkage cracking of fiber reinforced concrete. *Materials Journal, 87*(2), 138-148.

237. Banthia, N., Azzabi, M., & Pigeon, M. (1993). Restrained shrinkage cracking in fibre-reinforced cementitious composites. *Materials and Structures, 26*(7), 405-413.

238. Ong, K. C. G., & Paramasivam, P. (1989). Cracking of steel fibre reinforced mortar due to restrained shrinkage. *Fibre Reinforced Cements and Concretes: Recent Developments*, 179-187.

239. Dinh, H. H., Parra-Montesinos, G. J., & Wight, J. K. (2010). Shear strength model for steel fiber reinforced concrete beams without stirrup reinforcement. *Journal of Structural Engineering*, *137*(10), 1039-1051.

240. Parra-Montesinos, G. J. (2006). Shear strength of beams with deformed steel fibers. *CONCRETE INTERNATIONAL DETROIT*, *28*(11), 57.

241. Ding, Y., Zhang, F., Torgal, F., & Zhang, Y. (2012). Shear behaviour of steel fibre reinforced self-consolidating concrete beams based on the modified compression field theory. *Composite Structures*, 94(8), 2440-2449.

242. Minelli, F., Conforti, A., Cuenca, E., & Plizzari, G. (2014). Are steel fibres able to mitigate or eliminate size effect in shear? *Materials and Structures*,47(3), 459-473.

243. Manual, L. D. K. U. S. (2007). Version 971. Livermore Software Technology Corporation, 7374.

244. Murray, Y. D. (2007). User's manual for LS-DYNA concrete material model 159 (No. FHWA-HRT-05-062).

245. Murray, Y. D., Abu-Odeh, A. Y., & Bligh, R. P. (2007). Evaluation of LS-DYNA concrete material model 159 (No. FHWA-HRT-05-063).

246. Nowak, A. S., & Collins, K. R. (2000). Reliability of Structures (pp. 360). New York: McGraw-Hill.

247. ASCE. (2010). Minimum design loads for buildings and other structures. ASCE/SEI 7-10-2013.

248. Nawy, E. G. Reinforced Concrete: A Fundamental Approach, Prentice Hall, 1996, New Jersey.

249. Nowak, A. S., & Szerszen, M. M. (2003). Calibration of design code for buildings (ACI 318): Part 1- Statistical models for resistance. *ACI Structural Journal*, *100*(3), 377-382.

250. Lu, R., Luo, Y., & Conte, J. P. (1994). Reliability evaluation of reinforced concrete beams. *Structural Safety*, *14*(4), 277-298.

251. Mirza, S. A., & MacGregor, J. G. (1979). Variations in dimensions of reinforced concrete members. *Journal of the Structural Division*, *105*(4), 751-766.

252. USACE, 1997. Engineering and design: Introduction to probability and reliability methods for use in geotechnical engineering. U.S. Army Corps of Engineers, Dept. of the Army, Washington, D.C.

253. Szerszen, M. M., & Nowak, A. S. (2003). Calibration of design code for buildings (ACI 318): Part 2—Reliability analysis and resistance factors. *ACI Structural Journal*, 100(3), 383-391.